

Multiple Scaled Experimentation in Fatigue Crack Growth: Finite Similitude Theory

A thesis submitted to The University of Manchester
for the degree of Doctor of Philosophy
in the Faculty of Science and Engineering

2022

Osagie P. Akhigbe-Midu

**School of Engineering
Department of Mechanical, Aerospace and Civil Engineering
The University of Manchester**

List of Contents

List of Contents	2
List of Figures	6
List of Tables.....	9
Abstract	11
Declaration	12
Copyright Statement	13
Acknowledgments.....	14
Nomenclature	15
Chapter 1 Introduction	18
1.1 Motivation	18
1.2 Research Aim and Objectives	22
1.3 Research Methodology	23
1.3.1 Fracture Mechanics Method	23
1.3.2 Cohesive Zone Model.....	24
1.3.3 Extended Finite Element Method	25
1.3.4 Finite Similitude Theory	26
1.4 Thesis Outline.....	27
Chapter 2 Literature Review	30
2.1 Introduction	30
2.2 Fracture Mechanics	32
2.2.1 Near Crack Tip Stress Field.....	33
2.3 Mechanism of Fatigue	36
2.3.1 Fatigue Crack Initiation	36
2.3.2 Fatigue Crack Propagation.....	37
2.4 Fatigue Crack Growth Models	39
2.5 Mixed Mode Fatigue	41
2.5.1 Crack Growth Rate	41
2.5.2 Crack Propagation Direction	43

2.6 Numerical Methods for Fatigue Crack Growth Analysis.....	43
2.6.1 Cohesive Zone Model (CZM)	44
2.6.2 Finite Element Method (FEM)	46
2.6.3 Extended Finite Element Method (XFEM)	47
2.7 Scaled Experimentation in Fatigue.....	50
2.7.1 Historical Overview.....	51
2.7.2 Similitude (Similarity Laws)	52
2.7.3 Dimensional Analysis (Buckingham- Pi Theorem).....	54
2.8 Size Effects in Fatigue.....	56
2.9 Application of Dimensional Analysis to Fatigue	57
2.10 Microstructural Size Effects in Fatigue	59
Chapter 3 Scaled Cohesive Zone Models for Fatigue Crack Propagation.....	62
3.1 Introduction	62
3.2 Recap on Finite Similitude	65
3.2.1. The metaphysics of space scaling.....	65
3.2.2. Moving control volumes.....	66
3.2.3. Projected Transport Equations.....	67
3.2.4. First-order finite similitude theory.....	72
3.3 One-Dimensional Cohesive Elements.....	76
3.3.1 The scaling of Model A-a	78
3.3.2. The scaling of Model A-b.....	81
3.3.3. The scaling of Model A-c	82
3.3.4. The scaling of Model B-a	83
3.3.5. The scaling of Model B-b	85
3.3.6. The scaling of Model B-c	85
3.4 General Applicability of First Order Scaling	86
3.4.1. Analytical study detailing the application of finite similitude rules.....	87

3.5 Numerical Experimentation	90
3.5.1. Verification of numerical results	91
3.5.2 Evaluation of the fatigue crack growth rate of ASTM E647 specimens	92
3.5.3 Results.....	98
3.6 Conclusions	106
Chapter 4 Scaled Empirical Fatigue Laws	108
4.1. Introduction	108
4.2. A Brief Recap on Finite Similitude	110
4.2.1. The effects of space scaling	111
4.2.2. The projection of transport equations	113
4.2.3. Defining similitude rules	115
4.3. Finite Similitude Applied to Solid Mechanics and Fracture	116
4.3.1. Projected transport equations.....	117
4.3.2. Fracture and fatigue on Ω_β	119
4.3.3. Practical application of first order finite similitude rules.	121
4.3.4. Empirical fatigue equations on Ω_β	122
4.4. Experimental Investigation.....	123
4.4.1. Case study I: Three-point bending fatigue test of concrete	123
4.4.2. Case study II: Three-point bending fatigue test of concrete	126
4.5. Numerical Experimentation	128
4.5.1. Verification of numerical results	130
4.5.2. Case study I: Single edge notched tensile specimen (SENT).....	131
4.5.3. Case study II: Semi-elliptical crack in a pipeline	136
4.5.4. Case study III: Semi-elliptical Crack in a Pressure Vessel.....	139
4.6. Conclusions	144
Chapter 5 Scaled Fatigue Cracks Under Service Loads.....	146
5.1 Introduction	146

5.2 A Description of the Finite Similitude Theory	150
5.2.1 Definition (High-order finite similitude)	152
5.3 Finite Similitude Applied to Fatigue	154
5.4 Practical Application of First Order Finite Similitude Rules.	157
5.5 Numerical Experimentation	158
5.5.1. Verification of numerical results	160
5.5.2. Case study I: Compact tension shear specimen (CTS)	164
5.5.3. Case study II: Fatigue of wing-fuselage attachment lug of a light aircraft.....	172
5.5.4. Case study III: Friction stir welded t-joint with an inclined semi- elliptical crack	175
5.6 Conclusions	181
6. Discussion	183
7. Conclusions	190
8. Recommendations for future work.....	194
Appendix: Publications	197
References	198
Word count 51587	

List of Figures

Figure 1.1: Sketch for the prediction of the structural behaviour of a prototype, based on the experimental results of a scaled model.	20
Figure 1.2: Propagating crack with enrichment nodes in XFEM formulation.....	26
Figure 2.1: Schematic of basic fracture modes [46].	33
Figure 2.2: Infinite plate with centre crack of length $2a$ under uniform biaxial traction.....	34
Figure 2.3: Fatigue crack initiation and propagation process [45].....	37
Figure 2.4: Fatigue crack growth curve	39
Figure 2.5: Fracture model of Dugdale [73]	45
Figure 2.6: Various traction separation laws.....	45
Figure 2.7: Timeline of development of similarity techniques [13]	52
Figure 3.1: Space scaling and its geometrical effect on a cyclically loaded rod modelled as a combined spring-cohesive element.	66
Figure 3.2: Synchronous moving-control volumes in trial space and physical spaces tracking a moving cyclically loaded rod.	69
Figure 3.3: Cohesive zone model for a crack and its associated traction-separation curve. 77	
Figure 3.4: Stress-separation and strain envelopes for simple models for bulk material (BM) and cohesive element (CE).....	77
Figure 3.5: Scaling procedure of a rod represented by a spring and cohesive element.	78
Figure 3.6: The construction of a virtual cohesive model for the same-material scaling. ...	81
Figure 3.7: Local plasticity captured exactly for replica scaling in first-order theory.....	83
Figure 3.8: Non-linear bulk and LCZM captured exactly for replica scaling in first-order theory.....	85
Figure 3.9: Crack length vs stress intensity factor for full scale, virtual and scaled-down models and comparison with full-scale ΔK analytical ASTM E647 prediction, experimental data [175] and numerical data in ref. [175].....	89
Figure 3.10: Loading and geometry of middle tension specimen and comparison between the numerical results of the current study and London et al. [177].....	92
Figure 3.11: Fatigue test specimens considered in case studies.	94
Figure 3.12: Mesh sensitivity study for compact tension specimen.	95
Figure 3.13: Reaction force vs displacement for full-scale and virtual models.....	99
Figure 3.14: Von Mises stress upon unloading for full scale and scaled models at the crack tip for load case 2.	99

Figure 3.15: Reaction force vs time plot for full scale CT specimen and virtual models for load type 2.....	100
Figure 3.16: Stress in the y direction at t=20s for CT specimen for full scale, virtual and all projected trial space models for load type 3.....	102
Figure 3.18: Stress in the vertical direction for full scale MT model at different crack lengths.	103
Figure 3.19: Traction-separation curve at the crack tip element at t=33s of MT specimen for the full-scale model and virtual models 5 to 8.	104
Figure 3.20: Fatigue crack growth outputs for full scale models for all specimens and virtual models 1-12.	105
Figure 3.21: Von Mises stress distribution at the crack tip of ESET specimen for the full-scale model and the two scaled models for virtual model 11.	106
Figure 4.1. The interrelationship between the reference and moving control volumes in the trial and physical spaces and the space $\Omega\beta$	112
Figure 4.2: Specimens at final fatigue fracture [129]	127
Figure 4.3: Fatigue crack growth rate vs stress intensity factor for full scale, virtual, projected scaled and Kirane & Bazant's [129] models.....	128
Figure 4.4: Geometry of single edge notched tension specimen and comparison between the numerical results of the current study and Busari et al. [192].....	130
Figure 4.5: Mesh sensitivity study for single edge notched tensile specimen	132
Figure 4.6: Von Mises stress distribution at the crack tip of SENT specimen for the full-scale model and the two scaled models for virtual model 1.	134
Figure 4.9: Meshed pipe with crack mesh at the centre.....	137
Figure 4.10: Crack growth rate vs stress intensity factor of pipe for full scale and virtual models	138
Figure 4.11: Dimensions and mesh of pressure vessel	139
Figure 4.12: Crack length vs number of cycles for full scale and virtual models of pressure vessel	141
Figure 4.13: Stress intensity factor distribution at the crack front of the pressure vessel for the full-scale model and the two scaled models for virtual model 11 after 2mm crack growth.	142
Figure 4.14: Stress intensity factor distribution across the crack front of pressure vessel for the full-scale model and virtual models at final crack length of 7 mm.....	143

Figure 4.15: Crack growth rate vs stress intensity factor of pressure vessel for full scale, scaled down and virtual models	144
Figure 5.1: Velocity fields and associated reference and moving control volumes in the scaling spaces.	152
Figure 5.2: Compact tension shear (CTS) specimen dimensions and mesh.	162
Figure 5.3: Comparison of fatigue life between the numerical results obtained from Ansys, experimental data [212] and numerical data [215] for 30° and 60° loading angles.	162
Figure 5.4: Comparison of crack paths between the numerical results of the current study and experimental study of Sajith et al. [212]	164
Figure 5.5: Von Mises stress distribution at the crack tip of CTS specimen after 25 sub steps for the full-scale model and the two scaled models for virtual model 1 at loading angle 60°	167
Figure 5.6: Evolution of mode 1 and 2 stress intensity factor with crack length for CTS specimen for full scale model and virtual models 1-3 at a loading angle of 30 degrees ...	169
Figure 5.7: Crack length vs number of cycles for full scale and all virtual models for the CTS specimen	170
Figure 5.8: Crack path for full scale and all virtual models of the CTS specimen at 30° and 60° loading angles	171
Figure 5.9: Safran O3- Wing fuselage attachment lug geometry and dimensions [213] ...	172
Figure 5.10: Meshed wing-fuselage attachment lug.	173
Fig 5.11: Crack length vs number of cycles for full scale and all virtual models of lug ...	175
Figure 5.13: Crack length vs number of cycles for full scale and virtual models of t-joint	178
Figure 5.14: Final crack path comparisons between the full-scale model, virtual model and scaled models 1 and 2.	180
Figure 5.15: Crack growth rate vs equivalent stress intensity factor for the full-scale model and all virtual models of t-joint.....	181

List of Tables

Table 2.1: Governing variables of fatigue crack growth.....	57
Table 3.1. Necessary and sufficient zeroth order identities	71
Table 3.2. Necessary and sufficient first order identities.....	75
Table 3.3. Stress intensity factors (MPa mm ^{1/2}) for scaled and virtual models, and ASTM full-scale prediction.....	89
Table 3.4: Mechanical properties of 6061 aluminium alloy used for all tests [179].	90
Table 3.5: The dimensions of CT specimen for the full-scale and scaled down models.....	95
Table 3.6: Loading conditions of CT specimen at different scales.....	96
Table 3.7: The dimensions of MT specimen at different scales	96
Table 3.8: The dimensions of ESET specimen at different scales	97
Table 3.9: Loading conditions of ESET specimen at different scales	97
Table 3.10: Value of the scaling factors with different dimensional scaling factors	97
Table 3.11. Reaction force and crack length values for all virtual models at maximum displacement for load type 1.	98
Table 4.1. First-order finite similitude identities	119
Table 4.2: Specimen dimensions [14].....	124
Table 4.3: Experimental data for number of cycles to failure nf and Paris law parameters C and m for concrete beams of different sizes [14]	124
Table 4.4: Comparison of Paris law exponents for the large beam between experimental data, first order theory and the scaling model in ref. [14].....	125
Table 4.5: Specimen dimensions [129].....	126
Table 4.6: Experimental data for number of cycles to failure nf and Paris law parameters C and m for concrete beams of different sizes [129]	126
Table 4.7: Mechanical properties of materials used in numerical analysis [192,193].....	130
Table 4.8: Dimensions of SENT specimen at all scales.....	132
Table 4.9: The loading conditions of SENT specimen at all scales.....	132
Table 4.10: Value of the scaling factors with different dimensional scaling factors	133
Table 4.11. Stress intensity factor and number of cycles at final crack length of 10 mm after 25 sub steps for full scale, virtual and scaled down models	134
Table 4.12: Dimensions of pressurized pipe for the full-scale and scaled models	137
Table 4.13: The loading conditions of pipe at all scales	137

Table 4.14. Stress intensity factors and number of cycles at final crack length of 7 mm for full scale and virtual models	138
Table 4.15: Dimensions of pressure vessel for the full-scale and scaled down models	140
Table 4.16: The loading conditions of pressure vessel at all scales.....	140
Table 4.17. Stress intensity and number of cycles at final crack length of 7 mm for full scale and virtual models	140
Table 5.1. First-order finite similitude identities	154
Table 5.2: Mechanical properties of materials used in numerical analysis [212-214].....	160
Table 5.3. Comparison of crack propagation angle for 30° and 60° loading angles of numerical model, experimental data [212] and numerical data [212]	163
Table 5.4: Dimensions of CTS specimen at all scales	165
Table 5.5: The loading conditions of CTS specimen at all scales	165
Table 5.6: Value of the scaling factors with different dimensional scaling factors	166
Table 5.7. Stress intensity factor and number of cycles at final crack length of 55 mm for full scale and virtual models for 30° loading angle.....	167
Table 5.8. Stress intensity factor and number of cycles at final crack length of 50 mm for full scale and virtual models for 60° loading angle.....	168
Table 5.9. Crack propagation angle for full scale and virtual models for 30° and 60° loading angle	170
Table 5.10: Dimensions of wing-fuselage attachment lug at all scales	173
Table 5.11: The loading conditions of wing fuselage attachment lug at all scales	174
Table 5.12. Stress intensity factors and number of cycles at final crack length of 4.5 mm for full scale and virtual models.....	174
Table 5.13: Geometrical dimensions of t-joint at all scales	177
Table 5.14: The loading conditions of t-joint at all scales	177
Table 5.15. Stress intensity factors and number of cycles at final crack length of 5.85 mm for full scale and virtual models.....	178

Abstract

A high percentage of all structure or products failures can be attributed to fatigue and fracture. In analysing the behaviour of cracked components, the existence of size effects remains a problem in the prediction of the full-scale fatigue response of structures using sub scale models. The smaller models appear “stronger” exhibiting a higher fatigue life than the prototype. Thus, fatigue tests performed in the laboratory using small specimens cannot be reliably used to predict the fatigue behaviour of a larger structure e.g., bridges, aircrafts, boiler pressure vessels etc. Experimental testing for fracture mechanics can be expensive, especially if the structure/component is large or if the material used is expensive. Scaled modelling is a possible method of decreasing experimental costs. Scaling techniques such as dimensional analysis are currently used in fracture mechanics and fatigue to design meaningful scaled experiments; however, it has several limitations primarily in its inability to account for size effects. This necessitates the need for a new method; first order finite similitude theory which can offer a cost-effective solution and more reliable results. A novel mathematical equation has been formulated in this thesis that establishes a precise analytical relationship between fatigue life and scale providing new insights into scaled experimentation in fatigue. Unlike dimensional analysis, the theory of finite similitude connects information across scales and links more than one scaled experiment. It is shown for the first time that conducting two scaled experiments is the correct scaling approach for the analysis of fatigue as the geometric size effects that are present in both mode I and mixed mode (mode I/II) fatigue crack growth with a change of scale are eliminated. Several case studies commonly employed in laboratory fatigue tests are examined numerically such as the ASTM E647 standard specimens and compact tension shear specimen. Practical case studies such as pressure vessel, pipe under pressure load, welded t-joint, pin loaded lug among others are also investigated numerically. The relevant experimental data and finite element models demonstrate clearly that the new rules for predicting fatigue life and crack growth rate provide good accuracy. Errors in lifecycle and stress intensity factor predictions ranged between 0.1-9% whereas the crack path and shape were predicted with 99% accuracy. The hitherto difficult task of achieving complete similarity in Paris law is proven possible in this thesis by performing an extra scaled experiment as Paris law constants C and m are predicted with up to 99.9% accuracy. The promising results demonstrated in this thesis confirm the value of employing this scaling approach to scaled fatigue experimentation in any industrial setting that employs a damage tolerant design approach.

Declaration

No portion of the work referred to in the thesis has been submitted in support of an application for another degree or qualification of this or any other university or other institute of learning.

Osagie Akhigbe-Midu

Copyright Statement

- i. The author of this thesis (including any appendices and/or schedules to this thesis) owns certain copyright or related rights in it (the “Copyright”) and he has given The University of Manchester certain rights to use such Copyright, including for administrative purposes.
- ii. Copies of this thesis, either in full or in extracts and whether in hard or electronic copy, may be made only in accordance with the Copyright, Designs and Patents Act 1988 (as amended) and regulations issued under it or, where appropriate, in accordance with licensing agreements which the University has from time to time. This page must form part of any such copies made.
- iii. The ownership of certain Copyright, patents, designs, trademarks and other intellectual property (the “Intellectual Property”) and any reproductions of copyright works in the thesis, for example graphs and tables (“Reproductions”), which may be described in this thesis, may not be owned by the author and may be owned by third parties. Such Intellectual Property and Reproductions cannot and must not be made available for use without the prior written permission of the owner(s) of the relevant Intellectual Property and/or Reproductions.
- iv. Further information on the conditions under which disclosure, publication and commercialization of this thesis, the Copyright and any Intellectual Property and/or Reproductions described in it may take place is available in the University IP Policy (see <http://documents.manchester.ac.uk/DocuInfo.aspx?DocID=487>), in any relevant Thesis restriction declarations deposited in the University Library, The University Library’s regulations (see <http://www.manchester.ac.uk/library/aboutus/regulations>) and in The University’s policy on Presentation of Theses.

Acknowledgments

I would like to thank God for the direction and guidance to complete this study.

I would like to sincerely express my appreciation to my supervisors, Dr Keith Davey, and Dr Rooholamin Darvizeh, for their guidance and advice, throughout the whole duration of my research. This work would not be possible without their assistance.

I would like to express my gratitude to my parents Dr Christopher Akhigbe-Midu and Dr Julie Akhigbe-Midu for their financial support to facilitate my doctoral research at the University of Manchester.

I would like to express my heartfelt appreciation to Mr and Mrs Ehimigbai for their support emotionally throughout this programme.

I would like to thank all my colleagues at The University of Manchester for their invaluable support throughout this degree.

Nomenclature

α_0^Ψ	Scalar for transport equation for field Ψ in 0^{th} -order theory
α_1^Ψ	Scalar for transport equation for field Ψ in 1^{st} -order theory
α_k^Ψ	Scalar for transport equation for field Ψ in k^{th} -order theory
$\alpha_0^\Psi T_0^\Psi$	Scaled transport equation for field Ψ in 0^{th} -order theory
$\alpha_1^\Psi T_1^\Psi$	Scaled transport equation for field Ψ in 1^{st} -order theory
$\alpha_k^\Psi T_k^\Psi$	Scaled transport equation for field Ψ in k^{th} -order theory
a	Crack length
a_0	Initial crack length
a_f	Critical crack length
A	Static yield stress
A_0	Cross section area of rod
A_{pl}	Area under the load-displacement curve
\mathbf{b}_{ts}^Ψ	Source term in the trial space transport equation
C	Paris law parameter
da/dn	Crack growth rate
$d\Gamma^*$	Elemental control volume surface area
E	Young's modulus
F	Coefficient of invariant
g	Time scalar
G_c	Fracture energy per unit area (critical energy for fracture)
K_C	Fracture toughness
K_{eq}	Equivalent Stress intensity factor
K_I	Mode I Stress intensity factor
K_{II}	Mode II Stress intensity factor
K_{III}	Mode III Stress intensity factor
m	Paris law parameter
\mathbf{n}	Outward pointing normal on control volume boundary
\mathbf{n}	Unit normal vector
n_f	Number of cycles to fatigue failure
P	Load
R_1^Ψ	Differential scaling parameter in 1^{st} order for field Ψ

t	Time
T_{ps}^{Ψ}	Transport equation of physical space for field Ψ
T_{k+1}^{Ψ}	Transport equation for field Ψ in $(k + 1)^{th}$ -order theory
\mathbf{u}	Material displacement vector field
U_e	Elastic strain energy per unit thickness
\mathbf{v}	Material velocity field
\mathbf{v}^*	Control volume velocity field
V	Volume
P	Load
ν	Poisson's ratio
W	Width of the test specimen
\mathbf{x}	Function of coordinate points in affine map
χ	Coordinate point in reference control volume
β	Length scalar
ΔK	Stress intensity factor change
$\boldsymbol{\varepsilon}$	Small displacement strain tensor field
$\boldsymbol{\tau}$	Surface traction vector
V	Volume
ρ	Material density
σ_c	Critical stress
σ_Y	Yield stress
σ_{TS}	Tensile strength
$\boldsymbol{\sigma}$	Cauchy stress tensor field
ε	Strain
ε_Y	Yield strain
ε^p	Plastic strain
$\dot{\varepsilon}$	Strain rate
$\dot{\varepsilon}^0$	Reference strain rate
δ_j^j	Kronecker delta symbol
δ	Separation value in load-displacement curve of CZM
δ_c	Critical separation in load-displacement curve of CZM
Ω^*	Control volume

Ω_β	Scaling space
Ω_{ps}	Physical space
Ω_{ts}	Trial space

Chapter 1 Introduction

1.1 Motivation

Engineering structures such as bridges, power plants, aeroplanes, trains, cars, offshore platforms, and others have played an important role in human life since the beginning of the industrial revolution [1]. However, these structures can suffer from mechanical failures caused by crack propagation leading to catastrophic failures, which could result in loss of human lives and significant financial costs. Fatigue failure is a type of failure that occurs in structures subjected to sub critical cyclic loads due to damage accumulation [2]. Cracks in engineering structures can form as a result of manufacturing defects, design flaws, defects in the material, or as a result of cyclic loading. The potential cracks will then propagate under monotonic or cyclic applied load ultimately resulting in failure. Fracture mechanics is the branch of engineering concerned with the structural response of loaded components with a pre-existing defect [3]. It is commonly referred to as the damage tolerance approach. Damage tolerant design is the design of engineering components and structures using the principles of fracture mechanics. It involves calculating the time it takes for an initial defect of size a_0 to grow to a critical defect size a_f where the structure/component experiences a loss of function.

The study of fracture mechanics became prominent after the failure of the Liberty ships during the Second World War [4]. The Liberty ships featured fully welded hulls instead of the traditional riveted hull. Many of these ships failed during service due to the propagation of cracks through the hull, some cases being so severe the ships were split into two. Today, fracture mechanics is an indispensable element of solid mechanics analysis and is key in calculating the working life and reliability of loaded structures. One of the most well-known and often mentioned accidents within fatigue failure is probably the disintegration of two of the first commercial jetliners (de Havilland Comet jetliners) during flights in 1953 [5]. The first incident resulted in loss of life of the six crew and five passengers on board. Another well-known instance of fatigue failure is the capsizing of the Alexander L. Kielland oil platform [6] killing 123 people. A fatigue crack emanating from a poor weld on one of the six bracings reduced the fatigue strength of the structure leading to eventual collapse. Both tragedies highlight the importance of designing a structure to resist fatigue failure through its service life.

With technological advancements such as rapid prototyping, 3D printing to name a few, innovative products are now released to the market quicker than ever before. The fatigue strength of the structure is a critical parameter that must be evaluated in the design stage before manufacturing can take place [7]. Within the framework of fracture mechanics, the fatigue strength refers to the critical or limiting defect (crack) size before the component/structure experiences a loss of function [8]. This is usually when safe working operation of structure no longer possible. Currently, full scale experimental testing is still the most accurate method of determining fatigue strength of a new material as scaled experimentation in fatigue is fraught with issues [7]. Numerical experimentation can be an alternative but with new materials, appropriate material models might not exist thus physical testing is the recourse. The application of a scaling theory that can deal with size effects would help to keep pace with innovation in industry and eliminate the current bottlenecks associated with fatigue “certification” in both the design and service stage. It would lead to more accurate determination of service inspection intervals and could be of use in the life extension phase of ageing assets that are still in operation past their initial design life.

Fatigue and fracture phenomena have been investigated for more than 150 years. However, complete solutions for these issues have not yet been discovered [9]. In the 1900s, many failures of structures were recorded. Since then, many researchers started to investigate the underlying cause of the problems. For example, Wohler [10] found that metallic components could work for a very long time if they were subjected to a constant load below the yield point of their material, but that they could fail if subjected to cyclic loading, even if it was below the yield point of the material. At that time, due to researchers not being able to see the damage on the surface of the components, fatigue was considered a puzzling phenomenon as the only indicator of the problem was a hidden crack inside the material. Researchers have developed a greater understanding of the different mechanisms by which fatigue cracks develop over the last century. The process of fatigue failure can be broadly divided into three parts: crack initiation, crack propagation and fast fracture, which leads to failure [11]. Different factors such as mechanical, microstructural, or environmental can affect the fatigue behaviour of a component.

Scaled down models have long been an avenue with which service life and behaviour of larger models can be predicted since the 19th century by means of similitude theory [12]. Similitude theory is a branch of engineering science concerned with establishing the necessary and sufficient conditions of similarity among phenomena and has been applied to

a multitude of fields such as structural engineering, vibration and impact problems helping engineers and scientists to accurately predict the behaviour of the prototype, through scaling laws applied to the experimental results of a scale model related to the prototype by similarity conditions.

Currently multiple methods capable of scaling exist; notably dimensional analysis, differential equations, fractal methods and energetic methods [13]. All these methods have various limitations to their scope of applicability. Within the field of fracture mechanics and fatigue, dimensional analysis is the most widely used method but is fraught with several limitations. Chief of which being its inability to deal with size/scale effects inherent to fatigue. This has resulted in the need for an appropriate similarity theory for scaled fatigue experimentation. Figure 1.1 illustrates the framework of similitude theory highlighting how predictions of the prototype can be made from scaled tests.

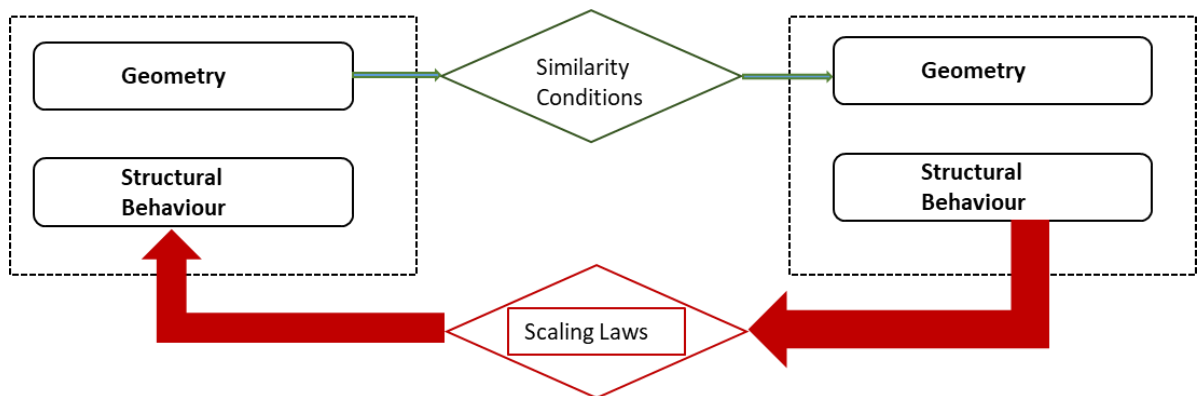


Figure 1.1: Sketch for the prediction of the structural behaviour of a prototype, based on the experimental results of a scaled model.

Limited work has been done to study the behaviour of propagating fatigue cracks as the scale changes. The first contribution to scaling in fatigue was by Bazant in 1991 [14] where he put forward a law to address the size dependence of the Paris law constants. This work extended the size effect law he proposed earlier for fracture [15]. Further size studies effect in fatigue have been undertaken by various researchers mainly employing the dimensional analysis approach [16-18] or fractal concepts [19-22].

A key consideration, however, is that dimensional analysis in its traditional form does not account for scale effects as it is based on invariance of dimensionless groups. However, size effects are a type of scale effect thus the presence of them in fatigue means the governing

dimensionless groups that control fatigue do in fact change with specimen size. Other studies performed simply attempt to show the effect of a change in geometrical dimensions on fatigue crack growth rate [23-25] and do not attempt to reconcile the observed differences by means of a scaling law in order to make fatigue life predictions of the prototype using the scaled models.

Scaled experimentation is not widely adopted in fatigue due to the lack of a robust scaling law that enables meaningful scaled fatigue experiments to be performed. Such a law should facilitate full scale predictions using the data obtained from the scaled models. Numerical simulations and full-scale testing are the predominant choice for fatigue analysis in academia and industry for a few reasons. One is that fatigue is a largely semi empirical science and analytical solutions do not exist for most geometries thus full-scale testing and numerical simulation is the only option. Full scale testing is expensive and rather time consuming thus, to save costs and reduce time to launch of new products numerical simulation is the preferred choice. Numerical simulation is not without limitations however, as it is only as reliable as the inputs fed in. In the case of new materials where the constitutive relationships are not known or unique applications with the boundary conditions unclear, numerical analysis cannot be used, and physical experimentation must be performed to make fatigue life predictions.

In light of all the current shortcomings in scaled fatigue experimentation, a robust scaling framework is needed that can accommodate size scale effects present in fatigue enabling accurate fatigue life predictions to be made using sub scale models. Successful scaled experimentation in fatigue would lead to positive outcomes such as reduced costs and time. This is the aim of this thesis to apply an alternative scaling theory to fatigue. Finite similitude theory is a scaling theory based on the concept of scaling space developed at the University of Manchester in 2017 [26]. Transport equations in the physical space (prototype) and trial space (scaled down model) are compared and the necessary conditions for achieving similitude between both models. This theory would be applied in this work to fatigue within the fracture mechanics framework. It is hoped that the successful outcomes of this thesis would lead to increased adoption of scaled experimentation in fatigue in both industry and academia enjoying the many benefits this tool can offer.

1.2 Research Aim and Objectives

The primary aim of the research is to investigate the efficacy of the first order finite similitude theory as applied to fatigue analysis within the linear elastic fracture mechanics framework with the view to alleviate the current challenges associated with fatigue life predictions using scaled experiments. The first order finite similitude theory can reproduce the behaviour of the full scaled model using two scaled down experiments (trial models).

Scaled experimentation does not feature heavily in fatigue due to the existence of size effects creating difficulties in predicting full scale behaviour using scaled experiments. Current scaling strategies have been proven inadequate in capturing the size effect thus leading to issues in the transferability of laboratory fatigue test data to real full-scale components. The ability of the first order similitude theory to account for size effects is examined. If size effects present in fatigue can be accounted for by the finite similitude theory, then the numerous benefits of scaled experimentation such as reduced cost and time can be realised by various industries in evaluating the structural integrity of their products, structures and processes. Another benefit would be the lower “lead” time to market for new products thereby encouraging rapid innovation as fatigue integrity is a key consideration in the design stage.

Critical physical quantities that describe the fatigue behaviour of the full-scale model within a damage tolerant design approach are investigated with a view to examining how they differ with scale. These parameters are then predicted by using two smaller scaled models designed according to first order similitude rules. Several types of cracks are considered in both the low and high cycle fatigue regime. Different types of loading, boundary conditions, materials and case studies are investigated to highlight the practicality of the approach.

The primary objectives to achieve the aim of the study are summarised as follows:

1. Design and conduct geometrically similar scaled propagating fatigue crack experiments within the linear elastic fracture mechanics framework designed according to first order similitude rules using commercial CAE software ABAQUS® and Ansys®.
2. Evaluate the relevant physical fracture mechanics quantities within both the linear elastic fracture mechanics framework and also pertaining to the cohesive zone model. Investigate the predictive capability of the two-experiment theory in replicating the full-scale behaviour of the cohesive zone model under low cycle fatigue loading. This

objective was achieved by both analytical and 2D numerical studies of fatigue experiments conducted according to ASTM E647 standards. Numerical experimentation was performed using Abaqus software with the cohesive zone model, Paris law and extended finite element method were all used in tandem to successfully simulate propagating fatigue cracks.

3. Apply the first order finite similitude theory to both low and high cycle fatigue with a view to establishing a precise analytical relationship between fatigue life and change in scale. Investigate if the well documented size effects present in one scaled experiment be eliminated by performing an extra sub scale experiment. This objective was achieved by applying the similarity laws prescribed by the first order similitude theory to relevant experimental data, developing a novel mathematical equation for change of fatigue life with scale and scaling the most popular empirical fatigue law (Paris law). 3D numerical models were created in ANSYS to further validate the efficacy of the theory.
4. Apply the first order finite similitude theory to practical fatigue problems (mixed mode fatigue) to determine if both the crack growth rate and path can be evaluated accurately via scaled experiments conforming to first order similitude rules. This objective was achieved by considering different practical case studies that are similar to those encountered in industry. Outcomes of the research show tremendous potential in the transferability of the theory to solving industrial fatigue crack growth prediction challenges.

Successful achievement of these objectives highlights the practicality of the theory. A positive consequence is that technological advancements in new designs and materials are able to proceed without any bottlenecks in the fatigue life certification stage as full-scale fatigue behaviour can be extracted from two properly designed scaled experiments.

1.3 Research Methodology

The relevant methods used in this thesis are described in this section.

1.3.1 Fracture Mechanics Method

Fracture mechanics method provides a framework for the analysis of structures containing an initial defect. It is based on the idea that when a structure containing an initial crack is loaded either monotonically or cyclically the crack propagates till final failure. Irwin

described the stress state around the crack tip by introducing a new parameter called the stress intensity factor [27].

The stress intensity factor for any structure is given as [27]:

$$K = Y\sigma\sqrt{\pi a} \quad (1.1)$$

Where K is the stress intensity factor, Y is the geometry shape factor which is dependent on the specimen geometry, σ is the applied stress, and a is the defect (crack) size.

Material failure of a cracked component occurs when the value of stress intensity factor (K) reaches a critical value known as the fracture toughness (K_C) of the material which is the point where failure occurs. Under cyclic loading, the Paris law [28] can be used to evaluate the crack growth rate of a structure as long as the stress intensity factors are known:

$$\frac{da}{dN} = C\Delta K^m \quad (1.2)$$

Paris law provides a simple relation to evaluate the number of cycles taken to propagate an initial defect/crack to the critical defect size which informs structural integrity decisions in the field. The fatigue crack growth model used in numerical simulations in this thesis is Paris law.

1.3.2 Cohesive Zone Model

The cohesive zone model was introduced by Dugdale [29] and Barenblatt [30] to overcome the limitation of stress singularity (infinite stresses) at the crack tip in the fracture mechanics framework. They introduced the fracture process zone (FPZ) which is a small area around the crack tip, where the normal stress perpendicular to the crack growth direction is equal to the yield stress according to Dugdale but decreases as deformation increases eventually vanishing at full separation. Hillerborg [31] was the first to numerically simulate crack growth using a bilinear cohesive zone model in conjunction with the Finite element method with great success.

The constitutive relationship describing material damage in the CZM is the traction separation law (TSL). The general idea is that material damage begins when the traction reaches a critical value called the critical cohesive stress. The crack propagates until the displacement jump between the cracked surfaces reaches a critical value, δ_c where the cohesive stress becomes zero and all the cohesive energy is dissipated. The main advantage

of the CZM over other analysis methods lies in its ability to predict both crack initiation and propagation.

1.3.3 Extended Finite Element Method

The extended finite element method (XFEM) grounded on the concept of partition of unity [32] was first introduced by Belytschko and Black [33] in 2002, to address the short comings of the traditional finite element method in dealing with discontinuities such as cracks, voids etc. It can be viewed as an extension to the FEM as it adds enrichment functions with additional degrees of freedom to the FEM formulation.

Two enrichment functions are used for crack growth analysis namely the crack-tip asymptotic function and discontinuous function. The former represents the stress singularity around the crack tip whereas the latter describes the displacement jump- along the crack surface. Mathematically, the displacement of a gauss point [32] can be written as:

$$u(x) = \sum_{j=1}^n N_j(x)u_j + \sum_{h=1}^{mh} N_h(x)(H(x) - H(x_h))\mathbf{a}_h + \sum_{k=1}^{mt} N_k(x) \left[\sum_{l=1}^4 (F_l(x) - F_l(x_k))\mathbf{b}_k^l \right] \quad 1.3$$

Here n is the number of standard finite element nodal, $N_i, N_j, N_k(x)$ are continuous shape functions, u_j is the freedom vector of standard finite element nodal, $H(x)$ is the Heaviside function of gauss point x and $H(x_h)$ is the Heaviside function of enrichment nodal h , \mathbf{a}_h is the freedom vector of sides around the crack, $F_l(x)$ and $F_l(x_k)$ are the crack-tip enrichment function at gauss point x and enrichment nodal k , and \mathbf{b}_k^l is the freedom vector of crack-tip enrichment nodal. The Heaviside function jumps between two discrete values of 1 and -1 depending on the side of the crack surface.

The crack-tip asymptotic function is written as:

$$\{F_l(r, \theta)\}_{l=1}^4 = \left\{ \sqrt{r} \sin \frac{\theta}{2}, \sqrt{r} \cos \frac{\theta}{2}, \sqrt{r} \sin \theta \sin \frac{\theta}{2}, \sqrt{r} \sin \theta \cos \frac{\theta}{2} \right\} \quad 1.4$$

where (r, θ) is the polar coordinate at point x , and $\theta = 0$ for the tangent direction of crack. Fig 1.2 highlights a propagating crack with enrichment nodes where the nodes highlighted are enriched with the appropriate functions.

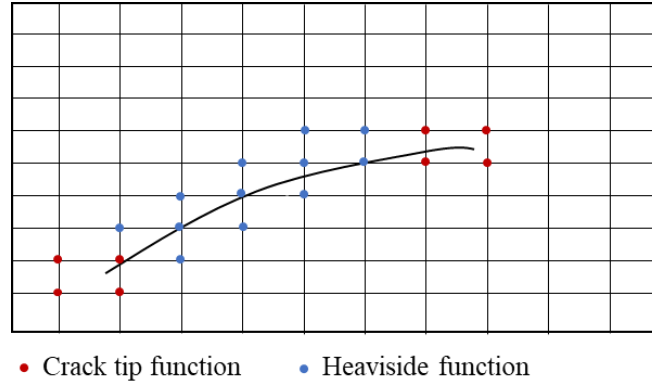


Figure 1.2: Propagating crack with enrichment nodes in XFEM formulation.

To simulate fatigue crack growth in Abaqus/Standard, XFEM is used in conjunction with the CZM and Paris law to simulate crack initiation and propagation. The bi-linear elastic traction separation law is used with damage initiation controlled by the maximum principal stress and crack propagation described by Paris law.

1.3.4 Finite Similitude Theory

In order to perform scaled fatigue experiments such that the results are meaningful and can be related back to the full-scale model, an appropriate similarity theory must be employed. The similarity theory prescribes scaling factors that are applied to the outputs from the scaled experiment to predict the behaviour of the full-size model. The scaling theory used in this research is finite similitude theory specifically the first order finite similitude theory [34]. It prescribes the set of rules used to design the scaled fatigue crack growth experiments and relate the data across scales reconstructing full scale behaviour. The theory is founded on the metaphysical concept of space scaling i.e., contracting or expanding space. Evidently, this is impossible to achieve practically but if one can think of a large space containing the full-scale experiment/ model and a small space that holds the scaled down experiment then there must exist a link between the two. The concept of control volume describes the movements in both spaces where an affine map can be used to link corresponding points in both spaces. The transport equations hold true in both spaces. The conservation equations stipulate rules for setting parameters such as geometric size, materials, strain, stress, velocity etc for the design of experiments by means of scaling factors. These rules simultaneously reveal how to combine the outputs of the scaled experiments to accurately recreate the behaviour of the full-scale model. One advantage of the finite similitude theory is the ability to choose a material for the smaller experiment that differs from the prototype. One obvious benefit would be a reduction in experimental cost as a cheaper material could be used for scaled

models. In this thesis, the same material is used for the full-scale model and all scaled down models (replica scaling).

1.4 Thesis Outline

This thesis is organised into seven chapters.

Chapter 1 introduces the motivation for the research and outlines the aims and objectives of this work alongside a brief description of the research methods used to accomplish the aim of the research.

Chapter 2 presents a comprehensive literature review on fatigue. The fundamental mechanism of fatigue damage is introduced along with analytical, experimental and numerical attempts by researchers to predict fatigue life of structures. Subsequently, the concept of scaling and similitude methods are introduced with the most common method being dimensional analysis. A review of the works by previous researchers in applying dimensional analysis is presented and here it is shown conclusively that dimensional analysis cannot deal with the size effect problem in fatigue thus necessitating the need for a new scaling theory known as finite similitude theory.

Chapter 3 attempts to establish an equivalence between the cyclic cohesive zone model and two scaled experiments designed according to first order similitude rules. The cohesive zone model is a very common damage model in fracture mechanics with extensive applications in both fracture and fatigue. It is shown for the first time that the exact behaviour of cohesive zone model under fatigue loads can be replicated using two scaled experiments. Analytical relationships are examined and a further 2D fatigue numerical study is undertaken using Abaqus XFEM with cohesive segments implementation. This publication presents for the first time a two-experiment approach to fatigue experimentation.

Chapter 4 consists of a publication that attempts to solve the size/ scale effect in fatigue by detailing the correct similitude rules for scaling fatigue. A new modified version of the first order finite similitude theory is presented for the first time, introducing an additional scaling space that facilitates the projection of differential equations in the scaling space. Various empirical fatigue laws are tested via means of previous experimental data and numerical experimentation using Ansys. A precise analytical relationship is proposed that enables fatigue life measurement at different scales to be combined to predict the fatigue behaviour at full scale. This is a major milestone in the field of fatigue as previously the number of

cycles to failure could not be scaled as it is a dimensionless term, however within the framework of the new theory this limitation is overcome. Excellent lifecycle predictions are obtained. It is shown that the correct approach to fatigue scaling is by conducting two experiments at different scales. Following the successful results in chapter 4 and establishment of the correct similitude rules for fatigue, it is of interest to examine if similarly promising results can be achieved for more complicated case studies.

Chapter 5 shows the application of the new scaling theory to more realistic structures/ loads. The intention here is to evaluate if this theory can be applied in the industry to determine fatigue life of real structures. Mixed mode fatigue is studied via means of a modified compact tension specimen. Fatigue crack growth of a through thickness crack in a pin loaded lug is examined using two scaled experiments. This case study is chosen as pin loaded lugs are a common and critical aerospace part. The ability of the theory to handle propagating mixed mode cracks in a realistic structure is examined by means of experimentation on a welded T-joint with an inclined semi elliptical crack. Excellent predictions of residual life, critical crack length, crack path and equivalent stress intensity factor are achieved affirming that the first order theory can be applied to industrial case studies. Paris law parameters C and m are predicted by the virtual models with up to 99.9% accuracy.

Chapter 6 presents the discussion of the key findings of this research. The numerical techniques employed to set up and post process the scaled numerical models are discussed in more depth with guidelines provided on how to apply the theory to conduct physical scaled fatigue crack growth tests in a laboratory. The impact of this work on industrial fatigue testing and structural integrity assessment design codes is highlighted. A novel hypothesis demonstrating how the theory can be applied to conduct meaningful scaled down stress/strain-based fatigue assessments based on the findings of this work is introduced and finally the limitations of the current study are elucidated.

Chapter 7 presents the overall conclusions of this research.

Chapter 8 highlights the recommendations for future work.

This thesis is presented in the alternative journal format thus it is critical to emphasise how each publication is connected to and complements one another thus forming a coherent thesis. The investigations recorded in the three publications of this thesis were carefully designed to be coherent and feed into each other. The first journal publication (chapter 3) was an attempt to discover if the stress fields at the tip of a fatigue crack can be replicated

exactly using two scaled experiments. The cohesive zone model is commonly used to describe fatigue damage in the near crack tip region. Thus, if the cohesive zone behaviour can be replicated via scaled experimentation, then crack tip behaviour is expected to be implicitly replicated as well. This hypothesis was tested using 2D finite element models for a relatively small number of cycles (50) i.e., low cycle fatigue. The importance of this first step cannot be understated as the cohesive zone model is implemented in one form or another in most commercially available software to predict fatigue life. Once an exact match was achieved it was of interest to examine if the promising results achieved still hold true for more detailed 3D models and high cycle fatigue.

This led to the work presented in Chapter 4 and the second journal publication. With increased number of cycles, the size effect problem became more pronounced and a solution to relate the number of cycles across scales was needed. The hypothesis employed here is that the product of the stress intensity factor and number of cycles is a constant. A relatively simple relationship relating the number of cycles to a change in scale is proposed. This was a major milestone of the research as previously the number of cycles was thought to be a dimensionless number, hence no previous relationship existed to quantify the observed change with scale. The question of how Paris law constants change with scale is answered here. It is proven that Paris law follows exactly the first order rule.

The next step of the research project was to evaluate if the first order finite similitude theory applies to more complicated case studies. That is the basis of the investigation in the final journal publication and Chapter 5. The results from the complicated studies in this publication demonstrate conclusively that full-scale fatigue behaviour (crack growth rate and crack path) can be reconstructed with very high accuracy using two scaled experiments. The data from this research conclusively prove that fatigue analysis of practical engineering structures can be approached using two scaled models.

Chapter 2 Literature Review

The details of an extensive literature review spanning the different topics relevant to this thesis is presented in this chapter. Firstly, a historical overview is given about fatigue in section 2.1 detailing the state of the art in fatigue research outlining key incidents that have shaped the knowledge base of fatigue in academia and industry. Then the focus shifts to the fracture mechanics method in section 2.2 with an explanation about the mechanisms of fatigue in section 2.3. Current models available in literature for predicting fatigue crack growth are highlighted in section 2.4. Fatigue crack growth models capable of predicting mixed mode fatigue crack growth are presented in section 2.5. A description of the numerical methods used in this thesis to facilitate fatigue crack growth predictions are highlighted in section 2.6. Section 2.7 describes the state of the art of scaled experimentation in fatigue with the current similitude laws available. Section 2.8 presents the types of size effects that can occur in fatigue with special focus on the geometric size effect that arises in fatigue which is the focus of this thesis. The application of dimensional analysis arguments to Paris law is presented in section 2.9. The limitations of the most common scaling method (dimensional analysis) in the field of fatigue i.e., the existence of size scale effects are demonstrated, necessitating the need for a new scaling theory (first order finite similitude theory) which is applied in this thesis to propagating fatigue cracks in subsequent chapters.

2.1 Introduction

After the industrial revolution in the early 19th century, machines with either rotating or vibrating parts became a staple of human life with its adoption proliferating over the years. These machines began to fail due to propagating fatigue cracks necessitating designers to provide solutions to mitigate against this. Fatigue failure leads to severe consequences, as the structural integrity of the component is compromised. Downtime in machinery is an obvious one resulting in reduced profits for companies. Furthermore, fatigue failure in critical components can lead to loss of life see for example the railway crash in Hatfield caused by fatigue failure of the railway axle [35].

This led researchers around the world to concentrate their efforts in studying this hitherto unknown subject and provide design solutions. Full scale experimental testing of mechanical parts has been performed but it is an expensive process and can be massively time consuming. In addition to this mix, the variable nature of fatigue requires multiple fatigue tests consequently the time and cost associated becomes an even bigger consideration in the

design process. The alternatives are employing analytical methods, numerical simulations or performing scaled experiments to forecast crack growth. Many of the conventional methods for fatigue life predictions are based on linear elastic fracture mechanics which is now well developed. One such useful analytical relation based on linear elastic fracture mechanics (LEFM) framework, is the Paris law which is the most common empirical fatigue law used till this day despite some of the deviations observed experimentally.

The principle of similitude is used in structural engineering, solid mechanics, fluid mechanics and a whole host of other disciplines. Similitude rules are essential to enable meaningful sub scale testing that can be used to estimate the performance of larger prototypes with confidence. The similitude rules are prescribed by the scaling strategy/approach and defines the rules for the design of experiments. Numerous scaling techniques have been developed over the years due to the great benefits afforded by sub scale testing such as reduced costs, time and ease of understanding variables that affect the full-scale process/ structure in a timely manner. The first scaling strategy hypothesized is dimensional analysis in 1914 by Rayleigh [36] with a formalised approach by Buckingham in 1921 [37]. Others such as scaling founded on differential equations, statistical models, energetic methods [13] among others have been put forward for the design of sub scale experiments in multiple research fields with great success.

However, scaled experimentation in fatigue is not as developed with the analysis techniques appearing in literature mostly limited to dimensional analysis historically and more recently fractal concepts. A major drawback to scaled experimentation in fatigue is the existence of size effects. This is defined as the observed changes in a process with scale. Thus, accurate estimation of the behaviour at the full scale cannot be gleaned from the scaled models. The drawback of dimensional analysis lies in its inability to account for these effects.

In this chapter a comprehensive literature review is undertaken, detailing the fracture mechanics framework, fatigue crack mechanisms of initiation and propagation, empirical fatigue crack growth laws, mixed mode fatigue, numerical fatigue simulation techniques, types of size effects present in fatigue and a historical overview of scaling with a focus on dimensional analysis as applied to fatigue. Finally, the limitations of the present scaling strategies as applied to fatigue is elucidated demonstrating the necessity for a new scaling strategy.

2.2 Fracture Mechanics

Typically, the design and analysis methods available to forecast fatigue damage can be broadly split into three categories viz; stress-based approach [38], strain-based approach [39] and fracture mechanics approach [40]. Stress based methods examine the stresses in the area under fatigue load of interest whereas strain-based methods evaluate the plastic deformation in the vicinity of stress raisers such as edges and notches in the structure. The fracture mechanics method is limited to structures containing an initial crack or notch. Fatigue analysis in this thesis is strictly within the confines of fracture mechanics.

The origins of fracture mechanics can be traced back to the work of English researcher Griffith in World War 1 [41]. He suggested that when a crack is inserted into a stressed plate of an elastic material, the decrease in potential energy must be balanced by the increase in surface energy caused by the crack. This has now become known as the energetic framework of linear elastic fracture mechanics. His explanation solved the puzzling question as to why the actual strength of brittle materials such as glass (100 MPa) is lower than the theoretical strength [1000 MPa] [42]. The fracture stress can be related to the crack size using the famous Griffith relationship:

$$U_e = \frac{\pi c^2 \sigma^2}{E} \quad (2.1)$$

Where U_e is the elastic strain energy per unit thickness, a is the crack length, and σ is the fracture stress and E is the elastic modulus of the material.

Westgaard [43] proposed analytical relations which was modified by Irwin in 1957 [44] shaping the framework of fracture mechanics as we know it today. He developed the fundamentals of fracture mechanics after his investigation of the stress fields and crack driving force at the crack tip. He invented the well-known parameter called the stress-intensity factor K which is the crack driving force and describes the stress state at the crack tip. This was significant at the time as it established a clear relationship between the nominal stress and the crack length to determine the stress distribution around the crack. Another important parameter discovered by Irwin is the fracture toughness denoted by K_c . It represents the ability of a material to resist fracture in the presence of cracks as once the stress intensity factor of the crack exceeds the fracture toughness value the material fails.

The crack process can only be accurately described by the stress intensity factor under specific conditions. In the first instance, the behaviour of the bulk material must be elastic,

in addition the plastic deformation around the crack tip must be significantly small in comparison to the crack length (this is known as small –scale yielding). When, the plastic zone size is comparable to crack length then the framework of LEFM is no longer suitable and elastoplastic fracture mechanics method (EPFM) is needed to accurately model the fracture process. In this thesis, the fatigue models employed are within the confines of LEFM thus this review is mainly focused on this framework.

2.2.1 Near Crack Tip Stress Field

Accurate characterisation of crack growth requires an accurate evaluation of the stress fields around the crack tip. Evidently, the stress fields at the crack tip are dependent on the type of loading applied to the structure. In fracture mechanics, there are three types (modes) of crack growth which are characterised by the different types of loads that can be applied either individually or as a combination to the specimen. Figure 2.1 describes all three possible modes. The first and most dominant mode in fracture problems is mode I (opening or tensile mode). Here the applied load is in a direction perpendicular to the crack surface and causes the crack surfaces to move directly apart. The sliding or in plane shear mode (mode II) is the second mode with the load applied acting in the same plane as the crack. The crack surfaces slide over one another. Finally, the third mode is mode III (tearing or anti-plane shear mode) with the load acting out of the plane of the crack direction. The fracture behaviour for each mode would be determined by the state of stresses, strains and displacement near the crack tip. Furthermore, any fracture can be represented by one of these three modes of fracture or superposition of these [45].

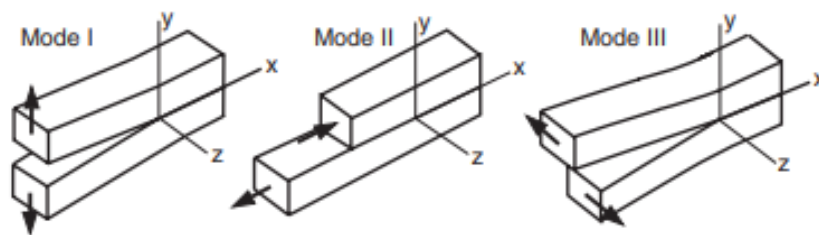


Figure 2.1: Schematic of basic fracture modes [46].

Consider then, a semi elliptical crack of length $2a$ in an infinite plate with the geometry as depicted in Fig. 2.2, r and θ , are the distance and orientation angle of an arbitrary point from the crack tip respectively.

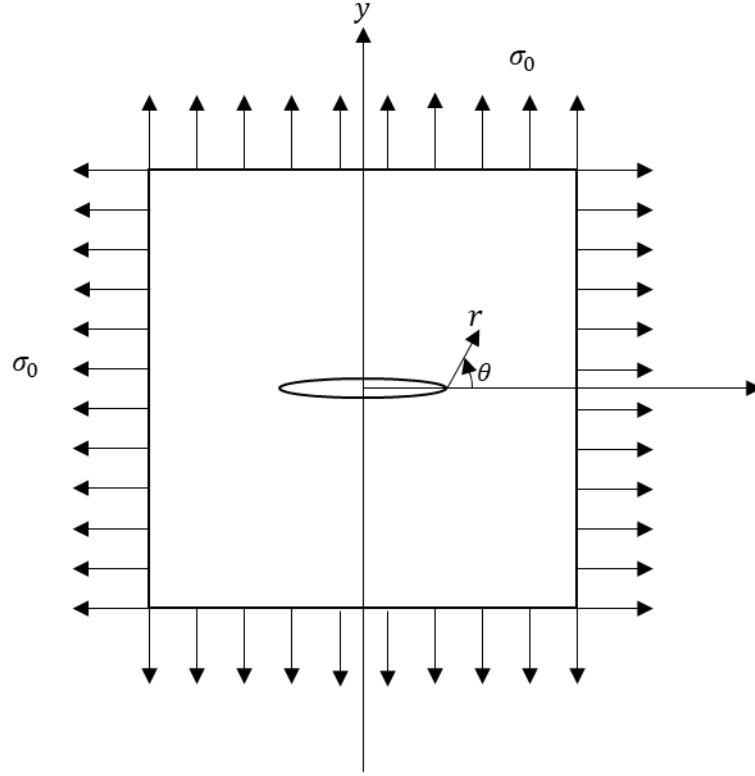


Figure 2.2: Infinite plate with centre crack of length $2a$ under uniform biaxial traction
 Westegaard [43] published a set of equations describing the stress singularity around the crack tip as follows:

$$\sigma_x = \sigma_0 \sqrt{\frac{a}{2r}} \cos \frac{\theta}{2} \left(1 - \sin \frac{\theta}{2} \sin \frac{3\theta}{2} \right) + \dots \quad (2.2)$$

$$\sigma_y = \sigma_0 \sqrt{\frac{a}{2r}} \cos \frac{\theta}{2} \left(1 + \sin \frac{\theta}{2} \sin \frac{3\theta}{2} \right) + \dots \quad (2.3)$$

$$\sigma_{xy} = \sigma_0 \sqrt{\frac{a}{2r}} \sin \frac{\theta}{2} \cos \frac{\theta}{2} \cos \frac{3\theta}{2} + \dots \quad (2.4)$$

Irwin [44] noticed a pattern in the published solutions by Westegaard [43] culminating in the proposal of a new fracture mechanics parameter called the stress intensity factor. The stress intensity factor K provides an elegant solution to characterize the strength of the stress field near the crack tip. More than one basic mode can be encountered in a structure at the same time, but typically mode 1 fracture is the most common. The stress intensity factor depends on the applied stresses and geometry, including specimen size and crack configuration. It transpires that Eqs. (2.2 - 2.4) can be written in a more general form in 2D as:

$$\sigma_{ij} = \frac{1}{\sqrt{r}} [K_I f_{ij}^I(\theta) + K_{II} f_{ij}^{II}(\theta)] \quad (2.5)$$

Where K_I is the mode I stress intensity factor and K_{II} is the mode II stress intensity factor.

The stress intensity factors for mode I and mode II loading are defined as:

$$K_I = \lim_{r, \theta \rightarrow 0} (\sigma_{yy} \sqrt{2\pi r}) \quad (2.6)$$

$$K_{II} = \lim_{r, \theta \rightarrow 0} (\sigma_{xy} \sqrt{2\pi r}) \quad (2.7)$$

An alternative method to describe cracks within the fracture mechanics frameworks is by means of the energy method [45]. Specifically, the parameter known as the strain energy release rate; G can be used to characterise the crack tip driving force. The strain energy release rate is decrease in the total potential energy of a structure per increase in fracture surface area [45]. One advantage over empirical formulations containing the stress intensity factor is that it can be used to study fatigue crack growth in both elastic materials and materials with significant plasticity. The failure point of the material is determined by the critical strain energy release rate G_c . A convenient expression exists that relates the strain energy release rate to the stress intensity factor in an elastic material and is given by:

$$G_i = \frac{K_{Ic}^2}{E'} \quad (2.8)$$

$$E' = E \text{ (Plane stress condition)} \quad (2.9)$$

$$E' = \frac{E}{1-\nu^2} \text{ (Plane strain condition)} \quad (2.10)$$

Where G_i is the strain energy release rate for the different modes, K_{Ic} is the fracture toughness for different modes, ν is the Poisson's ratio, E is the Young's Modulus.

Quantitative expressions have been put forward to determine the validity of LEFM assumptions and when EPFM might be required for more accurate fatigue analysis. LEFM assumptions hold when the yielding zone ahead of the crack tip is within the region of K -dominance. Within the region of K -dominance the stress intensity factors provide a unique measure of the intensity of the strains. Therefore, LEFM is applicable if small-scale yielding conditions prevail. The yielding of the crack tip is assumed to increase the effective crack length. The plastic zone radius r_y under plain stress can be calculated as:

$$r_y = \frac{1}{2\pi} \left(\frac{K_I}{\sigma_{yield}} \right)^2 \quad (2.11)$$

Where: r_y is the plastic zone radius, σ_{yield} is the yield strength of the material and K_I is the mode I stress intensity factor. According to Stephens et al. [1], under cyclic loading conditions, the restriction is defined by $r_y \leq a/4$ where a is the crack size.

2.3 Mechanism of Fatigue

The mechanism by which fatigue damage occurs is very complex as it occurs over very different scales. However, it is widely accepted that the process of fatigue failure can be divided into three stages. The first stage is the formation of an initial flaw due to accumulated cyclic damage this is known as crack initiation, subsequently these flaws grow and propagate on a macro scale (crack propagation) and finally catastrophic failure where the structure loses its load bearing capability completely.

2.3.1 Fatigue Crack Initiation

The precursor to fatigue crack initiation is the accumulation of cyclic plastic deformation. Fatigue cracks predominantly initiate at the surface or at grain boundaries in the direction of local maximum shear [45]. The dislocation movement is critical to fatigue crack initiation. If the slip occurs in the loading part of the. When a surface is cyclically loaded, the stress at the surface is higher than at the interior causing a stress concentration. Examples of stress concentrations in engineering applications on a macro scale would be voids, notches or components undergoing bending or twisting which results in stress gradients with the highest stress occurring on the surface. Stress concentrators also exist at the micro scale. The stresses at the surface are sensitive to the surface topography/ roughness. Inclusions and precipitates that possess different elastic properties from the matrix are also potential crack initiation points. [46] Repeated cyclic loading causes strain hardening in the slip band under tensile loads and greater shear stress in the opposite direction during compression. The accumulation of these slips bands forms a stress concentration hotspot. This process is highlighted in Fig. 2.3 (a-d)

In addition, the material surface roughness could play a similar role and lead to crack initiation [45]. Microcracks are nucleated at the stress concentration sites at the surface. Many micro cracks are generated on the surface which then coalesce into a larger micro crack. It is only when these cracks reach a certain size that they begin to propagate till final fatigue failure. The critical size depends on the material and is typically around a few tenths of a millimetre for low strength materials and in the hundredths of a millimetre for high strength materials.

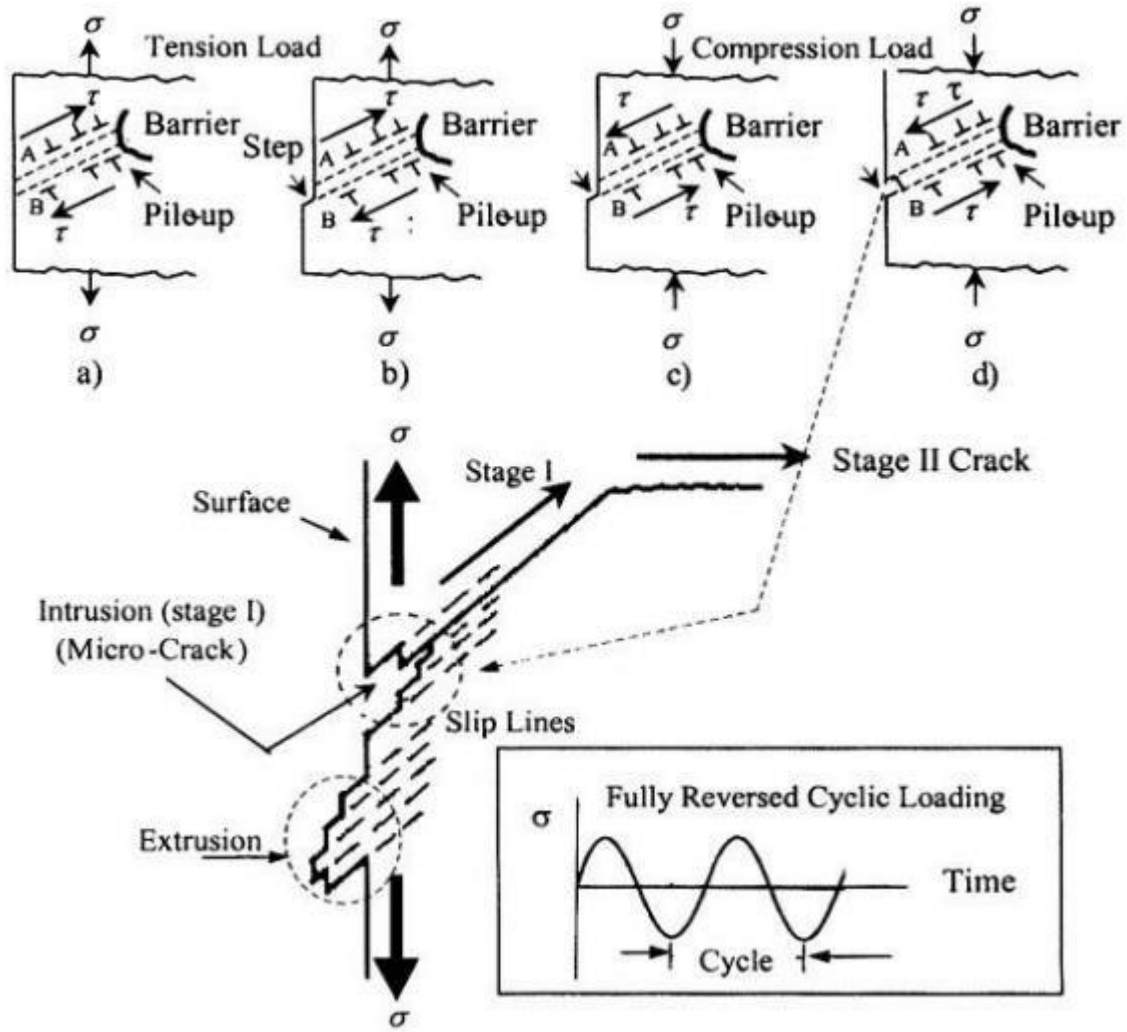


Figure 2.3: Fatigue crack initiation and propagation process [45].

2.3.2 Fatigue Crack Propagation

Micro cracks that were formed in the crack nucleation phase lie along slips planes with maximum shear stress values. The crack propagation phase can be further divided into two stages as shown in Fig. 2.3. In stage I (crystallographic propagation), the micro cracks propagate along the active slip lanes which tend to be at an angle of 45 degrees to the direction of applied stress for uniaxial loads. These micro cracks propagate for only a short length approximately two grain sizes. The crack tip plasticity at this stage is heavily influenced by the slip characteristics, grain size and load as the crack length is relatively small compared to the microstructure size.

In general, when a crack tip reaches a grain boundary the growth rate decreases, however, it will speed up again as soon as the crack passes through the boundary. Once the crack tip

propagates through the grain boundary it deviates from the 45-degree orientation and propagates in a direction perpendicular to the maximum tensile stress. This is the second stage of crack propagation. At this stage, the plastic zone ahead of the crack tip is much larger than the material grain size, which makes the crack growth at this stage less sensitive to the material microstructure than the first stage. In many engineering structures, fatigue crack growth in both the first and second stage represents the largest part of the total material life. According to Perez, (2004) [45], the crack propagation stage accounts for 70% of the total fatigue life. Therefore, it is important to accurately predict the fatigue crack growth rate in these stages to get a good estimation of the total fatigue life. Cracks can also appear in mechanical parts due to surface roughness or defects during the production process.

Fatigue life of engineering structures is usually dominated by the crack propagation phase. Hence accurate prediction of the growth rate of cracks is essential to provide a good estimate of useful life of a component or structure. Tremendous experimental work has been undertaken over the years to understand crack growth rates and path taken in a material. The parameters measured typically are the crack extension, number of cycles to failure and the stress intensity factor. Typically, this information is depicted on a fatigue crack growth (FCG) curve on a log- log scale. The abscissa is the stress intensity factor ΔK whereas the ordinate is the crack growth rate $\frac{da}{dN}$ see Figure 2.4. The FCG can be divided into three regions. The lower limit of the abscissa is the threshold stress intensity factor K_{th} where it is assumed that if the stress intensity factor is less than the value of K_{th} cracks will not propagate. The upper limit is K_c and corresponds to the fracture toughness of the material. At K_c the material experiences complete failure under the fatigue load. In region I, the crack growth rate decreases sharply until K_{th} is reached. Region III is the unstable crack growth region. Here the crack growth rate speeds up until it the stress intensity factor reaches K_c . Both regions are heavily affected by the microstructure with the mean stress and thickness additional factors affecting crack growth in region III. Region II is the steady crack growth region.

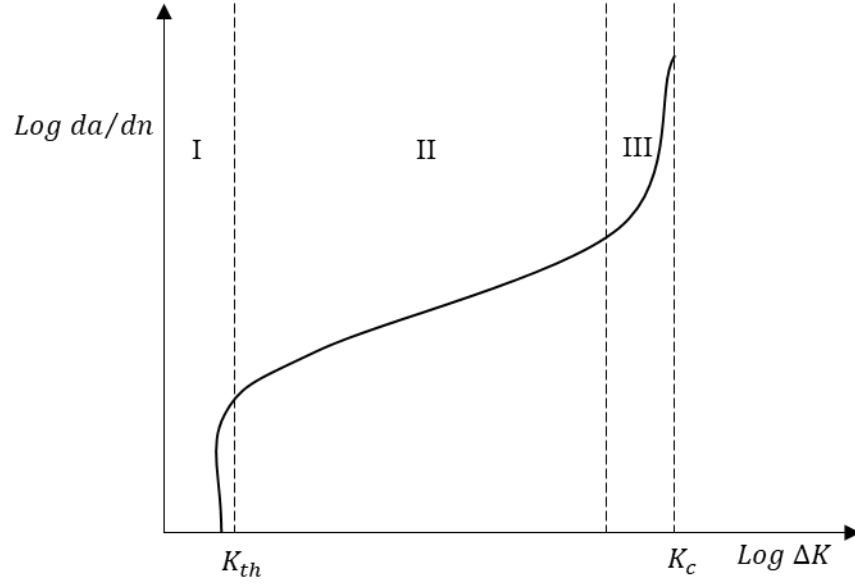


Figure 2.4: Fatigue crack growth curve

2.4 Fatigue Crack Growth Models

The focus of this thesis is on propagating cracks thus some light is shed on the various fatigue crack propagation models available in the literature in this section. FCG models are empirical models based on the fracture mechanics framework that describe data from experiments on an empirical curve with fitting parameters of the form:

$$\frac{da}{dN} = f(\Delta K, R) \quad (2.12)$$

It is important to appreciate that no “universal law” exists to model fatigue crack growth that is suitable for all materials, loading conditions, environments etc as fatigue is very much an empirical science [47]. Notwithstanding, a variety of models are available in literature to predict crack growth rate and due care must be taken to ensure the model is appropriate for the fatigue problem in question.

The foremost and still most widely used FCG model was postulated by Paris in 1961 [28] upon realisation that his experimental fatigue data could be presented in a power law form as:

$$\frac{da}{dN} = C \Delta K^m \quad (2.13)$$

Paris law describes the data in region II correctly but cannot describe the data in other regions of the FCG curve. Furthermore, the model does not account for the effects of stress ratio, the results depend upon the material used and most important Paris law are only for pure mode

I loading. Paris' law can be modified to be applicable to mixed mode loading by the use of equivalent stress intensity factor, further described in section 2.5.

Industrial standards for conducting fatigue analysis such as the BS7910 [48] and the API 579 [49] suggest the use of Paris law for conducting fatigue analysis. Thus, the focus in this thesis is primarily on Paris law. Since Paris law does not include the effect of the stress ratio, the Paris law constants used in the analysis must be obtained from experimental tests conducted at the same stress ratio for accurate predictions.

To capture the dependence of FCG rate on the stress ratio R , Walker [50] proposed an improved model of Paris law in 1971 as follows:

$$\begin{aligned}\frac{da}{dN} &= C_0 \left(\frac{\Delta K}{(1-R)^{1-\gamma}} \right)^m \\ \Delta K &= K_{max}(1-R) \\ R &= K_{min}/K_{max}\end{aligned}\tag{2.14}$$

Where the constants C_0 and m are similar to the constants in the Paris model, R is the stress ratio, K_{min} is the minimum stress intensity factor and K_{max} is the maximum stress intensity factor. The third curve fitting parameter, γ is a constant for the material. This parameter may be obtained from data of various R values, linear regression or trial and error.

Correct modelling of region III of the FCG curve requires a dependence on the fracture toughness K_C in the formulation for the crack growth rate. Forman [51] proposed a FCG model that models the unstable crack growth region accurately as:

$$\frac{da}{dN} = \frac{B \Delta K^m}{[(1-R) K_C - \Delta K]}\tag{2.15}$$

Where B and m are constants, R is the stress ratio and K_C is the fracture toughness.

The NASGRO equation [52] can mathematically represent all the three propagation regions, also including the effect of the mean stress and the crack closure. The mathematical representation of the NASGRO equation is:

$$\frac{da}{dN} = C \left(\frac{1-f}{1-R} \Delta K \right)^n \frac{\left(1 - \frac{K_{th}}{\Delta K} \right)^p}{\left[\left(1 - \frac{K_{max}}{K_C} \right)^q \right]}\tag{2.16}$$

where, C , n , p , q are empirical coefficients, R is the stress ratio, ΔK is the stress-intensity factor (SIF) range, K_{th} is the threshold stress intensity factor, K_{max} is maximum stress intensity factor and K_c is the fracture toughness. f denotes Newman's function describing crack closure [53].

Paris law is the most common empirical fatigue law in practice as it fits experimental data well and it is easy to implement. However, it has a few limitations as its applications is limited to constant amplitude loading, small scale yielding and large cracks [54]. As a result of the observed deviations from the Paris law, different modifications have been proposed by other researchers to widen its applicability.

However, all Paris-based models are still limited to large crack growth and, in general, all the models founded on the stress-intensity factor are limited to small-scale yielding. If the plastic zone at the crack tip is large, LEFM approaches will fail to represent the fracture process, so another approach should be adopted to describe the crack driving force. These approaches come under the field of elasto-plastic fracture mechanics (EPFM) [55-57].

2.5 Mixed Mode Fatigue

The loads experienced by a structure or component in service are often multi directional in nature [58]. This means more than one mode of crack growth is present at the same time and in some cases all three modes are present. These types of cracks are referred to as mixed mode fatigue cracks. When more than one mode of crack growth is involved, the fatigue crack growth analysis process is significantly more cumbersome. The primary reason is that standard handbook analytical expressions for mixed mode cracks are not readily available thus full-scale laboratory tests and numerical experimentation are the only two reliable methods to evaluate the fatigue resistance of structures encompassing mixed mode cracks. The latter is more commonly used in the industrial settings as sometimes it is impossible to conduct full scale testing e.g. (life extension phase of offshore structures past their original design safe life) leaving numerical experimentation as the only option. In this section, the models available to accurately model realistic fatigue cases (mixed mode fatigue) are explained.

2.5.1 Crack Growth Rate

The FCG models described in section 2.4 are only applicable to mode I loading. However, in practice structures and components are subjected to more than one type of loading (mixed mode fatigue) at the same time thus modifications need to be made to the FCG models to

accurately predict the crack growth rate. This is realised by replacing the stress intensity factor change with a new expression termed the equivalent stress intensity factor ΔK_{eq} that takes into account the combinations of the different modes of loading.

Tanaka [59] was the first to propose how the different mixed mode stress intensity factors should be combined. He proposed the equivalent stress intensity factor; ΔK_{eq} to be defined as such:

$$\Delta K_{eq} = [\Delta K_I^4 + 8\Delta K_{II}^4]^{0.25} \quad (2.17)$$

Where ΔK_I is the mode I stress intensity factor and ΔK_{II} is the mode II stress intensity factor. This criterion has been widely used due to its simplicity and is widely supported by numerous experimental interventions. Some of the notable works where this criterion has been applied successfully can be found in refs. [60,61 & 62].

The maximum circumferential stress criterion [63] postulates the following relationship:

$$\Delta K_{eq} = \frac{1}{2} \cos \frac{\theta_0}{2} [\Delta K_I (1 + \cos \theta_0) - 3\Delta K_{II} \sin \theta_0], \quad (2.18)$$

Where θ_0 is the circumferential stress the constants, ΔK_I is the mode I stress intensity factor and ΔK_{II} is the mode II stress intensity factor.

Irwin [44] proposed the following relationship for the equivalent stress intensity factor:

$$\Delta K_{eq} = [\Delta K_I^2 + \Delta K_{II}^2]^{0.5} \quad (2.19)$$

Richard et. al [64] proposed the following relationship for the equivalent stress intensity factor:

$$\Delta K_{eq} = 0.5\Delta K_I + 0.5\sqrt{\Delta K_I^2 + 4(1.155\Delta K_{II}^2)} \quad (2.20)$$

The equivalent stress intensity factor from any of the aforementioned criteria can be inserted into the Paris law in Eq. (2.13) giving the following expression valid for mixed mode fatigue life predictions:

$$\frac{da}{dN} = C\Delta K_{eq}^m \quad (2.21)$$

Evidently, the number of cycles (fatigue life) needed to grow a given crack size a_0 to the critical defect size a_f can be evaluated by integrating Eq. (2.21) as follows:

$$N = \frac{1}{C} \int_{a_0}^{a_f} \left(\frac{1}{\Delta K_{eq}} \right)^m \quad (2.22)$$

Once again, no single criterion works for all loading conditions thus sound engineering judgement is required to use the appropriate criterion.

2.5.2 Crack Propagation Direction

The challenge of mixed mode fatigue is that crack growth ceases to be planar and thus the crack path is not obvious. The direction of crack propagation is controlled by the mixed mode stress intensity factors. Several criteria have been put forward to evaluate the direction of crack growth with different degrees of success when contrasted with experimental data.

The most common is the maximum tangential stress criterion proposed by Erdogan and Sih [65]. They suggested that the crack grows perpendicular to the maximum tangential stress at the crack tip. The deflection angle ϕ_0 is given by the following relation:

$$\phi_0 = -\arccos \left(\frac{3K_{II}^2 + K_I \sqrt{K_I^2 + 8K_{II}^2}}{K_I^2 + 9K_{II}^2} \right) \quad (2.23)$$

Richard's criterion [63] defines the deflection angle ϕ_0 according to:

$$\phi_0 = \mp \left[155.5^\circ \frac{|K_I|}{|K_I + K_{II}|} \right] - 83.4^\circ \left[\frac{|K_I|}{|K_I + K_{II}|} \right]^2 \quad (2.24)$$

2.6 Numerical Methods for Fatigue Crack Growth Analysis

Fatigue life of a structure containing a propagating crack can be predicted by a variety of methods. Experimental full-scale testing is one with the inherent drawbacks associated with it. Analytical and numerical methods provide alternative solutions, however analytical methods are limited to select geometries and load configurations where analytical relationships for the crack tip driving force (stress intensity factor) exist [66]. Subsequently, some crack propagation law, usually Paris law can then be used to predict the crack growth rate. The process of determining analytical relations for the stress intensity factor is very involved and requires multiple iterations of either physical or numerical experimentation. Because the shape factors used in the stress intensity factor equations are determined by some best fit method, inaccuracies exist in the calculated values thus extensive validation is

needed. For mixed mode fatigue problems, analytical expressions are more complex to obtain thus industrial fatigue crack growth problems are assessed numerically to save time and costs while still accurately predicting the fatigue resistance of a structure [67]. Numerical methods have been of interest for fatigue problems and the last two decades has seen a proliferation of different techniques namely the finite element method [68], boundary element method [69], extended finite element method [70], meshfree methods [71,72] to varying degrees of success. Crack growth analysis numerically is a challenging problem because the material response of the bulk material must be resolved first in addition to the fatigue crack behaviour.

This section describes in more depth the numerical techniques used in this thesis to successfully simulate fatigue crack growth. The cohesive zone model is treated in more depth along with the various traction separation laws that describe damage evolution. The finite element method with its specific application in ANSYS for modelling crack growth is explained and more light is shed on the extended finite element method as applied to fracture mechanics and fatigue.

2.6.1 Cohesive Zone Model (CZM)

The cohesive zone model (CZM) has become an important method for modelling fracture problems with extensive numerical implementation. The theory was firstly proposed by Dugdale [29] and Barenblatt [30]. Fig 2.5 represents Dugdale's model. The crack is split into two parts, the one is the free surface and the other one is under the cohesion. Cohesive zone model does not represent any physical material but describes the cohesive forces which occur when material elements are being pulled apart.

As the surfaces (known as cohesive surfaces) separate, traction first increases until a maximum is reached, and then subsequently reduces to zero which results in complete separation. The variation in traction in relation to displacement is plotted on a curve and is called the traction-separation curve. Fig 2.6 presents the different types of traction separation laws possible. The area under this curve is equal to the energy needed for separation. The CZM eliminates the unrealistic stress singularity at the crack tip predicted by LEFM by limiting the maximum stress to the cohesive strength of the material.

The traction-displacement curve provides the constitutive behaviour of the failure process. The amount of fracture energy dissipated in the work region depends on the shape of the model considered. Dugdale assumes the cohesive stress, σ_0 acting on the length of the

cohesive zone is constant and is equal to the yield stress. Barenblatt's model allows the cohesive stress to vary as a function of crack opening displacement [30]. A main attraction in the use of CZM for fatigue modelling is that it requires the identification of only two of the main cohesive parameters if the shape of the traction separation law is known.

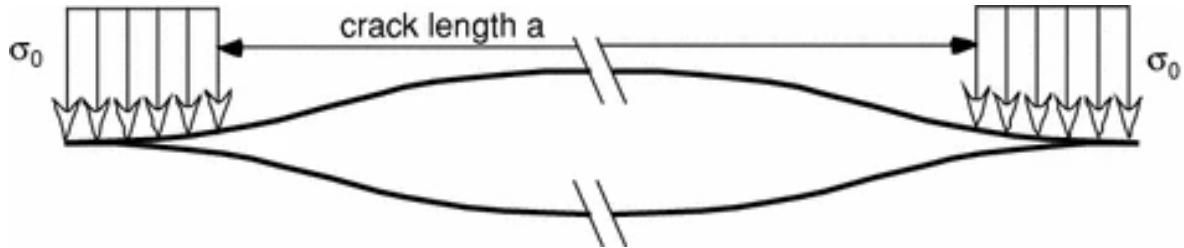


Figure 2.5: Fracture model of Dugdale [73]

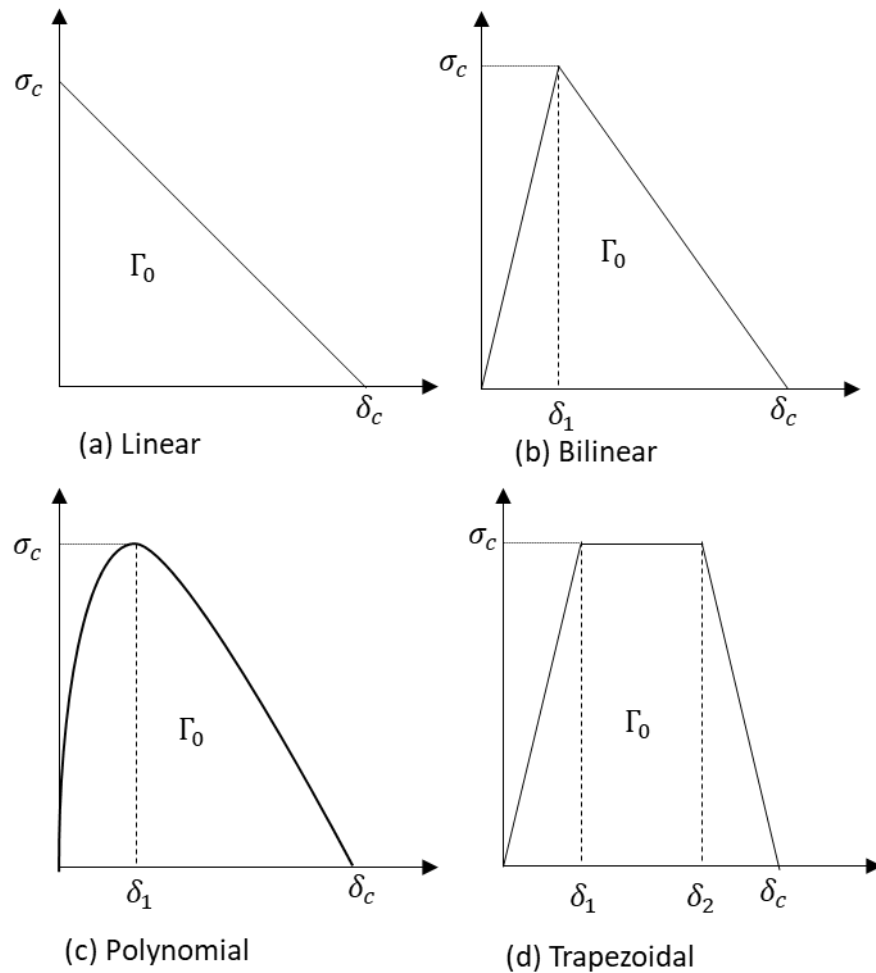


Figure 2.6: Various traction separation laws.

Hillerborg et al. [31] proposed a model based on Barenblatt [30] cohesive crack in which the stress is not constant and is a function of the crack opening. Roth et al. [74] used a cyclic cohesive zone model to model fatigue failure in metals. Fatigue behaviour of composites was modelled successfully using CZM in the work of Nojavan et al [75]. There is no consensus on the ‘best’ traction separation laws but their applicability should be judged on a case-by-case basis depending on the material [76]. For numerical reasons, continuously differentiable traction separation laws (polynomial, exponential) are preferred [74].

2.6.2 Finite Element Method (FEM)

The finite element method (FEM) is a numerical technique for solving partial differential equations. Partial differential equations are of widespread interest as they represent the governing equations for problems in economics, science, engineering, finance etc. FEM works by dividing the system of interest into smaller parts called elements which are connected together by the mesh. FEM has been applied to a whole host of problems in both solid and fluid mechanics including fatigue [77-80].

In FEM, crack propagation problems are resolved computationally in a step-wise manner. The crack is advanced a small length in each step and a crack propagation law is used to estimate the number of cycles for the next crack increment. According to [81] for a computational method to successfully simulate FCG, the following tasks need to be accomplished within each step:

- 1: Calculation of the minimum and maximum stress and displacement fields within the cracked component.
2. Appraisal of the minimum and maximum stress intensity factors for the crack.
3. Determination of the direction for further crack propagation.
4. Generation of a representation of the advanced crack.

This process is repeated until the critical stress intensity factor is reached; $K_{max} = K_c$, and the number of experienced cycles are summed to obtain the crack propagation life.

In order to determine the most critical fracture mechanics parameter i.e., stress intensity factor several techniques are available in literature with different pros and cons and varying degrees of accuracy. Some of these methods are displacement extrapolation method [82], domain integral approach [83] among others [84].

Many software solutions have been developed to model fatigue crack growth problems, but most of the solutions were developed by research groups and not commercially available. Examples of commercially available software based on FEM that can simulate fatigue crack growth include FRANC3D [85], ADAPCRACK [86], ZENCRACK [87,88], and PROCRACK [89,90]. FEM has been used successfully to predict fatigue crack growth in structures for several decades. Richard et al. [91] simulated the fatigue crack growth in a rubber-sprung railway wheel of a high-speed train involved in an accident using ADAPCRACK3D. The fatigue crack growth of twin coplanar elliptical-arc surface cracks in round bars under tension was also addressed by Lin and Smith [92]. Hou et al. [93] analysed the fatigue crack growth in turbine discs of military aircraft engines using ZENCRACK. A review of fatigue modelling techniques and case studies using FEM can be found in [81,94].

Mesh size is closely linked to solution accuracy in FEM thus the sub-modelling technique is typically used to create a finer mesh near the crack tip with a denser mesh in the global model. For 3D meshing this can become very computationally expensive. Another drawback of FEM as applied to fatigue is that the solution accuracy can be affected when mapping the outputs from the old to the new mesh. The need for remeshing in traditional FEM makes automatic fatigue crack propagation simulation challenging as the mesh must be updated after each step. This major bottleneck was removed by the advent of Selective Adaptive Remeshing Tool (SMART) solver in the commercial software package ANSYS [95]. The software automatically remeshes the crack as it propagates thus eliminating the major shortcoming of traditional FEM. Furthermore, the tetrahedral elements are employed using the unstructured mesh method that provide similar levels of fidelity to what can be obtained using an “ideal” hex mesh but with a significant reduction in computational processing times. Hence 3 D fatigue simulations that may otherwise take days can be solved in minutes using the ANSYS SMART solver. The solver has been widely used since inception to model fatigue problems and also validated against experimental results [96-100].

Ansys SMART solver is employed in chapters 4 and 5 of this thesis as the vehicle for fatigue experimentation.

2.6.3 Extended Finite Element Method (XFEM)

XFEM developed by Belytschko and Black [33] is a finite element method that was designed to alleviate the issues faced by traditional FEM in solving problems containing

discontinuities. It achieves this, by adding enrichment functions to the spaces of interest using the concept of partition of unity [32]. Discontinuities can be divided into either strong or weak discontinuities. Strong discontinuity occurs when there is a discontinuity in the solution variable of a problem whereas a discontinuity in the derivate of the solution variable is classed as a weak discontinuity. In the analysis of structures, the solution variable is typically the displacement. Thus, an example of a strong discontinuity would be problems containing displacement jumps such as cracks, holes etc. Weak discontinuities can be observed in bi-material problems where there is a jump in strain at the transition point of the materials.

The partition of unity concept forms the mathematical basis of XFEM. Partition of unity is a set of n function f that satisfies the relationship:

$$\sum_{i=1}^n f_i(x)g(x) = g(x) \quad (2.25)$$

The interpolation shape functions used in FEM also satisfy the partition of unity as shown below:

$$\sum_{i=1}^n N_i(X)f(X) = f(X) \quad (2.26)$$

Taking advantage of this property, the field in a finite element approximation space can be enriched as follows:

$$u(x) = \sum_{i=1}^n N_i(X)u_i \quad (2.27)$$

Thus the a priori knowledge of the system can be used to represented mathematically as such:

$$(x) = \sum_{i=1}^n N_i(X)u_i + \sum_{i=1}^n N_i(X)u_i \sum_{j=1}^k p_j a_{ij} \quad (2.28)$$

Where:

p_j are enrichment functions

u_i are the FE degrees of freedom,

a_{ij} are the extra degrees of freedom

The enrichment functions offer a great deal of flexibility to the XFEM method as it allows for a variety of problems to be solved depending on the type of enrichment function employed. Customising the enrichment function can offer improvements in certain key areas for a specific problem e.g., shear strain accuracy. Furthermore, a decision needs to be made on the size of the approximation space requiring enrichment. For cracks, the discontinuity in the displacement, stress and strain fields only occur at the crack tip or along the crack thus local enrichment of only the nodes around the crack would suffice.

Mathematically, the displacement of a gauss point [32] can be written as:

$$u(x) = \sum_{j=1}^n N_j(x)u_j + \sum_{h=1}^{mh} N_h(x)(H(x) - H(x_h))\mathbf{a}_h + \sum_{k=1}^{mt} N_k(x) \left[\sum_{l=1}^4 (F_l(x) - F_l(x_k))\mathbf{b}_k^l \right] \quad (2.29)$$

Here n is the number of standard finite element nodal, $N_i, N_j, N_k(x)$ are continuous shape functions, u_j is the freedom vector of standard finite element nodal, $H(x)$ is the Heaviside function of gauss point x and $H(x_h)$ is the Heaviside function of enrichment nodal h , \mathbf{a}_h is the freedom vector of sides around the crack, $F_l(x)$ and $F_l(x_k)$ are the crack-tip enrichment function at gauss point x and enrichment nodal k , and \mathbf{b}_k^l is the freedom vector of crack-tip enrichment nodal.

The crack-tip asymptotic function is written as:

$$\{F_l(r, \theta)\}_{l=1}^4 = \left\{ \sqrt{r} \sin \frac{\theta}{2}, \sqrt{r} \cos \frac{\theta}{2}, \sqrt{r} \sin \theta \sin \frac{\theta}{2}, \sqrt{r} \sin \theta \cos \frac{\theta}{2} \right\} \quad (2.30)$$

where (r, θ) is the polar coordinate at point x , and $\theta = 0$ for the tangent direction of crack.

The asymptotic crack tip enrichment function models the singularity at the crack tip. The analytical solutions for the stresses, strains and displacement are known from LEFM form the basis of the asymptotic crack tip function. The near tip enrichment basis functions aid greatly with convergence despite the high stress gradients present at the crack tip. All nodes in elements whose nodal support contains the crack tip are enriched with this function.

The Heaviside function is a discontinuous function that represents the gap in the crack surfaces. All nodes in elements whose nodal support are intersected by the crack are enriched by this function. The Heaviside function oscillates between 0 and 1.

Crack modelling in FEM requires explicit modelling of the crack. It is a requirement for the nodes to be placed all along the crack and the crack tip. The flexibility offered by the enrichment functions has led to its application in unique cases where a priori information about localised behaviour can be represented by a basis function.

XFEM was applied in the work of Singh et al. [101] to study the effect of holes and inclusions on the stress intensity factor values. It was then successfully applied to interfacial fatigue cracks present in bi-layered functional graded materials in the work of Bhattacharya et al. [102]. Pathak et al showed 3D fatigue crack simulations was possible with XFEM [103]. The work of Bergara et al [104] showed that fatigue crack propagation in complex stress fields can be solved using XFEM by investigating fatigue crack growth in four-point bend specimens. The XFEM formulation has been widely used to study crack propagation under different conditions [105-108].

Despite the widespread success of XFEM for fatigue analysis it is not without drawbacks however, as it suffers from poor convergence due to blended elements. Although touted as a mesh independent method the work of Ren and Guan [109], clearly shows a direct correlation between mesh refinement and accurate representation of a three -dimensional crack. For 3D fatigue crack growth problems, the increase in the DOF compared to 2D case may cause computational costs to become prohibitive. Another limitation is that the crack must propagate through a whole element at a time this can cause an overestimation of the crack growth rate. A state-of-the-art review of XFEM as applied in the fracture mechanics can be found in the work of Yazid et al [110].

Finite element modelling in chapter 3 of this thesis was conducted in ABAQUS, using the eXtended Finite Element Method (XFEM) for crack modelling in conjunction with the direct cyclic solver and Paris law to simulate fatigue loading.

2.7 Scaled Experimentation in Fatigue

This section describes the state of the art in scaled fatigue experimentation. A historical review of the evolution of similitude theory is presented with special detail given to dimensional analysis. The concept of similitude is introduced with the conditions necessary to achieve complete similarity emphasized. The Buckingham pi theorem is the most common

method of applying dimensional analysis and the procedure is described here. The advantages and limitations associated with dimensional analysis are elucidated as well.

2.7.1 Historical Overview

Similitude theory is a branch of engineering science concerned with establishing the necessary and sufficient conditions of similarity among phenomena, and has been applied to different fields such as structural engineering, vibration and impact problems [13]. Before delving into the current state of the art on fatigue scaling it would be prudent to give an overview of the various methods available in the literature for scaled testing.

The first reference to similitude theory dates back to the 18th century. In fact, Galilei and Weston stated that size and strength of an object do not decrease in the same ratio: if dimensions decrease, the strength increases [111]. The curious aspect of this statement is that Galileo in the 18th century, was already facing the problem of size effects. However, the first work in which scientific models based on dimensional analysis are discussed is by Rayleigh in 1915 [36]. Although Rayleigh's article aimed to emphasize the importance of similitude methods, especially in engineering thirty years had to pass before the publication of another work in which the usefulness of similitude methods is highlighted: the NACA technical report [112] and the book by Goodier [113]. In these publications, dimensional analysis was applied for the first time with a systematic procedure to simple and complex problems. This resulted in a deep insight on the modelling of materials with nonlinear stress–strain characteristics, large deflections and buckling. [114]

Soedel [115] derived similitude conditions for free and forced vibrations of shells from Love's equations. The most used method after dimensional analysis is Similitude Theory Applied to Governing Equations (STAGE) [13]. Kline, (2012) was the first to introduce this method [116]. Similitude theory is applied directly to the field equations of the system, including boundary and initial conditions, which characterize the systems behaviour in terms of its variables and parameters. Similar models are governed by an equivalent set of field equations and conditions; thus similitude conditions may be derived by defining the scale factors and comparing the equations of both prototype and model. The derived conditions relate geometric (length, width, thickness, etc.), excitation (force amplitude, excitation frequency, etc.), and material properties (Young's modulus, Poisson's ratio, density etc.) of the system to its response. When all of them are satisfied, then complete similitude is achieved, else the model is said to be distorted.

De Rosa, (1997) introduced the finite similitude method known as asymptotical scaled modal analysis also based on energy [117]. It was developed to solve the prohibitive computational cost of high frequency problems solved using FEM. Despite the plethora of similarity laws available, the most commonly used by some distance in fatigue scaling is dimensional analysis.

Figure 2.7 shows a summary of the scaling techniques introduced in the literature over the years.

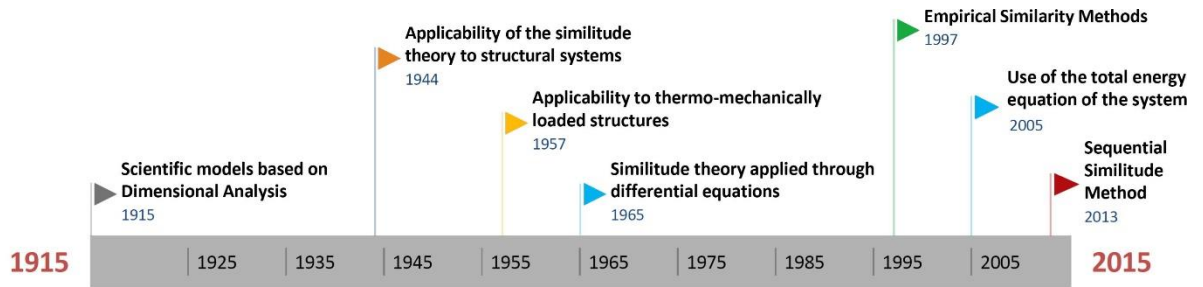


Figure 2.7: Timeline of development of similarity techniques [13]

2.7.2 Similitude (Similarity Laws)

Similitudes can be distinguished according to the parameters taken into account [118]. There are three necessary conditions for complete similarity between a model and a prototype.

Geometric similarity: the model must be the same shape as the prototype, but may be scaled by some constant factor.

$$\frac{L_{model}}{L_{prototype}} = L_{ratio} \quad (2.31)$$

Where L_{model} is simply the length of the scaled model in any direction and $L_{prototype}$ is the length of the prototype in the same direction. The ratio L_r is the scaling factor and is the same in the x, y and z directions for isotropic scaling.

Kinematic similarity: the velocity at any point in the model flow must be proportional by a constant scale factor to the velocity at the homologous point in the prototype flow. (That is, the flow streamlines must have the same shape.)

A formal definition of kinematic similitude, that also introduces the concept of scale factor, is given by Westine et al. [118]:

The function f' is similar to function f , provided the ratio f'/f is a constant, when the functions are evaluated for homologous points and homologous times. The constant $\lambda = f'/f$ is called the scale factor for the function f . The term homologous is defined as *corresponding but not necessarily equal values*).

The two main fundamental quantities, which describe the motion of an object are distance and time. If the ratios of length and the ratio of time interval for each system is constant, then, the velocities of corresponding particles will also be in a fixed ratio and hence Kinematic similitude is satisfied. Mathematically, it is expressed as:

$$\frac{V_m}{V_p} = \frac{L_m/T_m}{L_p/T_p} = \frac{L_m}{L_p} \div \frac{T_m}{T_p} = \frac{L_r}{T_r} \quad (2.32)$$

Where V_m is the velocity of the model (scaled down experiment) and V_p is the velocity of the prototype (full scaled experiment).

A similar expression for acceleration is:

$$\frac{a_m}{a_p} = \frac{\frac{L_m}{T_m^2}}{\frac{L_p}{T_p^2}} = \frac{L_m}{L_p} \div \frac{T_m^2}{T_p^2} = \frac{L_r}{T_r^2} \quad (2.33)$$

Where a_m is the acceleration of the model (scaled down experiment) and a_p is the velocity of the prototype (full scaled experiment).

Dynamic similarity: all forces in the model flow must scale by a constant factor to the corresponding forces in the prototype flow. In other words, the relative importance of different types of forces (e.g., viscous and inertial forces) must be the same for the model and prototype. Let f_i be the force due to inertia and f_v is the force due to viscosity then:

$$\frac{f_{i_{model}}}{f_{v_{model}}} = \frac{f_{i_{full}}}{f_{v_{full}}} \text{ or } Fr = \frac{F_{full}}{F_{model}} \quad (2.34)$$

In dimensional analysis, the requirement is that the model and prototype have the same dimensionless parameters (e.g., the same Reynolds number), although they may (and usually do) have different dimensional variables. Mathematically, for all pi groups that can be defined for two different flow situations, dynamic similarity requires that geometric and kinematic similarity are necessary but insufficient conditions for dynamic similarity. It is possible to have geometric and kinematic similarity, but not dynamic similarity.

2.7.3 Dimensional Analysis (Buckingham- Pi Theorem)

Dimensional analysis is a method whereby the behaviour of a phenomenon can be deduced based on the premise that any phenomenon can be represented by a dimensionally consistent set of variables [119]. Similarity in physical terms refers to some equivalence that exists between two things or phenomena that are actually different. For example, the forces acting on a large ship, and the forces acting on an identical small-scale model of the ship are related. Mathematically, similarity refers to a transformation of variables that leads to a reduction in the number of independent variables that specify the problem. Dimensional analysis is based on invariance.

The fundamental argument of dimensional analysis is that the form of any physically significant equation must be such that the relationship between the actual physical quantities remains valid independent the magnitudes of the base units. Dimensional analysis can shed more light on a particular problem/process. However, it does not give a solution to the problem completely. The knowledge gained from dimensional analysis can be a useful tool to find a complete solution [120].

The application of dimensional analysis to any problem assumes that certain variables in the problem are independent, in other words they are inconsequential to the problem at hand and only the dependent variables (ones affecting the problem) should be considered. The Buckingham Pi theorem [37] is commonly used to apply dimensional analysis to scale problems. It states that if n number of physical variables (relevant to the phenomena) and these variables are expressed in k number of fundamental physical quantities (i.e., dimensions), then Π ($\pi = n - k$) dimensionless groups are present for this specific problem [121]. This results in decreasing the number of variables involved to smaller (Π) number of dimensionless groups, obtaining a functional relationship between the independent dimensionless groups [121].

A general step by step procedure for the dimensional analysis of a problem is presented below, based on the procedure outlined by Zohuri [119]:

1. List all problem variables (n) (chosen by user).
2. Select primary dimensions (k).
3. List dimensions of all variables in terms of primary dimensions.
4. Select a number of repeating variables equal to the number of primary dimensions (k) from list of selected variables.

5. Write Pi parameters in terms of unknown exponents and write the equation such that the sum of the exponents is equal to zero, solving the equation results in $(n-k)$ number of dimensionless groups.
6. Verify the Pi groups created are dimensionless. If the dimensionless parameters of the scaled and unscaled processes match, then the two processes can be denoted as similar.

Mathematically, consider a set of independent quantities, for example $Q_1, Q_2 \dots Q_n$ that determine the value of a target function Q_0 . Q_0 can be expressed as:

$$Q_0 = f(Q_1, Q_2 \dots Q_n) \quad (2.35)$$

Each independent quantity (Q) will not influence each other, and the value of the target function Q_0 is dictated by the independent quantities. Applying step 5 of the aforementioned procedure, the number of independent quantities that appear is reduced from n to $n-k$, where k is the maximum number of the original n that are dimensionally independent. The independent parameters in terms of their basic dimensions can be described as:

$$Q_i = L^{l_i} M^{m_i} T^{t_i} \quad (2.36)$$

where L, M, T are fundamental dimensions in physics, and here l_i, m_i , and t_i are dimensionless numbers that follow from each quantity's definition. Dimensionless forms of the $n - k$ remaining independent variables are defined by dividing each variable with the product of powers of $Q_1, Q_2 \dots Q_k$ that have the same dimension, and thus:

$$\Pi_i = \frac{Q_{k+i}}{Q_1^{N_{(k+i)1}} Q_2^{N_{(k+i)2}} \dots Q_k^{N_{(k+i)k}}} \quad (2.37)$$

where $i = 1, 2, \dots, n - k$ and for the dependent variable

$$\Pi_0 = \frac{Q_0}{Q_1^{N_{01}} Q_2^{N_{02}} \dots Q_k^{N_{0k}}} \quad (2.38)$$

Thus, the problem can be made simpler and expressed solely in terms of the dimensionless groups as such:

$$\Pi_0 = f(\Pi_1, \Pi_2 \dots \Pi_{n-k}) \quad (2.39)$$

where Π_i represents the different dimensionless groups.

Despite the advantages offered by dimensional analysis, it still suffers from some limitations. The choice of dimensionless groups is not unique and as such might not be “physically

meaningful”. Furthermore, similarity of highly complex problems is often not possible with dimensional analysis as it does not account for size scale effects.

2.8 Size Effects in Fatigue

Extensive research [122-125] has confirmed the existence of size effects in fracture mechanics and fatigue regardless of material type. Broadly speaking, size effects can be categorised into three, which are statistical, technological, and geometric [126]. Statistical size effect is the observed differences in fatigue strength of same size specimens with identical surface finish. Technological size effect is the observed difference in fatigue strength of identical components with different surface finish.

The focus in this thesis is solely on the observed difference in fatigue crack growth (FCG) rate with geometry change with replica scaling (i.e., identical materials throughout). Geometric size effects are highlighted in the work of Brose and Dowling [24], where they examined the fatigue crack growth rate of compact tension (CT) specimens. An increase in the width of the specimen from 25mm to 400mm whilst maintaining constant other dimensions resulted in a decrease by a factor of 5 of the FCG rate of AISI 304 steel. Similarly, Garr and Hesko confirmed that different sized CT specimens resulted in varying FCG rates in Inconel 718 alloy [25]. However, in these studies, they focused on comparing showing how a change in any of the geometrical dimensions affects the fatigue behaviour with no solution or scaling law proposed to reconcile the size scale effects.

The pioneering work of Barenblatt and Botvina [127] confirmed, on application of dimensional analysis to the Paris law, that complete self-similarity is impossible for a material under fatigue loading. The special condition was if the Paris law exponent m was equal to 2 which is almost never the case. This has not stopped researchers attempting to solve the incomplete similarity inherent to fatigue by proposing some scaling laws founded majorly on dimensional analysis. Bazant and Xu expressed the change in crack length per cycle as a power function of the amplitude of a size-adjusted stress intensity factor [33]. Manning et al. [128] proposed a scaling law to reconcile the size effects observed experimentally in sandstone. Kirane and Bazant [129] extended the work of Manning et al. [128] to account for the size effects observed in concrete. Carpinteri proposed a mono-fractal approach to deal with the dependence of the Paris law exponent on initial crack length [19]. Other multifractal approaches have been put forward by different researchers [20-22]. However, it should be recognised that adaptations of the Paris law will not satisfy the similitude invariance provided by dimensional analysis. The existence of a size effect

in and of itself is sufficient to confirm that dimensionless empirical laws must change with scale.

2.9 Application of Dimensional Analysis to Fatigue

Barenblatt and Botvina [127] applied dimensional analysis to Paris law to describe its inherent incomplete self-similarity. Since then, different researchers have applied the same approach extending it to quasi brittle materials [16], short cracks [17] and to characterise the many observed deviations from the Paris law regime [130]. They examined Paris law to determine if it is a true scaling law that reproduces itself at all scales. Paris law is given in Eq. 2.40:

$$\frac{da}{dN} = C \Delta K^m \quad (2.40)$$

Consider a generalised approach, where the crack growth rate $\frac{da}{dN}$ is assumed to be a function of the stress-intensity-factor amplitude, $\Delta K = K_{max} - K_{min}$, stress-intensity factor asymmetry $R = K_{min}/K_{max}$, the characteristic length scale of the specimen h , e.g., its diameter, or thickness, the material's yield stress σ_y , fracture toughness K_{IC} , loading frequency ω and time t . The governing variables of fatigue crack growth and the corresponding dimensions are presented in Table 2.1.

The crack growth rate can be expressed as such:

$$\frac{da}{dN} = f(\Delta K, R, K_{IC}, t, h, \omega, \sigma_y) \quad (2.41)$$

Considering only the primary variables, in terms of dimensional analysis Eq. 2.41 can be written as:

$$\frac{da}{dN} = \left(\frac{\Delta K}{\sigma_y} \right)^2 \Phi \left(\frac{\Delta K}{K_{IC}}, R, Z, \omega t \right) \quad (2.42)$$

where:

$$Z = \frac{\sigma_y \sqrt{h}}{K_{IC}} \quad (2.43)$$

Table 2.1: Governing variables of fatigue crack growth.

Variable	Definition	Dimensions
σ_y	Tensile yield stress	FL^{-2}

K_{IC}	Material fracture toughness	FL^{-2}
ω	Frequency of loading cycle	T^{-1}
ΔK	Stress intensity range	$FL^{-3/2}$
t	Time	T
h	Characteristic length	L
R	Load ratio	-

In the absence of significant environment effects, the effect of ωt is negligible, two possible modes of similarity exist by considering the asymptotic relations in Eq. 2.51 and Eq. 2.52 where $\frac{\Delta K}{K_{IC}} \ll 1$ (Paris law regime). They are complete similarity and incomplete similarity. Complete similarity means all similarity parameters can be deduced from dimensional analysis alone, this is not the case with incomplete similarity.

Complete similarity as $\frac{\Delta K}{K_{IC}} \ll 1$ would imply that Eq. 2.42 becomes:

$$\frac{da}{dN} = \left(\frac{\Delta K}{\sigma_y} \right)^2 \Phi(R, Z) \quad (2.44)$$

Contrasting this to the form of Paris law in equation 2.49 this would imply that the Paris law exponent has to be equal to 2 for complete similarity to be achieved. Experimental evidence suggests that this is not reality, for some aluminium alloys m is close to 2, but nevertheless always larger than 2. For the vast majority of cases m is substantially larger than 2. Experimentally measured Paris law exponents typically vary between 2 and 4 for ductile materials, and can be considerably larger for brittle materials, i.e., approaching 10 in low toughness metals [131] and even higher in intermetallics and ceramics [132]. If incomplete self-similarity is assumed as $\frac{\Delta K}{K_{IC}} \ll 1$ then:

$$\Phi = \left(\frac{\Delta K}{K_{IC}} \right)^\alpha \Phi_1(R, Z) \quad (2.45)$$

$$\frac{da}{dN} = \frac{(\Delta K)^{2+\alpha}}{\sigma_y^2 K_{IC}^\alpha} \Phi_1(R, Z) \quad (2.46)$$

Which now represents Paris law with $C = \frac{\Phi_1(R, Z)}{\sigma_y^2 K_{IC}^\alpha}$ and $m = 2 + \alpha(R, Z)$. This clearly indicates that the Paris law parameters C and m are not material properties as the dependence on characteristic length is obvious. The fatigue-crack growth data of Heiser and Mortimer

[133] on AISI 4340 steel confirm a change in m with structural size. h was identified with the specimen thickness in their study.

One key point to make is that although Paris law is limited to the region II of the FCG rate curve, $\frac{da}{dN}$ vs. ΔK data from tests on small specimens is still widely used to characterize crack-growth behaviour of larger structures. Thus, observations that the growth rates of fatigue cracks may vary with specimen size present a concern as the FCG rate cannot be extrapolated from small specimens to large structures. The dimensional analysis approach involves a lot of assumptions, thereby making it a tedious and complicated one. Furthermore, the choice of dimensionless numbers is not unique and more simplifications are required to extract the similarity parameters as they are not readily obtained through dimensional analysis alone [134].

As a consequence of the aforementioned drawbacks associated with dimensional analysis as applied to fatigue there is a need for a scaling theory that can accurately capture the size scale effect in fatigue with precision.

2.10 Microstructural Size Effects in Fatigue

Microstructure plays a role in both fatigue crack initiation and predominantly early stages of fatigue crack growth propagation. Whenever a metallic component experiences deformation, the grain boundaries block the dislocation slip, and as a consequence, the dislocations pile up leading to build up of stress concentrations in the component. Nevertheless, there are some other grain boundaries that allow dislocations to transmit across them. Micro cracks initiate at the grain and then propagate across the grain. Thus, grain size is a critical parameter that determines mechanical properties of a metal. Reduction in grain size improves mechanical properties as it means more boundaries reduces dislocation movement within the microstructure. The effect of the grain size on the fatigue behaviour of aluminium was investigated by Turnbull et al. [135] experimentally. An increase in the fatigue strength was observed with the decrease in grain size.

Microstructure parameters such as grain boundary, grain orientation, and interaction between adjacent microscopic cracks precipitation all affect fatigue crack initiation and small crack fatigue crack growth. The work of Suresh & Ritchie [136] showed how short cracks defined according to the crack length proportional to grain size dimensions propagate faster than long cracks under the same applied stress intensity factor range. This is known as material based size effect. Similar observations have been made by other researchers see the work of

Mughrabi [137,138], McEvily et al. [139] among others [140-142]. The Tanaka-Mura relation is most commonly empirical law used to relate microstructure properties such as the shear stress of the slip band and grain size to predict crack initiation life [143].

Experimental work by Zhu et al. [144] on fatigue crack growth of single edge notched tensile specimens made from nickel superalloy show how when the crack length is comparable to the grain size the fatigue crack growth rates are heavily influenced by the microstructural factors. Increase in grain sizes resulted in an increase in both crack initiation life and total fatigue life. More rapid stage I crack growth is observed in materials with an increase in grain size.

From the literature, it is clearly seen that the microstructure effects are the dominant factor controlling short crack fatigue growth. In this work, long crack fatigue growth is the focus thus microscopic effects are ignored as the crack length of the smallest scale models are several magnitudes higher than the grain size dimensions. Material based size effect is not a considered as the scale separation conditions are satisfied.

Summary

This chapter attempts to give a holistic understanding of the many topics of relevance to this thesis with the aim to give the reader a better understanding of the concepts necessary to aid comprehension of subsequent sections containing the research publications of this PhD project. A historical overview of scaling techniques in general was presented with greater depth given to the most common scaling theory; dimensional analysis. The existence of size effect in fatigue and LEFM in particular are explained with the different types of size effects possible explained. The focus of this work is narrowed down to the type of size effect that occurs in geometrically similar structures under fatigue loads due to changes in stress gradient. The pioneering work of Barenblatt and Botvina [127] is explained in greater detail where the current short comings associated with scaled experimentation in fatigue are completely demonstrated. By means of applying dimensional analysis to Paris law arguments, they discovered that Paris law does not reproduce itself at all scales. In simple terms, fatigue data obtained using small scale experiments cannot be reliably used to predict full scale behaviour. In addition, the Paris law constants C and m are shown to not be material constants as once believed and do in fact change with a geometric sizing update.

From the extensive literature review it is made abundantly clear that the observed change in behaviour of the fatigue process with scale (geometric size effect) cannot be captured by

dimensional analysis. Thus, there exists a need for a scaling theory that can capture such effects by effectively designing scaled fatigue experiments that can be related to the full-scale prototype effectively capturing all the fracture mechanics parameters of interest relevant to fatigue. Due to the limitations of dimensional analysis a different approach to scaled experimentation using the first order finite similitude theory [34] would be used to study fracture and fatigue response. The uniqueness and subsequently advantage of this scaling theory is that it is not limited by the requirement of proportional fields between the scaled model and prototype like the dimensional analysis approach (and zeroth order finite similitude theory). Instead, it allows for divided differences in the fields of the scaled experiments and then reconstructs the full-scale behaviour from the scaled experimental output parameters. The first order finite similitude theory is applied in the subsequent sections to design and conduct fatigue testing at smaller scales to evaluate the predictive ability of the scaling theory. The outcomes of the investigations show that two appropriately designed scaled experiments better recreate the fatigue behaviour of a defect laden component under fatigue loading.

Chapter 3 Scaled Cohesive Zone Models for Fatigue Crack Propagation

3.1 Introduction

Reports indicate that fatigue failure accounts for approximately 90% of all mechanical failures in engineering components during their service life [1]. Although fatigue failures cannot be completely eradicated, knowledge of crack growth rates and paths taken through a component, provides a means for the evaluation and monitoring of structural integrity. The remaining life of a component under normal service conditions can consequently be estimated along with the establishment of inspection and maintenance protocols. There are situations where monitoring is not feasible however and consequently there is a continual need for experimental and theoretical developments. Experiments can be performed on standard test specimens or on full-sized components but testing on scaled models is also a possibility if the data obtained can be related to the full-size component. The situation presently is that scaled experimentation does not feature heavily because of the issues associated with relating data across the scales [134]. Problems are also a facet of full-scale testing however, which include the expense of time, computation, and human resources. To a certain degree, modern numerical approaches mitigate some of these difficulties although other challenges arise related to representation, with possible disparities between outputs from models and experimental data. A particularly convenient example of a modern approach for the modelling and analysis of fatigue crack growth is the extended finite element method (XFEM). This is based on the partition of unity concept and employing enrichment functions around the crack tip [32,33]. These functions improve the description of stress and displacement fields around the crack tip and consequently reduce the need for mesh refinement. The XFEM formulation has been widely used to study crack propagation under different conditions see refs. [103,104, 145-150]. Farukh et al. (2015) predicted the crack growth of a three-point bend specimen under thermo-mechanical fatigue conditions using XFEM, making use of an accumulated strain criterion [150]. Scaled experimentation is a solution to the time and cost problem however its widespread applicability has been hampered by the existence of scale and size effects. Scale effects are the observed changes in behaviour of a process with varying scale that consequently leads to an inability to predict the behaviour of processes occurring at the full scale. An early reference to similitude theory is by Galilei and Weston [151], where the problem of size effect is noted. They observed that the size and strength of an object do not change with the

same ratio. Scaled models based on dimensional analysis were first introduced by Rayleigh [36], where similitude-based rules were applied to a variety of problems. The work of Kline & Radbill (1966) was the first to combine dimensional analysis with governing equations to achieve similitude [152]. It is well appreciated in the scientific literature that size effects are a particular concern in fracture mechanics (see for example the works refs. [127-134,153]). This is further compounded by the unique challenge faced in performing fatigue analysis experimentally whereby specimens with the same geometry and surface finish exhibit different fatigue crack growth rates due to inherent inhomogeneity at the micro scale as shown in the work of Virkler et al. (1978) [154]. Barenblatt and Botvina [127] confirmed that incomplete self-similarity is inherent in Paris law, which explains why efforts to perform scaled experiments have been met with relatively little success. They showed that the Paris law exponent m would have to equal 2 for the Paris law to have complete similarity. However, analysis of experimental data reveals that m varies and is invariably larger than 2, thus similarity is not typically a feature of the Paris law. Different power law empirical formulations based on some form of Paris law exist, but they suffer from the same limitation [155]. Notwithstanding, there have been various attempts by different authors to achieve similitude in fatigue. Carpinteri et al. (2002) [156] proposed a fractal approach to deal with the dependence of the Paris law exponent on initial crack length. Tomaszewski et al. (2014) proposed a multifractal scaling law for high cycle fatigue of an aluminium alloy [157]. They described phenomenologically, the observed phenomenon whereby the fatigue strength of material decreases with an increase in cross sectional area by applying the fractal dimension. In the work of Ray & Kishen (2012) [158] they used dimensional analysis to predict fatigue crack growth rate of a three-point bend specimen due to overloads. They were able to achieve good agreement with experimental data (within 10%) for the number of cycles to failure. However, the exponents of the dimensionless groups could not be determined solely by dimensional analysis and needed experimental calibration therefore restricting the usability of the approach.

Overall, there does not exist a unique or universal scaling approach for fatigue and this gap in literature is the focus here. Attention is directed towards the combined use of cohesive zone models with the application of a scaling theory known as *finite similitude* first introduced in the reference Al-Tamimi et al. (2016) [159]. Although this publication is limited to one scaled experiment applied to metal forming processes it provided the starting point for the similitude theory (now termed zeroth-order finite similitude). Zeroth-order finite similitude is equivalent to dimensional analysis in the sense that both approaches

involve proportional fields. This and a two-experiment formulation have subsequently been applied to different areas such as impact mechanics in refs. [160-163], earthquake [164-165], bioengineering [166-167] and fracture mechanics [168].

The work presented here for the first time, applies first order finite similitude (involving two scaled experiments) to fatigue crack propagation processes. The principal advantage of the finite-similitude formulation over dimensional analysis is that it is not limited to a specific invariance, and it is of interest to discover therefore whether fatigue analysis and experimentation can benefit from a two-experiment approach. Although the investigation here is principally analytical and numerical involving cohesive zone models the wide success of these approaches for fatigue analysis (see ref. [169]) indicates such an investigation has merit. The finite-similitude theory for the sake of readability is re-examined in Section 3.2, where the peculiar metaphysical concept of space scaling is introduced. Scaling in finite similitude is viewed as a continuous process involving either the expansion or contraction of space. Although space scaling cannot be achieved practically it nevertheless provides the mathematical foundation for a calculus of scaling and the route to representing scale effects. Another feature peculiar to the finite similitude theory discussed in Section 3.2 is that governing equations are represented in integral transport form. The physics of interest is captured on moving control volume to reflect the immediacy between space, a region of space (i.e., control volume) and the governing equations (i.e., transport equations). A generic form of transport equation is also introduced in Section 3.2 and the effect space scaling has on it is examined. The projection of trial space physics onto the physical space is shown, which is a critical step as it reveals all scale dependencies in fatigue. Proportional relationships typical to dimensional analysis are revealed in this section on application of the simple assumption that the projected transport equations do not change with scale. The possibility of transport equations changing with scale is then considered with the first-order finite similitude rule, where two scaled experiments can be combined to eliminate certain scale effects, which is simply not possible with dimensional analysis. Analytical applications are examined in Section 3.3 for a range of 1-D cohesive zone models, where exact representations of full-scale behaviours are returned using the first-order finite similitude rule. The application of the theory is the focus of Section 3.4 where an analytical example is considered to illustrate the ease of implementation the theory. Numerical studies are presented in Section 3.5 to demonstrate the practical benefits of the new scaling approach for fatigue, where exact behaviours (within numerical error) are again returned on

application of the commercial code Abaqus employing XFEM cohesive zone methods. The paper concludes with a conclusions' section.

3.2 Recap on Finite Similitude

Finite similitude theory can be found in references [159-163] but it is fitting to go over the concepts here prior to advancing the theory in the field of fatigue analysis. The scaling theory is unusual in that it is founded on a metaphysical concept, where the idea is that space can be expanded or contracted for the purpose of scaled experimentation. Evidently there exists no practical means to distort space in this manner, but what is possible is the ability to assess the impact of a space-scaling operation on the underpinning physics dictating the fatigue behaviour of a part in an experiment. This process provides a means to assess in an intuitive manner how scaling influences behaviour and consequently provides the backdrop for designing experiments.

3.2.1. The metaphysics of space scaling

Newtonian mechanics is founded on the concepts of inertial frames and absolute time and to enact the space-scaling concept therefore requires two inertial frames and two clocks. One frame resides in the physical space where the full-scale process sits and the other resides in the trial space which houses the scaled experiment. The characterisation of space is achieved through an affine map $\mathbf{x}_{ps} \mapsto \mathbf{x}_{ts}$, which in differential terms is $d\mathbf{x}_{ts} = F d\mathbf{x}_{ps}$, where F is both temporally and spatially invariant. This is equivalent to $dx_{ts}^i = F^i_j dx_{ps}^j$ when expressed in coefficient form with $F^i_j = \partial x_{ts}^i / \partial x_{ps}^j$, and where x_{ps}^i and x_{ts}^i are coordinate functions in the physical space (full-sized process) and the trial space (scaled-sized process), respectively. The matrix F characterises the nature of the scaling process and depending on the form F takes both anisotropic and isotropic scaling is representable. The work presented here is limited to isotropic and for this case $F = \beta I$ or in coefficient terms $F^i_j = \beta \delta_j^i$, where the Kronecker delta symbol δ_j^i is either one or zero. The extent of linear scaling is quantified by the parameter β , which is positive and should $0 < \beta < 1$ then the space is contracted; no space scaling takes place for $\beta = 1$ and expansion is the result for $\beta > 1$. Space scaling is pictorially presented in Fig. 3.1 along with its impact on a cyclically loaded rod for isotropic scaling with contraction, expansion and no scaling depicted. Observe the clocks in Fig. 3.1 labelled with t_{ts} and t_{ps} to reflect the possibility that time runs at different rates in the highlighted spaces. This feature allows for processes to run over different time intervals and

it is assumed here that $dt_{ts} = g dt_{ps}$, which is a differential identity with g being a positive scalar that quantifies the extent of the difference in rate at which processes proceed in the two spaces. Note that the differential map $d\mathbf{x}_{ts} = \beta d\mathbf{x}_{ps}$ provides all the necessary information needed to relate differential volumes and areas in the physical and trial spaces. Nanson's identities [159] provide $dV_{ts} = \beta^3 dV_{ps}$ and $d\mathbf{\Gamma}_{ts} = \beta^2 d\mathbf{\Gamma}_{ps}$, where $d\mathbf{\Gamma}_{ts} = \mathbf{n}_{ts} d\Gamma_{ts}$, $d\mathbf{\Gamma}_{ps} = \mathbf{n}_{ps} d\Gamma_{ps}$ and \mathbf{n}_{ts} and \mathbf{n}_{ps} are unit normal vectors. The quantities dV_{ts} and dV_{ps} are differential measures of volume and similarly for $d\Gamma_{ts}$ and $d\Gamma_{ps}$, which are differential measures of area.

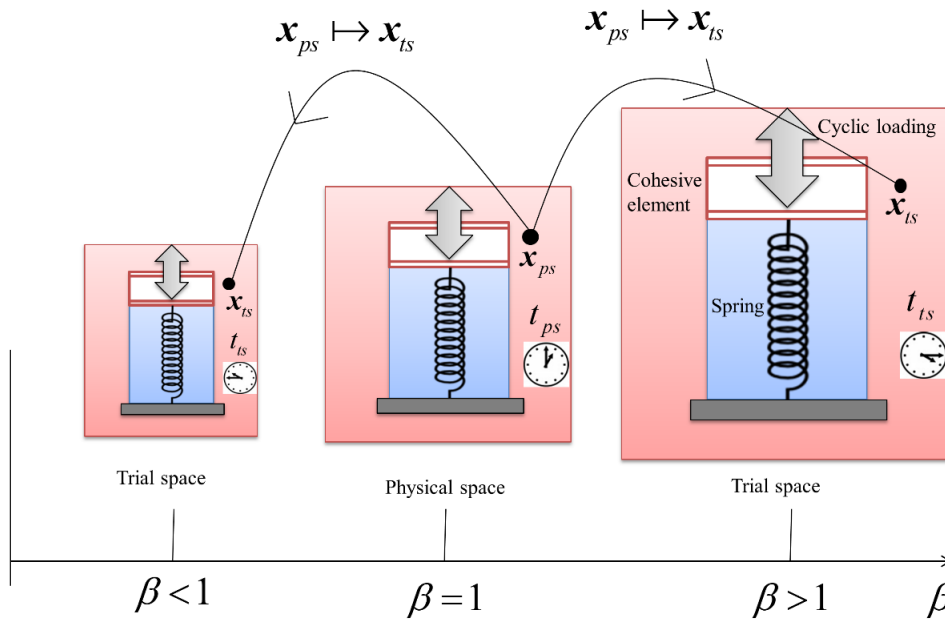


Figure 3.1: Space scaling and its geometrical effect on a cyclically loaded rod modelled as a combined spring-cohesive element.

3.2.2. Moving control volumes

Space scaling provides the backdrop but to understand the behaviour of systems when scaled it is necessary for the physics involved to be correctly represented. The most appropriate formulation for fatigue analysis is possibly unexpectedly a control-volume approach. Control volumes are no more than regions of space and therefore capture any change resulting from space scaling, which is a feature absent from point-based formulations. A control-volume can move, distort, and can be reduced to be arbitrarily small and hence facilitates the focus of any analysis on any region of space of interest. In mathematical terms a control volume takes the form of a continuous open domain Ω_{ts}^* (in the trial space) whose

closure contains the orientable boundary Γ_{ts}^* with outward pointing unit normal \mathbf{n}_{ts} . In scaling the focus is invariably on two regions of space (i.e., physical and trial) and evidently therefore the exact same apparatus applies to the physical space. It can be anticipated that the movement of Ω_{ps}^* and Ω_{ts}^* is synchronised in some manner. The arrangement is depicted in Fig. 3.2, where the movement of Ω_{ts}^* is related to the velocity field \mathbf{v}_{ts}^* using the identity $\mathbf{v}_{ts}^* = D^* \mathbf{x}_{ts}^* / D^* t_{ts}^*$. The temporal derivative $D^* / D^* t_{ts}^*$ is a partial derivative that holds constant points in a reference control volume Ω_{ts}^{*ref} , i.e. $D^* / D^* t_{ts}^* \equiv \partial / \partial t_{ts}^* |_{\mathbf{x}_{ts}}$, where $\mathbf{x}_{ts} \in \Omega_{ts}^{*ref}$. This description of control volume motion provides a precise mathematical formularisation with movement of a coordinate point defined by the solution of the differential equation $\mathbf{v}_{ts}^* = D^* \mathbf{x}_{ts}^* / D^* t_{ts}^*$ (with \mathbf{v}_{ts}^* known) or the map $\Omega_{ts}^{*ref} \rightarrow \Omega_{ts}^*$ (i.e. $\mathbf{x}_{ts} \mapsto \mathbf{x}_{ts}^*$). As illustrated in Fig. 3.2 the exact same apparatus applies in the physical space with the identity $\mathbf{v}_{ps}^* = D^* \mathbf{x}_{ps}^* / D^* t_{ps}^*$. The assumed synchronous motion suggests a relationship between \mathbf{x}_{ts}^* and \mathbf{x}_{ps}^* in the form of a map $\mathbf{x}_{ps}^* \mapsto \mathbf{x}_{ts}^*$. It can be readily shown that the differential identity $d\mathbf{x}_{ts}^* = \beta d\mathbf{x}_{ps}^*$ holds and in view of the temporal relationship $dt_{ts} = g dt_{ps}$, the velocities \mathbf{v}_{ts}^* and \mathbf{v}_{ps}^* are related by $\mathbf{v}_{ts}^* = \beta g^{-1} \mathbf{v}_{ps}^*$. Note that thus far no reference is made to the physical processes in the two spaces, which is an important aspect as it provides the foundations for a generic approach.

3.2.3. Projected Transport Equations

The key step in the finite-similitude theory is the projection of the governing trial-space physics represented by transport equations onto the physical space. It is through this projection that scale dependencies are revealed in a form that is either explicit in the case of geometrical measures or implicit as is the case for most other fields. This step is important as it transforms scaling into a procedure where the objective is the discovery of hidden (implicit) scale dependencies. It is fair to say in transport equations are somewhat neglected due to the relative dominance of variational methods in solid mechanics (see ref. [170]). Some application of control-volume theory to fracture mechanics underpins the concept of configurational forces and additionally shock physics make use of them in the capture of discontinuous behaviour but otherwise their application is limited. Consider then a transport equation in its most generic form in the trial space, which takes the form [159]

$$\begin{aligned}
& \frac{D^*}{D^* t_{ts}} \int_{\Omega_{ts}^*} \rho_{ts} \boldsymbol{\Psi}_{ts} dV_{ts}^* + \int_{\Gamma_{ts}^*} \rho_{ts} \boldsymbol{\Psi}_{ts} (\mathbf{v}_{ts} - \mathbf{v}_{ts}^*) \cdot \mathbf{n}_{ts} d\Gamma_{ts}^* \\
& = - \int_{\Gamma_{ts}^*} \mathbf{J}_{ts}^\Psi \cdot \mathbf{n}_{ts} d\Gamma_{ts}^* + \int_{\Omega_{ts}^*} \rho_{ts} \mathbf{b}_{ts}^\Psi dV_{ts}^*
\end{aligned} \tag{3.1}$$

where ρ_{ts} , $\boldsymbol{\Psi}_{ts}$, \mathbf{v}_{ts} , \mathbf{J}_{ts}^Ψ , \mathbf{b}_{ts}^Ψ , \mathbf{n}_{ts} are material density, a physical field, material velocity, a boundary flux, a source term and the unit normal to boundary Γ_{ps}^* of the control volume Ω_{ps}^* .

The equations of interest to fatigue in the frame of continuum mechanics are conservation equations for volume, mass, and momentum along with a non-conservation equation for movement, which are:

$$\frac{D^*}{D^* t_{ts}} \int_{\Omega_{ts}^*} dV_{ts}^* - \int_{\Gamma_{ts}^*} \mathbf{v}_{ts}^* \cdot \mathbf{n}_{ts} d\Gamma_{ts}^* = 0 \tag{3.2a}$$

$$\frac{D^*}{D^* t_{ts}} \int_{\Omega_{ts}^*} \rho_{ts} dV_{ts}^* + \int_{\Gamma_{ts}^*} \rho_{ts} (\mathbf{v}_{ts} - \mathbf{v}_{ts}^*) \cdot \mathbf{n}_{ts} d\Gamma_{ts}^* = 0 \tag{3.2b}$$

$$\frac{D^*}{D^* t_{ts}} \int_{\Omega_{ts}^*} \rho_{ts} \mathbf{v}_{ts} dV_{ts}^* + \int_{\Gamma_{ts}^*} \rho_{ts} \mathbf{v}_{ts} (\mathbf{v}_{ts} - \mathbf{v}_{ts}^*) \cdot \mathbf{n}_{ts} d\Gamma_{ts}^* \tag{3.2c}$$

$$= - \int_{\Gamma_{ts}^*} \boldsymbol{\sigma}_{ts} \cdot \mathbf{n}_{ts} d\Gamma_{ts}^* + \int_{\Omega_{ts}^*} \rho_{ts} \mathbf{b}_{ts}^v dV_{ts}^*$$

$$\frac{D^*}{D^* t_{ts}} \int_{\Omega_{ts}^*} \rho_{ts} \mathbf{u}_{ts} dV_{ts}^* + \int_{\Gamma_{ts}^*} \rho_{ts} \mathbf{u}_{ts} (\mathbf{v}_{ts} - \mathbf{v}_{ts}^*) \cdot \mathbf{n}_{ts} d\Gamma_{ts}^* = \int_{\Omega_{ts}^*} \rho_{ts} \mathbf{v}_{ts} dV_{ts}^* \tag{3.2d}$$

where $\boldsymbol{\sigma}_{ts}$ is Cauchy stress and \mathbf{b}_{ts}^v is a body force.

Although Eq. (3.2c) plays a prominent role in fracture mechanics other equations are required in finite-similitude theory. Eq. (3.2a) is typically absent from fracture mechanics as it has no field associated with it but its role in finite similitude is the enforcement of the synchronous control volume relationship $\mathbf{v}_{ts}^* = \beta g^{-1} \mathbf{v}_{ps}^*$. The continuity equation Eq. (3.2b) is usually absent also as density is typically fixed in fracture theory but with physical modelling a consideration density change is a feature albeit with scale. The equation for movement Eq. (3.2d) was introduced by Davey and Darvizeh (2016) [170] to make transport equations more relevant to solid mechanics. The movement equation brings the displacement field \mathbf{u}_{ts} into the family of transport equations and since displacement is a critical field in fracture mechanics (providing a description for distortion) it has its place. To project Eq. (3.1) (and subsequently Eqs. (3.2)) into the physical space it is first necessary to substitute the identities $dV_{ts}^* = \beta^3 dV_{ps}^*$, $d\Gamma_{ts}^* = \beta^2 d\Gamma_{ps}^*$, $dt_{ts} = g dt_{ps}$, and multiply

throughout by g and scalar α_0^Ψ ; this gives rise to the critically important scaled transport equation as following

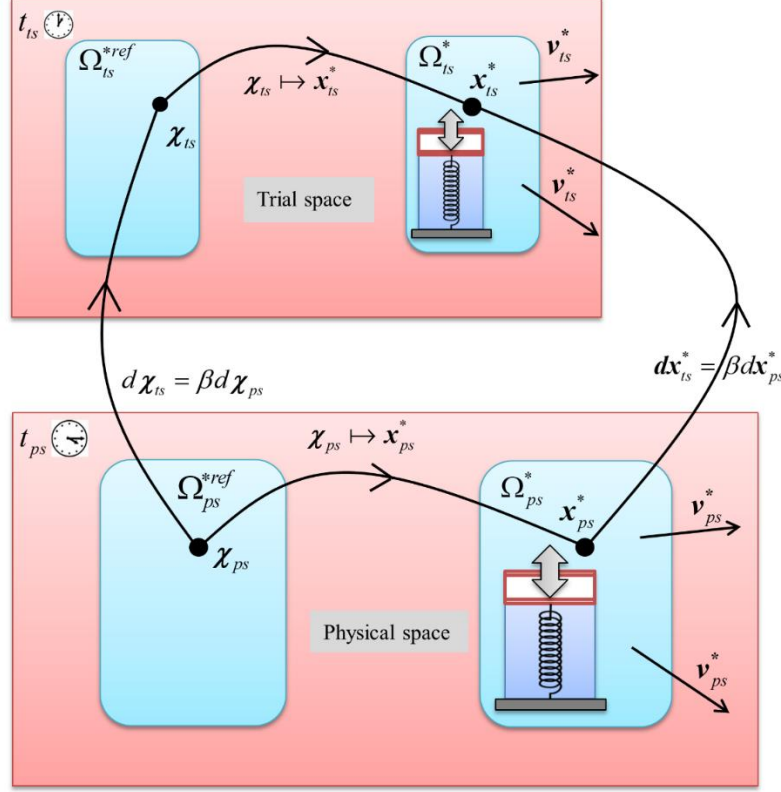


Figure 3.2: Synchronous moving-control volumes in trial space and physical spaces tracking a moving cyclically loaded rod.

$$\begin{aligned}
 \alpha_0^\Psi T_0^\Psi(\beta) &= \frac{D^*}{D^* t_{ps}} \int_{\Omega_{ps}^*} \alpha_0^\Psi \rho_{ts} \beta^3 \Psi_{ts} dV_{ps}^* \\
 &+ \int_{\Gamma_{ps}^*} \alpha_0^\Psi \rho_{ts} \beta^3 \Psi_{ts} (\beta^{-1} g \mathbf{v}_{ts} - \beta^{-1} g \mathbf{v}_{ts}^*) \cdot \mathbf{n}_{ps} d\Gamma_{ps}^* \\
 &+ \int_{\Gamma_{ps}^*} \alpha_0^\Psi \beta^2 g \mathbf{J}_{ts}^\Psi \cdot \mathbf{n}_{ps} d\Gamma_{ps}^* - \int_{\Omega_{ps}^*} \alpha_0^\Psi \rho_{ts} \beta^3 g \mathbf{b}_{ts}^\Psi dV_{ps}^* = 0
 \end{aligned} \tag{3.3}$$

which is effectively Eq. (3.1) represented on the physical space; the role of the scalar α_0^Ψ is of critical importance and along with g are assumed to be smooth functions of β .

This equation is of fundamental importance to finite-similitude theory because in one form or another (explicitly or implicitly) it captures all scale dependencies. The assumed dependence on β of the fields, fluxes and sources provide the relationships: $\rho_{ts}(1) = \rho_{ps}$, $\mathbf{v}_{ts}(1) = \mathbf{v}_{ps}$, $\Psi_{ts}(1) = \Psi_{ps}$, $\mathbf{J}_{ts}(1) = \mathbf{J}_{ps}$ and $\mathbf{b}_{ts}(1) = \mathbf{b}_{ps}$, i.e., for $\beta = 1$ the obvious requirement is that trial-space physics matches what transpires in the physical space. This

requirement also imposes the identities $\alpha_0^\Psi(1) = 1$ and $g(1) = 1$. It is important to appreciate that $\alpha_0^\Psi T_0^\Psi(\beta) = 0$ is not an approximation as it is fully representative of the trial-space physics but projected onto the physical space. Note how all β – dependencies are revealed through this projection with those arising from geometrical measures being revealed in an explicit form (i.e., β^3 and β^2 terms) and others are hidden but expressed as functions of β , nevertheless in the form $\rho_{ts}(\beta)$, $\mathbf{v}_{ts}(\beta)$, $\boldsymbol{\Psi}_{ts}(\beta)$, $\mathbf{J}_{ts}(\beta)$ and $\mathbf{b}_{ts}(\beta)$.

Eq. (3.3) is a generic form that is useful in the abstract but with regards to Eqs. (3.2) and fracture mechanics the following projected equations are revealed:

$$\alpha_0^1 T_0^1(\beta) = \frac{D^*}{D^* t_{ps}} \int_{\Omega_{ps}^*} \alpha_0^1 \beta^3 dV_{ps}^* - \int_{\Gamma_{ps}^*} \alpha_0^1 \beta^3 (\beta^{-1} g \mathbf{v}_{ts}^* \cdot \mathbf{n}_{ps}) d\Gamma_{ps}^* = 0 \quad (3.4a)$$

$$\begin{aligned} \alpha_0^\rho T_0^\rho(\beta) &= \frac{D^*}{D^* t_{ps}} \int_{\Omega_{ps}^*} \alpha_0^\rho \rho_{ts} \beta^3 dV_{ps}^* \\ &+ \int_{\Gamma_{ps}^*} \alpha_0^\rho \rho_{ts} \beta^3 (\beta^{-1} g \mathbf{v}_{ts} - \beta^{-1} g \mathbf{v}_{ts}^*) \cdot \mathbf{n}_{ps} d\Gamma_{ps}^* = 0 \end{aligned} \quad (3.4b)$$

$$\begin{aligned} \alpha_0^v T_0^v(\beta) &= \frac{D^*}{D^* t_{ps}} \int_{\Omega_{ps}^*} [\alpha_0^v g^{-1} \beta \rho_{ts} \beta^3] (\beta^{-1} g \mathbf{v}_{ts}) dV_{ps}^* \\ &+ \int_{\Gamma_{ps}^*} [\alpha_0^v g^{-1} \beta \rho_{ts} \beta^3] (\beta^{-1} g \mathbf{v}_{ts}) (\beta^{-1} g \mathbf{v}_{ts} \\ &- \beta^{-1} g \mathbf{v}_{ts}^*) \cdot \mathbf{n}_{ps} d\Gamma_{ps}^* + \int_{\Gamma_{ps}^*} \alpha_0^v \beta^2 g \boldsymbol{\sigma}_{ts} \cdot \mathbf{n}_{ps} d\Gamma_{ps}^* \\ &- \int_{\Omega_{ps}^*} \alpha_0^v \rho_{ts} \beta^3 g \mathbf{b}_{ts}^v dV_{ps}^* = 0 \end{aligned} \quad (3.4c)$$

$$\begin{aligned} \alpha_0^u T_0^u(\beta) &= \frac{D^*}{D^* t_{ps}} \int_{\Omega_{ps}^*} \alpha_0^u \beta \rho_{ts} \beta^3 (\beta^{-1} \mathbf{u}_{ts}) dV_{ps}^* \\ &+ \int_{\Gamma_{ps}^*} \alpha_0^u \beta \rho_{ts} \beta^3 (\beta^{-1} \mathbf{u}_{ts}) (\beta^{-1} g \mathbf{v}_{ts} - \beta^{-1} g \mathbf{v}_{ts}^*) \cdot \mathbf{n}_{ps} d\Gamma_{ps}^* \\ &- \int_{\Omega_{ps}^*} \alpha_0^u \beta \rho_{ts} \beta^3 (\beta^{-1} g \mathbf{v}_{ts}) dV_{ps}^* = 0 \end{aligned} \quad (3.4d)$$

where a possible role for α_0^Ψ has materialised, which is the attempted removal of β terms.

The simplest assumption to make is that the physics of the problem do not change in the trial space when contrasted with the physical space this is zeroth order similitude same as the invariance associated with dimensional analysis and is termed zeroth order finite similitude.

The projected transport equation does not change with scale β . This is mathematically represented by the zeroth order identity:

$$\frac{d}{d\beta}(\alpha_0^\psi T_0^\psi) \equiv 0 \quad (3.5)$$

Application of Eq. (3.5) to the transport equations produces the zeroth order identities.

Table 3.1. Necessary and sufficient zeroth order identities

Eq. No	Field	Scalars	Flux	Source
(3.4a)	$\mathbf{v}_{ps}^* = \beta^{-1} g \mathbf{v}_{ts}^*$	$\alpha_0^1 \beta^3 = 1$		
(3.4b)	$\rho_{ps} = \alpha_0^\rho \rho_{ts} \beta^3$	$\alpha_0^\rho(1) = 1$ $g(1) = 1$		
(3.4c)	$\mathbf{v}_{ps} = \beta_1^{-1} g_1 \mathbf{v}_{ts}$	$\alpha_0^\rho = \alpha_0^v g^{-1} \beta$	$\boldsymbol{\sigma}_{ps}$ $= \alpha_{01}^v g_1 \beta_1^2 \boldsymbol{\sigma}_{ts}$	\mathbf{b}_{ps}^v $= g_1^2 \beta_1^{-1} \mathbf{b}_{ts}^v$
(3.4d)	$\mathbf{u}_{ps} = \beta_1^{-1} \mathbf{u}_{ts}$	$\alpha_0^\rho = \alpha_0^u \beta$		\mathbf{v}_{ps} $= \beta_1^{-1} g_1 \mathbf{v}_{ts}$

Table 3.1 presents those identities in a system where scale effects are absent. The role of Eq. (3.4a) is the determination of the identity $\mathbf{v}_{ps} = \beta_1^{-1} g_1 \mathbf{v}_{ts}$, which is required so that control-volume movement in the trial space at any scale can be described in the physical space. In links the behaviour of the trial space system is played out on the physical space enabling differences to be gauged. In order to satisfy Eq. (3.5) for Eq. (3.4b) it is necessary and sufficient to set $\beta^{-1} g \mathbf{v}_{ts}^* = \mathbf{v}_{ps}^*$, $\alpha_0^\rho \rho_{ts} \beta^3 = \rho_{ps}$, $\mathbf{v}_{ps} = \beta_1^{-1} g_1 \mathbf{v}_{ts}$, $\alpha_0^\rho(1) = 1$ and $\mathbf{v}_{ps} = \mathbf{v}_{ts}(1)$.

Although continuity plays little part in fracture mechanics it is needed for similitude to establish a relationship for density with scale (i.e. $\alpha_0^\rho \rho_{ts} \beta^3 = \rho_{ps}$), which opens up the possibility of selecting different materials for a scaled experiment. Note that the velocity relationship $\mathbf{v}_{ps} = \beta_1^{-1} g_1 \mathbf{v}_{ts}$ is particularly constraining as it effectively restricts all scaled experiments to the same pattern of deformation, which is unrealistic in practice.

The momentum transport Eq. (3.4c) has a critical role in fracture mechanics and in order to satisfy Eq. 3.5 with $\mathbf{v}_{ps} = \beta_1^{-1} g_1 \mathbf{v}_{ts}$ it is necessary and sufficient to set $\alpha_0^v g^{-1} \beta = \alpha_0^\rho$ as

well as $\mathbf{v}_{ps} = \beta_1^{-1} g_1 \mathbf{v}_{ts}$, $\mathbf{v}_{ps}^* = \beta^{-1} g \mathbf{v}_{ts}^*$, $\boldsymbol{\sigma}_{ps} = \alpha_{01}^v g_1 \beta_1^2 \boldsymbol{\sigma}_{ts}$, $\mathbf{b}_{ps}^v = g_1^2 \beta_1^{-1} \mathbf{b}_{ts}^v$ and $\alpha_0^v(1) = 1$. In order for the movement equation, Eq. (3.4d) to satisfy $\alpha_0^\rho \rho_{ts} \beta^3 = \rho_{ps}$, it is necessary and sufficient to set $\alpha_0^u \beta = \alpha_0^\rho$ and ($\mathbf{v}_{ps} = \beta_1^{-1} g_1 \mathbf{v}_{ts}$, $\mathbf{v}_{ps}^* = \beta^{-1} g \mathbf{v}_{ts}^*$, $\mathbf{u}_{ps} = \beta_1^{-1} \mathbf{u}_{ts}$, $\mathbf{u}_{ps} = \mathbf{u}_{ts}(1)$, $\alpha_0^u(1) = 1$).

Overall, it is fairly evident that identity Eq. (3.5) is very restrictive on the behaviour of the trial-space systems and unlikely to be satisfied for realistic problems. The reality in practice therefore is that the inequality:

$$\frac{d}{d\beta}(\alpha_0^\psi T_0^\psi) \not\equiv 0 \quad (3.6)$$

which of course provides scale effects, and these can be expected to change with scale, i.e. be dependent on β .

Eq. (3.5) provides the framework for the analysis of scale dependence but contains hidden dependencies that require information on such things such as material behaviour (e.g. size dependence) and boundary conditions (e.g. surface conditions) to uncover them. However, an alternative (and the approach adopted here) is to simply enforce a global β – invariant condition and apply this in the design of experiments.

3.2.4. First-order finite similitude theory

The principal advantage of the finite-similitude formulation over dimensional analysis is that it is not limited to a specific invariance. A simple assumption to make is that the physics in the trial spaces do not change with scale, mathematically this can be represented by the identity:

$$\frac{d}{d\beta}(\alpha_0^\psi T_0^\psi) \equiv 0 \quad (3.7)$$

which when satisfied is termed *zeroth-order finite similitude*.

However, since scale effects are present in fatigue, higher-order similitude conditions are required involving higher derivatives by enforcing a suitably defined global β – invariant condition. Higher order finite similitude examines an alternative to Eq. (3.7) that involves additional scaled experiment(s) to shed additional light on changes that are taking place and to add extra flexibility. The concept of k^{th} -order finite similitude is defined by the lowest derivative that satisfies:

$$T_{k+1}^\psi = \frac{d}{d\beta}(\alpha_k^\psi T_k^\psi) \equiv 0 \quad (3.8)$$

$\forall \beta > 0$, with $\alpha_0^\Psi T_0^\Psi$ defined by Eq. (3.3) and scalars α_k^Ψ are functions of β with $\alpha_k^\Psi(1) = 1$.

The scaling theory corresponding to this definition is termed k^{th} -order finite similitude and under this notation zeroth-order finite similitude (i.e., Eq. (3.5)) is the identity $T_1^\Psi \equiv 0$. The focus in this thesis is the identity $T_2^\Psi \equiv 0$, i.e., first-order finite similitude and takes the form:

$$T_2^\Psi = \frac{d}{d\beta}(\alpha_1^\Psi T_1^\Psi) = \frac{d}{d\beta} \left(\alpha_1^\Psi \frac{d}{d\beta}(\alpha_0^\Psi T_0^\Psi) \right) \equiv 0 \quad (3.9)$$

To apply the first order identity (Eq. 3.9) to the transport equations of momentum, mass, displacement, it is useful to substitute the zeroth order identities first into the projected transport equations Eq. (3.4 b) to Eq. (3.4d).

$$\alpha_0^\rho T_0^\rho(\beta) = \frac{D^*}{D^* t_{ps}} \int_{\Omega_{ps}^*} \rho_{ps} dV_{ps}^* + \int_{\Gamma_{ps}^*} \rho_{ps} (\mathbf{V}_{ps} - \mathbf{v}_{ps}^*) \cdot \mathbf{n}_{ps} d\Gamma_{ps}^* = 0 \quad (3.10a)$$

$$\begin{aligned} \alpha_0^v T_0^v(\beta) &= \frac{D^*}{D^* t_{ps}} \int_{\Omega_{ps}^*} \rho_{ps} \mathbf{V}_{ps} dV_{ps}^* + \int_{\Gamma_{ps}^*} \rho_{ps} \mathbf{V}_{ps} (\mathbf{v}_{ps} - \mathbf{v}_{ps}^*) \cdot \mathbf{n}_{ps} d\Gamma_{ps}^* \\ &\quad + \int_{\Gamma_{ps}^*} \Sigma_{ps} \cdot \mathbf{n}_{ps} d\Gamma_{ps}^* - \int_{\Omega_{ps}^*} \mathbf{B}_{ps} dV_{ps}^* = 0 \end{aligned} \quad (3.10b)$$

$$\begin{aligned} \alpha_0^u T_0^u(\beta) &= \frac{D^*}{D^* t_{ps}} \int_{\Omega_{ps}^*} \rho_{ps} \mathbf{U}_{ps} dV_{ps}^* + \int_{\Gamma_{ps}^*} \rho_{ps} \mathbf{U}_{ps} (\mathbf{v}_{ps} - \mathbf{v}_{ps}^*) \cdot \mathbf{n}_{ps} d\Gamma_{ps}^* \\ &\quad - \int_{\Omega_{ps}^*} \rho_{ps} \mathbf{V}_{ps} dV_{ps}^* = 0 \end{aligned} \quad (3.10c)$$

Where $\mathbf{V}_{ps}^* = \beta_1^{-1} g_1 \mathbf{v}_{ts}^*$, $\mathbf{V}_{ps} = \beta_1^{-1} g_1 \mathbf{v}_{ts}$, $\Sigma_{ps} = \alpha_{01}^v g_1 \beta_1^2 \sigma_{ts}$, $\mathbf{B}_{ps}^v = \alpha_0^\rho \rho_{ts} \beta^3 g \mathbf{b}_{ts}^v$, $\mathbf{U}_{ps} = \beta_1^{-1} g_1 \mathbf{u}_{ts}$.

Eq. (3.4a) is not included here since it satisfies the zeroth-order condition Eq. (3.5) and evidently automatically satisfies Eq. (3.9). The first order transport equations are obtained by differentiating Eqs. (3.10a to 3.10c) as follows:

$$\alpha_1^\rho T_1^\rho(\beta) = \int_{\Gamma_{ps}^*} \alpha_1^\rho \rho_{ps} \mathbf{V}_{ps}' - \mathbf{v}_{ps}^*) \cdot \mathbf{n}_{ps} d\Gamma_{ps}^* = 0 \quad (3.11a)$$

$$\begin{aligned} \alpha_1^v T_1^v(\beta) &= \frac{D^*}{D^* t_{ps}} \int_{\Omega_{ps}^*} \rho_{ps} \mathbf{V}_{ps}' dV_{ps}^* + \int_{\Gamma_{ps}^*} \rho_{ps} \mathbf{V}_{ps}' (\mathbf{v}_{ps} - \mathbf{v}_{ps}^*) \cdot \mathbf{n}_{ps} d\Gamma_{ps}^* \\ &\quad + \int_{\Gamma_{ps}^*} \Sigma_{ps}' \cdot \mathbf{n}_{ps} d\Gamma_{ps}^* - \int_{\Omega_{ps}^*} \mathbf{B}_{ps}' dV_{ps}^* = 0 \end{aligned} \quad (3.11b)$$

$$\begin{aligned} \alpha_1^u T_1^u(\beta) &= \frac{D^*}{D^* t_{ps}} \int_{\Omega_{ps}^*} \rho_{ps} \mathbf{U}'_{ps} dV_{ps}^* + \int_{\Gamma_{ps}^*} \rho_{ps} \mathbf{U}'_{ps} (\mathbf{v}_{ps} - \mathbf{v}_{ps}^*) \cdot \mathbf{n}_{ps} d\Gamma_{ps}^* \\ &\quad - \int_{\Omega_{ps}^*} \rho_{ps} \mathbf{V}'_{ps} dV_{ps}^* = 0 \end{aligned} \quad (3.11c)$$

Where the dash “ ’ ” signifies derivative with respect to β and note that these equations have a similar appearance to their corresponding counterparts in Eqs. (3.9). Zeroth-order finite similitude requires that the integrands in Eqs. (3.10) do not vary with β and similarly for first order the integrands in Eqs. (3.11) are required to be invariant of β .

An alternative but equivalent approach is the direct integration of identity Eq. (3.9) which links two scaled experiments to the full-scale prototype. This achieved by forming a divided-difference table for $\alpha_0^\Psi T_0^\Psi$ with three distinct pivot points $\{\beta_2, \beta_1, \beta_0\}$. A mean-value theorem is applied to return exact identities in the divided-difference table. As defined above $T_1^\Psi = \frac{d(\alpha_0^\Psi T_0^\Psi)}{d\beta}$, which in the form of a divided difference gives

$$\alpha_1^\Psi |_{\hat{\beta}_2^1} \frac{\alpha_0^\Psi T_0^\Psi(\beta_1) - \alpha_0^\Psi T_0^\Psi(\beta_2)}{\beta_1 - \beta_2} = \alpha_1^\Psi |_{\hat{\beta}_2^1} T_1^\Psi(\beta_2^1) \quad (3.12a)$$

$$\alpha_1^\Psi |_{\hat{\beta}_1^o} \frac{\alpha_0^\Psi T_0^\Psi(\beta_0) - \alpha_0^\Psi T_0^\Psi(\beta_1)}{\beta_0 - \beta_1} = \alpha_1^\Psi |_{\hat{\beta}_1^o} T_1^\Psi(\beta_1^o) \quad (3.12b)$$

where $\beta_i \leq \beta_i^{i-1} \leq \beta_{i-1}$ and recall that first order satisfies $\frac{d(\alpha_1^\Psi T_1^\Psi)}{d\beta} \equiv 0$, then any subsequent divided differences return zero and in particular

$$\frac{\alpha_1^\Psi |_{\hat{\beta}_1^o} T_1^\Psi(\beta_1^o) - \alpha_1^\Psi |_{\hat{\beta}_2^1} T_1^\Psi(\beta_2^1)}{\beta_1^o - \beta_2^1} \equiv 0 \quad (3.13)$$

where substitution of Eqs (3.9) returns an exact first-order similitude identity for transport equations i.e.,

$$\alpha_0^\Psi T_0^\Psi(\beta_0) \equiv \alpha_0^\Psi T_0^\Psi(\beta_1) + R_1^\Psi (\alpha_0^\Psi T_0^\Psi(\beta_1) - \alpha_0^\Psi T_0^\Psi(\beta_2)) \quad (3.14)$$

where the scaling parameter R_1^Ψ is

$$R_1^\Psi = \left(\frac{\alpha_1^\Psi |_{\hat{\beta}_2^1}}{\alpha_1^\Psi |_{\hat{\beta}_1^o}} \right) \left(\frac{\beta_0 - \beta_1}{\beta_1 - \beta_2} \right) \quad (3.15)$$

Eq. (3.14) reveals that the first-order finite similitude is about proportional relationships between the differences in the transport equations at different scales. Eq. (3.14) is now

applied to the transport equations pertinent to fracture mechanics (Eqs. 3.4) to produce the first order identities:

$$\mathbf{v}_{ps} = \beta_1^{-1} g_1 \mathbf{v}_{ts}(\beta_1) + R_1^\rho (\beta_1^{-1} g_1 \mathbf{v}_{ts}(\beta_1) - \beta_2^{-1} g_2 \mathbf{v}_{ts}(\beta_2)) \quad (3.16a)$$

$$\mathbf{v}_{ps} = \beta_1^{-1} g_1 \mathbf{v}_{ts}(\beta_1) + R_1^v (\beta_1^{-1} g_1 \mathbf{v}_{ts}(\beta_1) - \beta_2^{-1} g_2 \mathbf{v}_{ts}(\beta_2)) \quad (3.16b)$$

$$\boldsymbol{\sigma}_{ps} = \alpha_{01}^v g_1 \beta_1^2 \boldsymbol{\sigma}_{ts}(\beta_1) + R_1^v (\alpha_{01}^v g_1 \beta_1^2 \boldsymbol{\sigma}_{ts}(\beta_1) - \alpha_{02}^v g_2 \beta_2^2 \boldsymbol{\sigma}_{ts}(\beta_2)) \quad (3.16c)$$

$$\mathbf{b}_{ps}^v = g_1^2 \beta_1^{-1} \mathbf{b}_{ts}^v(\beta_1) + R_1^v (g_1^2 \beta_1^{-1} \mathbf{b}_{ts}^v(\beta_1) - g_2^2 \beta_2^{-1} \mathbf{b}_{ts}^v(\beta_2)) \quad (3.16d)$$

$$\mathbf{u}_{ps} = \beta_1^{-1} \mathbf{u}_{ts}(\beta_1) + R_1^u (\beta_1^{-1} \mathbf{u}_{ts}(\beta_1) - \beta_2^{-1} \mathbf{u}_{ts}(\beta_2)) \quad (3.16e)$$

$$\mathbf{v}_{ps} = \beta_1^{-1} g_1 \mathbf{v}_{ts}(\beta_1) + R_1^u (\beta_1^{-1} g_1 \mathbf{v}_{ts}(\beta_1) - \beta_2^{-1} g_2 \mathbf{v}_{ts}(\beta_2)) \quad (3.16f)$$

where a consistent velocity requires that $R_1 = R_1^\rho = R_1^u = R_1^v$, where it is assumed that the zeroth-order conditions: $\alpha_0^1 \beta^3 = 1$, $\beta^{-1} g \mathbf{v}_{ts}^* = \mathbf{v}_{ps}^*$, $\alpha_0^\rho \rho_{ts} \beta^3 = \rho_{ps}$, $\alpha_0^v g^{-1} \beta = \alpha_0^\rho$ and $\alpha_0^u \beta = \alpha_0^\rho$. The first order identities that arise as a result of applying Eq. (3.14) to the conservations equations of mass momentum and movement are necessary to account for variations in fields of interest such as velocity, displacement and body forces in the sub scaled model spaces (trial space). Hence physical experiments can be designed without being limited to the invariance prescribed by dimensional analysis. Table 3.2 presents the necessary and sufficient first order identities. The Eq. no column in the table highlights the relevant conservation transport equation that generates the first order identity.

Table 3.2. Necessary and sufficient first order identities.

Eq. No	Field	Scalars	Flux	Source
(3.4a)	$\mathbf{v}_{ps}^* = \beta^{-1} g \mathbf{v}_{ts}^*$	$\alpha_0^1 \beta^3 = 1$		
(3.4b)	$\rho_{ps} = \alpha_0^\rho \rho_{ts} \beta^3$	$\alpha_0^\rho(1) = 1$ $g(1) = 1$		

(3.4c)	\mathbf{v}_{ps} $= \beta_1^{-1} g_1 \mathbf{v}_{ts}(\beta_1)$ $+ R_1^v(\beta_1^{-1} g_1 \mathbf{v}_{ts}(\beta_1)$ $- \beta_2^{-1} g_2 \mathbf{v}_{ts}(\beta_2))$	α_0^ρ $= \alpha_0^v g^{-1} \beta$	$\boldsymbol{\sigma}_{ps}$ $= \alpha_{01}^v g_1 \beta_1^2 \boldsymbol{\sigma}_{ts}(\beta_1)$ $+ R_1^v(\alpha_{01}^v g_1 \beta_1^2 \boldsymbol{\sigma}_{ts}(\beta_1)$ $- \alpha_{02}^v g_2 \beta_2^2 \boldsymbol{\sigma}_{ts}(\beta_2))$	\mathbf{b}_{ps}^v $= g_1^2 \beta_1^{-1} \mathbf{b}_{ts}^v(\beta_1)$ $+ R_1^v(g_1^2 \beta_1^{-1} \mathbf{b}_{ts}^v(\beta_1)$ $- g_2^2 \beta_1^{-1} \mathbf{b}_{ts}^v(\beta_1))$
(3.4d)	\mathbf{u}_{ps} $= \beta_1^{-1} \mathbf{u}_{ts}(\beta_1)$ $+ R_1^u(\beta_1^{-1} \mathbf{u}_{ts}(\beta_1)$ $- \beta_2^{-1} \mathbf{u}_{ts}(\beta_2))$	$\alpha_0^\rho = \alpha_0^u \beta$		\mathbf{v}_{ps} $= \beta_1^{-1} g_1 \mathbf{v}_{ts}(\beta_1)$ $+ R_1^v(\beta_1^{-1} g_1 \mathbf{v}_{ts}(\beta_1)$ $- \beta_2^{-1} g_2 \mathbf{v}_{ts}(\beta_2))$

The first-order finite-similitude theory as revealed in Eqs. (3.16) is about proportional differences between experiments. Note that application of the identities $\mathbf{d}\mathbf{x}_{ts}(\beta_1) = \beta_1 \mathbf{d}\mathbf{x}_{ps}$ and $\mathbf{d}\mathbf{x}_{ts}(\beta_2) = \beta_2 \mathbf{d}\mathbf{x}_{ps}$ to Eq. (3.15e) provides the small strain relationship:

$$\boldsymbol{\varepsilon}_{ps} = \boldsymbol{\varepsilon}_{ts}(\beta_1) + R_1(\boldsymbol{\varepsilon}_{ts}(\beta_1) - \boldsymbol{\varepsilon}_{ts}(\beta_2)) \quad (3.17)$$

which confirms that strain can be unequal in the trial and physical spaces, which is the reality in most physical experiments. First order finite similitude identity is a less constrained similitude relationship that allows more flexibility and accommodates scale effects in different trial spaces by enforcing a global invariance. Thus, standalone sub scale experiments can be designed with more flexibility.

3.3 One-Dimensional Cohesive Elements

This section is concerned with the application of the new scaling concepts to cohesive zone models. A cohesive zone model represents damage that results in fatigue by means of a cohesive failure in the form of separating surfaces typically along a predefined path or along element edges in any finite element analysis. This type of damage takes place incrementally because of cyclic loading and the most rudimentary cohesive model is identified by a traction-separation curve consisting of only three properties, which are critical stress σ_c , critical separation δ_c and the area under the curve G_c , which is the cohesive fracture energy. The three properties are related and for the simplest linear case $G_c = 0.5\sigma_c\delta_c$, which confirms the nature of this relationship. A 2-D depiction of cohesive zone model is provided in Fig. 3.3 for the simplest traction separation law along with loading and unloading paths. The linear cohesive zone model (LCZM) is one of several possible forms and it is of interest

to explore the effect scaling has on some relatively simple models and the ones considered are presented in Fig. 3.4.

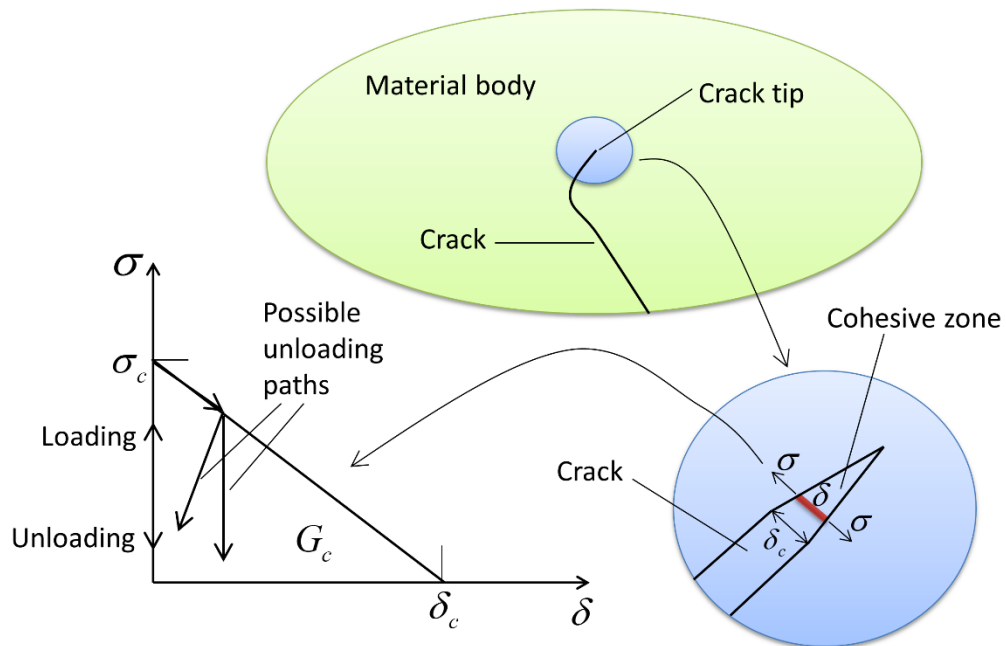


Figure 3.3: Cohesive zone model for a crack and its associated traction-separation curve.

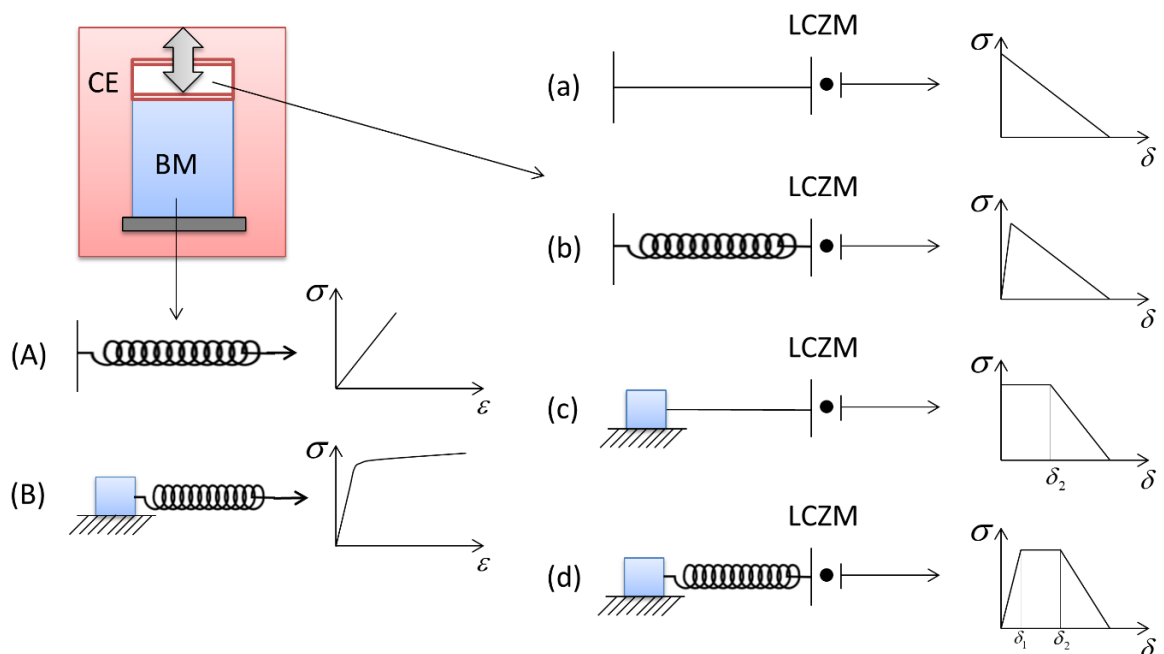


Figure 3.4: Stress-separation and strain envelopes for simple models for bulk material (BM) and cohesive element (CE).

3.3.1 The scaling of Model A-a

The model in this section is an elastic rod of length ℓ_0 and area A_0 subjected a displacement δ at the free end with its lower end fixed. The rod has the potential to crack if the stress level reaches the critical stress σ_c and this feature is modelled by means of a linear cohesive zone model (LCZM). The total extension of the rod consists of two parts therefore, i.e. $\delta = \delta^{el} + \delta^{coh}$ with applied stress $\sigma = \sigma^{el} = \sigma^{coh}$, where $\sigma^{el} = \frac{E\delta^{el}}{\ell_0}$ with $\sigma^{coh} = \sigma_c \left(1 - \frac{\delta^{coh}}{\delta_c}\right)$ (Salih et al. 2016) [171]. Note that E is young's modulus of the bulk material, δ^{el} and δ^{coh} are extensions arising from the spring and cohesive element, respectively. The equilibrium condition $\sigma^{el} = \sigma^{coh}$ provides the displacement-loading envelope,

$$\frac{\sigma}{\sigma_c} = \begin{cases} \frac{\delta}{\delta_c^{el}} & \text{if } 0 \leq \delta \leq \delta_c^{el} \\ \left(1 - \frac{\delta_c^{el}}{\delta_c}\right)^{-1} \left(1 - \frac{\delta}{\delta_c}\right) & \text{if } \delta_c^{el} < \delta \leq \delta_c \end{cases} \quad (3.18)$$

which is the expected bilinear behaviour depicted in Fig. 3.4 (see Model (b)), where $\delta_c^{el} = \frac{\sigma_c \ell_0}{E}$.

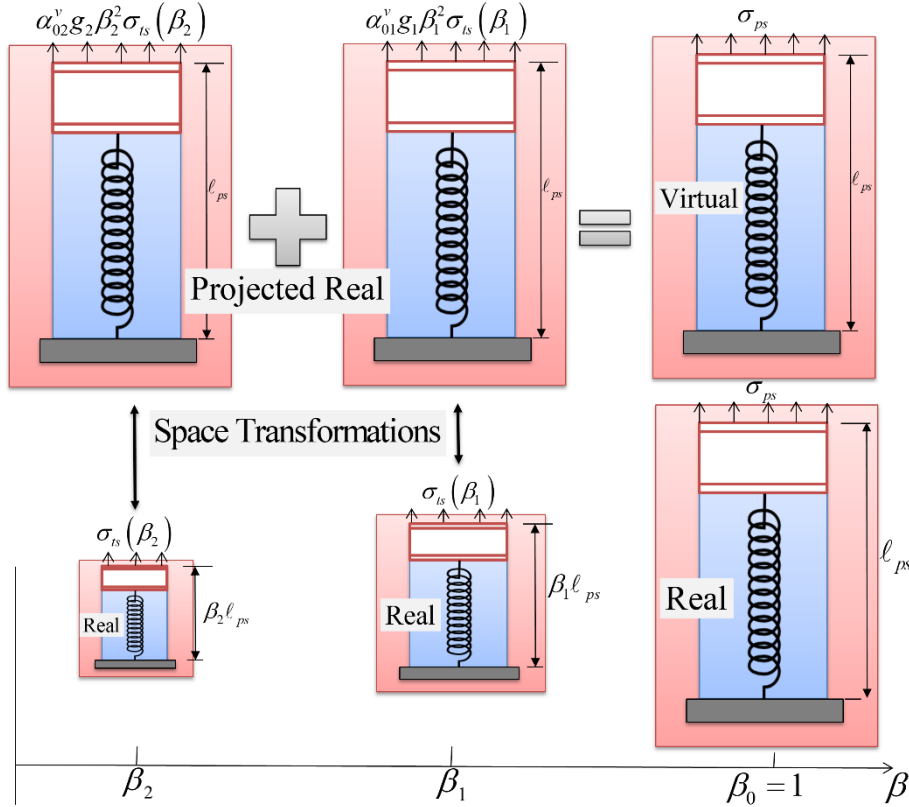


Figure 3.5: Scaling procedure of a rod represented by a spring and cohesive element.

The process of unloading and reloading can be assumed to be reversible and the two unloading paths depicted in Fig. 3.3 are constraints of the form $\sigma^{coh} = \frac{\sigma^{load}}{(\delta^{coh})^{load}} \delta^{coh}$ or $\delta^{coh} = (\delta^{coh})^{load}$, where δ^{load} and σ^{load} are the extension and stress reached by the system at the point of unloading with $\delta^{load} = (\delta^{el})^{load} + (\delta^{coh})^{load}$ and $(\delta^{el})^{load} = \frac{\ell_0 \sigma^{load}}{E}$. The former constraint is typically applied in commercial codes as it has the practical advantage of facilitating crack closure, whereupon a contact algorithm can be applied. The latter constraint is from the viewpoint of material damage with the assertion that damage cannot be undone by a reversal of load. The application of the first-order scaling theory for this setup is depicted in Fig. 3.5 where ℓ_0 takes up values of ℓ_{ps} , $\beta_1 \ell_{ps}$, and $\beta_2 \ell_{ps}$ for each of the lengths of the rods. Observe how space scaling brings the scaled experiments to the size of the full-scale system and note the effects on length and stress. Consider first zeroth-order scaling with $\sigma_{ps} = \alpha_{01}^v g_1 \beta_1^2 \sigma_{ts1}$ and $u_{ps} = \beta_1^{-1} u_{ts1}$; it can be deduced that displacements and stress terms in Eq. (3.16) behave like $\delta_{ps} = \beta_1^{-1} \delta_{ts1}$ and $\sigma_{ps} = \beta_1 \sigma_{ts1}$ (i.e. $\alpha_{01}^v g_1 = \beta_1^{-1}$) to ensure that $G_{c\,ts} = G_{c\,ps}$. This is problematic for replica scaling (i.e., identical material) since there is no expectation that σ_c and δ_c should change yet alone satisfy $\sigma_{c\,ps} = \beta_1 \sigma_{c\,ts1}$ and $\delta_{c\,ps} = \beta_1^{-1} \delta_{c\,ts1}$. These relationships could possibly be satisfied in a physical modelling scenario with a suitable material substitution available. Can first-order finite similitude provide any solution to this predicament, which arises from the inherent size effect in fracture mechanics? The equations of interest in this case stem from Eqs. (3.16c) and (3.16e), which are

$$\sigma_{ps} = \alpha_{01}^v g_1 \beta_1^2 \sigma_{ts1} + R_1 (\alpha_{01}^v g_1 \beta_1^2 \sigma_{ts1} - \alpha_{02}^v g_2 \beta_2^2 \sigma_{ts2}) \quad (3.19a)$$

$$\delta_{ps} = \beta_1^{-1} \delta_{ts1} + R_1 (\beta_1^{-1} \delta_{ts1} - \beta_2^{-1} \delta_{ts2}) \quad (3.19b)$$

which for identical materials throughout and on setting $\delta_{ps} = \delta_{ts1} = \delta_{ts2} = \delta_c$, $\sigma_{ps} = \sigma_{ts1} = \sigma_{ts2} = \sigma_c$ and $E_{ps} = E_{ts1} = E_{ts2} = E$ (Young's modulus) provides

$$1 = \alpha_{01}^v g_1 \beta_1^2 + R_1 (\alpha_{01}^v g_1 \beta_1^2 - \alpha_{02}^v g_2 \beta_2^2) \quad (3.20a)$$

$$\varepsilon_{ps} = \alpha_{01}^v g_1 \beta_1^2 \varepsilon_{ts1} + R_1 (\alpha_{01}^v g_1 \beta_1^2 \varepsilon_{ts1} - \alpha_{02}^v g_2 \beta_2^2 \varepsilon_{ts2}) \quad (3.20b)$$

$$1 = \beta_1^{-1} + R_1 (\beta_1^{-1} - \beta_2^{-1}) \quad (3.20c)$$

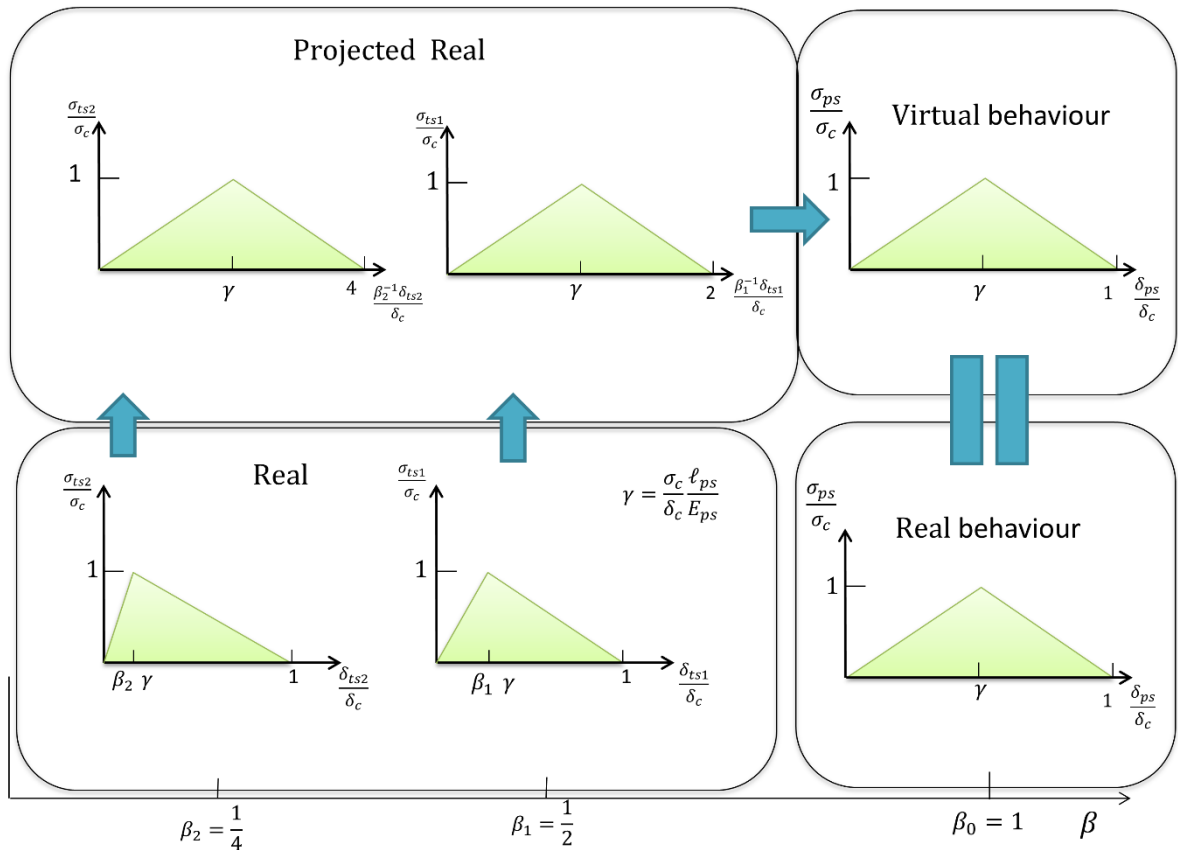
which are three equations (two algebraic and one field identity) with five unknowns $\alpha_{01}^v g_1$, $\alpha_{02}^v g_2$, R_1 , β_1 and β_2 and on setting $\beta_1 = 0.50$ and $\beta_2 = 0.25$ provides $R_1 = 0.50$ from Eq. (3.20c).

For Eqs. (3.20b) and (3.17) to match the zeroth-order conditions $1 = \alpha_{01}^v g_1 \beta_1^2$, (i.e., $\alpha_{01}^v g_1 = 4$) and $\alpha_{01}^v g_1 \beta_1^2 = \alpha_{02}^v g_2 \beta_2^2$ (i.e., $\alpha_{02}^v g_2 = 16$) apply, which also ensures Eq. (3.20a) is satisfied. Note that g_1 and g_2 play no part in this analysis as quasi-static loading is assumed. This simple analysis reveals the benefits of an extra experiment with greater flexibility provided and reveals the potential for making use of the extra freedom offered by expediently selected scales β_1 and β_2 ; this feature was not needed for this case. Eqs. (3.19) for this case are

$$\sigma_{ps} = \sigma_{ts1} + 0.50(\sigma_{ts1} - \sigma_{ts2}) \quad (3.21a)$$

$$\delta_{ps} = 2\delta_{ts1} + 0.50(2\delta_{ts1} - 4\delta_{ts2}) \quad (3.21b)$$

which provide the analytical behaviours in Fig. 3.6, where it is revealed that despite the non-proportional behaviour in the scaled experiments, the virtual model predicts the full-scale behaviour exactly. Regarding fatigue, provided the cyclic loading in the scaled models are



synchronised, then fatigue behaviour in both the real and virtual models can be readily made to coincide.

Figure 3.6: The construction of a virtual cohesive model for the same-material scaling.

3.3.2. The scaling of Model A-b

In this model the bulk material is elastic as above but additionally an elastic component is added to the cohesive element, which is a common feature found in commercial finite element software. In this case the total extension has three components $\delta = \delta^{el} + \delta_{el}^{coh} + \delta_{soft}^{coh}$ with applied stress $\sigma = \sigma^{el} = \sigma_{el}^{coh} = \sigma_{soft}^{coh}$, where $\sigma^{el} = \frac{E\delta^{el}}{\ell_0}$, $\sigma_{el}^{coh} = K^{coh}\delta_{el}^{coh}$ with $\sigma_{soft}^{coh} = \sigma_c \left(1 - \frac{\delta_{soft}^{coh}}{\delta_c}\right)$. The constant K^{coh} is the “stiffness” of the cohesive element and in practice under tensile loading is set equal to $\frac{E}{h^{coh}}$, where h^{coh} is the thickness of the cohesive element and note that the total separation of the cohesive element is $\delta^{coh} = \delta_{el}^{coh} + \delta_{soft}^{coh}$. The equilibrium condition provides the loading envelope described by Eq. (3.19) apart from one significant change, i.e., the term δ_c^{el} changes to

$$\delta_c^{el} = \sigma_c \left(\frac{\ell_0}{E} + \frac{1}{K^{coh}} \right) = \frac{\sigma_c}{E} (\ell_0 + h^{coh}) \quad (3.22)$$

which confirms that length scaling is dependent on h^{coh} .

The setting of K^{coh} is discussed in the open literature [172] but an additional consideration is the way it changes with scale. There are two possibilities, and both are shown here to satisfy the first-order finite similitude rule. Consider first the geometric view where h^{coh} scales with the geometry so that $h_{ts1}^{coh} = \beta_1 h_{ps}^{coh}$ and $h_{ts2}^{coh} = \beta_2 h_{ps}^{coh}$, then the behaviour in Fig. 3.6 for replica scaling applies. Consider second that h^{coh} is a material constant and for replica scaling it remains unchanged. In this case

$$\delta_{c\,ts1}^{el} = \frac{\sigma_c}{E} (\beta_1 \ell_{ps} + h_{ps}^{coh}) \quad (3.23a)$$

$$\delta_{c\,ts2}^{el} = \frac{\sigma_c}{E} (\beta_2 \ell_{ps} + h_{ps}^{coh}) \quad (3.23b)$$

But direct substitution of these equations into Eq. (3.19b) provides $\delta_{ps} = \frac{\sigma_c}{E} (\ell_{ps} + h_{ps}^{coh})$, which is as required and confirms that first-order scaling is exactly satisfied.

This relatively simple analysis confirms that even with the addition of cohesive stiffness the behaviour of the cohesive element transforms under the rules of the first-order finite similitude theory.

3.3.3. The scaling of Model A-c

In this model a plateau is added to the shape of the traction separation law and can be considered as the representative of localised plasticity at the crack tip, which is a feature of many materials. In mathematical terms the cohesive element is described as

$$\frac{\sigma}{\sigma_c} = \begin{cases} 1 & \text{if } 0 \leq \delta^{coh} \leq \delta_2 \\ \frac{\delta_c - \delta^{coh}}{\delta_c - \delta_2} & \text{if } \delta_2 < \delta^{coh} \leq \delta_c \end{cases} \quad (3.24)$$

where δ_2 marks the end of the plateau as shown in Fig. 4, and the behaviour of the system is readily shown to be

$$\frac{\sigma}{\sigma_c} = \begin{cases} \frac{\delta}{\delta_c^{el}} & \text{if } 0 \leq \delta \leq \delta_c^{el} \\ 1 & \text{if } \delta_c^{el} < \delta \leq \delta_c^{el} + \delta_2 \\ \left(1 - \frac{\delta_c^{el} + \delta_2}{\delta_c}\right)^{-1} \left(1 - \frac{\delta}{\delta_c}\right) & \text{if } \delta_c^{el} + \delta_2 < \delta \leq \delta_c \end{cases} \quad (3.25)$$

where $\delta_c^{el} = \frac{\sigma_c \ell_0}{E}$ and it is interest to ascertain whether this system satisfies the rules of first-order finite similitude theory.

The situation is portrayed in Fig. 3.7, where again first-order theory exactly represents the behaviour at full scale. The reason why the theory can reproduce cohesive behaviour in an elastic medium is clear from Figs. 3.6 and 3.7 with the ability to correctly interpret the three types of abscissae appearing on the separation coordinate axis, i.e., points that are constant and proportional to β and combinations thereof. More fundamentally this property arises from the nesting of zeroth-order relationships in first-order ones and highlights the importance of this feature. Model A-d offers no surprises, so it is of interest to examine the situation where dissipation is a feature of the surrounding bulk material.

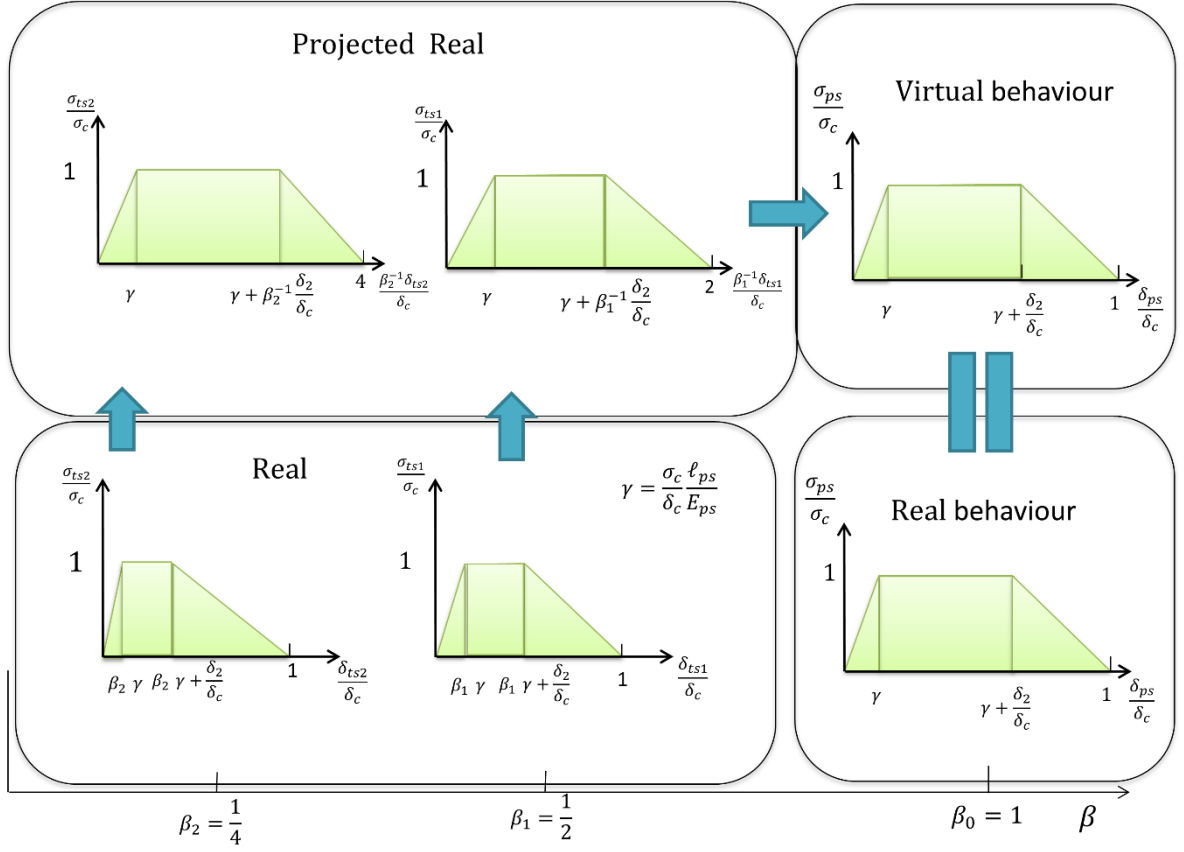


Figure 3.7: Local plasticity captured exactly for replica scaling in first-order theory.

3.3.4. The scaling of Model B-a

The spring-slider system in Model B is assumed to satisfy the power law relationship typical to HRR theory introduced in reference (Hutchinson, 1968) [173]

$$\frac{\sigma^{ep}}{\sigma_Y} = \left(\frac{\varepsilon^{ep}}{\varepsilon_Y} \right)^{\frac{1}{n}} \quad (3.26)$$

where $\varepsilon_Y = \frac{\sigma_Y}{E}$, σ_Y is reference yield stress, ε_Y is reference yield strain, and it is assumed here that damage as represented by the cohesive initiates at the point of necking, which is identified by the condition $\sigma = \frac{d\sigma}{d\varepsilon^{ep}}$, which provides $\varepsilon_c^{ep} = \frac{1}{n}$ and $\sigma_c = \sigma_Y (n\varepsilon_Y)^{-\frac{1}{n}}$.

The response of system can be considered to consist of three parts in the form $\delta = \delta^{ep} + \delta^{coh}$, with $\delta^{ep} = \delta^{pl} + \delta^{el}$, where δ^{pl} is the permanent plastic extension that remains on elastic unloading (Salih et al. 2016) [171]. Note that δ^{ep} is related to true strain in Eq. (3.18) by the relationship $\varepsilon^{ep} = \ln \left(1 + \frac{\delta^{ep}}{\ell_0} \right)$ and $\delta^{el} = \frac{\sigma \ell_0}{E}$. Moreover, unloading of the bulk

material is elastic and described by the relationship $\delta^{ep} = \delta_c^{pl} + \delta^{el}$ and the equilibrium condition $\sigma = \sigma^{ep} = \sigma^{coh}$ provides

$$\frac{E}{\ell_0} \delta^{el} = \sigma_c \left(1 - \frac{\delta^{coh}}{\delta_c} \right) = \sigma \quad (3.27)$$

where $\delta = \delta_c^{pl} + \delta^{el} + \delta^{coh}$ or equivalently

$$\delta - \delta_c^{pl} = \sigma \frac{\ell_0}{E} + \delta_c \left(1 - \frac{\sigma}{\sigma_c} \right) \quad (3.28)$$

and consequently, the displacement-loading envelope is

$$\frac{\sigma}{\sigma_c} = \begin{cases} \frac{\sigma_Y}{\sigma_c} \left(\frac{\ln \left(1 + \frac{\delta}{\ell_0} \right)}{\varepsilon_Y} \right)^{\frac{1}{n}} & \text{if } 0 \leq \delta \leq \delta_c^{ep} \\ \left(1 - \frac{\delta_c^{el}}{\delta_c} \right)^{-1} \left(1 - \frac{\delta - \delta_c^{pl}}{\delta_c} \right) & \text{if } \delta_c^{ep} < \delta \leq \delta_c^{pl} + \delta_c \end{cases} \quad (3.29)$$

where $\delta_c^{el} = \frac{\sigma_c \ell_0}{E}$.

It is of interest to examine whether this loading envelope scales exactly for replica scaling under first-order theory. The behaviour is presented in Fig. 3.8, where again it is revealed that first-order scaling provides the correct description. Note that the critical aspect to exact scaling is how the points δ_c^{ep} and $\delta_c^{pl} + \delta_c$ are related across the scales; the following relationships apply: $\delta_{c\,ps}^{ep} = \beta_1^{-1} \delta_{c\,ts1}^{ep} = \beta_2^{-1} \delta_{c\,ts2}^{ep}$, $\delta_{c\,ps}^{pl} = \beta_1^{-1} \delta_{c\,ts1}^{pl} = \beta_2^{-1} \delta_{c\,ts2}^{pl}$ and δ_c remains constant.

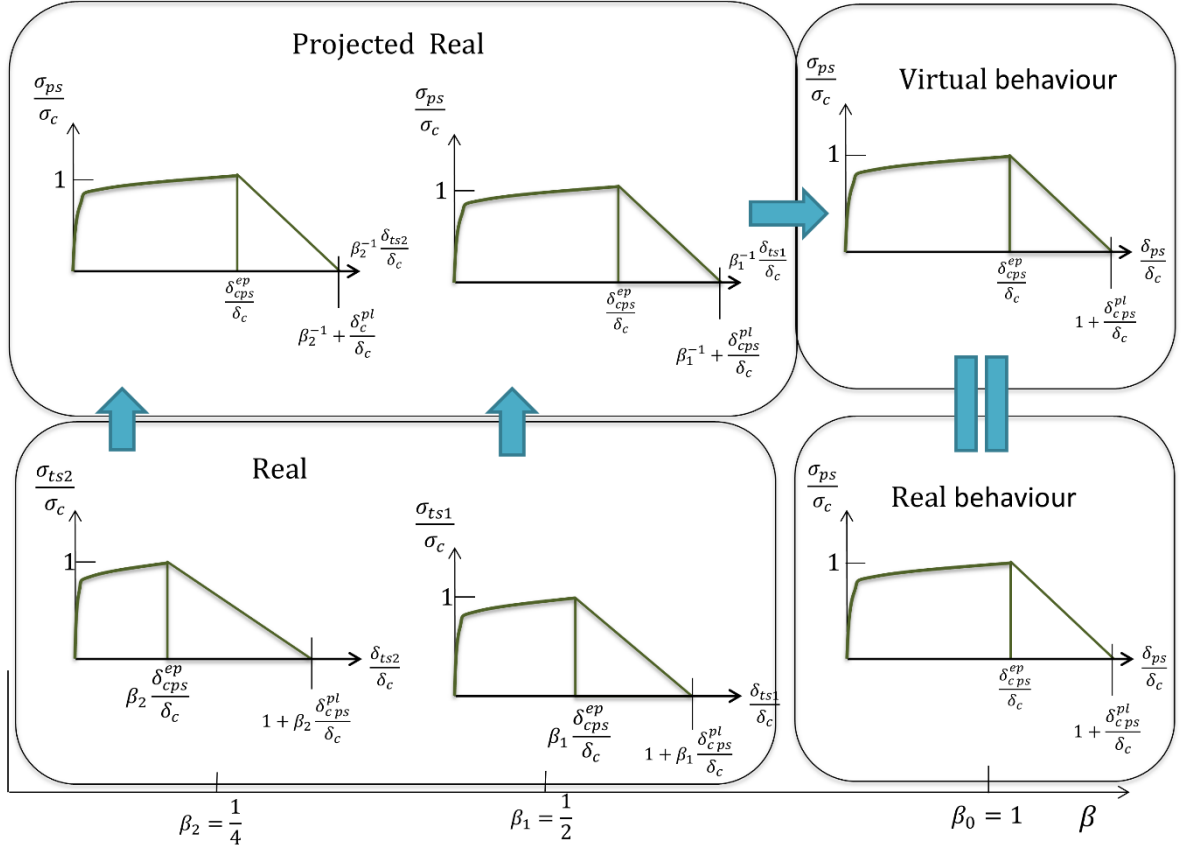


Figure 3.8: Non-linear bulk and LCZM captured exactly for replica scaling in first-order theory.

3.3.5. The scaling of Model B-b

The inclusion of a spring into the cohesive element adds no new difficulties for the first-order theory. The analysis to a large part follows that provided above where for $\varepsilon_c^{ep} \leq \frac{1}{n}$ and

$\sigma \leq \sigma_c = \sigma_Y (n\varepsilon_Y)^{\frac{1}{n}}$ the total extension has two components $\delta = \delta^{ep} + \delta_{el}^{coh}$ (although $\delta^{ep} = \delta^{pl} + \delta^{el}$) with applied stress $\sigma = \sigma^{ep} = \sigma_{el}^{coh}$, where σ^{ep} is constrained to follow Eq. (3.26) and $\sigma_{el}^{coh} = K^{coh} \delta_{el}^{coh}$. Once material softening is initiated then $\delta = \delta_c^{pl} + (\delta^{el} + \delta_{el}^{coh}) + \delta_{soft}^{coh}$, where $\delta_{soft}^{coh} = \sigma_c \left(1 - \frac{\sigma_{soft}^{coh}}{\sigma_c}\right)$ and the situation is effectively that for Model B-a but with $\delta^{el} + \delta_{el}^{coh}$ replacing δ^{el} .

3.3.6. The scaling of Model B-c

The bulk material and the material in the cohesive zone are assumed to differ in their plastic response with the bulk material constrained to follow Eq. (3.26) and a perfectly plastic

response in the cohesive zone. The initial loading is all about the bulk material with $\delta = \delta^{ep} = \delta^{pl} + \delta^{el}$ and $\varepsilon_c^{ep} = \ln\left(1 + \frac{\delta^{ep}}{\ell_0}\right) \leq \frac{1}{n}$. Softening is not initiated at δ_c^{ep} since cohesive plastic behaviour takes place and $\delta = \delta_c^{pl} + \delta_c^{el} + \delta_{pl}^{coh}$ for $\delta_{pl}^{coh} \leq \delta_2$ after which softening occurs and $\delta = \delta_c^{pl} + \delta_c^{el} + \delta_{soft}^{coh}$, where $\delta_c^{el} = \frac{\sigma_c \ell_0}{E}$ and $\delta_{soft}^{coh} = \sigma_c \left(1 - \frac{\sigma_{soft}^{coh}}{\sigma_c}\right)$. Thus, the displacement loading profile behaves as

$$\frac{\sigma}{\sigma_c} = \begin{cases} \frac{\sigma_Y}{\sigma_c} \left(\frac{\ln\left(1 + \frac{\delta}{\ell_0}\right)}{\varepsilon_Y} \right)^{\frac{1}{n}} & \text{if } 0 \leq \delta \leq \delta_c^{ep} \\ 1 & \text{if } \delta_c^{ep} < \delta \leq \delta_c^{ep} + \delta_2 \\ \left(1 - \frac{\delta_c^{el} + \delta_2}{\delta_c}\right)^{-1} \left(1 - \frac{\delta - \delta_c^{pl}}{\delta_c}\right) & \text{if } \delta_c^{ep} + \delta_2 < \delta \leq \delta_c^{pl} + \delta_c \end{cases} \quad (3.30)$$

and again, replica scaling can readily be shown to be exact under first-order theory and the same is true of Model B-d.

3.4 General Applicability of First Order Scaling

In the previous section it was demonstrated that under quasistatic loading, for a variety of 1-D cohesive elements and material types, that exact replication was possible with the first-order finite similitude rule. A question remains however about the general applicability of the approach to more complex situations in practical settings. Under quasistatic loading the first-order rule of Eq. (3.9), on application to the transport equations for momentum and movement, gives

$$\alpha_1^v T_1^v(\beta) = \int_{\Gamma_{ps}^*} \alpha_1^v \Sigma'_{ps} \cdot \mathbf{n}_{ps} d\Gamma_{ps}^* = 0 \quad (3.31a)$$

$$\alpha_1^u T_1^u(\beta) = \frac{D^*}{D^* t_{ps}} \int_{\Omega_{ps}^*} \alpha_1^u \rho_{ps} \mathbf{U}'_{ps} dV_{ps}^* - \int_{\Gamma_{ps}^*} \alpha_1^u \rho_{ps} \mathbf{U}'_{ps} (\mathbf{v}_{ps}^* \cdot \mathbf{n}_{ps}) = 0 \quad (3.31b)$$

where $\Sigma_{ps} = \alpha_0^v \beta^2 g \sigma_{ts}$ and $\mathbf{U}_{ps} = \beta^{-1} \mathbf{u}_{ts}$, and where the dash “'” signifies derivative with respect to β , and where the body force is not included.

Consider then the desired scale invariances $\sigma'_{ts} \equiv 0$ and $\mathbf{u}'_{ts} \equiv 0$ that feature in the cohesive elements considered in the previous section and note that $\mathbf{U}'_{ps} = (\beta^{-1} \mathbf{u}_{ts})' = (\beta^{-1})' \mathbf{u}_{ts} = (\beta^{-1})' \beta \mathbf{U}_{ps}$ and $\Sigma'_{ps} = (\alpha_0^v \beta^2 g \sigma_{ts})' = (\alpha_0^v \beta^2 g)' \sigma_{ts}$. Consequently setting $\alpha_1^u = \beta^2$

ensures Eq. (3.30b) is independent of β and gives $\alpha_1^u T_1^u(\beta) = \beta^2(\beta^{-1})' \beta \alpha_0^u T_0^u(\beta) = 0$ (see Eq. (3.4d)). Similarly, setting $\alpha_0^v g = \beta^{-2}$ provides $\alpha_1^v T_1^v(\beta) \equiv 0$ confirming that Eqs. (3.30) are satisfied and independent of β under the conditions of quasistatic loading and under the invariances $\sigma'_{ts} \equiv 0$ and $\mathbf{u}'_{ts} \equiv 0$ pertinent to cohesive elements. Moreover, the zeroth-order relationship $\mathbf{u}_{ts} = \beta \mathbf{u}_{ps}$ (which featured in Sec. 3) provides $\mathbf{U}'_{ps} = (\beta^{-1} \mathbf{u}_{ts})' = (\mathbf{u}_{ps})' = \mathbf{0}$ and therefore $\alpha_1^u T_1^u(\beta) \equiv 0$, confirming as expected that any zeroth-order relationship is contained within first order. Note additionally, that although constitutive laws do not directly feature in finite similitude theory the stress condition $\Sigma'_{ps} \equiv \mathbf{0}$ invariably ensures that a vast array of laws can be catered for. The elastic constitutive relationship $\sigma_{ts} = \mathbf{C}_{ts} : \epsilon_{ts}$ (with elasticity tensor \mathbf{C}_{ts}) for example gives $\sigma'_{ts} = \mathbf{C}'_{ts} : \epsilon_{ts} + \mathbf{C}_{ts} : \epsilon'_{ts}$ but $\sigma'_{ts} \equiv 0$, and with no change in material $\mathbf{C}'_{ts} \equiv 0$, so it follows that $\epsilon'_{ts} \equiv 0$ is a requirement. In the case of small deflection theory both the conditions $\mathbf{u}'_{ts} \equiv 0$ and $\mathbf{u}_{ts} = \beta \mathbf{u}_{ps}$ ensure $\epsilon'_{ts} \equiv 0$ confirming that linear elasticity poses no difficulty for the theory. Indeed, a nonlinear stress dependence of the form $\sigma_{ts}(\mathbf{C}_{ts}, \epsilon_{ts})$ follows the same pattern and consequently it can be concluded that the first-order rules are generally applicable to fracture mechanics and fatigue. It can be anticipated that good replication of full-scale behaviour is possible and expected.

3.4.1. Analytical study detailing the application of finite similitude rules

Despite the complexity involved in deriving the first-order finite similitude rules, its practical application is relatively straightforward and is outlined in the following steps:

- (i) Specify the geometry, material properties, loading and boundary conditions of the full-scale model.
- (ii) Specify the geometric scaling factors β_1 and β_2 , and material properties for the scaled models. Identical materials are applied to all models in this work.
- (iii) Calculate the dimensional scaling factors for scaled models by using the zeroth order setting $\alpha_{01}^v g_1 = \beta_1^{-2}$ and $\alpha_{02}^v g_2 = \beta_2^{-2}$.
- (iv) Calculate the scaling factor R_1 using Eq. (3.20c).
- (v) Calculate the applied loads and boundary conditions for the scaled models. If the loading condition of the full-scale model is an applied stress, then the same stress is applied to all scaled models. For the case of applied force or displacement, the dimensional scaling factors are used to calculate the suitable load for scaled models.
- (vi) Perform experimental tests on the scaled models.

- (vii) Combine the results of the desired outputs returned from the scaled model using the appropriate field equations (i.e., Eq. (3.16)).

To illustrate the application of the theory the procedure outlined is applied to an analytical approach for calculating the stress intensity factor in a compact tension (CT) specimen as provided in the ASTM E647 guideline [174]. The formula involved was validated experimentally and numerically by Farahani et al. (2017) [175], and the geometry and loading conditions are replicated here. The geometry for a typical CT specimen can be found in Fig. 3.11a; in this case the width $W = 40$ mm and the thickness $B = 2$ mm. The objective is to assess the ability of the theory to predict the crack extension and associated crack driving force (i.e., stress intensity factor) accurately. Farahani et al. [165] tested the CT specimen under a fatigue load range of 603 N and measured the stress intensity factor at seven discrete crack lengths using Digital Image Correlation (DIC) techniques. Comparisons were made between the analytical ASTM E647 solutions, DIC technique, the finite element method using Abaqus, and the meshless radial point interpolation method (RPIM). Consider then application of the procedure above:

- (i) The geometry is provided in Farahani et al. (2017) [175], where the material used is Aluminium alloy AA6082-T6 with Young's modulus 70 GPa and Poisson's ratio 0.33. The fatigue load $F_{ps} = F_{max} - F_{min} = 670 - 67 = 603$ N.
- (ii) Two scaled models are tested corresponding to scales $\beta_1 = 0.5$ and $\beta_2 = 0.25$.
- (iii) The scaling factors are $\alpha_{01}^v g_1 = \beta_1^{-2} = 4$ and $\alpha_{01}^v g_2 = \beta_2^{-2} = 16$.
- (iv) The value for $R_1 = (\beta_1^{-1} - \beta_2^{-1})^{-1}(1 - \beta_1^{-1}) = (2 - 4)^{-1}(1 - 2) = 0.5$.
- (v) Applied loads for the scaled models are calculated using $F_{ps} = \alpha_{01}^v g_1 F_{ts1}$ and $F_{ps} = \alpha_{01}^v g_2 F_{ts2}$ to give $F_{ts1} = 603 \times 4^{-1} = 150.75$ N and $F_{ts2} = 603 \times 16^{-1} = 37.69$ N.
- (vi) The ASTM expression for stress intensity factor as a function of crack length is

$$\Delta K = \frac{\Delta P}{B\sqrt{W}} \frac{(2 + \alpha)}{(1 - \alpha)^{3/2}} (0.866 + 4.64\alpha - 13.32\alpha^2 + 14.72\alpha^3 - 5.6\alpha^4) \quad (3.32a)$$

which is applied to the scaled models at crack length given by $a_{ts1} = \beta_1 a_{ps}$ and $a_{ts2} = \beta_2 a_{ps}$ for the seven values of a_{ps} recorded by Farahani et al. (2017).

- (vii) To combine the stress intensity factors of the scaled models the relationship

$$\Delta K_{ps} = \alpha_{01}^v g_1 \beta_1^{3/2} \Delta K_{ts1} + R_1 \left(\alpha_{01}^v g_1 \beta_1^{3/2} \Delta K_{ts1} - \alpha_{02}^v g_2 \beta_2^{3/2} \Delta K_{ts2} \right) \quad (3.32b)$$

is applied (derivable from Eq. (3.16c)) and the results are recorded in Table 3.3 and Fig. 3.9, where is apparent that the results from full scale model are predicted with 0% error.

Table 3.3. Stress intensity factors (MPa mm^{1/2}) for scaled and virtual models, and ASTM full-scale prediction.

Crack length	ΔK_{ASTM}	ΔK_{ts1}	ΔK_{ts2}	$\Delta K_{virtual}$	Error%
12.98	285.41	201.82	142.71	285.41	0
14.07	306.08	216.43	153.04	306.08	0
15.26	330.55	233.73	165.27	330.55	0
17.01	371.27	262.53	185.64	371.27	0
20.56	481.04	340.15	240.52	481.04	0
21.74	529.85	374.66	264.93	529.85	0
22.48	564.95	399.48	282.47	564.95	0

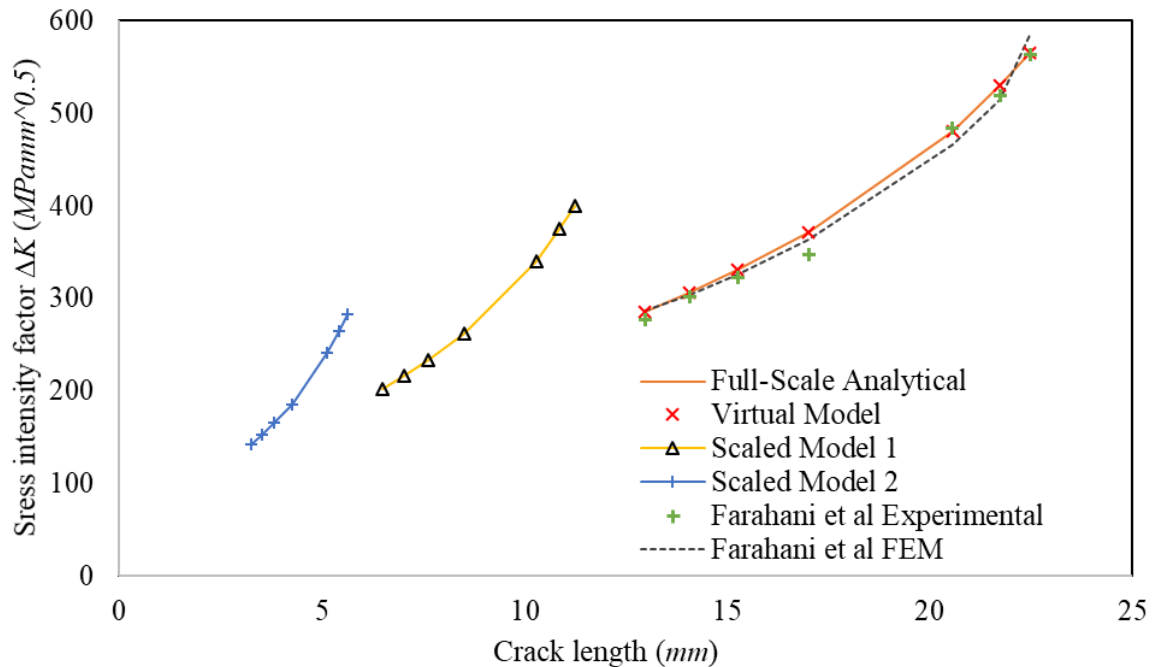


Figure 3.9: Crack length vs stress intensity factor for full scale, virtual and scaled-down models and comparison with full-scale ΔK analytical ASTM E647 prediction, experimental data [175] and numerical data in ref. [175]

3.5 Numerical Experimentation

The case studies considered here examine the fatigue response of standard specimens recommended by ASTM E647 to examine the fatigue life and crack growth rate of materials. The tests considered are compact tension (CT), middle tension specimen (MT) and eccentrically loaded single edge notched specimen (ESET), which are analysed by means of XFEM cohesive segments method using the popular finite element software Abaqus [176]. This method specifies the degradation of enriched elements using a bilinear traction separation cohesive zone law. A linear elastic bulk material is specified for all models and consequently the numerical models in this section correspond to model “A-b” in Section 3.3. To validate the fatigue crack growth results from Abaqus, the middle tension specimen analysis done by London et al. (2015) [177] is replicated and results compared. Constant amplitude loadings are applied in all case studies. In case studies 2 and 3 the loading is set such that the specimen reaches full failure. This is done to show the ability of the scaling theory to replicate the fatigue behaviour of full-scale specimens up to and including final failure. All case studies are 2D due to the high computational cost of simulating fatigue in three dimensions even for a relatively low cycle count. A structured mesh with plane stress elements (CP4SR) is used for all case studies. The element size is particularly important for an XFEM based approach since the crack traverses a whole element each time it propagates. Thus, the crack growth rate is heavily dependent on the element size. An element size of 0.2 mm was used around the crack path for all case studies as recommended by Zhang et al. (2016) [178]. Elements with a size of 0.50mm were used in the other regions of the specimen. This meshing is achieved by means of the partitioning technique, where some 24000 elements are generated in total for the full-scale model. The number of elements is kept the same for all scaled models to eliminate the effects of mesh dependency. This is achieved by multiplying the element sizes used in the full scale model by the β value of the scaled model. All models are created in the commercial finite element software Abaqus. Aluminium alloy 6061 is used for all models, with pertinent properties taken from Bray (1990) [179] and provided in Table 3.4.

Table 3.4: Mechanical properties of 6061 aluminium alloy used for all tests [179].

Material properties	Value
Young’s Modulus, E (MPa)	70000
Poisson’s ratio, ν	0.30

Yield strength (MPa)	276
Maximum principal stress σ_c (MPa)	310
Ultimate tensile strength (MPa)	310
Plastic strain	0.06
Fracture energy (kJm^{-2})	30
Paris law parameters C ($\text{m/cycleMPam}^{0.5}$)	3.807×10^{-10}
Paris law parameters m	3.034

The maximum principal stress criterion is adopted for crack initiation. Thus, the crack propagates when the stress exceeds the maximum principal stress, in a direction orthogonal to the maximum principal stress. Previous studies by Liu et al. (2012) [180] show that a better correlation between numerical and experimental results is achieved when the maximum principal stress is set to the value of the tensile strength of the material. Thus, the same criterion is adopted in this paper.

3.5.1. Verification of numerical results

Before any scaling laws are applied it is imperative to validate the numerical results to ensure the numerical modelling is correct and in agreement with published research. The work of London et al [177] is replicated here. They examined the fatigue growth rate of the middle-tension specimen using the same direct cyclic solver in Abaqus that is employed in all case studies for this paper. A cyclic membrane stress of 100MPa was applied to both the top and bottom edges, and the geometry and loading are shown in Fig. 3.10. The number of cycles in the reported study was 3000, but here validation is limited to 600 cycles as the number of cycles in all case studies does not exceed 50 cycles. The material is Al 6061 and 2D plane stress CPS4 elements are used for this study. It is revealed that there is good agreement between the results of the current study and the reported findings of London et al. [177] (less than 3% error in final crack length value). Note that although the focus in this work is on demonstrating that the finite-similitude approach replicates fatigue behaviour modelled using cohesive elements the use of plane stress (and strain) elements is justified in practical studies involving a small number of cycles.

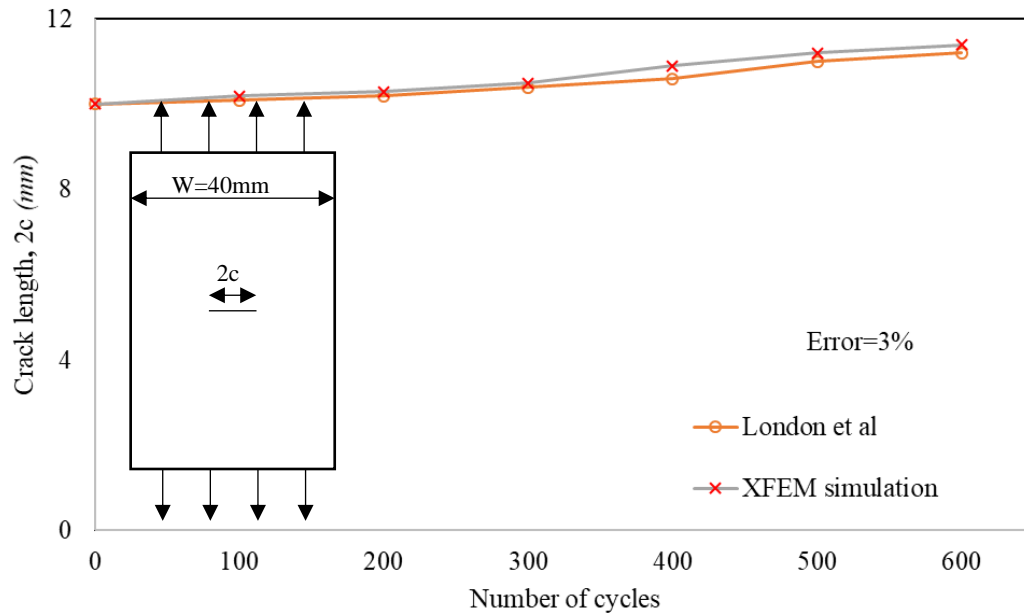
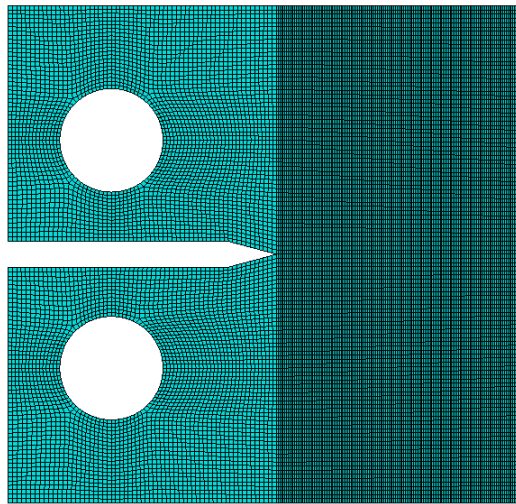
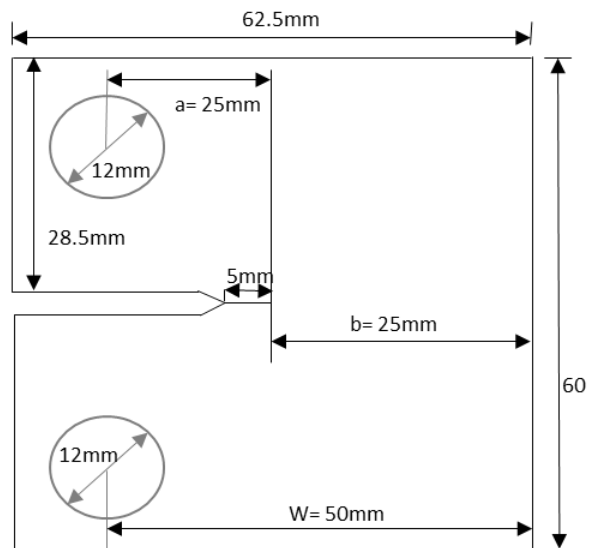


Figure 3.10: Loading and geometry of middle tension specimen and comparison between the numerical results of the current study and London et al. [177].

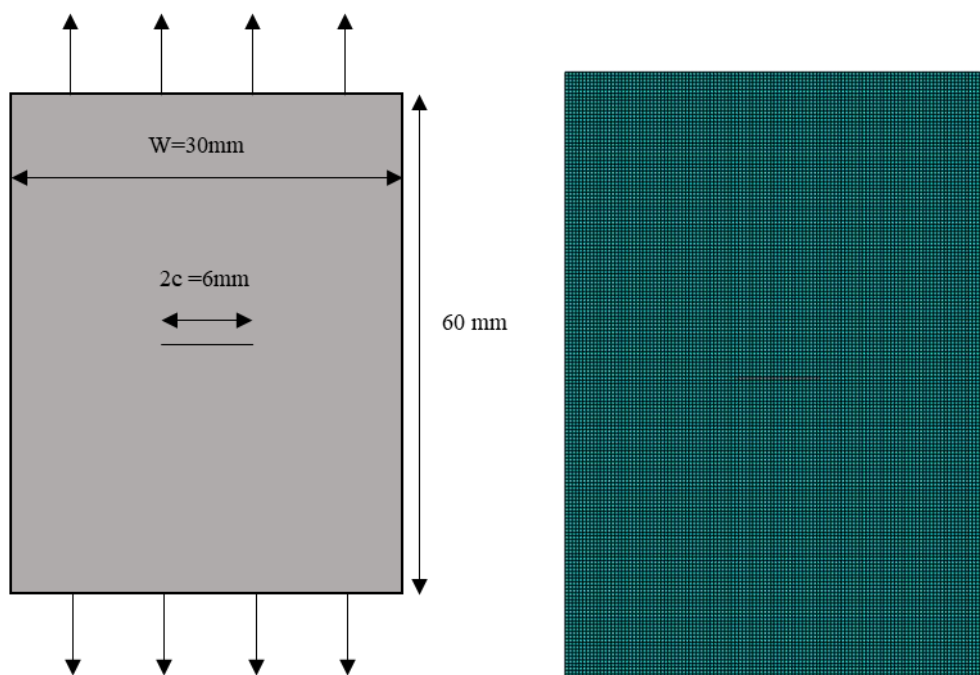
D'Angela & Ercolino [181] investigated the application of plane stress and strain elements to fatigue crack growth of a CT specimen using the same direct cyclic Abaqus solver applied in this study. Good agreement was found with experiment and analytical results for both plane stress and strain elements with insignificant differences recorded over the first few hundred cycles. The validated numerical procedure is employed in the next sections to investigate the efficiency of the proposed scaling method based on the first order theory.

3.5.2 Evaluation of the fatigue crack growth rate of ASTM E647 specimens

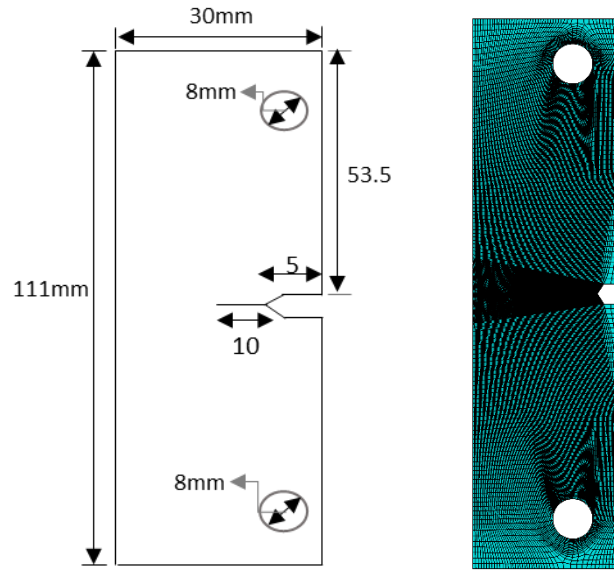
The numerical simulation for all case studies follows ASTM E647 procedure to evaluate the fatigue crack growth rate. The compact tension (CT), middle tension (MT) and eccentrically loaded single edge notched (ESET) model analysed are presented in Fig. 3.11, detailing mesh and the fatigue pre-crack. Abaqus is used for all simulations, and the specific geometry constraints in the ASTM E647 rules are adhered to. The procedure in section 3.4.1 is used to design and test the scaled specimens and correlate the obtained fracture mechanics outputs from scaled tests with the full scale specimen behaviour by means of virtual models.



(a) Compact tension specimen dimensions and mesh



(b) Middle tension specimen dimensions and mesh



(c) ESET specimen dimensions and mesh

Figure 3.11: Fatigue test specimens considered in case studies.

The scaling theory is then applied to different size scaled specimens. Three different load types are applied to the CT specimen to demonstrate the theory's capability. A simple static load with peak displacement of 0.3 mm is applied, then a single loading-unloading cycle with the same peak displacement of 0.3 mm and finally a cyclic displacement of 1.5mm is applied for a duration of 50 cycles. For all load types, the load is applied at the upper loading pin and the lower loading pin is fixed in all directions. For the MT specimen a cyclic displacement of 1mm is applied to both the top and bottom edges for a duration of 50 cycles. The ESET specimen is loaded with an initially high static load with a displacement of 1.5 mm at the upper pin and then cycled for 50 cycles with a constant amplitude displacement of 0.3 mm; the lower pin is fixed in all directions. This initial high loading is set such that an overload condition where a structure suddenly receives a load many times higher than normal operating loads can be simulated. Virtual models are constructed from the combination of data obtained from the scaled experiments. These models are then contrasted with the output from the full-scale model and ultimately it is shown that the fatigue behaviour of a full-scale specimen can be predicted exactly using two scaled experiments.

The procedure for measuring the fatigue crack growth rate (FCGR) as outlined in ASTM E647 involves two stages, the first is the measurement of the crack length against corresponding number of cycles and stress intensity factor. The slope of the curve da/dN is evaluated from the plot of crack length a vs number of cycles N to determine the crack

growth rate by the secant method. Finally, the materials resistance to crack growth is expressed in the form of da/dN vs ΔK on a log log scale. The slope of this gives the Paris constant m . Additional information can be extracted from the FE simulations such as reaction force, which is measured at the upper loading pin. To determine the appropriate element size for the numerical analysis, a mesh sensitivity study was performed, and the results are presented in Fig. 3.12.

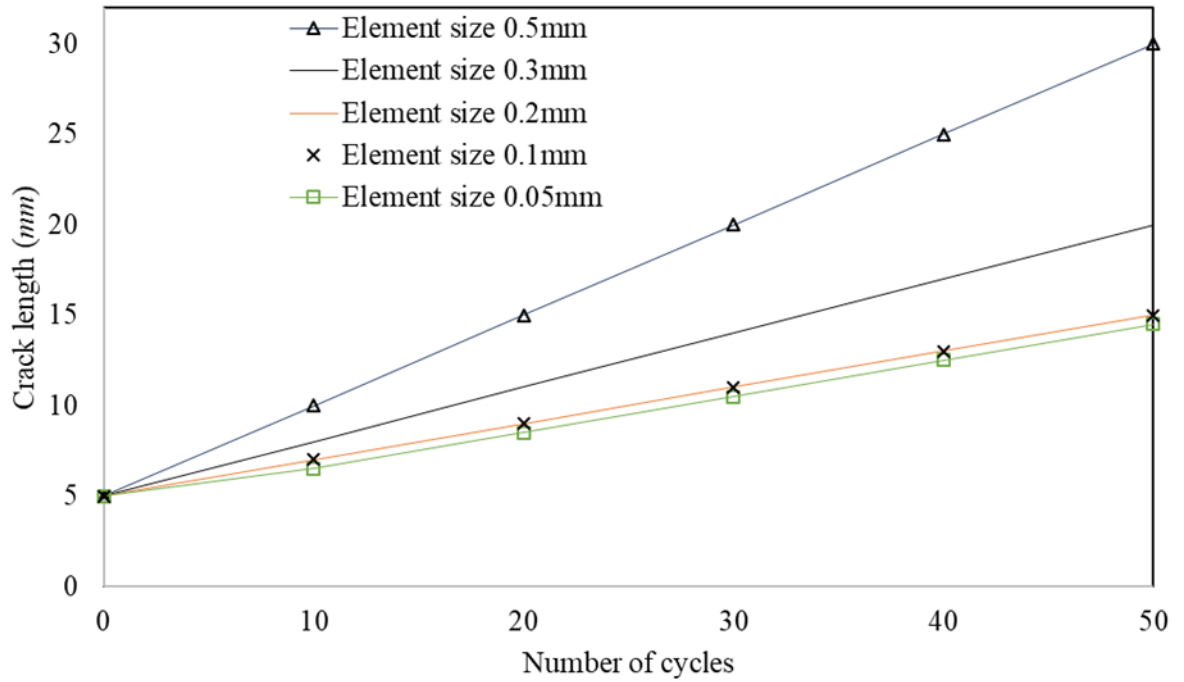


Figure 3.12: Mesh sensitivity study for compact tension specimen.

Fig. 3.12 shows that the crack in the CT specimen grows from 5 mm to 30 mm resulting in failure after 50 cycles for an element size of 0.50 mm at the crack tip. However, when an element size of 0.10 and 0.20 mm is adopted around the crack path, the specimen does not fail after 50 cycles and the final crack length of 10 mm is the same for both element sizes. Thus, an element size of 0.20 mm around the crack tip is selected in this study for all specimens. The specimen dimensions and loading conditions for all specimens can be found in Tables 3.5 to 3.9. Additionally, Table 3.10 presents the dimensional scaling factors for all three specimens. The first four virtual models pertain to the CT specimen, virtual models 5-8 are for the MT specimen and virtual models 9-12 are constructed from the scaled models of the ESET specimen.

Table 3.5: The dimensions of CT specimen for the full-scale and scaled down models

Space	β	Initial crack size a (mm)	Height (mm)	Ligament length (W-a) (mm)	Thickness (mm)	Width (mm)	Fatigue pre-crack length (mm)
Physical	1.00	25.00	60	25.00	5.00	62.50	5.00
Trial	0.80	20.00	48	20.00	4.00	50.00	4.00
	0.70	17.50	42	17.50	3.50	43.75	3.50
	0.50	12.50	30	12.50	2.50	31.25	2.50
	0.40	10.00	24	10.00	2.00	25.00	2.00
	0.25	6.25	15	6.25	1.25	15.63	1.25

Table 3.6: Loading conditions of CT specimen at different scales

Space	β	Displacement for fracture load (mm)	Displacement at maximum cyclic amplitude (mm)
Physical	1.00	0.30	1.50
Trial	0.80	0.24	1.20
	0.70	0.21	1.05
	0.50	0.15	0.75
	0.40	0.12	0.60
	0.25	0.075	0.375

Table 3.7: The dimensions of MT specimen at different scales

Space	β	Initial crack size 2c (mm)	Height (mm)	Ligament length (W-a) (mm)	Thickness (mm)	Width (mm)	Displacement at maximum amplitude cyclic (mm)
Physical	1.00	6.00	60	24.00	5.00	30.00	1.00
Trial	0.80	4.80	48	19.20	4.00	24.00	0.80
	0.70	5.60	42	16.80	3.50	21.00	0.70

	0.50	3.00	30	12.00	2.50	15.00	0.50
	0.40	2.40	24	9.60	2.00	12.00	0.40
	0.25	1.50	15	6.00	1.25	7.50	0.25

Table 3.8: The dimensions of ESET specimen at different scales

Space	β	Initial crack size a (mm)	Height (mm)	Ligament length (W-a) (mm)	Thickness (mm)	Width (mm)	Fatigue pre-crack length (mm)
Physical	1.00	5.00	111	20.00	5.00	30.00	10.00
Trial	0.80	4.00	48	16.00	4.00	24.00	8.00
	0.70	3.50	42	14.00	3.50	21.00	7.50
	0.50	2.50	30	10.00	2.50	15.00	5.00
	0.40	2.00	24	8.00	2.00	12.00	4.00
	0.25	1.25	15	5.00	1.25	7.50	2.50

Table 3.9: Loading conditions of ESET specimen at different scales

Space	β	Displacement for fracture load (mm)	Displacement at maximum cyclic amplitude (mm)
Physical	1.00	1.50	0.30
Trial	0.80	1.20	0.24
	0.70	1.05	0.21
	0.50	0.75	0.15
	0.40	0.60	0.12
	0.25	0.375	0.075

Table 3.10: Value of the scaling factors with different dimensional scaling factors

Virtual Model No.	β_1	β_2	$\alpha_{01}^v g_1$	$\alpha_{02}^v g_2$	R_1
1	0.80	0.50	1.56	4.00	0.33
2	0.80	0.25	1.56	16.00	0.09

3	0.50	0.25	4.00	16.00	0.50
4	0.70	0.40	2.04	6.25	0.09
5	0.80	0.50	1.56	4.00	0.33
6	0.80	0.25	1.56	16.00	0.09
7	0.50	0.25	4.00	16.00	0.50
8	0.70	0.40	2.04	6.25	0.09
9	0.80	0.50	1.56	4.00	0.33
10	0.80	0.25	1.56	16.00	0.09
11	0.50	0.25	4.00	16.00	0.50
12	0.70	0.40	2.04	6.25	0.09

3.5.3 Results

The results achieved on application of the scaling theory are presented in this section. The loading for the CT specimen starts with a simple monotonic load (load type 1) where the scaling theory is applied and results examined, then a single loading unloading load case (load type 2) then a constant amplitude cyclic load for 50 cycles (load type 3) with each cycle having a duration of 1s. The values of reaction forces and crack lengths upon application of load type 1 have been presented according to Table 3.11. Also, the reaction force versus displacement has been plotted according to Fig. 3.13 where the error refers to the difference in the area under the curve of the virtual model compared to the full-scale model. It is evident that the response of the full-scale model including the reaction force and crack length has been predicted with zero error using the virtual models.

Table 3.11. Reaction force and crack length values for all virtual models at maximum displacement for load type 1.

	β_1	β_2	a (mm)	Error%	F (kN)	Error%
PS	-	-	6	0	15306.20	-
Virtual Model 1	0.80	0.50	6	0	15309.90	0.02
Virtual Model 2	0.80	0.25	6	0	15307.70	0.01
Virtual Model 3	0.50	0.25	6	0	15297.80	0.03

Virtual Model 4	0.70	0.40	6	0	15300	0.03
-----------------	------	------	---	---	-------	------

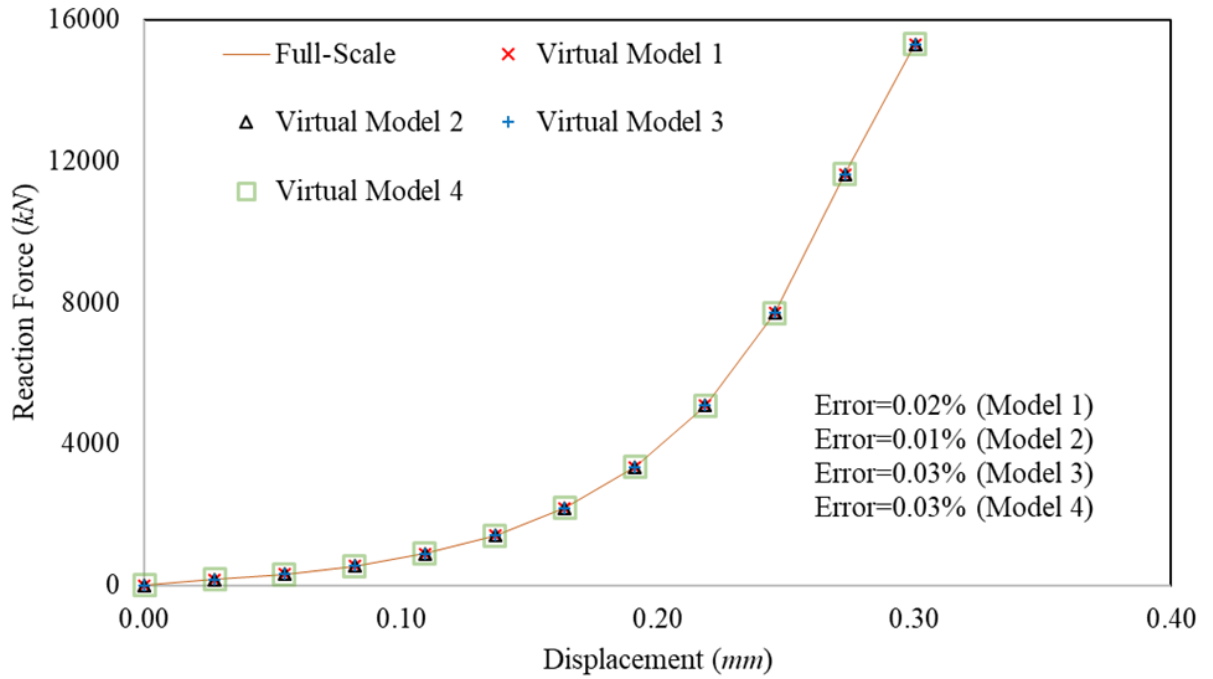


Figure 3.13: Reaction force vs displacement for full-scale and virtual models.

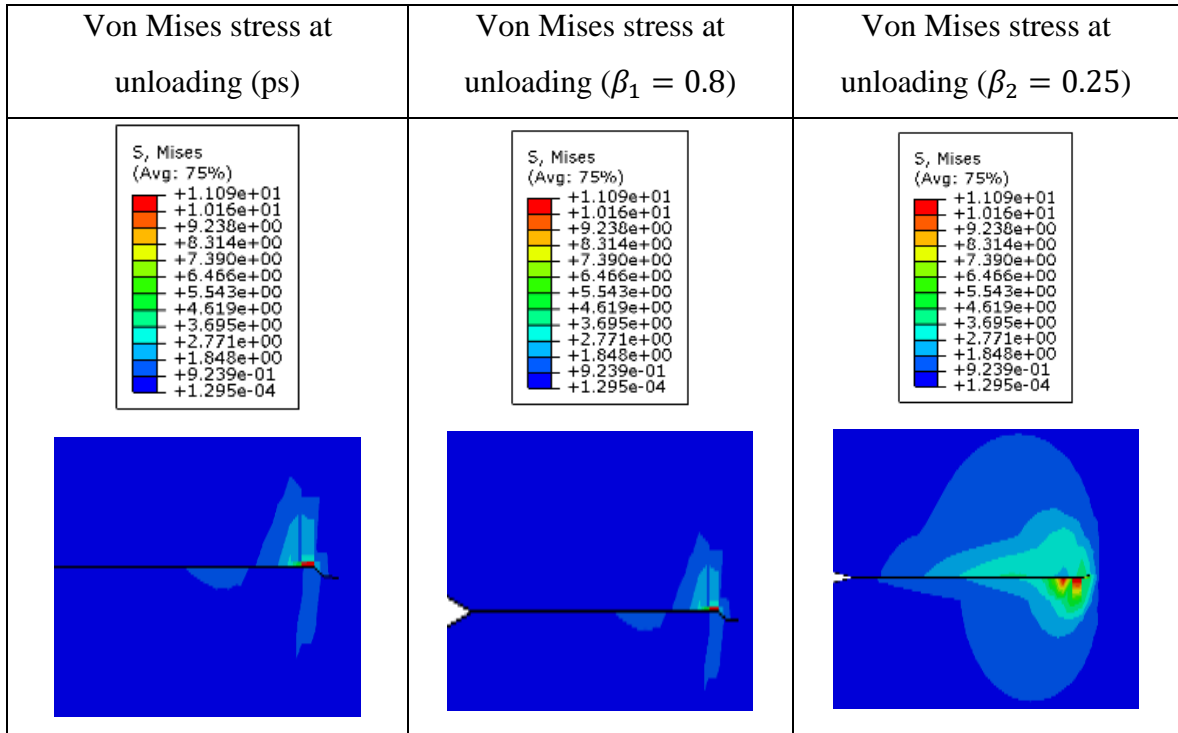


Figure 3.14: Von Mises stress upon unloading for full scale and scaled models at the crack tip for load case 2.

A single loading unloading cycle was then applied to determine if the theory can correctly capture the unloading part of the force curve. To understand the behaviour of the structure due to residual stresses upon unloading, the stress distribution around the crack tip on unloading is shown in Fig. 3.14. The stress states are very similar for the physical space and first scaled model ($\beta_1 = 0.80$). It can be observed however that there is a marked difference in the stress distribution for the second scaled model ($\beta_2 = 0.25$). Fig. 3.14 clearly shows a relatively larger region of residual stresses for the second scaled model. Despite this difference, the reaction force vs time curves for a single loading-unloading cycle as presented in Fig. 3.15 show a perfect match for curves for the virtual and full-scale models. Finally, a monotonic load of 0.30mm and a cyclic load with peak displacement of 1.50mm was then applied for fifty cycles. The stress in the y- direction for all models after 20 cycles are shown in Fig. 3.16. The crack length for the full-scale model at this point is 9 mm.

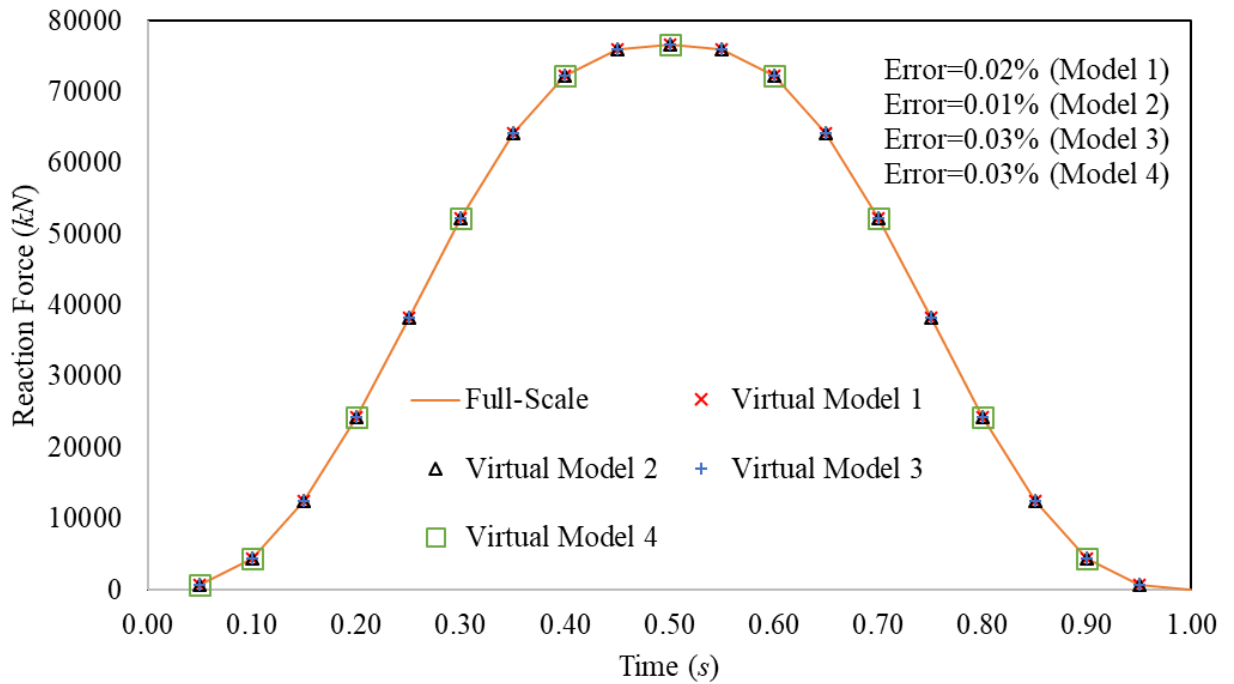
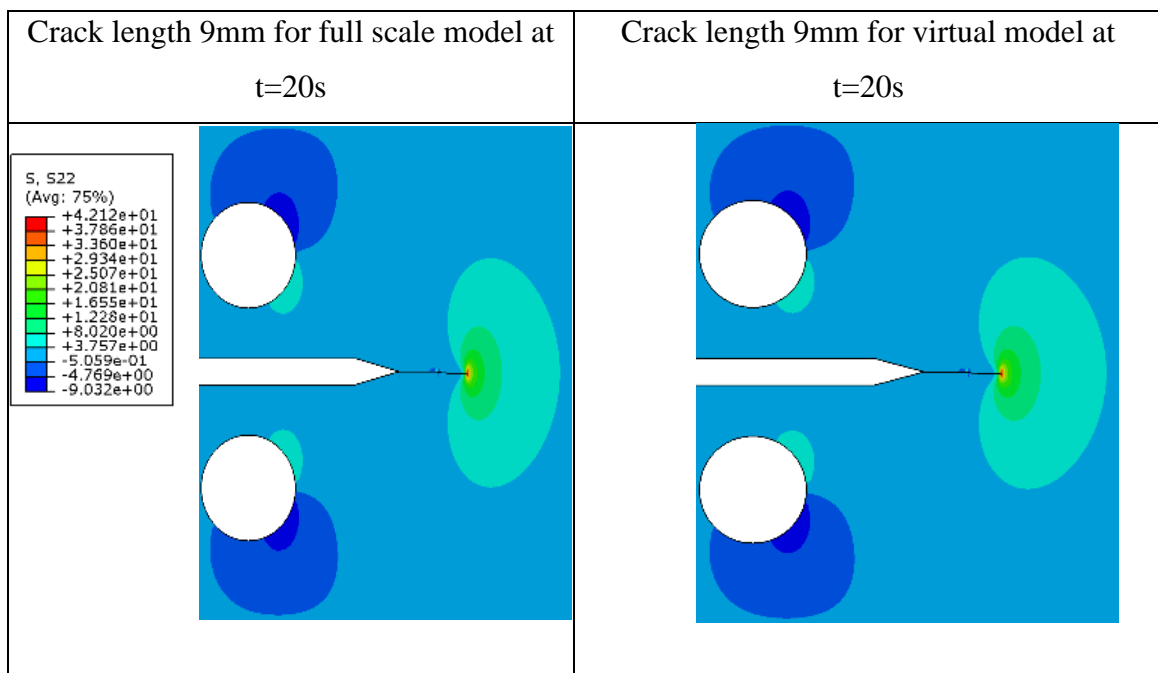


Figure 3.15: Reaction force vs time plot for full scale CT specimen and virtual models for load type 2.

The stress distributions in all scaled models are in good agreement and it is of interest to observe the crack paths during fatigue crack growth of the smaller specimens. All specimens follow the same path as the full-scale model, and consequently information about crack path can be readily gleaned from the scaled model. The crack path for the CT specimen under

load type 3 is plotted in Fig. 3.17, with the virtual model constructed on combining the crack paths of the scaled models, and accordingly perfectly match that of the full-scale model. Fig. 3.18 shows the increase in crack length of the MT specimen with the cyclic load and the associated vertical stress distribution at different points of the loading curve namely after 10, 30 and 48 cycles just before full failure for the full-scale model. Highest stresses are observed at the crack tip with the specimen losing its load bearing capacity as the crack grows. The crack lengths at these points are 10, 20 and 30mm, respectively. After a random number of cycles (33 is chosen), the stresses in the y-direction at the crack tip element are extracted. The stresses are of the same magnitude for all scaled specimens confirming the initial assumption about stress made in the scaling strategy is valid. The traction-separation curve of the crack tip element after 33 cycles is plotted in Fig. 3.19, which is accurately captured by the virtual models. Crack growth information for all the specimens is provided in Fig. 3.20a. Note that the stress intensity factor increases with increasing crack length which follows classical fracture mechanics theory and provides confidence in the Abaqus models. The MT specimen has the highest stress intensity factor after 50 cycles reaching a max value of $370 \text{ MPa}\sqrt{\text{mm}}$ ^{0.5}. This is due to the specimen failing at 48 cycles and thus having the biggest final crack length of all specimens. All virtual models have the same crack extension as the full-scale model thus providing an exact prediction of crack length of the full-scale model for all specimens.



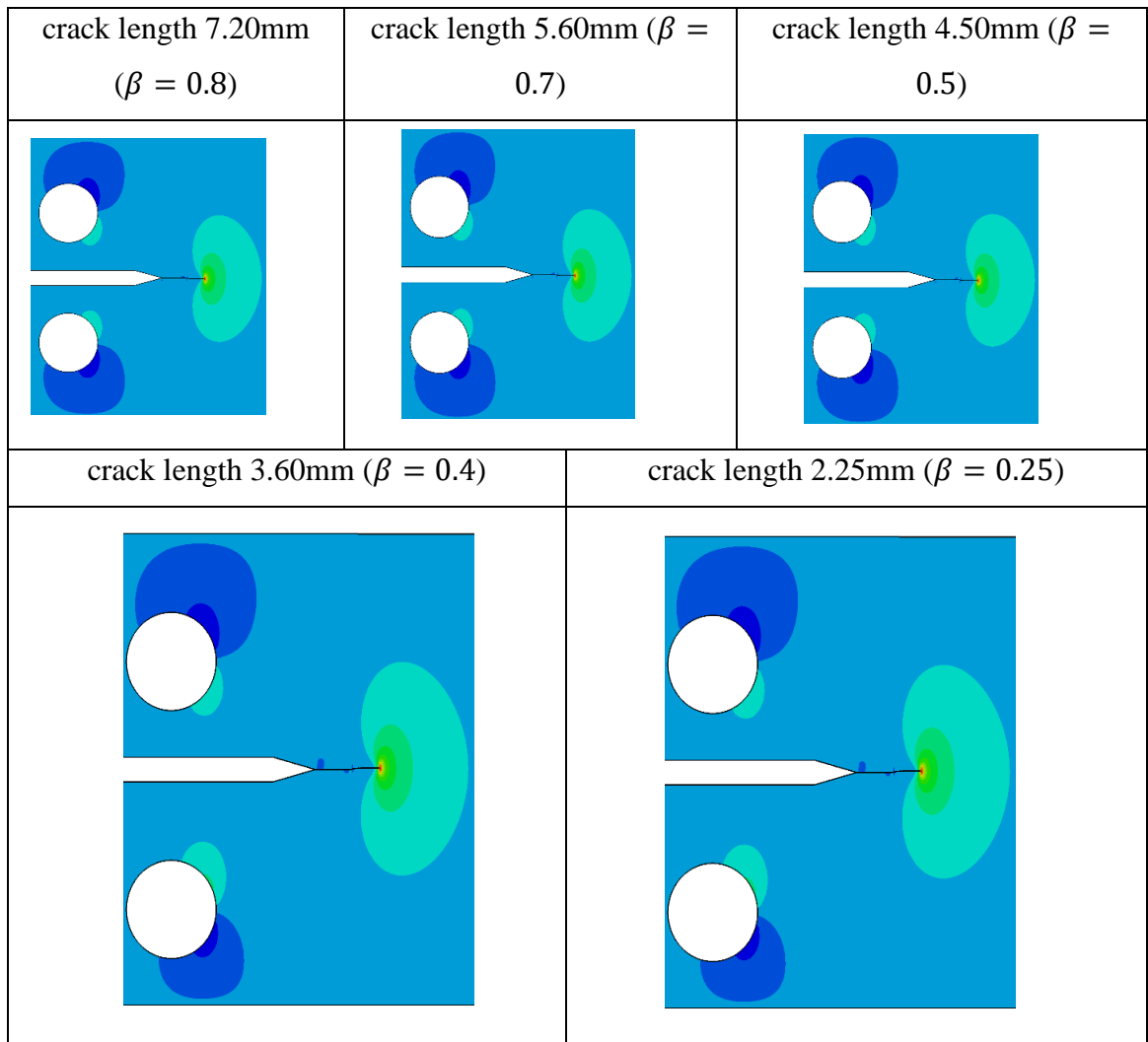


Figure 3.16: Stress in the y direction at $t=20s$ for CT specimen for full scale, virtual and all projected trial space models for load type 3.

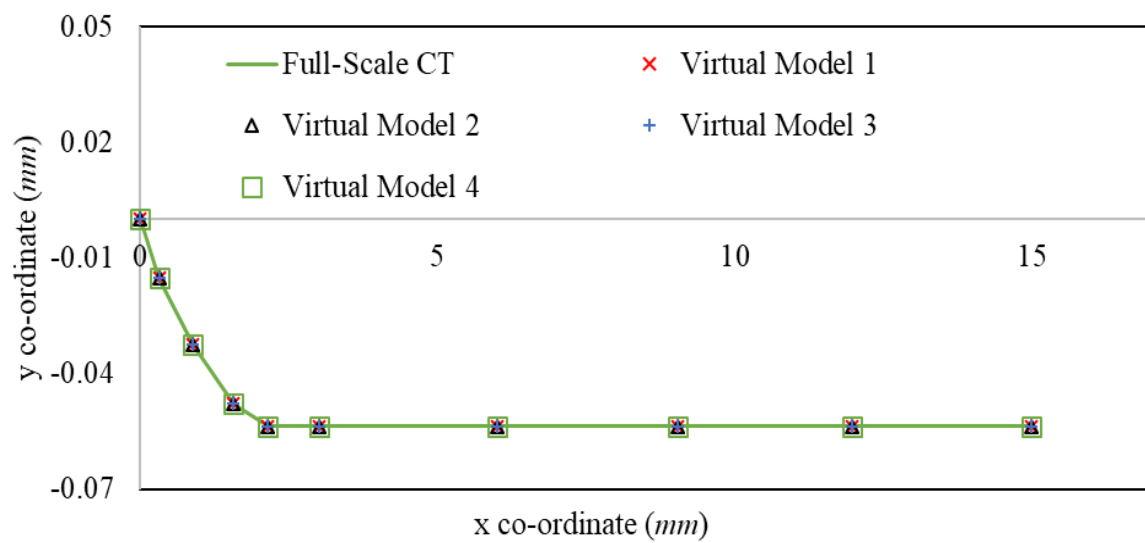


Figure 3.17: Crack path of full-scale CT specimen and virtual models 1-4.

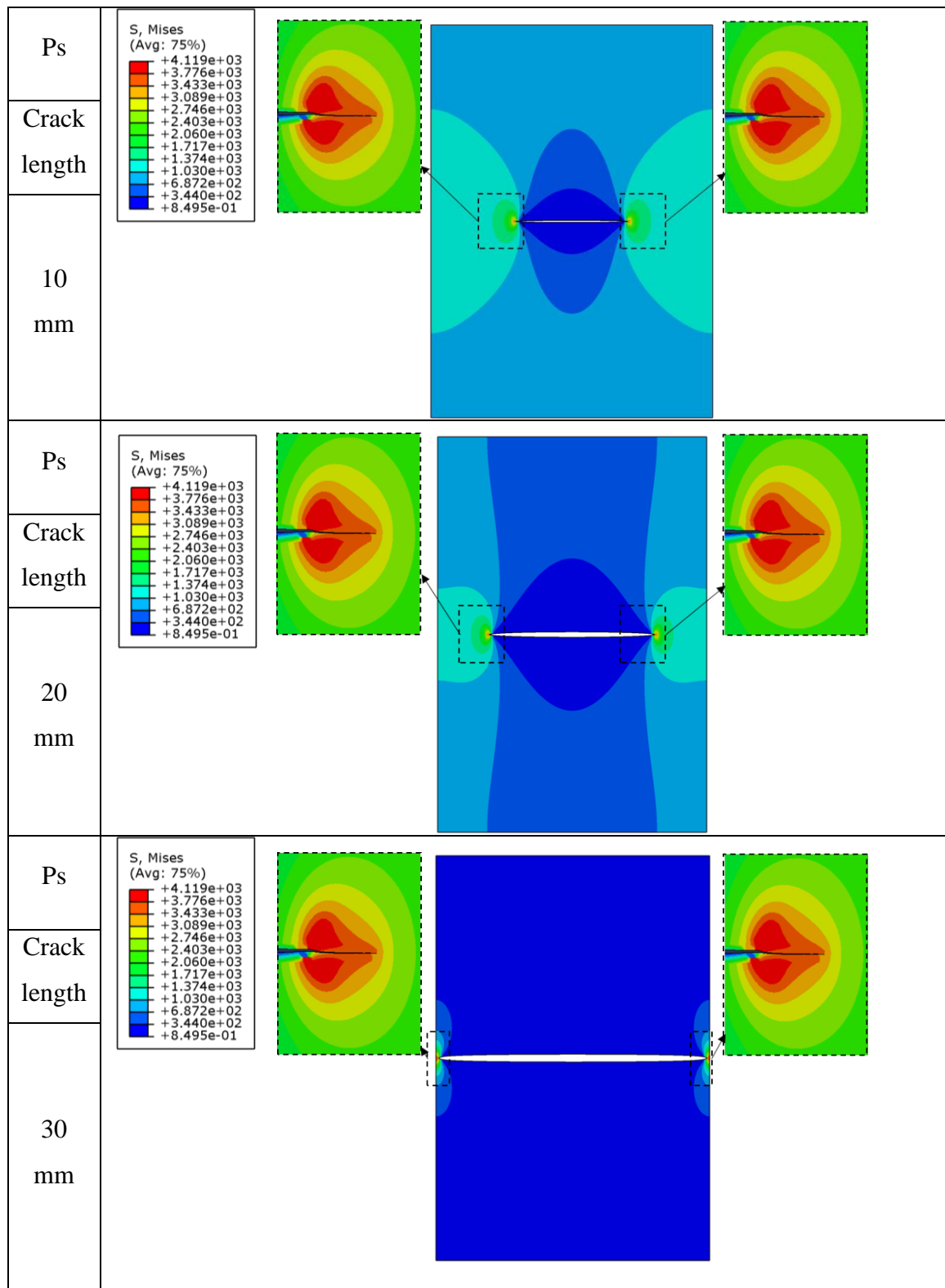


Figure 3.18: Stress in the vertical direction for full scale MT model at different crack lengths.

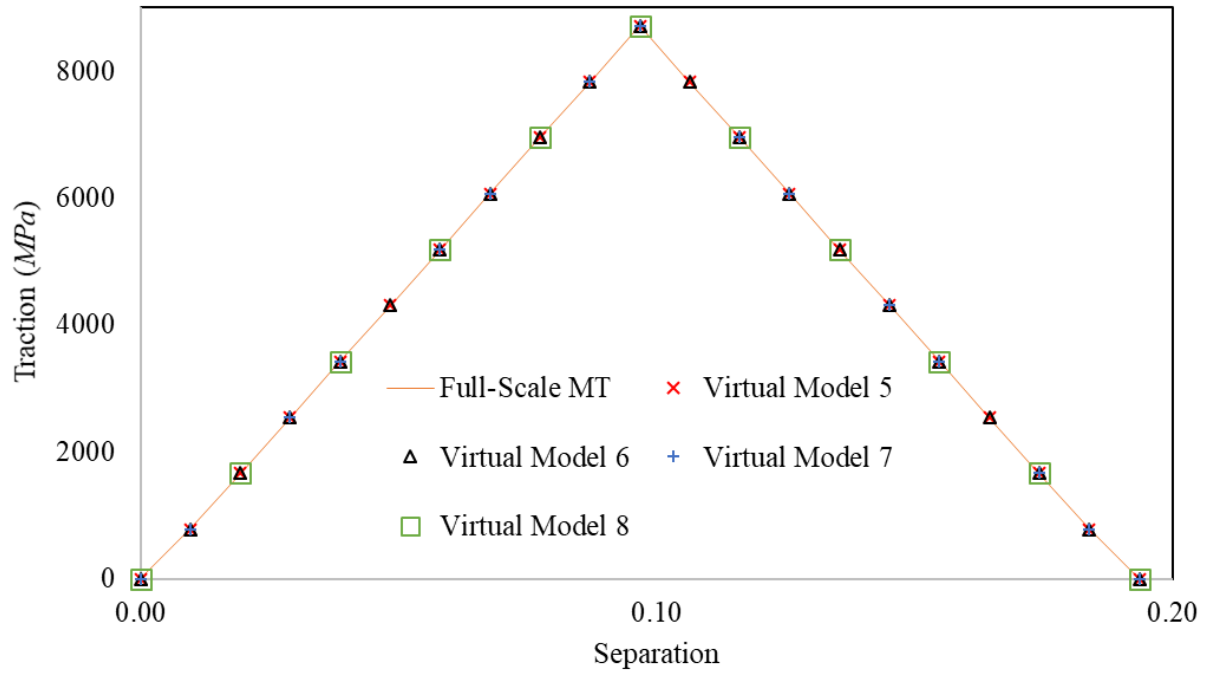
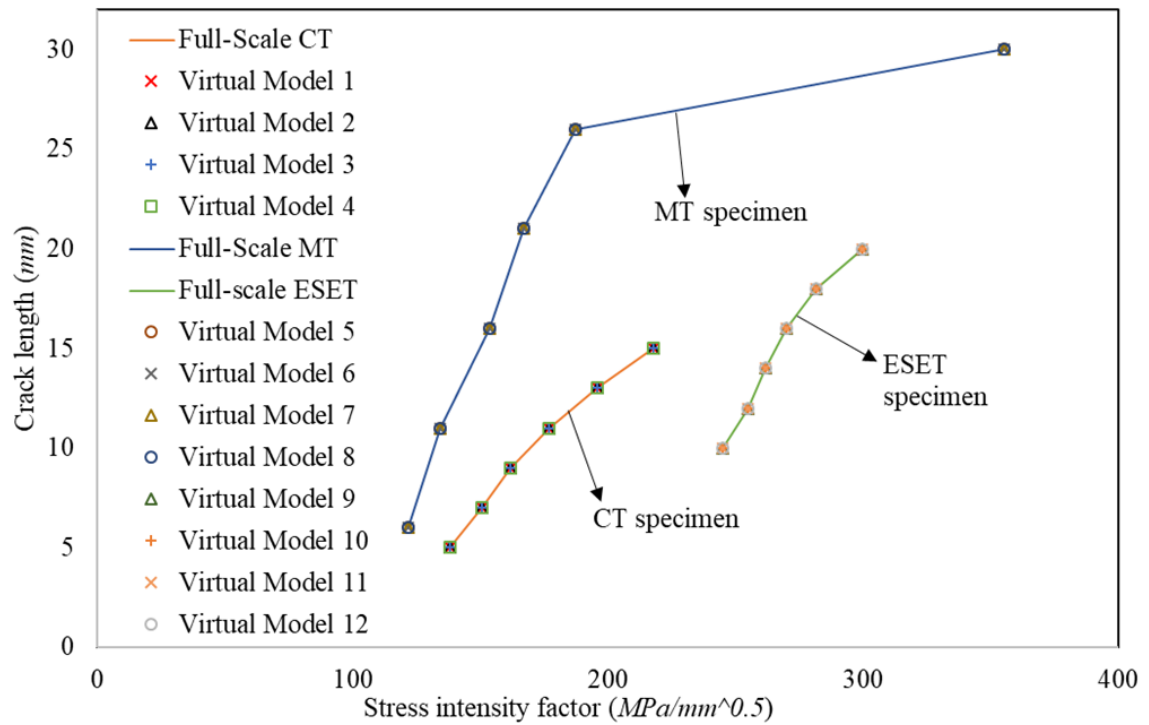
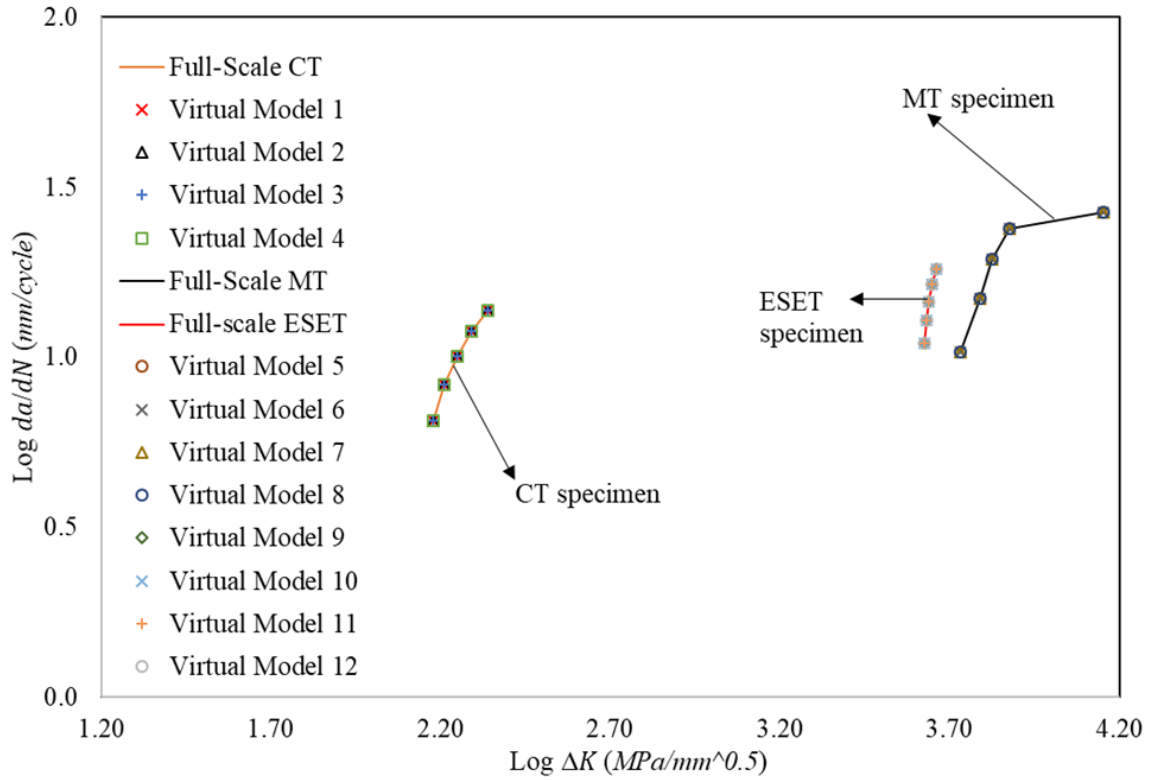


Figure 3.19: Traction-separation curve at the crack tip element at $t=33s$ of MT specimen for the full-scale model and virtual models 5 to 8.



(a) Crack length vs stress intensity factor



(b) Fatigue crack growth rate vs stress intensity factor

Figure 3.20: Fatigue crack growth outputs for full scale models for all specimens and virtual models 1-12.

In the full-scale model, the fatigue pre crack grows from 5mm to 15mm for the CT specimen, 10 mm to 20 mm for the ESET specimen and 6mm to 30 mm for the MT specimen, where it eventually fails after 48 cycles. The theory can also capture number of cycles to failure as seen in virtual models 5 to 8, where all virtual models fail at exactly 48 cycles. It is critical to capture the stress intensity factor, which is the driving force for crack growth. From Fig. 3.20a the stress intensity factor grows at a linear rate between 10 and 50 cycles. This corresponds to the stable crack growth region where Paris law holds. Thus, the evolution of stress intensity factor with time is perfectly captured for all cases. Fig. 3.20b plots the fatigue crack growth rate on a log-log scale as recommended by ASTM E647 standard. Once again, the MT specimen has the fastest FCGR as it has the biggest initial crack while the crack growth rate is the slowest in the CT specimen. The crack growth rate of the full-scale model and that predicted by virtual models for all specimens is the same. Fig. 3.21 shows the Von Mises stress distribution of the ESET specimen for the full-scale model, virtual model and trial models in case 3. The stress distribution is very similar for all models and the crack grows in the same direction (downwards) for all models.

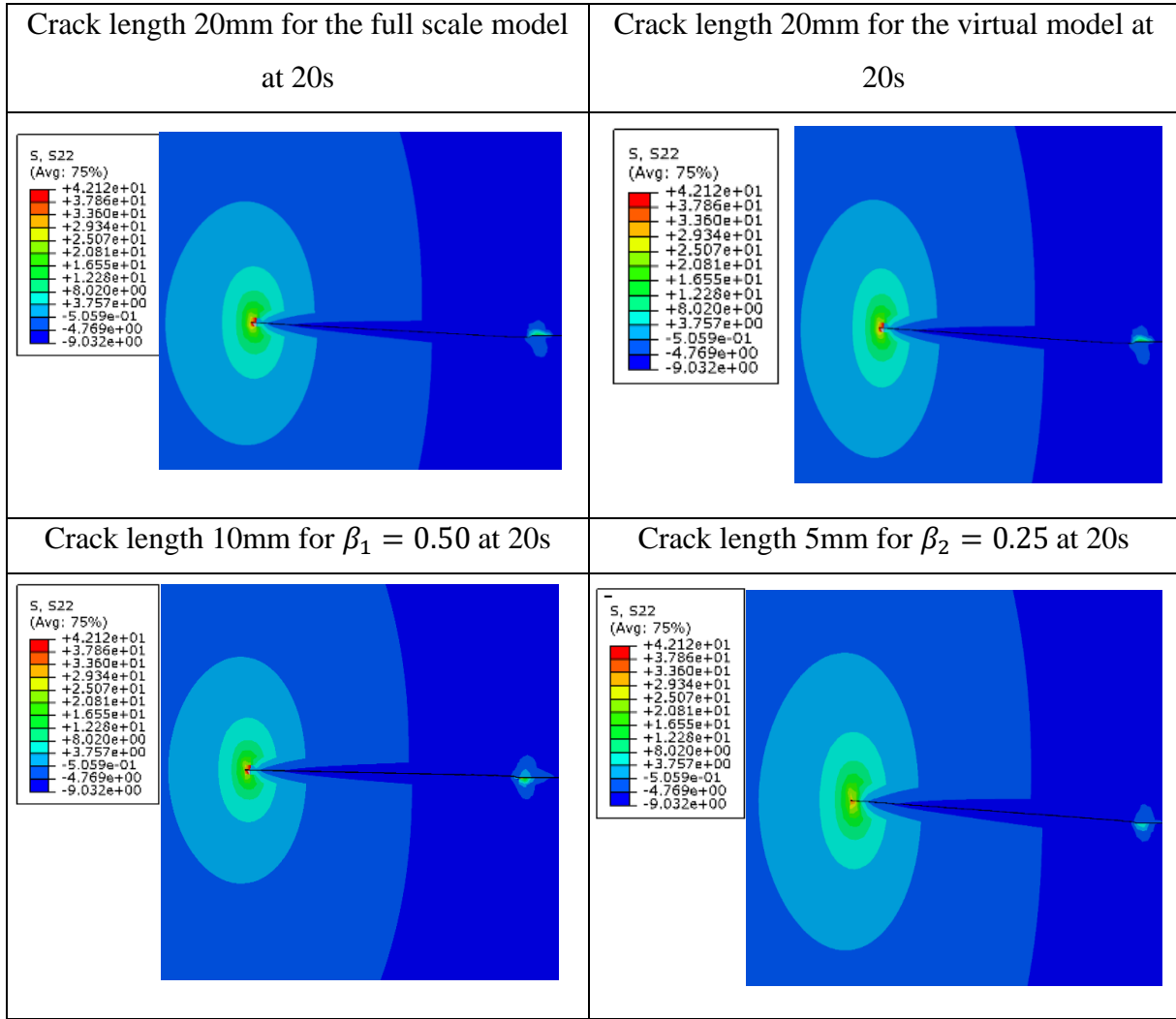


Figure 3.21: Von Mises stress distribution at the crack tip of ESET specimen for the full-scale model and the two scaled models for virtual model 11.

3.6 Conclusions

In this paper an equivalence is established between the first-order finite similitude theory involving two scaled models and a fatigue modelling approach founded on cohesive zone models. The first-order finite similitude theory combines information recorded at two scales to reproduce behaviours at the full scale. Being a similitude approach, it can be anticipated to be approximate in practical applications, unless it could be confirmed that all the conditions pertaining to the rule could be satisfied. It transpires and is confirmed in the paper (both analytically and numerically) that cohesive zone models satisfy all the requirements of the first-order finite similitude rule. The following conclusions were drawn from the analysis and results returned in the paper:

- The first-order finite similitude captures three critical behaviours necessary in representing fracture and fatigue, which are scale invariances for stress and displacement (or separation), and the linear change of displacement with scale (i.e., $\mathbf{u}_{ts} = \beta \mathbf{u}_{ps}$).
- For a range of 1-D cohesive models it has been confirmed how these three critical behaviours were sufficient to provide exact representations at full scale from information gleaned from two scaled models.
- Additionally, for three specimen types conforming to ASTM E647 (i.e., CT, MT and ESET specimens) analysed numerically by means of XFEM cohesive segments method in Abaqus, that full-scale fatigue crack growth could be matched exactly (within numerical error) by two scaled models for the selection of scales considered.
- The first-order finite similitude rules have been confirmed to be: (i) accurate for low-cycle fatigue only, indicating that high-cycle fatigue studies are required; (ii) applicable within the confines of a continuum-mechanics framework, indicating practical limitations on the size of the smallest scaled models; and (iii) able to replicate behaviours modelled by cohesive zone models, indicating that further studies are required to ascertain the true practical value of the approach.

Chapter 4 Scaled Empirical Fatigue Laws

4.1. Introduction

Fatigue is the phenomenon whereby a structure, experiencing subcritical cyclic load, deteriorates in loading capacity and ultimately fails [3]. It is estimated that 90% of all component failures during service life is attributable to fatigue, making it critically important in design considerations [1]. A particularly important consideration is *fatigue life*, which is typically determined using one of two approaches. These are namely cumulative fatigue damage (CFD) and fatigue crack propagation (FCP) [182]. The FCP approach is underpinned by the theory of fracture mechanics and highlights other aspects of importance for structural integrity monitoring purposes, which includes the rate at which a crack propagates after initiation and the path taken. Fatigue life is the number of cycles to failure, n it takes to grow a defect with an initial size, a to a critical defect size, a_f . Damage tolerant design for fatigue involves making fatigue life predictions of new components and structures using the FCP approach [183]. To calculate the number of cycles to failure, a suitable fatigue empirical law must be used. An important example of the many laws available is that proposed by Paris and Erdogan, which provides a relationship between the crack growth rate (i.e., da/dn) and the elastic stress intensity factor range (i.e., ΔK) [28]. The graph of da/dn vs ΔK is typically plotted on a log-log scale and three regimes are readily identifiable. Limitations apply to empirical relationships and in the case of Paris law its validity is limited to long cracks in region II and where small-scale yielding is a feature (linear elastic fracture mechanics; LEFM). To extend the scope of Paris law, various modifications have been proposed to account for all manner of influences on fatigue life [3].

An aspect that has been largely neglected in damage tolerant design is the use of scaled experiments. Its neglect is understandable since there exist difficulties in relating data across scaled experiments due to well-known size effects that feature in fracture mechanics and fatigue. Geometric size effects are those observed changes in behaviour for structures, processes, and systems that manifest with a change of scale. These effects make it difficult to use scaled experiments to predict the behaviour of full-scale structures, processes, and systems. It is widely accepted that size effects feature in fracture mechanics and in Paris law [124]. Most size-effect fatigue studies in literature typically focus on fatigue modelling by means of the CFD approach [23,126] thus involving the crack initiation mechanism, which is not the focus of the current study. The focus here is on geometric-size effects observed in specimens containing an initial crack or notch. The aim of this work is to reconcile the

observed differences in fatigue life of propagating cracks with scale within the linear elastic fracture mechanics framework.

A comprehensive review of size effects in fatigue can be found in ref [125]. Bazant's work on the fatigue of concrete [14] was the first experimental attempt to demonstrate the size effect in fatigue. Since then, multiple studies have confirmed the existence of size effects in fatigue within the fracture mechanics approach (see [184-187]). Barenblatt and Botvina confirmed that unless the Paris law exponent (usually denoted by the symbol, m) is identically equal to 2 it is impossible to achieve complete *self-similarity* [83]. The concept of complete *self-similarity* means a process reproduces itself exactly at all sizes. Experimental data for many materials confirm that m is rarely equal to 2 leading to the conclusion that the parameters C and m in Paris law are not material constants. Thus, extrapolation of fatigue crack growth data from smaller specimens to inform the design of larger structures is erroneous as the crack growth rate changes with scale. Typically, very large safety factors are used in industrial settings to mitigate this. There have been several attempts to deal with the size effect in fatigue with the proposition of a "universal" scaling law [134]. Most of the techniques, are founded on dimensional analysis and more recently fractal geometry concepts. Bazant and Xu expressed the change in crack length per cycle as a power function of the amplitude of a size-adjusted stress intensity factor [14]. Carpinteri proposed a fractal approach to deal with the dependence of the Paris law exponent on initial crack length [156]. However, it is important to appreciate that Paris law should not be expected to satisfy the similitude invariance provided by dimensional analysis. It is shown in this work how n is scaled and that reasonable results can be returned for an invariant (with scale) value of m in Paris law.

The FCP modelling approach is the focus, where both low and high cycle fatigue cases are considered with the application of a new scaling approach termed *finite similitude*, and where for the first-time, empirical fatigue relationships are considered. The finite similitude theory, which was first introduced in [26], introduces new similitude rules (a countable infinite number) with each rule connecting information across a specific number of scaled experiments. The similitude rule that is critical to fracture mechanics is called *first-order finite similitude* and involves two scaled experiments. The work in reference [26] applies to a single scaled experiment only and the approach is now termed *zeroth-order finite similitude*, which has been shown to be equivalent to dimensional analysis. The first order theory has now been applied to wide range of areas [153,158,188-189] including more recently to low cycle fatigue [190] and is extended here to empirical fatigue laws, which is

achieved with the introduction of a new scaling space Ω_β . The theory was shown to capture the behaviour at the crack tip as described by the cohesive zone model for monotonic [189] and cyclic loads [190]. Exact predictions for the analytical expression for the stress intensity factor of a compact tension specimen under fatigue load was achieved using two scaled models in ref. [190]. The aim here is to further test the predictive capabilities of the first order theory with regards to predicting the fatigue life of different specimens using two small-scaled models.

LEFM states that fatigue behaviour of a structure is controlled predominantly by behaviour around the crack tip. For quasibrittle materials however, the geometric size effect has been attributed to the presence of a fracture process zone (FPZ) of significant size around the crack tip [14]. Material damage in the FPZ has been modelled successfully using the cohesive zone model by other authors [31,191]. The hypothesis here is if the stresses at the crack tip and subsequently stress intensity factor can be captured using two scaled experiments then it should be possible to subsequently predict fatigue life of the large structure. A recap of the finite-similitude theory is presented in Section 4.2, where the new scaling space is introduced. Although integral forms of the governing equations are used in the similitude theory the introduction of Ω_β is shown to provide a route to consider alternative types of equation. The transport equations pertinent to solid mechanics, fatigue and fracture are examined in greater detail in Section 4.3. Additionally, by means of the space Ω_β , empirical fatigue relationships used in a damage tolerant design approach can be scaled, with a particular focus on Paris law in this work. An explicit expression relating the number of cycles to failure and scale is derived, which is the principal objective of the work. In Section 4.4 the new theory is contrasted with experimental work published in the open literature. It should be appreciated that it is only with the advent of the finite similitude theory that the rules for scaling two experiments are now known. Despite this limitation good agreement is achieved with the experimental data. Numerical case studies are considered in Section 4.5 involving different types of cracks, low and high cycle fatigue and excellent predictions for fatigue life is achieved. The paper finishes with a conclusions section.

4.2. A Brief Recap on Finite Similitude

The theory of finite similitude theory and its application can be found in the open literature [159-165] and first appeared in 2017 [26]. It is useful however to briefly recap the basic concepts since a new feature is required to facilitate the definition of scalable differential

equations for fatigue analysis. A peculiarity of the finite-similitude approach is that it is based on a metaphysical concept that cannot be enacted, which is space scaling, where for the purpose of scaled experimentation, space is contracted or expanded. There is no practical means to do this, physically nor is it required but what can be achieved is an assessment of the impact space scaling has on the physics constraining the fatigue behaviour of a component undergoing cyclic loading.

4.2.1. The effects of space scaling

Space scaling is characterised by a linear map $\mathbf{x}_{ps} \mapsto \mathbf{x}_{ts}$ between the physical and trial space inertial coordinate systems. The full-scale equipment resides in the physical space and a scaled version resides in the trial space. In differential terms the map takes the form $d\mathbf{x}_{ts} = \beta d\mathbf{x}_{ps}$, where β is a continuous parameter that dictates the extent of the scaling involved. Space scaling is isotropic for orthonormal inertial coordinate frames in the two spaces. The parameter β is positive, and space is contracted for $0 < \beta < 1$, with no space scaling taking place for $\beta = 1$ and expansion for $\beta > 1$. The focus on Newtonian physics means that a single measure of time is applied to each space, i.e., t_{ts} and t_{ps} , which are assumed related by the differential identity $dt_{ts} = g dt_{ps}$, where g is positive scalar, which is taken to be a continuous function of β . To capture the impact of space scaling on the governing physics the finite similitude approach makes use of control volumes (being mere regions of space) since these reflect the immediacy of any change taking place. Although control-volume approaches hardly feature in fatigue analysis this is nonetheless the route necessary to engage global physical laws in transport form prior to examining point-based formulations. A control-volume can be of any size and made arbitrarily small to capture localised effects but also provides the means to target and analyse any spatial region of peculiar interest. The movement of a control volume Ω_{ts}^* (in the trial space) is describable by a smooth velocity field \mathbf{v}_{ts}^* with coordinate points transported by the differential equation $d\mathbf{x}_{ts}^* = \mathbf{v}_{ts}^* dt_{ts}$. The closure for Ω_{ts}^* (which is an open domain) in the space Ω_{ts} contains the orientable boundary Γ_{ts}^* with outward pointing unit normal \mathbf{n}_{ts} . Two spaces (i.e., physical Ω_{ps} and trial Ω_{ts}) are of interest to scaling but introduced here is a third space Ω_{β} that sits between these two spaces but is closely related to each. The reason for the creation of an additional space (as will be revealed) is to draw a clear distinction between phenomena that similitude identities

describe in Ω_{ps} and phenomena that takes place. In addition, Ω_β is the space on which scalable differential equations are to be defined, which is of particular interest in this work.

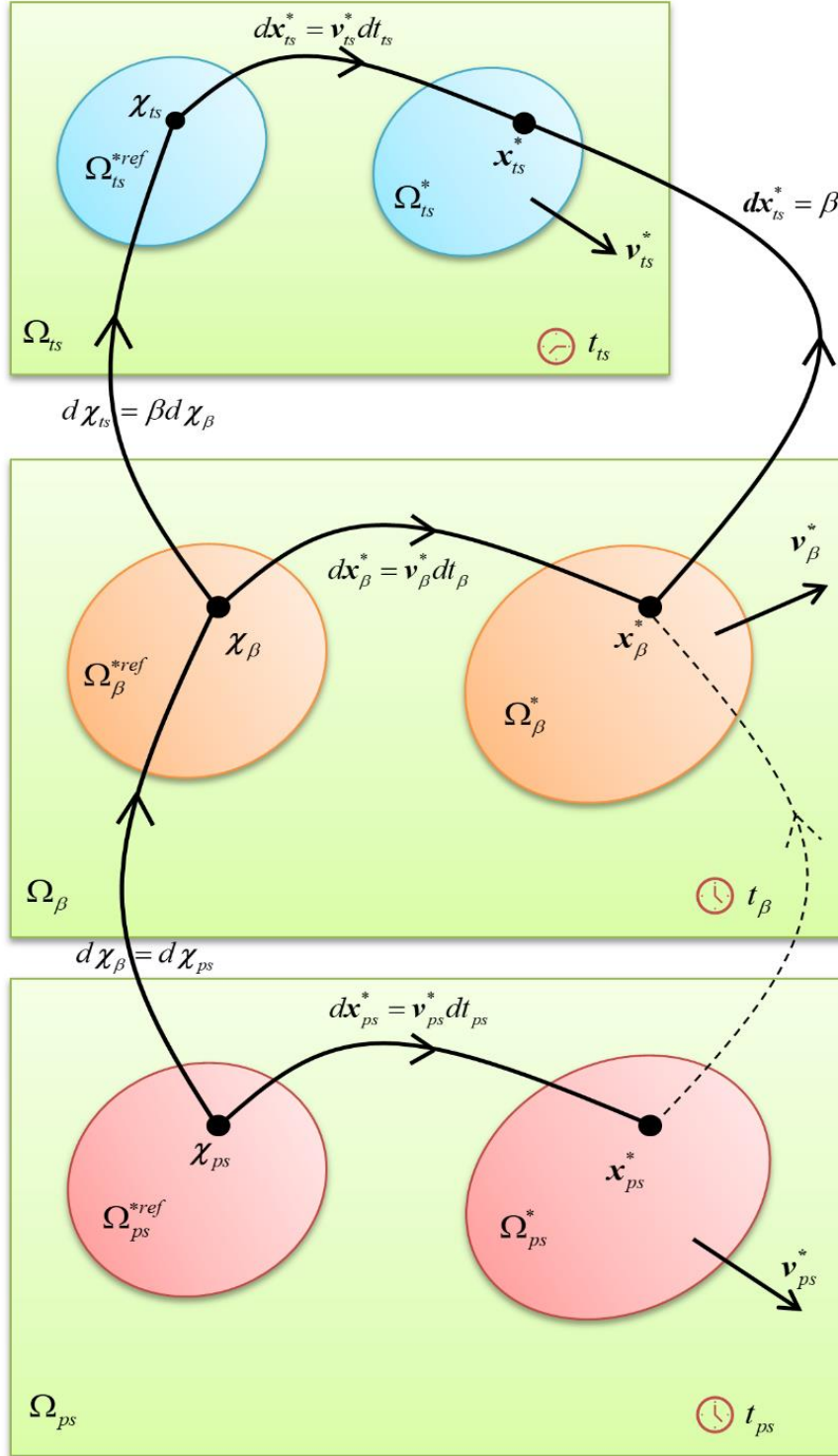


Figure 4.1. The interrelationship between the reference and moving control volumes in the trial and physical spaces and the space Ω_β .

It is further assumed that Ω_β^* is a control volume transported in Ω_β by velocity field \mathbf{v}_β^* with coordinate point movement satisfying $d\mathbf{x}_\beta^* = \mathbf{v}_\beta^* dt_\beta$, where $\mathbf{v}_\beta^* = g\beta^{-1}\mathbf{v}_{ts}^*$ and $dt_\beta = g^{-1}dt_{ts}$ (which makes $dt_\beta = dt_{ps}$). Substitution of these latter two identities into $d\mathbf{x}_\beta^* = \mathbf{v}_\beta^* dt_\beta$ provides $d\mathbf{x}_\beta^* = \beta^{-1}\mathbf{v}_{ts}^* dt_{ts} = \beta^{-1}d\mathbf{x}_{ts}^*$ or identically $d\mathbf{x}_{ts}^* = \beta d\mathbf{x}_\beta^*$, which can be contrasted against the space scaling map $d\mathbf{x}_{ts} = \beta d\mathbf{x}_{ps}$. Thus, geometric measures of the control volumes Ω_β^* and Ω_{ts}^* can be readily related, i.e., $dV_\beta^* = \beta^{-3}dV_{ts}^*$ and $d\Gamma_\beta^* = \beta^{-2}d\Gamma_{ts}^*$. The interconnections between the various spaces and control volumes are depicted in Fig. 4.1, where the motion of Ω_β^* and Ω_{ts}^* is synchronised. Note that the motion of the moving control volumes are defined relative to fixed control volumes, which provides for example the identity $\mathbf{v}_\beta^* = D^*\mathbf{x}_\beta^*/D^*t_\beta^*$, where the temporal derivative $D^*/D^*t_\beta^*$ is a partial derivative that holds constant points in the reference control volume Ω_β^{*ref} , i.e. $D^*/D^*t_\beta^* \equiv \partial/\partial t_\beta^*|_{\chi_\beta}$, where $\chi_\beta \in \Omega_\beta^{*ref}$, and similarly for the other spaces.

Observe from Fig. 4.1 that there presently exists no defined relationship between the moving control volumes Ω_β^* and Ω_{ps}^* . A feature of the finite similitude approach is that it ultimately establishes similitude relationships between fields in Ω_{ps}^* and Ω_{ts}^* and consequently this relationship should fall out as part of that process. This involves establishing a connectivity between the velocity fields \mathbf{v}_β^* and \mathbf{v}_{ps}^* . Note additionally that the relationships between the fixed reference control volumes are completely determined by the scaling of the space that they reside in. The generality of the finite similitude approach underpins its ability to tackle all classical physics and all forms of analysis, be it Eulerian, Lagrangian or arbitrary-Eulerian-Lagrangian. To proceed further requires the physics under scrutiny to be presented in transport equation form.

4.2.2. The projection of transport equations

A critical component of the finite-similitude theory is the projection of the governing trial-space physics represented by transport equations onto the space Ω_β^* . It is through this projection that scale dependencies are revealed in an implicit form for all the fields involved. The subsequent application of similitude rules connects Ω_β^* to Ω_{ps}^* and reveals the similitude identities connecting scaled experiments and makes explicit the relationships between the fields and β . It is reasonable to claim that in their integral form transport equations have been somewhat neglected principally because of the relative advantages offered by

alternative approaches (see [160]). In solid mechanics, niche applications of the control-volume approach include configurational forces in fracture and shock models for impact but otherwise their application is not universal. A transport equation in its most generic form [159] in the trial space is:

$$\begin{aligned} \frac{D^*}{D^* t_{ts}} \int_{\Omega_{ts}^*} \rho_{ts} \boldsymbol{\Psi}_{ts} dV_{ts}^* + \int_{\Gamma_{ts}^*} \rho_{ts} \boldsymbol{\Psi}_{ts} (\mathbf{v}_{ts} - \mathbf{v}_{ts}^*) \cdot \mathbf{n}_{ts} d\Gamma_{ts}^* \\ = - \int_{\Gamma_{ts}^*} \mathbf{J}_{ts}^\Psi \cdot \mathbf{n}_{ts} d\Gamma_{ts}^* + \int_{\Omega_{ts}^*} \rho_{ts} \mathbf{b}_{ts}^\Psi dV_{ts}^* \end{aligned} \quad (4.1)$$

where ρ_{ts} , $\boldsymbol{\Psi}_{ts}$, \mathbf{v}_{ts} , \mathbf{J}_{ts}^Ψ , \mathbf{b}_{ts}^Ψ , \mathbf{n}_{ts} are density, physical field, velocity, boundary flux, a source term and the unit normal to boundary Γ_{ts}^* of the control volume Ω_{ts}^* .

Substitution of the measure identities $dV_\beta^* = \beta^{-3} dV_{ts}^*$ and $d\Gamma_\beta^* = \beta^{-2} d\Gamma_{ts}^*$, and the temporal relationship $dt_\beta = g^{-1} dt_{ts}$, along with multiplication by g and the scalar α_0^Ψ returns,

$$\begin{aligned} \alpha_0^\Psi T_0^\Psi(\beta) &= \frac{D^*}{D^* t_\beta} \int_{\Omega_\beta^*} \alpha_0^\Psi \rho_{ts} \beta^3 \boldsymbol{\Psi}_{ts} dV_\beta^* \\ &+ \int_{\Gamma_\beta^*} \alpha_0^\Psi \rho_{ts} \beta^3 \boldsymbol{\Psi}_{ts} (\beta^{-1} g \mathbf{v}_{ts} - \beta^{-1} g \mathbf{v}_{ts}^*) \cdot \mathbf{n}_\beta d\Gamma_\beta^* \\ &+ \int_{\Gamma_\beta^*} \alpha_0^\Psi \beta^2 g \mathbf{J}_{ts}^\Psi \cdot \mathbf{n}_\beta d\Gamma_\beta^* - \int_{\Omega_\beta^*} \alpha_0^\Psi \rho_{ts} \beta^3 g \mathbf{b}_{ts}^\Psi dV_\beta^* = 0 \end{aligned} \quad (4.2)$$

which is a critically important equation in the finite similitude theory and is essentially Eq. (4.1) but projected onto the space Ω_β .

The scalar functions α_0^Ψ and g are assumed functions of β and it useful to present Eq. (4.2) in the form

$$\begin{aligned} \alpha_0^\Psi T_0^\Psi(\beta) &= \frac{D^*}{D^* t_\beta} \int_{\Omega_\beta^*} \rho_\beta \boldsymbol{\Psi}_\beta dV_\beta^* + \int_{\Gamma_\beta^*} \rho_\beta \boldsymbol{\Psi}_\beta (\mathbf{v}_\beta - \mathbf{v}_\beta^*) \cdot \mathbf{n}_\beta d\Gamma_\beta^* + \int_{\Gamma_\beta^*} \mathbf{J}_\beta^\Psi \cdot \mathbf{n}_\beta d\Gamma_\beta^* \\ &- \int_{\Omega_\beta^*} \rho_\beta \mathbf{b}_\beta^\Psi dV_\beta^* = 0 \end{aligned} \quad (4.3)$$

where $\rho_\beta \boldsymbol{\Psi}_\beta = \alpha_0^\Psi \rho_{ts} \beta^3 \boldsymbol{\Psi}_{ts}$, $\mathbf{v}_\beta = \beta^{-1} g \mathbf{v}_{ts}$, $\mathbf{v}_\beta^* = \beta^{-1} g \mathbf{v}_{ts}^*$, $\mathbf{J}_\beta^\Psi = \alpha_0^\Psi \beta^2 g \mathbf{J}_{ts}^\Psi$ and $\rho_\beta \mathbf{b}_\beta^\Psi = \alpha_0^\Psi \rho_{ts} \beta^3 g \mathbf{b}_{ts}^\Psi$.

It is evident that Eq. (4.3) is identical in form to Eq. (4.1) and consequently can be viewed as a transport equation on Ω_β^* . A necessary requirement is for this equation to match the

physical space transport equation at $\beta = \beta_0 = 1$, which is ensured by $\rho_1 \Psi_1 = \rho_{ps} \Psi_{ps}$, $\mathbf{v}_1 = \mathbf{v}_{ps}$, $\mathbf{v}_1^* = \mathbf{v}_{ps}^*$, $\mathbf{J}_1^\Psi = \mathbf{J}_{ps}^\Psi$ and $\rho_1 \mathbf{b}_1^\Psi = \rho_{ps} \mathbf{b}_{ps}^\Psi$, and additionally $\alpha_0^\Psi(1) = 1$ and $g(1) = 1$. This set of conditions indicates what is required with similitude rules describing the fields at $\beta = \beta_0 = 1$ in order to represent behaviours in the physical space. Note additionally that all fields are implicitly defined to be functions of β as suggested by the notation, i.e., $\rho_\beta, \mathbf{v}_\beta, \Psi_\beta, \mathbf{J}_\beta^\Psi$ and \mathbf{b}_β^Ψ . It is important to appreciate that Eq. (4.3) (of the form $\alpha_0^\Psi T_0^\Psi(\beta) = 0$) suffers no approximation and provides an exact description of trial-space behaviours but projected onto Ω_β . All β – dependencies of the fields involved are implicitly exposed by this projection, making the scaling problem one, where the objective is to reveal these hidden dependencies. The significant advantage of this formulation is that unlike dimensional analysis it is not limited to a single invariance.

4.2.3. Defining similitude rules

The projection of trial-space physics onto the space Ω_β provides a representation of scaling that is continuous and smooth and as a result gives rise to a calculus for scaled experimentation. Although discrete identities are sought to link experiments at distinct scales the existence of a calculus for scaling provides scope for analysis and the involvement of differential equations and identities. The starting point of finite similitude is the recursive definition (previously introduced in ref. [26]).

Definition (High-order finite similitude)

The concept of k^{th} -order finite similitude is identified by the lowest derivative that satisfies,

$$T_{k+1}^\Psi = \frac{d}{d\beta}(\alpha_k^\Psi T_k^\Psi) \equiv 0 \quad (4.4)$$

$\forall \beta > 0$, with $\alpha_0^\Psi T_0^\Psi$ defined by Eq. (3) and scalars α_k^Ψ are functions of β with $\alpha_k^\Psi(1) = 1$, where the symbol “ \equiv ” in Eq. (4.4) signifies that the derivative is identically zero.

The simplest invariance (equivalent to dimensional analysis) is obtained on setting $k = 0$ (which is $T_1^\Psi \equiv 0$) is the identity:

$$\frac{d}{d\beta}(\alpha_0^\Psi T_0^\Psi) \equiv 0 \quad (4.5)$$

which infers that the transport equation $\alpha_0^\Psi T_0^\Psi = 0$ is absent of β – terms on Ω_β and therefore suffers no scale effects as traditionally defined.

Observe the role of α_0^Ψ , being selected is to eliminate if possible β – terms to satisfy Eq. (4.5). Systems that conform to Eq. (4.5) are called *zeroth order*, and give rise to the following relationships between the physical space at $\beta = 1$ and the trial space at β_1 :

$$\rho_{ps}\Psi_{ps} = \rho_1\Psi_1 = \rho_{\beta_1}\Psi_{\beta_1} = \alpha_{01}^\Psi\beta_1^3\rho_{ts1}\Psi_{ts1} \quad (4.6a)$$

$$\mathbf{v}_{ps} = \mathbf{v}_1 = \mathbf{v}_{\beta_1} = g_1\beta_1^{-1}\mathbf{v}_{ts1} \quad (4.6b)$$

$$\mathbf{J}_{ps}^\Psi = \mathbf{J}_1^\Psi = \mathbf{J}_{\beta_1}^\Psi = \alpha_{01}^\Psi g_1 \beta_1^2 \mathbf{J}_{ts1}^\Psi \quad (4.6c)$$

$$\rho_{ps}\mathbf{b}_{ps}^\Psi = \rho_1\mathbf{b}_1^\Psi = \rho_{\beta_1}\mathbf{b}_{\beta_1}^\Psi = \alpha_{01}^\Psi g_1 \beta_1^3 \rho_{ts1}\mathbf{b}_{ts1}^\Psi \quad (4.6d)$$

where the identity $\mathbf{v}_{ps}^* = \mathbf{v}_1^* = \mathbf{v}_{\beta_1}^* = g_1\beta_1^{-1}\mathbf{v}_{ts1}^*$ is assumed to apply (more on this below) to arrive at Eq. (4.6b), and where the following subscript notation is applied: $g_1 = g(\beta_1)$, $\alpha_{01}^\Psi = \alpha_0^\Psi(\beta_1)$, $\rho_{ts1} = \rho_{ts}(\beta_1)$, $\Psi_{ts1} = \Psi_{ts}(\beta_1)$, $\mathbf{v}_{ts1} = \mathbf{v}_{ts}(\beta_1)$, $\mathbf{J}_{ts1}^\Psi = \mathbf{J}_{ts}^\Psi(\beta_1)$ and $\mathbf{b}_{ts1}^\Psi = \mathbf{b}_{ts}^\Psi(\beta_1)$.

The identities in Eq. (4.6) are returned on integration of Eq. (4.5) between the limits β_1 and $\beta_0 = 1$. Similarly, *first-order finite similitude* requires setting $k = 1$ (i.e., $T_2^\Psi \equiv 0$) in the definition above to reveal the identity

$$T_2^\Psi = \frac{d}{d\beta}(\alpha_1^\Psi T_1^\Psi) = \frac{d}{d\beta}\left(\alpha_1^\Psi \frac{d}{d\beta}(\alpha_0^\Psi T_0^\Psi)\right) \equiv 0 \quad (4.7)$$

which contains two derivatives making integration a little more involved, and similarly for second order

$$\begin{aligned} T_3^\Psi &= \frac{d}{d\beta}(\alpha_2^\Psi T_2^\Psi) = \frac{d}{d\beta}\left(\alpha_2^\Psi \frac{d}{d\beta}(\alpha_1^\Psi T_1^\Psi)\right) \\ &= \frac{d}{d\beta}\left(\alpha_2^\Psi \frac{d}{d\beta}\left(\alpha_1^\Psi \frac{d}{d\beta}(\alpha_0^\Psi T_0^\Psi)\right)\right) \equiv 0 \end{aligned} \quad (4.8)$$

where although the focus in this work is on first order a particular result for fatigue requires second order, so is included here.

A facet of the definition above is that these identities are unique in the sense that they can represent any other identity of the same order (proof formalised but not yet published) and their form is ideal for integration and a unified procedure exist for this.

4.3. Finite Similitude Applied to Solid Mechanics and Fracture

To focus the finite similitude theory onto the problem under scrutiny it is first necessary to list those transport equations that contain the fields of interest. In the case of solid mechanics

involving cyclic loading, transport equations for volume, mass, momentum, and movement are of prime interest. The velocity field \mathbf{v}_{ts}^* for example is constrained by the transport equation for volume and is needed to define a relationship for \mathbf{v}_β^* , so should be included. The continuity equation brings density ρ_{ts} and material velocity \mathbf{v}_{ts} into play. The momentum transport equation additionally provides information on the stress tensor field $\boldsymbol{\sigma}_{ts}$ and specific body force \mathbf{b}_{ts}^v . The movement transport equation introduced in reference [170] constrains the behaviour of the displacement field \mathbf{u}_{ts} , which is important to solid mechanics.

4.3.1. Projected transport equations

The four transport equations mentioned above are multiplied by g and respectively by the scaling functions α_0^1 , α_0^ρ , α_0^v , and α_0^u and projected onto Ω_β . The application of the identity Eq. (4.5) returns zeroth-order connections between these scalars, i.e., $\alpha_0^1 = \beta^{-3}$, $\alpha_0^v g^{-1} \beta = \alpha_0^\rho$ and $\alpha_0^u \beta = \alpha_0^\rho$ (or $\alpha_0^u = \alpha_0^v g^{-1}$) (details provided in ref. [159]). In addition, two zeroth-order field relationships are assumed to be sufficient, which are $\mathbf{v}_{ps}^* = \mathbf{v}_1^* = \mathbf{v}_\beta^* = g\beta^{-1}\mathbf{v}_{ts}^*$ and $\rho_{ps} = \rho_1 = \rho_\beta = \alpha_0^\rho \rho_{ts} \beta^3$. The former condition is required for point-based rules and the latter is viewed as sufficient since density is typically considered invariant in solid mechanics and captured therefore by the single scalar function α_0^ρ . The four projected transport equations, with the zeroth-order conditions inserted, are:

$$\alpha_0^1 T_0^1(\beta) = \frac{D^*}{D^* t_\beta} \int_{\Omega_\beta^*} dV_\beta^* - \int_{\Gamma_\beta^*} \mathbf{v}_1^* \cdot \mathbf{n}_\beta d\Gamma_\beta^* = 0 \quad (4.9a)$$

$$\alpha_0^\rho T_0^\rho(\beta) = \frac{D^*}{D^* t_\beta} \int_{\Omega_\beta^*} \rho_1 dV_\beta^* + \int_{\Gamma_\beta^*} \rho_1 (\mathbf{v}_\beta - \mathbf{v}_1^*) \cdot \mathbf{n}_\beta d\Gamma_\beta^* = 0 \quad (4.9b)$$

$$\begin{aligned} \alpha_0^v T_0^v(\beta) &= \frac{D^*}{D^* t_\beta} \int_{\Omega_\beta^*} \rho_1 \mathbf{v}_\beta dV_\beta^* + \int_{\Gamma_{ps}^*} \rho_1 \mathbf{v}_\beta (\mathbf{v}_1 - \mathbf{v}_1^*) \cdot \mathbf{n}_\beta d\Gamma_\beta^* \\ &\quad + \int_{\Gamma_\beta^*} \boldsymbol{\sigma}_\beta \cdot \mathbf{n}_\beta d\Gamma_\beta^* - \int_{\Omega_\beta^*} \rho_1 \mathbf{b}_\beta dV_\beta^* = 0 \end{aligned} \quad (4.9c)$$

$$\begin{aligned} \alpha_0^u T_0^u(\beta) &= \frac{D^*}{D^* t_\beta} \int_{\Omega_{ps}^*} \rho_1 \mathbf{u}_\beta dV_\beta^* + \int_{\Gamma_\beta^*} \rho_1 \mathbf{u}_\beta (\mathbf{v}_1 - \mathbf{v}_1^*) \cdot \mathbf{n}_\beta d\Gamma_\beta^* \\ &\quad - \int_{\Omega_\beta^*} \rho_1 \mathbf{v}_\beta dV_\beta^* = 0 \end{aligned} \quad (4.9d)$$

where $\mathbf{v}_\beta = \beta^{-1} g \mathbf{v}_{ts}$, $\boldsymbol{\sigma}_\beta = \alpha_0^v \beta^2 g \boldsymbol{\sigma}_{ts}$, $\rho_1 \mathbf{b}_\beta = \alpha_0^v \rho_{ts} \beta^3 g \mathbf{b}_{ts}^v$, and $\mathbf{u}_\beta = \beta^{-1} \mathbf{u}_{ts}$.

To remove higher order terms and to reflect the fact that convection is negligible in solid mechanics the terms $\mathbf{v}_\beta(\mathbf{v}_\beta - \mathbf{v}_1^*)$ and $\mathbf{u}_\beta(\mathbf{v}_\beta - \mathbf{v}_1^*)$ have been approximated by $\mathbf{v}_\beta(\mathbf{v}_1 - \mathbf{v}_1^*)$ and $\mathbf{u}_\beta(\mathbf{v}_1 - \mathbf{v}_1^*)$ in Eq. (4.9c) and Eq. (4.9d). Note how the condition $\mathbf{v}_{ps}^* = \mathbf{v}_1^* = \mathbf{v}_\beta^*$ means that Eq. (4.9a) is independent of β and (with $\Omega_\beta^* = \Omega_{ps}^*$) and consequently the identity Eq. (4.5) is satisfied. However, none of the other equations disappear completely with differentiation with respect to β . The next set of transport equations $\alpha_1^\psi T_1^\psi = 0$ are obtained on differentiation of Eq. (4.5) and multiplication by α_1^1 , α_1^ρ , α_1^v , and α_1^u , giving rise to the first-order equations:

$$\alpha_1^\rho T_1^\rho(\beta) = \int_{\Gamma_\beta^*} \alpha_1^\rho \rho_1 \mathbf{v}_\beta' \cdot \mathbf{n}_\beta d\Gamma_\beta^* = 0 \quad (4.10a)$$

$$\begin{aligned} \alpha_1^v T_1^v(\beta) = & \frac{D^*}{D^* t_\beta} \int_{\Omega_\beta^*} \alpha_1^v \rho_1 \mathbf{v}_\beta' dV_\beta^* + \int_{\Gamma_\beta^*} \alpha_1^v \rho_1 \mathbf{v}_\beta' (\mathbf{v}_1 - \mathbf{v}_1^*) \cdot \mathbf{n}_\beta d\Gamma_\beta^* \\ & + \int_{\Gamma_\beta^*} \alpha_1^v \boldsymbol{\sigma}_\beta' \cdot \mathbf{n}_{ps} d\Gamma_{ps}^* - \int_{\Omega_{ps}^*} \alpha_1^v \rho_1 \mathbf{b}_\beta' dV_\beta^* = 0 \end{aligned} \quad (4.10b)$$

$$\begin{aligned} \alpha_1^u T_1^u(\beta) = & \frac{D^*}{D^* t_\beta} \int_{\Omega_\beta^*} \alpha_1^u \rho_1 \mathbf{u}_\beta' dV_\beta^* + \int_{\Gamma_\beta^*} \alpha_1^u \rho_1 \mathbf{u}_\beta' (\mathbf{v}_1 - \mathbf{v}_1^*) \cdot \mathbf{n}_\beta d\Gamma_\beta^* \\ & - \int_{\Omega_\beta^*} \alpha_1^u \rho_1 \mathbf{v}_\beta' dV_\beta^* = 0 \end{aligned} \quad (4.10c)$$

where here the dash “'” signifies differentiation with respect to β , and observe that these equations are similar in appearance to their corresponding counterparts in Eq. (4.9).

The equations in Eq. (4.10) are assumed independent of β under the rule of first-order finite similitude (i.e., Eq. (4.7)). It can be readily shown that under quasistatic loading the Eq. (4.10) can be identically satisfied for conditions prevailing in fracture mechanics (more on this below). In addition, identity Eq. (4.7) (and all high-order identities in fact) can be integrated exactly by the divided difference procedure provided in Appendix A. The integrated first-order identities of interest here are presented in Table 4.1 in two formats, i.e., compact and expanded, with latter useful for application of the method and the former helpful for further developments.

Table 4.1. First-order finite similitude identities

Fields	Compact representation	Expanded representation
Displacement	$\mathbf{u}_1 = \mathbf{u}_{\beta_1} + R_1 (\mathbf{u}_{\beta_1} - \mathbf{u}_{\beta_2})$	$\mathbf{u}_1 = \beta_1^{-1} \mathbf{u}_{ts1} + R_1 (\beta_1^{-1} \mathbf{u}_{ts1} - \beta_2^{-1} \mathbf{u}_{ts2})$
Velocity	$\mathbf{v}_1 = \mathbf{v}_{\beta_1} + R_1 (\mathbf{v}_{\beta_1} - \mathbf{v}_{\beta_2})$	$\mathbf{v}_1 = g_1 \beta_1^{-1} \mathbf{v}_{ts1} + R_1 (g_1 \beta_1^{-1} \mathbf{v}_{ts1} - g_2 \beta_2^{-1} \mathbf{v}_{ts2})$
Body force	$\mathbf{b}_1 = \mathbf{b}_{\beta_1} + R_1 (\mathbf{b}_{\beta_1} - \mathbf{b}_{\beta_2})$	$\rho_1 \mathbf{b}_1^v = \alpha_{01}^v \rho_{ts1} g_1 \beta_1^3 \mathbf{b}_{ts1}^v + R_1 (\alpha_{01}^v \rho_{ts1} g_1 \beta_1^3 \mathbf{b}_{ts1}^v - \alpha_{02}^v \rho_{ts2} g_2 \beta_2^3 \mathbf{b}_{ts2}^v)$
Stress	$\boldsymbol{\sigma}_1 = \boldsymbol{\sigma}_{\beta_1} + R_1 (\boldsymbol{\sigma}_{\beta_1} - \boldsymbol{\sigma}_{\beta_2})$	$\boldsymbol{\sigma}_1 = \alpha_{01}^v g_1 \beta_1^2 \boldsymbol{\sigma}_{ts1} + R_1 (\alpha_{01}^v g_1 \beta_1^2 \boldsymbol{\sigma}_{ts1} - \alpha_{02}^v g_2 \beta_2^2 \boldsymbol{\sigma}_{ts2})$
Force	$\mathbf{F}_1 = \mathbf{F}_{\beta_1} + R_1 (\mathbf{F}_{\beta_1} - \mathbf{F}_{\beta_2})$	$\mathbf{F}_1 = \alpha_{01}^v g_1 \mathbf{F}_{ts1} + R_1 (\alpha_{01}^v g_1 \mathbf{F}_{ts1} - \alpha_{02}^v g_2 \mathbf{F}_{ts2})$
Strain	$\boldsymbol{\varepsilon}_1 = \boldsymbol{\varepsilon}_{\beta_1} + R_1 (\boldsymbol{\varepsilon}_{\beta_1} - \boldsymbol{\varepsilon}_{\beta_2})$	$\boldsymbol{\varepsilon}_1 = \boldsymbol{\varepsilon}_{ts1} + R_1 (\boldsymbol{\varepsilon}_{ts1} - \boldsymbol{\varepsilon}_{ts2})$
Strain rate	$\dot{\boldsymbol{\varepsilon}}_1 = \dot{\boldsymbol{\varepsilon}}_{\beta_1} + R_1 (\dot{\boldsymbol{\varepsilon}}_{\beta_1} - \dot{\boldsymbol{\varepsilon}}_{\beta_2})$	$\dot{\boldsymbol{\varepsilon}}_1 = g_1 \dot{\boldsymbol{\varepsilon}}_{ts1} + R_1 (g_1 \dot{\boldsymbol{\varepsilon}}_{ts1} - g_2 \dot{\boldsymbol{\varepsilon}}_{ts2})$

In addition to those fields obtained directly from the transport equations extra field relationships for the force, strain and strain rate are included into Table 4.1. This is a feature of the finite similitude approach, which provides all the fields needed to analyse a problem despite not invoking constitutive laws.

4.3.2. Fracture and fatigue on Ω_β

The compact identities in Table 4.1 are identical in form because each satisfies the exact same differential equation of the form $\frac{d}{d\beta} \left(\alpha_1 \frac{d\mathfrak{X}_\beta}{d\beta} \right) = 0$, where \mathfrak{X}_β is any of the fields in

Table 4.1. This equation is the first-order identity Eq. (4.7) but now applied to fields defined on Ω_β as opposed to transport equations. It is readily deduced that the second-order identity similarly provides the differential equations of the form $\frac{d}{d\beta} \left(\alpha_2 \frac{d}{d\beta} \left(\alpha_1 \frac{d\aleph_\beta}{d\beta} \right) \right) = 0$ for the same fields.

Proposition: The product of two first order fields is second order in the sense that fields \aleph_β and Ξ_β defined on Ω_β satisfying $\frac{d}{d\beta} \left(\alpha_1 \frac{d\aleph_\beta}{d\beta} \right) = 0$ and $\frac{d}{d\beta} \left(\alpha_1 \frac{d\Xi_\beta}{d\beta} \right) = 0$, respectively, then the product $\aleph_\beta \Xi_\beta$ with $\alpha_2 = \alpha_1$ satisfies $\frac{d}{d\beta} \left(\alpha_2 \frac{d}{d\beta} \left(\alpha_1 \frac{d\aleph_\beta \Xi_\beta}{d\beta} \right) \right) = 0$.

Proof: Note that

$$\alpha_1 \frac{d}{d\beta} \left(\alpha_1 \frac{d\aleph_\beta \Xi_\beta}{d\beta} \right) = \alpha_1 \frac{d}{d\beta} \left(\alpha_1 \aleph_\beta \frac{d\Xi_\beta}{d\beta} + \alpha_1 \frac{d\aleph_\beta}{d\beta} \Xi_\beta \right) = 2 \left(\alpha_1 \frac{d\aleph_\beta}{d\beta} \right) \left(\alpha_1 \frac{d\Xi_\beta}{d\beta} \right) \quad (4.11)$$

which is identically zero on differentiation with respect to β , which confirms the result.

This proposition is particularly pertinent to fatigue as the product $\Delta K_{ts} n_{ts}$ plays a significant role in characterising the fatigue process, where on the trial space, ΔK_{ts} is the change in the stress intensity (assumed constant with cycle momentarily) and n_{ts} is the number of cycles (often the number of cycles to failure). The product arises on consideration of the sum

$$S = \sum_{i=1}^{n_{ts}} (\Delta K_{ts})_i = \Delta K_{ts} n_{ts} \quad (4.12)$$

where the simplified result $S = \Delta K_{ts} n_{ts}$ is returned if cyclic loading is such to return no change in ΔK_{ts} between cycles.

Hypothesis: The product $\Delta K_{ts} n_{ts}$ is second order with $\Delta K_{ts} n_{ts} = \Delta K_\beta n_\beta$, where ΔK_β and n_β are the stress intensity and number of cycles on Ω_β .

Prior to examining the implications of this hypothesis, it is worth contrasting the product $\Delta K_\beta n_\beta$ with $\aleph_\beta \Xi_\beta$ in the proposition above. These are not quite the same thing with the latter being a product of fields and the former being a product of parameters. Note however that K_{ts} can be connected to a field with the relationship $\Delta K_{ts} = F_{ts} \Delta \sigma_{ts} \sqrt{\pi a_{ts}}$, where F_{ts} is a shape factor, a_{ts} is crack length, and $\Delta \sigma_{ts}$ is the change in stress amplitude. Given that $\sigma_\beta = \alpha_0^v \beta^2 g \sigma_{ts}$ and $a_\beta = \beta^{-1} a_{ts}$ it follows that $\Delta K_\beta = \alpha_0^v \beta^{3/2} g \sigma_{ts} \Delta K_{ts}$, and note that the condition $\sigma_\beta = \sigma_{ts}$ provides $\alpha_0^v g = \beta^{-2}$ and ultimately $\Delta K_\beta = \beta^{-1/2} \Delta K_{ts}$. The conditions $\sigma_\beta = \sigma_{ts}$ and $\Delta K_\beta = \beta^{-1/2} \Delta K_{ts}$ are physically meaningful with the expectation that stress

on Ω_β and Ω_{ts} around the crack tip are the similar but stress intensity is different because of the change in crack length under the projection from Ω_{ts} to Ω_β . The hypothesis $\Delta K_{ts} n_{ts} = \Delta K_\beta n_\beta$ immediately implies that $n_\beta = \beta^{1/2} n_{ts}$, and additionally since ΔK_β is first order it follows from the proposition above that n_β is first order. In summary, ΔK_β and n_β satisfy the differential equations $\frac{d}{d\beta} \left(\alpha_1 \frac{d\Delta K_\beta}{d\beta} \right) = 0$ and $\frac{d}{d\beta} \left(\alpha_1 \frac{dn_\beta}{d\beta} \right) = 0$ (despite ΔK_β and n_β not being fields) and integrate to produce discrete identities

$$\Delta K_1 = \Delta K_{\beta_1} + R_1 (\Delta K_{\beta_1} - \Delta K_{\beta_2}) \quad (4.13a)$$

$$= \beta_1^{-1/2} \Delta K_{ts1} + R_1 (\beta_1^{-1/2} \Delta K_{ts1} - \beta_2^{-1/2} \Delta K_{ts2})$$

$$n_1 = n_{\beta_1} + R_1 (n_{\beta_1} - n_{\beta_2}) = \beta_1^{1/2} n_{ts1} + R_1 (\beta_1^{1/2} n_{ts1} - \beta_2^{1/2} n_{ts2}) \quad (4.13b)$$

which are important relationships connecting information from two scaled experiments to the full scale.

Note that the expressions in Eq. (4.13) are not yet definitive since R_1 remains undefined, which is linked to the stipulation of the scalar α_1 . The specification of α_1 and R_1 arise out of a peculiar invariance that is needed to represent crack separation across the scales. Note the relationship for displacement is $\mathbf{u}_\beta = \beta^{-1} \mathbf{u}_{ts}$ satisfying $\frac{d}{d\beta} \left(\alpha_1 \frac{d\mathbf{u}_\beta}{d\beta} \right) = 0$, which under the assumption that \mathbf{u}_{ts} is invariant of β provides $\frac{d}{d\beta} \left(\alpha_1 \frac{d\beta^{-1}}{d\beta} \right) = 0$, which is satisfied by $\alpha_1 = \beta^2$ (recall the requirement $\alpha_1(1) = 1$). Similarly, the expression for displacement in Table 1 returns

$$R_1 = \frac{1 - \beta_1^{-1}}{\beta_1^{-1} - \beta_2^{-1}} \quad (4.14)$$

where on stimulation of the scales β_1 and β_2 provides is a definitive expression for R_1 . It is important to appreciate that although invariances for stress and displacement are invoked to determine $\alpha_0^v g$ and α_1 , respectively different behaviours are possible. The invariances are desirable behaviours that can be captured (should they feature) by the similitude rules under settings $\alpha_0^v g = \beta^{-2}$ and $\alpha_1 = \beta^2$.

4.3.3. Practical application of first order finite similitude rules.

Despite the mathematical nature of the theory, its application in practice is relatively straightforward. Detailed description of the procedure for application of the theory in fracture mechanics and fatigue can be found in references [189] and [190] respectively and is recapped here as follows:

- (viii) Specify the geometry, material properties, loading and boundary conditions of the full-scale model.
- (ix) Specify the geometric scaling factors β_1 and β_2 , and material properties for the scaled models. Identical materials are applied to all models in this work.
- (x) Calculate the dimensional scaling factors for scaled models by using the zeroth order setting $\alpha_{01}^v g_1 = \beta_1^{-2}$ and $\alpha_{02}^v g_2 = \beta_2^{-2}$.
- (xi) Calculate the scaling factor R_1 using Eq. (4.14).
- (xii) Calculate the applied loads and boundary conditions for the scaled models. If the loading condition of the full-scale model is an applied stress, then the same stress is applied to all scaled models. For the case of applied force or displacement, the dimensional scaling factors $\alpha_{01}^v g_1$ and $\alpha_{02}^v g_2$ are used to calculate the suitable load for scaled models.
- (xiii) Conduct experimental tests on the scaled models.
- (xiv) Combine the results of the desired outputs returned from the scaled model using the appropriate field equations given in Table 4.1.
- (vii) For the case of fatigue within the LEFM framework, the desired outputs are the crack length, crack growth rate, stress intensity factor and number of cycles to failure.

The crack length outputs from the scaled models can be combined using the first-order approximation,

$$a_{ps} = \beta_1^{-1} a_{ts1} + R_1 (\beta_1^{-1} a_{ts1} - \beta_2^{-1} a_{ts2}) \quad (4.15a)$$

and similarly for crack growth rate the following equation is assumed to apply,

$$\left(\frac{da}{dn}\right)_{ps} = \beta_1^{-\frac{3}{2}} \left(\frac{da}{dn}\right)_{ts1} + R_1 \left(\beta_1^{-\frac{3}{2}} \left(\frac{da}{dn}\right)_{ts1} - \beta_2^{-\frac{3}{2}} \left(\frac{da}{dn}\right)_{ts2} \right) \quad (4.15b)$$

which is a first-order relationship for $(da/dn)_\beta$ and realised on substitution of $da_\beta = \beta^{-1} da_{ts}$ and $dn_\beta = \beta^{1/2} dn_{ts}$.

Finally, the stress intensity factor and number of cycles to failure outputs are combined using Eq. (4.13a) and Eq. (4.13b), respectively. In this way, the first order theory provides a framework that describes the necessary conditions for performing scaled fatigue tests.

4.3.4. Empirical fatigue equations on Ω_β

Power law empirical differential relationships are commonly used to represent fatigue behaviour with a particular focus on the relationship between crack length a_{ts} and the

number of cycles n_{ts} . The focus here is on Paris law which on Ω_β takes the form $(da_\beta/dn_\beta) = C_\beta(\Delta K_\beta)^m$ with $n_\beta = \beta^{1/2}n_{ts}$, $a_\beta = \beta^{-1}a_{ts}$, $\Delta K_\beta = \beta^{-1/2}\Delta K_{ts}$, and $C_\beta = C_{ts}\beta^{-3/2}\beta^{m/2}$. Note additionally, that $\Delta K_\beta = F_\beta\Delta\sigma_\beta\sqrt{\pi a_\beta}$ and since the shape factor F_β and stress amplitude $\Delta\sigma_\beta$ are zeroth order, it follows that $\sqrt{a_\beta}$ has the same order as ΔK_β , i.e., both are first order. This observation along with the hypothesis above ($\Delta K_\beta n_\beta$ is second order) leads to the following important proposition.

Proposition: Paris law $(da_\beta/dn_\beta) = C_\beta(\Delta K_\beta)^m$ is a first-order relationship.

Proof: The proof is relatively simple and follows from the observation that a_β is second order being the product of two first order terms (i.e., $a_\beta = \sqrt{a_\beta}\sqrt{a_\beta}$) and n_β is first order leads to the realisation that the derivative da_β/dn_β is first order and consequently it follows immediately that Paris law is first order.

This is an important result as it confirms that Paris law adheres exactly to first order rules and therefore Eq. (4.15b) is exact. The first-order relationship provided by Eq. (4.15a) is approximate (as a_β is second order) but this transpires to be sufficient to return good accuracy.

4.4. Experimental Investigation

In this section, previous experimental data is examined, and the first order theory applied. Although scaled fatigue investigations into the geometrical size effect are detailed in the literature, few conform to the rules of first-order finite similitude. They do not apply the identities in Table 4.1 nor conform to the procedure outlined in Section 4.3. In addition, the CFD approach [23,126] is predominantly applied yet the focus here is FCP. The closest match from the literature is the experimental data from a three-point bending fatigue test on concrete performed by Bazant & Xu [14] and Kirane & Bazant [129].

4.4.1. Case study I: Three-point bending fatigue test of concrete

Three-point bending fatigue tests of normal strength concrete were carried out in the pioneering work of Bazant and Xu [14] for three different geometrically similar beam sizes with loading ratio $R = 0$. This was the first comprehensive experimental investigation into size effect in fatigue. Each specimen size was tested twice and the number of cycles to failure were recorded. The beams have an elastic modulus of 27.12 GPa, mean compression strength of 32.8 MPa and Poisson's ratio equal to 0.18. The thickness B for all beams was 38.1 mm

(1.5 in) and the length-to-depth ratio S/D was held constant at a value of 2.5. Table 4.2 presents the geometry dimensions, geometric scaling factor B and the mean monotonic force as obtained from a load-CMOD monotonic test. The cyclic loading for each beam was set at 80% of peak load at its maximum and 5% of its peak load at its minimum. The fatigue strength expressed as the number of cycles to failure n_f for all specimens is presented in Table 4.3 alongside the Paris law exponents C and m . The predictions made using the size effect law proposed by Bazant and Xu [14] are reported.

Table 4.2: Specimen dimensions [14]

Specimen	Depth D (mm)	Length S (mm)	Thickness B (mm)	β_i	Force P (kN)
Small (ts2)	38.1	95.25	38.1	0.186	408
Medium (ts1)	76.2	190.5	38.1	0.432	671
Large (ps)	152.4	381	38.1	1	1165

Table 4.3: Experimental data for number of cycles to failure n_f and Paris law parameters C and m for concrete beams of different sizes [14]

Specimen	Small	Medium	Large
1	974	850	882
2	939	1286	1083
Mean n_f	957	1068	983
Mean $\log C$	-16.7	-18.2	-19.6
Mean m	11.78	9.97	9.27

The first order finite similitude rules provide the scaling factors needed to combine key fatigue outputs from the fatigue tests of the small-scale models (small and medium beam) to predict the corresponding fatigue parameters of the full-scale model (large beam). The practical procedure outlined in Section 4.3.3 is applied here. Eq. (4.13b) is used to predict the number of cycles to failure of the large specimen from the information provided at the two smaller scales. The mean number of cycles to failure for each of the specimen sizes in Table 4.3 is used to predict fatigue life. The dimensional scaling factor R_1 is calculated using Eq. (4.14). Substitution of the data for the scaled specimens into Eq. (4.13b) gives:

$$n_1 = 0.5^{0.5} \times 1068 + 0.5 (0.5^{0.5} \times 1068 - 0.25^{0.5} \times 957) \quad (4.16a)$$

$$= 893 \approx (n_{ps})_f$$

providing good agreement between the similitude prediction of 893 cycles and the experimental result of 983 cycles (9% error). Similarly, the final crack length of the large specimen can be predicted using Eq. (4.15a):

$$(a_1)_f = 0.5^{-1} \times 76.2 + 0.5 (0.5^{-1} \times 76.2 - 0.25^{-1} \times 38.1) \quad (4.16b)$$

$$= 152.4 \text{ mm} = (a_{ps})_f$$

providing an exact match between the predicted crack length by first-order similitude and the experimental result.

Despite the loading conditions for the experimental tests not being ideal, reasonable fatigue life predictions can still be achieved on application of the first order theory. Although the results for fatigue life are only indicative and introduced principally to show the application of Eq. (4.13b) and Eq. (4.15a) it is of interest nevertheless to examine the fatigue crack growth (FCG) curve to ascertain if the theory (despite these limitations) can capture the correct crack growth rate. A virtual model is constructed from the two projected scaled models (using the first-order identities) with the projected scaled models on Ω_β being akin to predictions returned from dimensional analysis. Table 4.4 compares the Paris law exponents for the large beam as obtained from experiments [14], proposed scaling model in [14] and the virtual model constructed using first order similitude rule identities. The Paris law exponent C is observed to exhibit a much stronger size effect than m [14]. Thus, in designing large structures, it is imperative that the prediction of C returned by the scaling theory is as accurate as possible. The error in $\ln C$ prediction returned by virtual model is 1.9% with the scaling models in ref. [14] returning an error of 6.1%.

Table 4.4: Comparison of Paris law exponents for the large beam between experimental data, first order theory and the scaling model in ref. [14]

Model	$\log C$	m	m error (%)	$\log C$ error (%)
Experimental [14]	-19.6	9.27	-	-
Bazant & Xu's model [14]	-18.4	10.6	14.3	6.1
Virtual model (Current work)	-19.976	10.65	14.9	1.9

Mean log C	-16.7	-18.2		-19.6
Mean m	11.78	9.97		9.27

4.4.2. Case study II: Three-point bending fatigue test of concrete

The experimental data from the work of Kirane and Bazant [129] involves three-point bending fatigue tests of concrete for three different beam sizes (see Fig. 4.2). Each specimen size was tested 6 times and the number of cycles to failure were recorded. To minimise the statistical size effect, the mean value of the number of cycles to failure of each specimen was used to validate the scaling theory in ref. [129] and the same method is adopted in this paper. Dimensions of the specimen are given in Table 4.5 for beams with elastic modulus of 41.4 GPa and Poisson's ratio equal to 0.18. Three different beam depths D were tested, which are 40, 93 and 215 mm. The thickness B for all beams was held constant at 40 mm (1.58 in) and the length-to-depth ratio S/D was held constant at a value of 2.4. The fatigue life expressed as the number of cycles to failure n_f for all specimens is presented in Table 4.6 alongside the Paris law exponents C and m .

Table 4.5: Specimen dimensions [129]

Specimen	Depth D (mm)	Length S (mm)	Thickness B (mm)	β_i
Small (ts2)	40	96	40	0.186
Medium (ts1)	93	223.2	40	0.432
Large (ps)	215	516	40	1

Table 4.6: Experimental data for number of cycles to failure n_f and Paris law parameters C and m for concrete beams of different sizes [129]

Specimen	Small	Medium	Large
Mean n_f	1000	564	418
Mean log C	-30.42	-31.11	-31.68
Mean m	8.59	8.36	8.02



Figure 4.2: Specimens at final fatigue fracture [129]

The first order finite similitude rules provide the scaling factors needed to combine key fatigue outputs from the fatigue tests of the small-scale models (small and medium beam) to predict the corresponding fatigue parameters of the full-scale model (large beam). The practical procedure outlined in Section 4.3 is applied here. Eq. (4.13b) is used to predict the number of cycles to failure of the large specimen from the information provided at the two smaller scales. The mean number of cycles to failure for each of the specimen sizes in Table 4.5 is used to predict fatigue life. The dimensional scaling factor R_1 is calculated using Eq. (4.14). Substitution of the data for the scaled specimens into Eq. (4.13b) gives:

$$\begin{aligned} n_1 &= 0.432^{0.5} \times 564 + 0.429 (0.432^{0.5} \times 564 - 0.186^{0.5} \times 1000) \\ &= 368 \approx (n_{ps})_f \end{aligned} \quad (4.17a)$$

providing good agreement between the similitude prediction of 368 cycles and the experimental result of 397 cycles (7% error). Similarly, the final crack length of the large specimen can be predicted using Eq. (4.15a):

$$\begin{aligned} (a_1)_f &= 0.432^{-1} \times 93 + 0.429 (0.432^{-1} \times 93 - 0.186^{-1} \times 40) \\ &= 215 \text{ mm} = (a_{ps})_f \end{aligned} \quad (4.17b)$$

providing an exact match between the predicted crack length by first-order similitude and the experimental result.

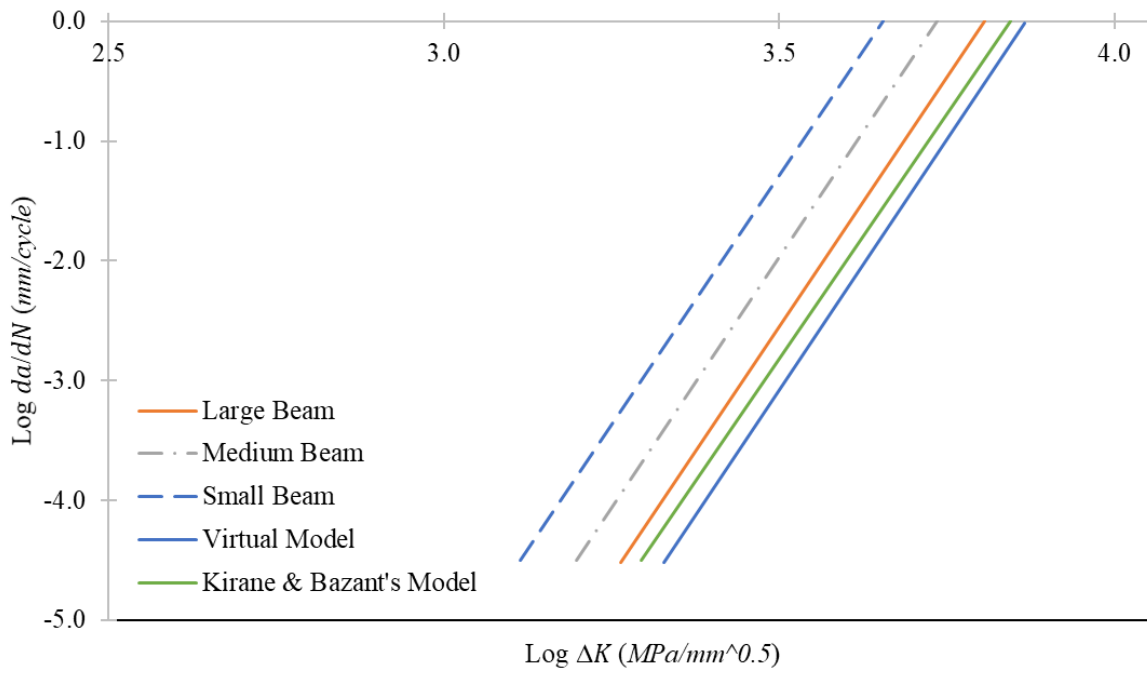


Figure 4.3: Fatigue crack growth rate vs stress intensity factor for full scale, virtual, projected scaled and Kirane & Bazant's [129] models.

The model by Kirane & Bazant based on a size adjusted Paris law [129] returned an impressive global error of only 3% when contrasted with the FCG curve of the large beam. The virtual model constructed using the finite similitude theory returns in this case the crack growth rate of the large concrete beam to good accuracy (6% error). The promising results shown in this section lend credence to the first order theory as an alternative approach to scaled experimentation of propagating fatigue cracks.

4.5. Numerical Experimentation

The experiments discussed above provided reasonable results despite these not strictly adhering to the finite similitude rules introduced by the new theory. An advantage of numerical approaches in scaling work is they can be applied at any scale and consequently can be used to test scaling theories. It is of interest therefore to explore the benefits of trials satisfying exactly the rules of finite similitude. This is examined in this section by means of numerical experiments for methods that are typically applied to model and investigate fatigue. The first-order finite similitude rule has the advantage of replicating exactly the macroscopic conditions at the crack tip (i.e., stress, stress gradients) [189-190] and consequently the expectation is that numerically produced results will be replicated with little error.

Three case studies are considered in this section with the principal aim to show the applicability of the theory to a diverse range of fatigue problems. The tests considered are the single edge notched tensile specimen (SENT), a hollow pipe, and a cylindrical pressure vessel with a semi elliptical crack. The ASTM E647 [174] procedure is employed in all case studies to evaluate the fatigue crack growth rate. ANSYS 2021 is the software of choice, and crack propagation is studied by means of the ANSYS SMART solver [95]. ANSYS can model three kinds of cracks: arbitrary, semi-elliptical, and pre-meshed. The pre-meshed crack is used for the SENT specimen whereas for the last two case studies a semi-elliptical crack is modelled. The cracks behaviour is described by a cohesive zone model in the software. For the pre-meshed crack, it is necessary to define the top and bottom surfaces of the crack and its crack front manually, whereas with the semi-elliptical crack it is done automatically.

The mode of operation using the smart crack growth-analysis tool is relatively straightforward. The crack front is advanced by a small amount Δa and the mesh is updated around the new crack front. As the crack propagates, the newly introduced crack segments are assumed to behave in accordance with the cohesive zone model. This process is repeated for a set number of sub steps till the desired final crack length is reached a_f . SMART automatically updates the mesh from crack geometry changes due to crack propagation at each solution stage, reducing the need for long pre-processing sessions.

To apply the procedure highlighted in section 4.3.3, the zeroth-order condition $\Delta a_{ts} = \beta \times \Delta a_{ps}$ is applied to the scaled models and the number of sub-steps are kept the same for both the full scale and scaled down models. This enables fracture mechanics outputs to be combined at each sub-step using the relevant first order identity. Δa_{ps} is set to 0.2 mm in all case studies. ΔK is evaluated at the mid-point of the crack point in all case studies.

The work of Busari et al. [192] on a SENT specimen is replicated first to validate the fatigue crack growth results in this paper. Constant amplitude loadings are applied in all case studies. An element size of 0.2 mm is employed local to the crack tip for all case studies as recommended by Zhang et al. [178]. Elements with a size of 1 mm are used in the other regions of the specimen to reduce computational time. The number of elements is kept the same for all scaled models to eliminate the effects of mesh dependency and SOLID187 [95] elements are employed in all case studies. S355 steel is used for the first two case studies, and 7% nickel steel is the material of choice for the pressure vessel with material properties according to ref. [193]. Material properties are provided in Table 4.7.

Table 4.7: Mechanical properties of materials used in numerical analysis [192,193]

Material	Young's Modulus (MPa)	Poisson's ratio, ν	Yield strength (MPa)	Ultimate tensile strength (MPa)	Paris law parameters	
					C (mm/cycleMPamm ^{0.5})	m
S355	213	0.3	400	450	1.67×10^{-12}	2.51
7% Nickel steel	205	0.3	475	510	1×10^{-13}	3

4.5.1. Verification of numerical results

The Ansys smart solver is validated in this section against previous experimental work to ensure the fatigue life predictions are accurate before applying scaling laws. Busari et al. [192] conducted fatigue tests on a single edge notched tensile (SENT) specimen for S355 and S960 steel at different load ratios and applied pressure. The fatigue response of the S355 steel is replicated here with a load ratio $R = 0$. Two types of crack measurement method were used for enhanced accuracy. A cyclic stress of 150MPa was applied to the top edge whereas the bottom edge was fixed. Details of the geometry are shown in Fig. 4.4. Due to computational resource limitations, the number of cycles is validated over 100,000 cycles only.

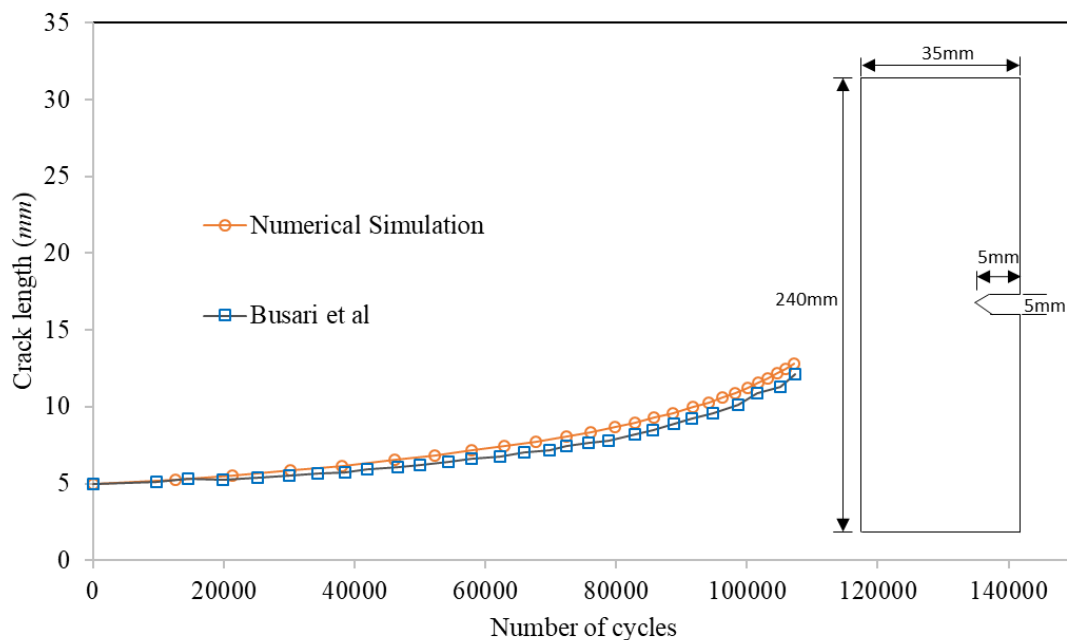


Figure 4.4: Geometry of single edge notched tension specimen and comparison between the numerical results of the current study and Busari et al. [192].

The numerical results predict a crack length of 10.5 mm at 100,000 cycles whilst experimental data gives 10 mm. The agreement achieved between numerical results from Ansys, and experimental data provides confidence in the Ansys SMART solver. The current study and the reported findings of Busari et al. [192] differ by a 5% error in final crack length. The validated numerical procedure is employed in the subsequent sections to investigate the efficacy of the proposed scaling method based on the first-order theory.

4.5.2. Case study I: Single edge notched tensile specimen (SENT)

The geometry of the SENT specimen is same as highlighted in Fig. 4.4. The material considered is S355 steel. A cyclic stress of 160 MPa with a load ratio $R = 0$ is applied to the top edge and the bottom edge is fixed. A mesh sensitivity study was performed to investigate the effect of different element sizes around the crack tip. Element sizes used are 0.2 mm, 0.5 mm and 1 mm. The simulation ran until final fracture of the specimen and the results are presented in Fig. 4.5. Based on the analysis 0.2 mm is chosen as element size around the crack tip as the crack growth rate is very similar with an element size of 0.1 mm or 0.2 mm up to 100,000 cycles where some deviation can be observed. All case studies are below 100,000 cycles so 0.2 mm is deemed sufficient. For the SENT specimen, the number of cycles taken to propagate the crack 5 mm in the full-scale model to critical final crack length a_f of 10 mm is examined. The crack-extension increment Δa of the full-scale model is set to 0.2 mm (i.e., $\Delta a_{ps} = 0.2$ mm). The number of sub-steps over which the crack is propagated is 25 which is kept the same for the scaled models. The stress distribution is not uniform across the crack front, so the stress intensity factors are evaluated at the midway point of the crack front for all case studies. Applied stress for the scaled models are calculated using the identities in Table 4.1.

The specimen dimensions and loading conditions for SENT specimen can be found in Table 4.8 and Table 4.9. Additionally, Table 4.10 presents the dimensional scaling factors for all three specimens.

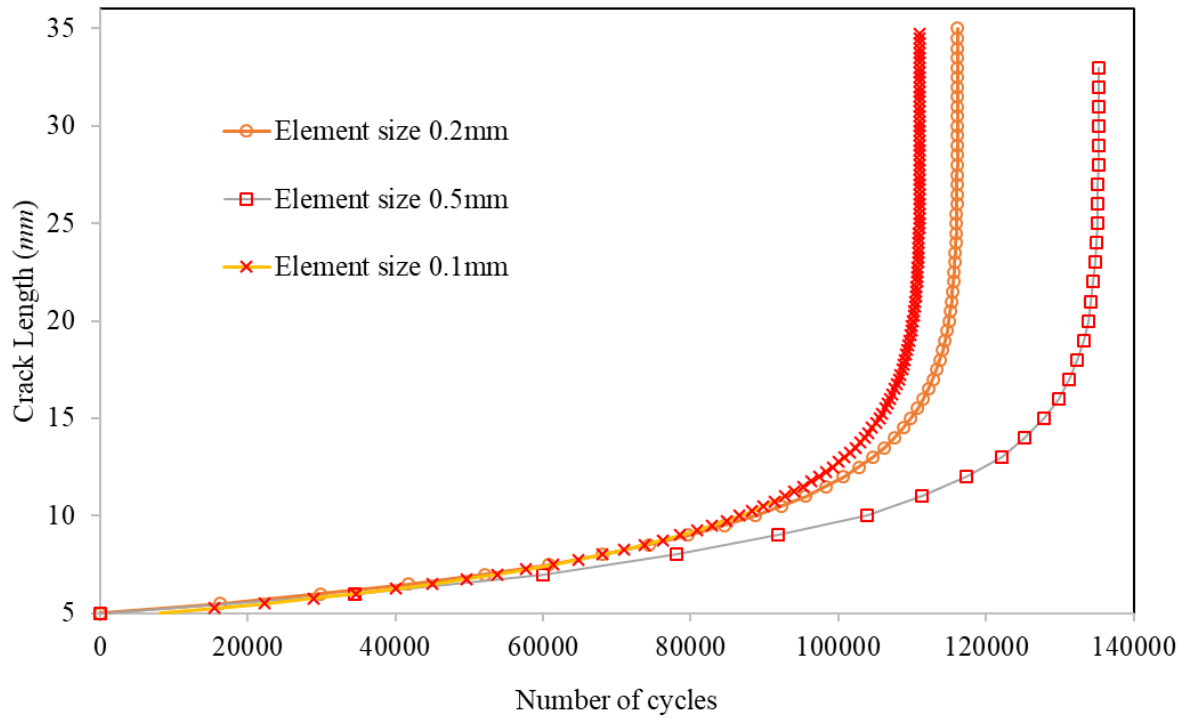


Figure 4.5: Mesh sensitivity study for single edge notched tensile specimen

Table 4.8: Dimensions of SENT specimen at all scales

Model	β	Initial crack size a (mm)	Height (mm)	Ligament length (W-a) (mm)	Thickness (mm)	Width (mm)
Full scale	1.00	5.00	240	30.00	5.00	35.00
Scaled Model 1	0.80	4.00	192	24.00	4.00	28.00
Scaled Model 2	0.50	2.50	120	15.00	2.50	17.50
Scaled Model 3	0.25	1.25	60	7.50	1.25	8.75

Table 4.9: The loading conditions of SENT specimen at all scales

Model	β	Crack extension Δa (mm)	Applied cyclic stress (MPa)	Load ratio R
-------	---------	---------------------------------	-----------------------------	----------------

Full scale	1.00	0.20	200	0
Scaled Model 1	0.80	0.16	200	0
Scaled Model 2	0.50	0.10	200	0
Scaled Model 3	0.25	0.05	200	0

Table 4.10: Value of the scaling factors with different dimensional scaling factors

Virtual Model No.	β_1	β_2	$\alpha_{01}^v g_1$	$\alpha_{02}^v g_2$	R_1
1	0.80	0.50	1.56	4.00	0.33
2	0.80	0.25	1.56	16.00	0.09
3	0.50	0.25	4.00	16.00	0.50

The first task undertaken is examining the stress distribution around the crack tip after 5mm of crack propagation; the results are shown in Fig. 4.6. It can be observed that the stress distribution is the same for both the full scale and scaled down models. The crack propagates through the midpoint of the specimen as it is a pure mode I case. These findings are consistent with that of previous researchers [192]. The next step is to investigate how accurately the crack tip driving force, i.e., the stress intensity factor and subsequently the crack propagation rate is predicted. The aim here is to predict the number of cycles, it takes the crack to grow 5 mm. The results are tabulated in Table 4.11. Excellent agreement is achieved for the stress intensity factor at 5 mm with a maximum error of 2% predicted by virtual model 3. Virtual model 1 gives the best lifecycle prediction where the crack grows 5 mm in 39,962 cycles as opposed to 40,624 cycles for the full-scale model (2% error). The plot of the crack length against number of cycles is shown in Fig. 4.7 with the effect of load ratio presented in Fig. 4.8.

Crack length 10mm for the full-scale model	Crack length 10mm for the virtual model
--	---

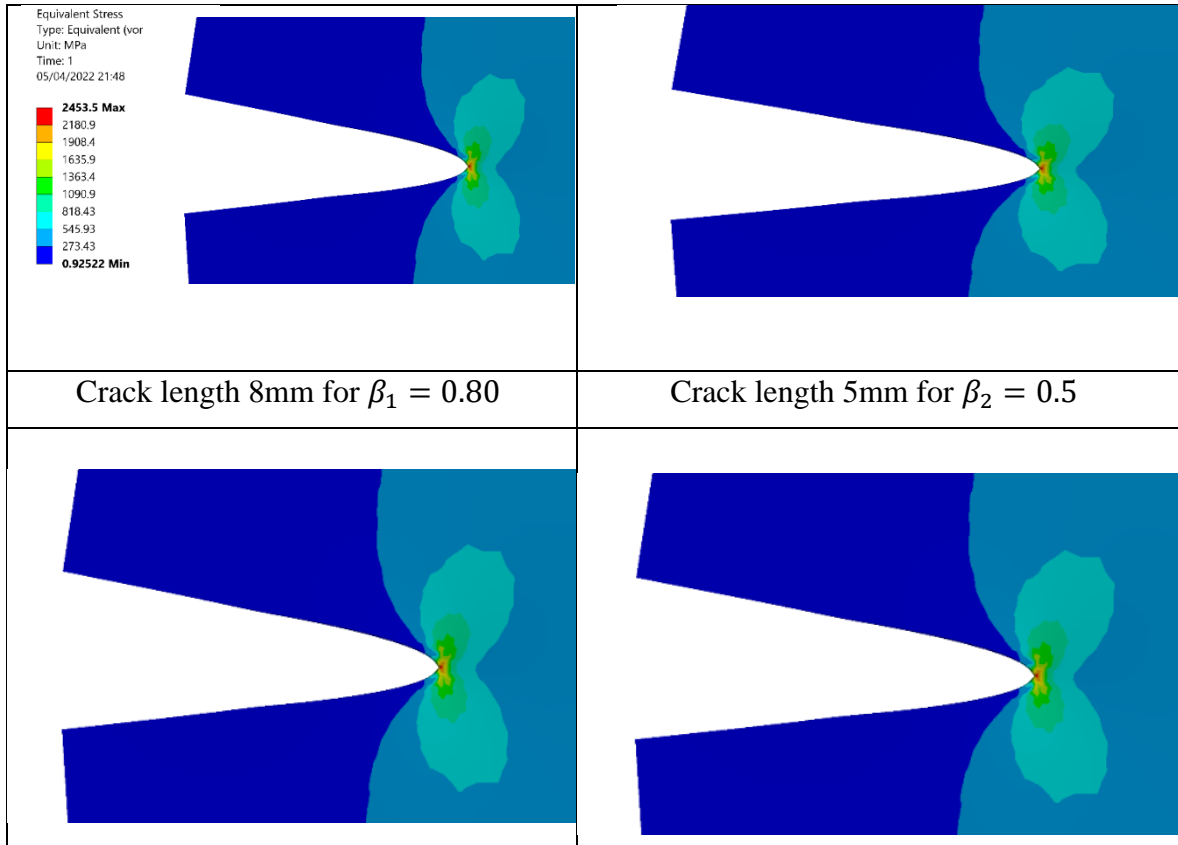


Figure 4.6: Von Mises stress distribution at the crack tip of SENT specimen for the full-scale model and the two scaled models for virtual model 1.

Table 4.11. Stress intensity factor and number of cycles at final crack length of 10 mm after 25 sub steps for full scale, virtual and scaled down models

Model	a_f (mm)	Error (%)	$K(MPamm^{0.5})$	Error (%)	n_{ps}	Error (%)
Full Scale	10	-	1684.4	-	40624	-
Virtual Model 1	10	0	1666.5	1	39962	2
Virtual Model 2	10	0	1664.6	1.2	39427	3
Virtual Model 3	10	0	1655.7	2	37068	9
Scaled Model 1	8	20	1490.4	12	43119	6
Scaled Model 2	5	50	1177.8	30	48623	20

Scaled Model 3	2.5	75	842.8	50	58016	43
----------------------	-----	----	-------	----	-------	----

Eq. (4.13b) is used to predict the number of cycles needed to propagate the crack 5 mm for the full-scale model. Eq. (4.14a) is used to predict the final crack length from the outputs of the scaled model. At the final crack length, a_f of 10 mm the number of cycles for the full scale is 40624. The corresponding cycle count for scaled models 1, 2 and 3 are 43119, 48623 and 58016, respectively. Substitution of the data for the scaled specimens 1 and 2 into Eq. (4.13b) and using the scaling factors provided in Table 4.9 gives:

$$(n_1)_f = 0.8^{0.5} \times 43119 + 0.33 (0.8^{0.5} \times 43119 - 0.5^{0.5} \times 48623) \quad (4.17)$$

which consequently provides the prediction for virtual model 1 of

$$(n_1)_f = 39962$$

which can be contrasted against the full-scale value of 40624 cycles; similarly, the predictions for virtual models 2 and 3 can be calculated in the same manner, and for virtual model 3 they are 39427 cycles and 37068 cycles, respectively.

The effect of mean stress on crack growth rate is examined and the first order theory applied to determine if this effect can be captured. To this end, the SENT specimen is subjected to two different R ratios of 0.1 and -1. The results are presented in Fig. 4.8, which reveals that the mean-stress effect is adequately captured by the theory as the virtual models give near exact predictions of the number of cycles. The global error for R ratios 0, 0.1 and -1 are 2%, 2% and 5 % respectively. The findings of this work are consistent with that of other researchers. Elber found that negative R ratios decrease fatigue life while low R ratios increase fatigue life [194].

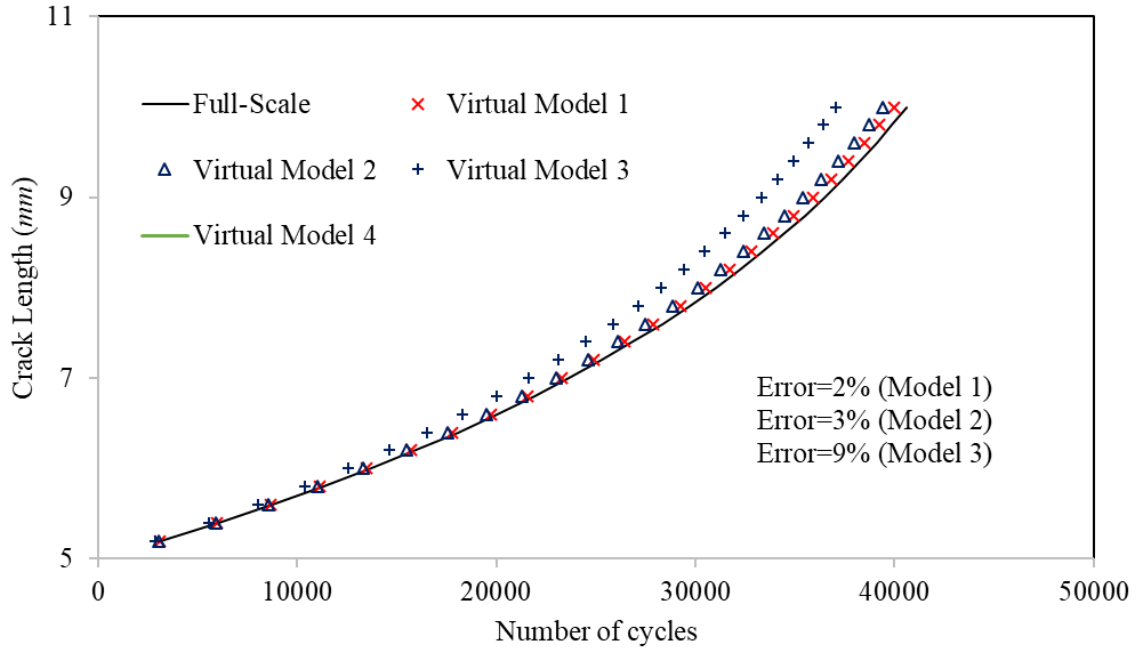


Figure 4.7: Crack length vs number of cycles for full scale and scaled down SENT models

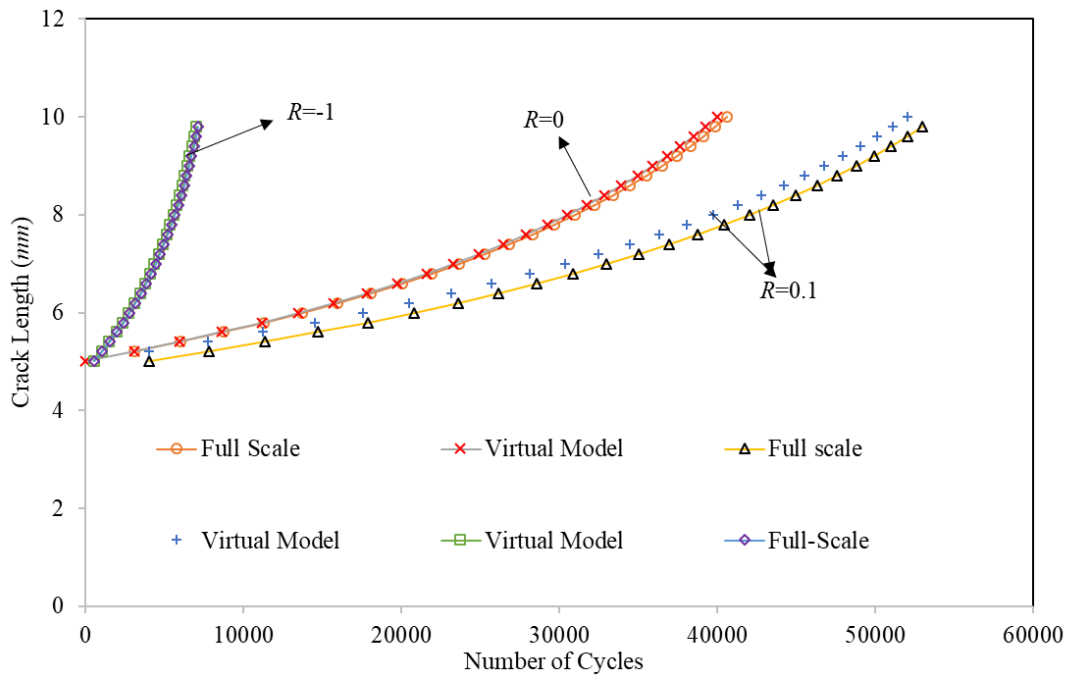


Figure 4.8: Crack length vs number of cycles for single edge notched tensile specimen for full scale model and virtual model 1 at R ratios 0, 0.1 and -1

4.5.3. Case study II: Semi-elliptical crack in a pipeline

A pipe of length 100 mm, outer radius 50 mm and inner radius 42 mm under an internal pressure load of 50 MPa is considered. A semi-elliptical crack with a major radius of 5 mm

and minor radius of 1 mm is inserted in the longitudinal direction at the midpoint of the pipe. The dimensions of the pipe are shown in Fig. 4.9 with trial details presented in Table 4.12. Three scaled models are considered and a pressure of 50 MPa is applied to all models; S355 steel is used throughout. The loading conditions are tabulated in Table 4.13. The dimensional scaling factors for all three specimens are identical to those in Table 4.10.

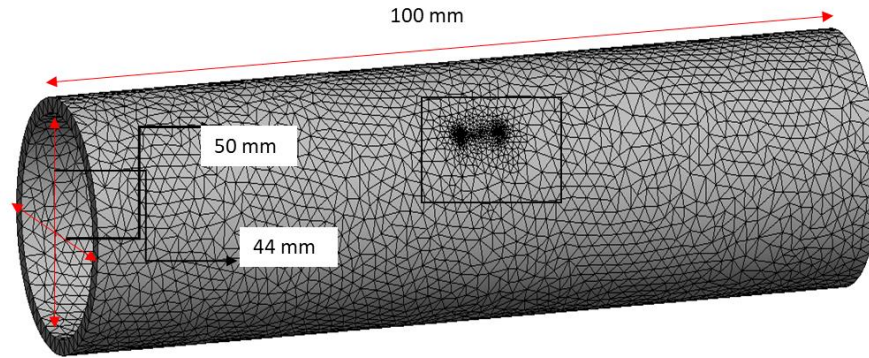


Figure 4.9: Meshed pipe with crack mesh at the centre.

Table 4.12: Dimensions of pressurized pipe for the full-scale and scaled models

Space	β	Crack length $2c$ (mm)	Crack depth a (mm)	Length (mm)	Outer radius (mm)	Inner radius (mm)
Full scale	1.00	5.00	1.00	100.00	50.00	42.00
Scaled Model 1	0.80	4.00	0.80	80.00	40.00	38.40
Scaled Model 2	0.50	2.50	0.50	50.00	25.00	26.00
Scaled Model 3	0.25	1.25	0.25	25.00	12.50	13.00

Table 4.13: The loading conditions of pipe at all scales

Model	β	Crack extension Δa (mm)	Applied pressure load (MPa)	Load ratio R
Full scale	1.00	0.20	50	0

Scaled Model 1	0.80	0.16	50	0
Scaled Model 2	0.50	0.10	50	0
Scaled Model 3	0.25	0.05	50	0

Table 4.14. Stress intensity factors and number of cycles at final crack length of 7 mm for full scale and virtual models

Model	a_f (mm)	Error (%)	K (MPa $\sqrt{\text{mm}}^{0.5}$)	Error (%)	n_{ps}	Error (%)
Full Scale	7	-	6452	-	783	-
Virtual Model 1	7	0	6678	1	782	0.1
Virtual Model 2	7	0	6613	1.2	769	2
Virtual Model 3	7	0	6321	2	710	9

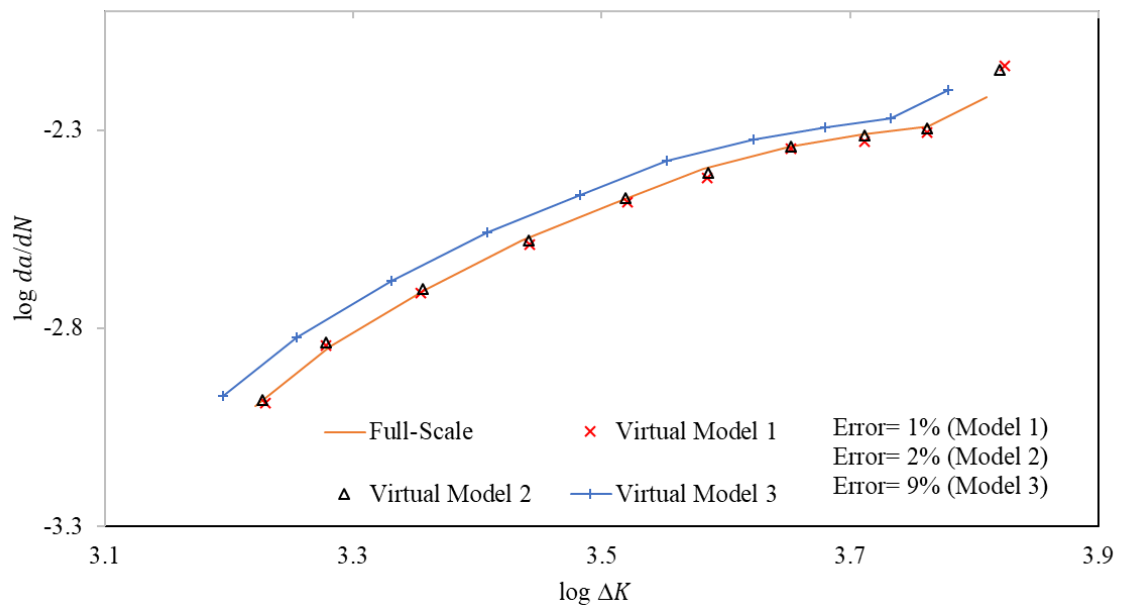


Figure 4.10: Crack growth rate vs stress intensity factor of pipe for full scale and virtual models

As evident from Fig. 4.10 the predictions of the crack growth rate by virtual models 1 and 2 are near enough exact throughout the range of ΔK in the test. Exact agreement is achieved at lower ΔK values with slight deviations observed as the stress intensity factor increases. Predictions made by virtual model 3, based on the smallest scaled models (see Table 4.10), produces slightly worse results than others yet still records results at less than 10% error. The stress intensity factors and number of cycles at final crack length are tabulated in Table 4.14.

4.5.4. Case study III: Semi-elliptical Crack in a Pressure Vessel

In this case study, a vertical pressure vessel with a semi elliptical crack at the centre is analysed with the geometry presented in Fig. 4.11. The crack is 5 mm long and 1 mm deep (aspect ratio 0.4). The top face is under a tensile loading of 250 MPa while the bottom end is fixed in all directions. The material 7% nickel steel is used for the full-scale model and scaled-down models. Table 4.15 and Table 4.16 presents the loading and geometry dimensions for all models. The semi-elliptical crack is propagated by 0.2mm for 10 substeps for a total crack growth of 2 mm in the full-scale model and the aim here is to evaluate the number of cycles it takes to reach the final crack length of 7 mm. A prediction is made from three different virtual models which are three permutations of the data (see Table 4.10) from the three scaled models. Lifecycle and stress intensity predictions are extremely accurate with only 1% deviation from the full-scale model for all virtual models. The stress intensity factors and number of cycles at final crack length are tabulated in Table 4.17.

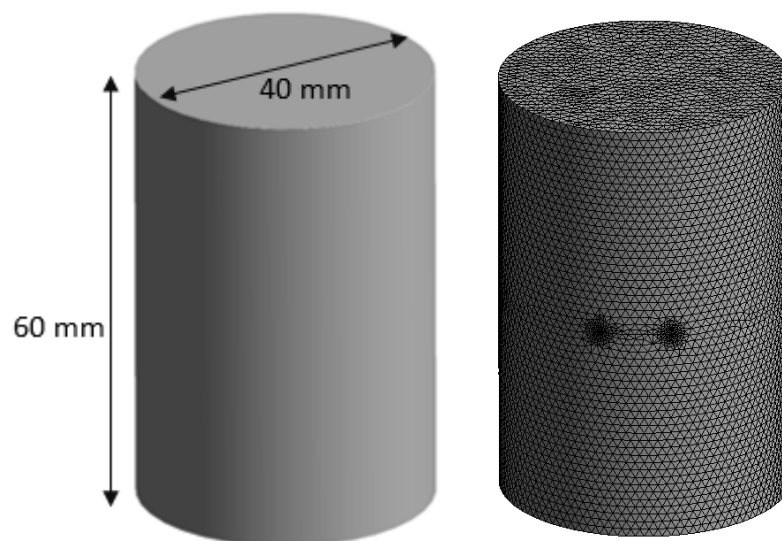


Figure 4.11: Dimensions and mesh of pressure vessel

Table 4.15: Dimensions of pressure vessel for the full-scale and scaled down models

Model	β	Crack length, $2c$ (mm)	Crack depth a (mm)	Δa (mm)	Length (mm)	Diameter (mm)
Full scale	1.00	5.00	1.00	0.20	60.00	40.00
Scaled Model 1	0.80	4.00	0.80	0.16	48.00	32.00
Scaled Model 2	0.50	2.50	0.50	0.10	30.00	20.00
Scaled Model 3	0.25	1.25	0.25	0.05	15.00	10.00

Table 4.16: The loading conditions of pressure vessel at all scales

Model	β	Crack extension Δa (mm)	Applied pressure load (MPa)	Load ratio R
Full scale	1.00	0.20	250	0
Scaled Model 1	0.80	0.16	250	0
Scaled Model 2	0.50	0.10	250	0
Scaled Model 3	0.25	0.05	250	0

Table 4.17. Stress intensity and number of cycles at final crack length of 7 mm for full scale and virtual models

Model	a_f (mm)	Error (%)	K (MPamm ^{0.5})	Error (%)	n_{ps}	Error (%)
Full Scale	7	-	1003.8	-	26702	-
Virtual Model 1	7	0	1014.6	1	26682	1
Virtual Model 2	7	0	1014.3	1	26673	1

Virtual Model 3	7	0	1012.8	1	26637	1
-----------------	---	---	--------	---	-------	---

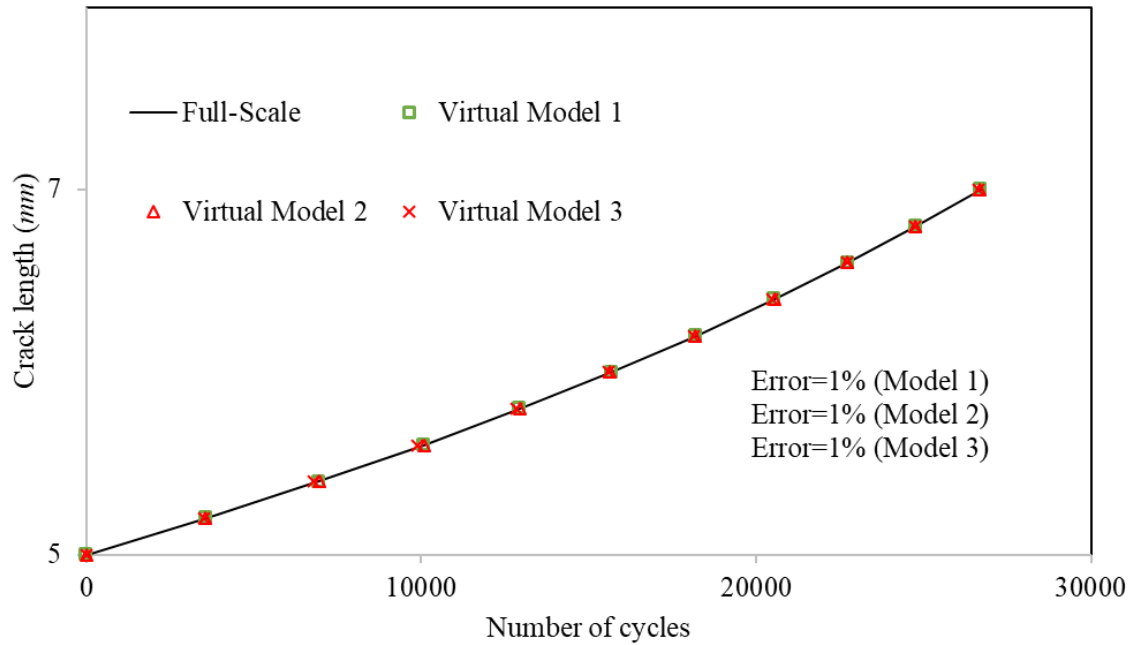
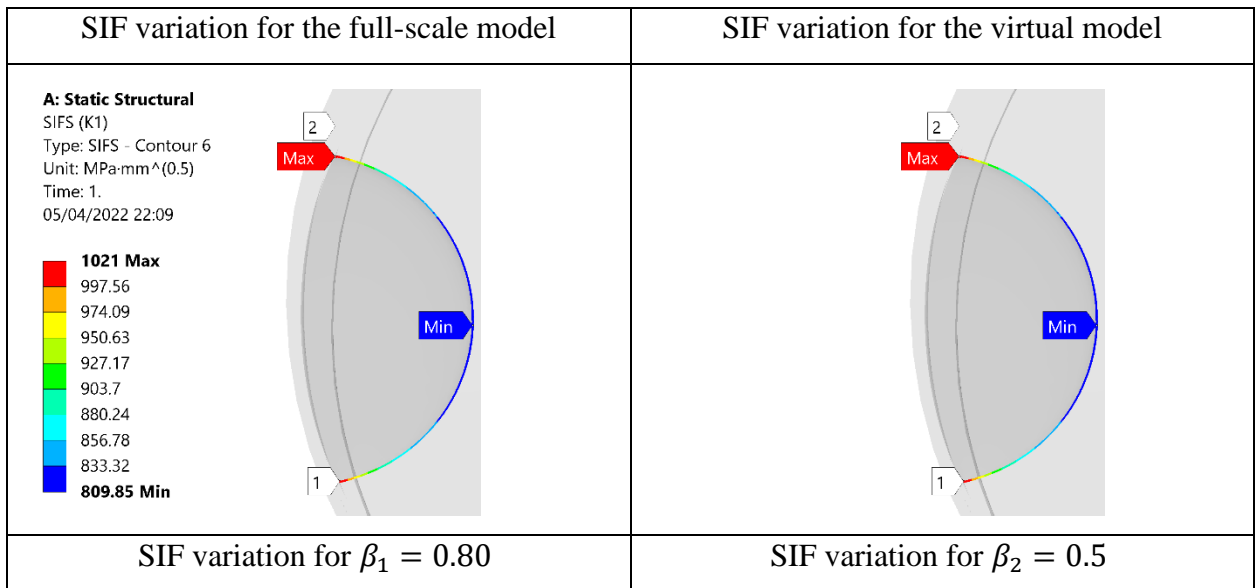


Figure 4.12: Crack length vs number of cycles for full scale and virtual models of pressure vessel



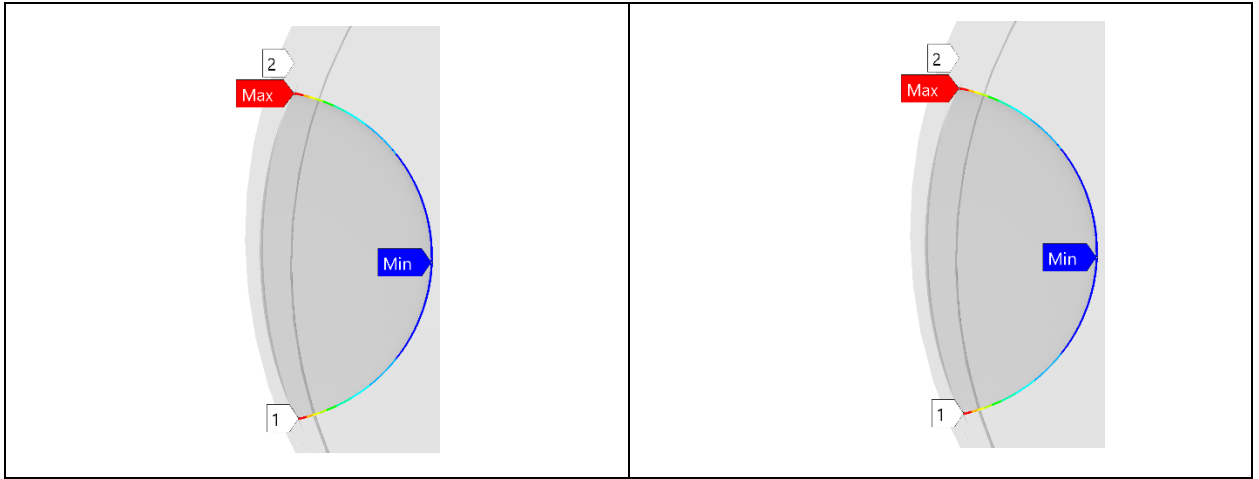


Figure 4.13: Stress intensity factor distribution at the crack front of the pressure vessel for the full-scale model and the two scaled models for virtual model 11 after 2mm crack growth.

The stress intensity factor after 2 mm of crack propagation in the full-scale model is $1003.8 \text{ MPamm}^{0.5}$. The first-order theory returns a value of approximately $1014 \text{ MPamm}^{0.5}$ for virtual models 1 and 2, and $1013 \text{ MPamm}^{0.5}$ for virtual model 3 translating to a 1% error. The lifetime prediction is within a 1% deviation from full-scale fatigue life for all virtual models. The plot of crack length vs number of cycles is presented in Fig. 4.12. Contrasted in Fig. 4.13 is the crack shape after 2mm of crack propagation for the scaled, virtual, and full-scale models. As can be readily seen from this figure, the final crack shape is predicted accurately by the theory. The locations of the maximum and minimum SIF are consistent across all scales. A quantitative analysis is made to determine how well the variation of the stress intensity factor across the crack front for the full-scale model can be predicted. It is appreciated that stress intensity factor for a semi-elliptical crack depends on the position along the crack front [195]. Fig. 4.14 shows the stress intensity factor distribution across the crack front for the full-scale model and virtual models. Excellent agreement is achieved between the virtual model and full-scale model with no more than 3% error.

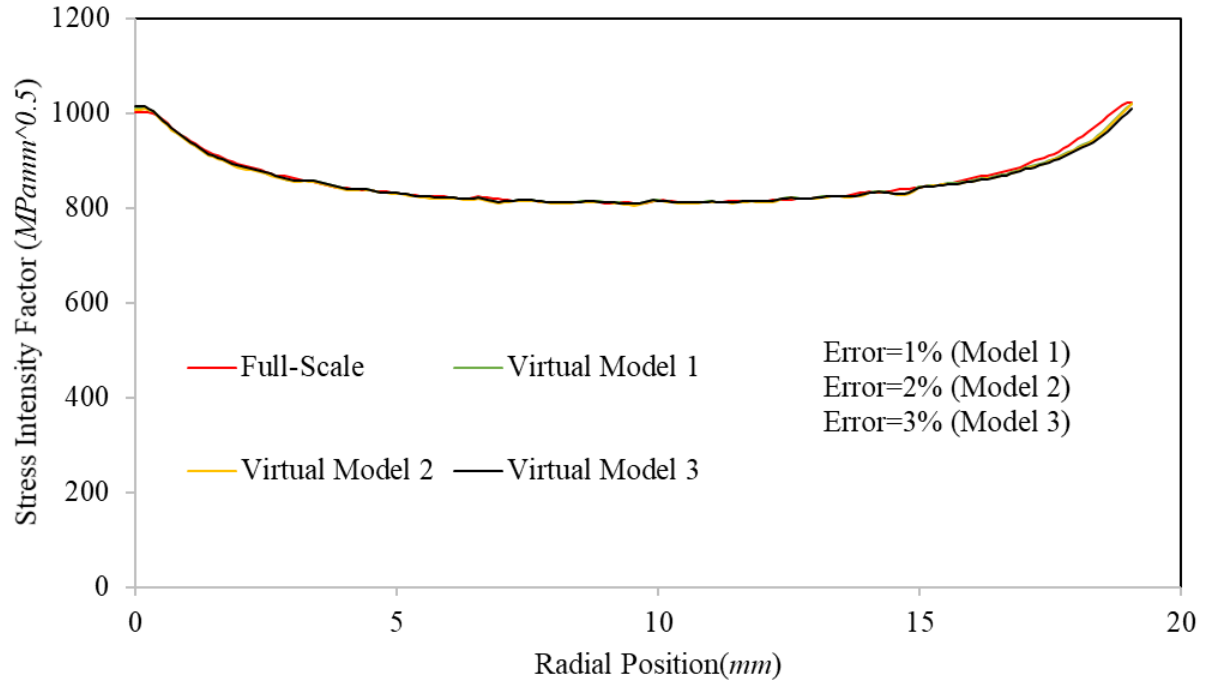


Figure 4.14: Stress intensity factor distribution across the crack front of pressure vessel for the full-scale model and virtual models at final crack length of 7 mm.

Presented in Fig. 4.15 is the fatigue crack growth curve (FCG) of 7% Nickel steel for the pressure vessel. The FCG curve is constructed according to ASTM E647 standard [174]. The crack growth rate da/dn is measured in $(mm/cycle)$ whereas ΔK is measured in $MPamm^{0.5}$. The first order identity is applied to the maximum ΔK values in order to return accurate C and m values. This is because crack extension in SMART solver using Paris law is controlled by the ΔK_{max} at the nodes. The location of the maximum stress intensity factor is at the crack tips in this case study, the left and right crack tip have roughly the same ΔK values see Fig. 4.14. Thus ΔK values at the crack tip are used for all models. The pattern of decreasing C with scale is observed here with m remaining unchanged. This is consistent with the findings of other researchers see [14, 129]. Remarkably, the virtual models predict the Paris law constants of the material with no error confirming the two-experiment approach is a potentially promising approach to fatigue scaling.

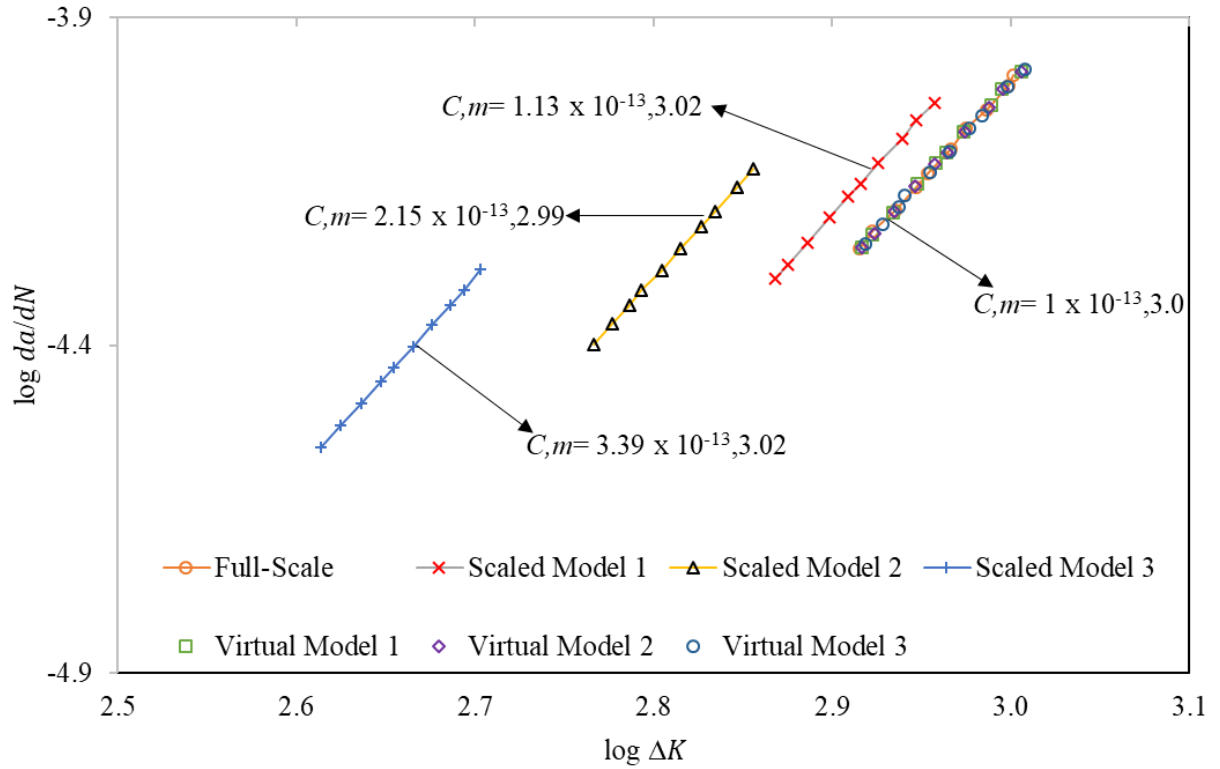


Figure 4.15: Crack growth rate vs stress intensity factor of pressure vessel for full scale, scaled down and virtual models

4.6. Conclusions

The first-order finite similitude theory combines information recorded at two scales to reproduce behaviours at the full scale. The approach has been extended to facilitate its application to empirical crack growth laws. New expressions for the number of cycles to fatigue failure and stress intensity increment with scale have been established under the hypothesis that their product satisfies a second-order finite similitude rule (i.e., $\Delta K_{ts} n_{ts}$ is second order). Previous experimental data for concrete was examined and it was found that, despite the presence of a geometric size effect, it is possible to capture full-scale fatigue behaviour from the results of two scaled experiments. Numerical studies for three different case studies based on Paris law confirmed the initial observations made on experimental data. Exact predictions for the Paris law constants C and m were achieved.

The following specific conclusions were drawn from the analysis and results returned in the paper:

- Application of the approach to available experimental data for concrete confirmed that reasonable predictions for crack growth was possible. Single digit percentage errors were returned for crack growth rate and the number of cycles to failure.

- Numerical experimental trials were employed to investigate fatigue crack growth in a single edge notched tensile specimen, pipe and pressure vessel with the experiments designed based on the exact application of the finite-similitude rules. Fatigue life was predicted very accurately in each case within a 0.1% error in the best models and no more than 9% deviation in the worst-case scenario. Furthermore, critical fracture mechanics parameters such as the stress intensity variation across the crack front was accurately captured by the theory.
- The results from the case studies suggest that use of two scaled models is a possible alternative approach to fatigue crack growth analysis within the fracture mechanics framework. However more experiments both physical and numerical would need to be conducted to further validate the effectiveness of this approach. Furthermore, practical fatigue case studies would need to be performed to determine if mixed crack growth fatigue life predictions can be resolved by the first order finite similitude theory.

Chapter 5 Scaled Fatigue Cracks Under Service Loads

5.1 Introduction

The presence of defects such as flaws, cracks, and voids in the microstructure is virtually unavoidable in engineering structures. Under repeated cyclic loading, these flaws grow eventually resulting in failure of the structure, which is a phenomenon known as fatigue [196]. The importance of designing a structure to withstand fatigue loads cannot be understated as it is estimated that up to 90% of structures fail due to fatigue fracture [1]. The mechanism of fatigue can be broadly divided into three stages, viz: crack initiation, propagation, and final failure. The fatigue life of a structure refers to the summation of time periods for crack initiation, crack propagation and final failure [3]. Fatigue largely remains an empirical science founded on experimental investigations and supported by analytical studies. The first and most popular law (widely known as Paris law [28]) describing steady fatigue growth was proposed by Paris and Erdogan in 1961. This law relates the crack growth rate da/dn (a is crack length and n is the number of cycles) with the elastic stress intensity factor range (ΔK). Since falling under the umbrella of linear elastic fracture mechanics (LEFM) the effects of residual stress, stress ratio and environmental conditions are not accounted for in the Paris law formulation [3]. This has led to various adaptations, which include Walker's formula, accounting for the influence of mean stress [50], and Wheeler's formula, which accommodates sudden overloads on structures [197]. A comprehensive review of different empirical fatigue laws can be found in refs. [3, 198-199]. Overall, there does not exist a universal fatigue model/law that considers the multitude of factors that affect fatigue-crack growth [134].

Because of the increased adoption of the damage tolerance design concept across various industries, there is increased demand for more accurate residual life predictions of components and structures [58]. There are three types of crack loading viz: mode I, mode II, and mode III, which is a categorisation based on the relative direction of the applied load to the direction of crack growth. In mode I, the loading is normal to the crack direction, whereas mode II it is parallel to the crack direction [200]. Most crack-growth studies focus mainly on mode I dominated fatigue loading, however, during the service of various structures, including those of aircraft, the loads experienced by a structure are multidirectional in nature and consequently crack directions are not necessarily normal to the loading direction [200]. All three modes of fracture exist, hence in such practical cases,

the direction of crack growth is not obvious. To successfully predict the crack growth rate of mixed-mode fatigue crack growth, it is convenient to define an equivalent stress intensity factor range (ΔK_{equiv}) that accommodates the stress intensity combination of the different modes. In practice, modes I and II are dominant with the contribution from mode III being usually negligible. Tanaka proposed a modification of Paris law in 1974 by replacing ΔK with an equivalent stress intensity factor range (ΔK_{equiv}) and relating it to crack growth rate [59]. Different ΔK_{equiv} models have been put forward by different researchers since 1974 and a summary can be found in refs. [58, 201-203]. In addition, several stress and energy-based fracture criteria have been postulated to predict the crack growth trajectory. The most popular criterion is the maximum tangential stress (MTS) criterion proposed by Erdogan [65]. This criterion has been widely applied with great success however there are instances where the data does not support its application (see the work of Tanaka [59]). The minimum strain energy density (SED) [204], maximum energy release rate (MERR) [205] and the maximum tangential strain (MTSN) [206] criteria are some of the more commonly used theories to predict crack trajectory under mixed mode conditions.

The consequences of fatigue failure of a structure are enormous with loss of life a very real threat. Consequently, structures must be designed to either resist crack initiation over its lifecycle (safe life approach) or permit crack growth (damage tolerant approach) in circumstances where there is no significant loss of function of the structure. The latter is the focus in this paper in combination with the application of scaled models. Full-scale experimental fatigue testing is a possibility for mixed-mode cracks, but these are invariably time intensive, costly and in some cases impractical due to limited testing capability. The cheaper alternative of scaled experimentation suffers a particular impediment however with size effects making it difficult to interpret the results from scaled studies. Due to the sheer size of structures, it is sometimes impossible to perform full scale testing with scaled testing the only recourse. The specimens tested can often be one or two orders magnitude smaller than the actual structure thus plagued by severe size-effects limiting the usefulness of predictions that can be forecast using scaled models. Engineers compensate for this with very conservative safety factors, but the benefit of reliable predictions from scaled testing is evident, through less conservative safety factors being applied leading to lighter and cheaper products. Size and scale effects were first recorded by Galilei in 1730 observing that the behaviour of structures, systems, and processes change with scale [151]. To make sense of the information recorded at scale an underpinning theoretical foundation is required, which

usually takes the form of similarity methods, which include dimensional analysis [116], energy methods [117], empirical methods [118] among others [13]. Extensive research [127-134] has confirmed the existence of size effects in fracture mechanics and fatigue regardless of material type. Broadly speaking, size effects can be categorised into three, which are statistical, technological, and geometric [126].

The focus in this paper is solely on the observed difference in fatigue crack growth (FCG) rate with geometry change with replica scaling (i.e., identical materials throughout). Geometric size effects are shown in the work of Brose and Dowling [24], where they examined the fatigue crack growth rate of compact tension (CT) specimens. Increasing the width from 25mm to 400mm whilst maintaining constant other dimensions resulted in a decrease by a factor of 5 of the FCG rate of AISI 304 steel. Similarly, Garr and Hesko confirmed that different sized CT specimens resulted in varying FCG rates in Inconel 718 alloy [25]. In addition, quasi-brittle materials such as concrete have been shown to exhibit a size effect [14] indicating that plasticity is not the principal cause. Special mention must be paid to the pioneering work of Barenblatt and Botvina who confirmed, on application of dimensional analysis to the Paris law, that complete self-similarity is impossible for a material under fatigue loading. The theoretical exception is a Paris law exponent m equal to 2 [134], but this cannot occur in the presence of a size effect, which is a contention supported by experimental observation. Alternative formulations to counter the lack of scalability of Paris law have been considered. Bazant and Xu expressed the change in crack length per cycle as a power function of the amplitude of a size-adjusted stress intensity factor [33]. Carpinteri proposed a mono-fractal approach to deal with the dependence of the Paris law exponent on initial crack length [207]. Other multifractal approaches have been put forward by different researchers [208,209]. However, it should be recognised that adaptations of the Paris law will not satisfy the similitude invariance provided by dimensional analysis. The existence of a size effect in and of itself is sufficient to confirm that dimensionless empirical laws must change with scale.

Numerical simulation techniques are increasingly used to support fatigue studies especially for complex geometries where analytical expressions for stress intensity factors are not available. Common methods used are the: boundary element method (BEM), finite difference method (FDM), extended finite element method (XFEM), and the traditional finite element method (FEM) [81]. The literature is replete with examples where these approaches are employed to model fatigue crack growth under a wide range of loading conditions [81]. The research presented in this paper is underpinned by the commercial software ANSYS

taking advantage of its selective adaptive remeshing algorithm (SMART) solver [95]. This solver automatically handles remeshing as the crack propagates into a structure. The advantage of numerical approaches in scaling work is that they can be applied at any scale and consequently can be used to test the validity of scaling theories at reasonable cost. The focus of this paper is on the new scaling approach termed *finite similitude* and its application to fatigue under realistic loads and artefacts. The finite similitude theory [26] introduces new similitude rules that communicate information across a defined number of scaled experiments. The work published in ref. [26] involves one scaled experiment and the associated similitude rule (termed *zeroth-order finite similitude*) is equivalent to scaling with dimensional analysis. The similitude rule involving two scaled experiments at distinct scales (termed *first-order finite similitude*) is the rule salient to fracture. The first order theory has been applied to a broad range of areas spanning different fields and scales [160-165], including low cycle fatigue [190], but limited to simple test samples. The aim of the work presented here is the establishment of rules for design and experimentation of two scaled down replica models (identical materials) to predict the full-scale fatigue behaviour of realistic structures subject to complex loading. A novel feature of the presented work is the application of the finite-similitude approach to mixed-mode fatigue crack growth. Rational relationships with scale are established for key parameters in fatigue-crack growth, which include stress intensity amplitude, and the number of cycles to fatigue failure. These relationships lead to a proof that establishes that Paris law is a first-order similitude rule. This means (and is confirmed in the paper) that the first-order, finite-similitude framework has the advantage of accuracy, that requires little calibration on comparison with alternative scaling approaches (e.g., dimensional analysis), which suffer uncertainty in parameter setting [134].

A brief recap of the finite-similitude theory is presented in Section 5.2, where transport equations for the trial space (where the scaled experiment resides) are projected onto a new scaling space Ω_β , which has similar features to the physical space (where the full-scale component resides). The space Ω_β matches the physical space both temporally and spatially but additionally permits alternative mathematical formulations including fatigue laws. Transport equations pertinent to fatigue and fracture are examined in greater detail in Section 5.3 along with the role played by Ω_β in investigating empirical fatigue relationships such as Paris law. Numerical case studies are considered in Section 5.4 involving different types of

cracks, low and high cycle fatigue and excellent predictions for fatigue life are achieved. The paper finishes with a conclusions section.

5.2 A Description of the Finite Similitude Theory

Details pertaining to the finite similitude theory are available in refs. [159-163] so only a brief description is provided here. Inertial coordinates in the trial and physical spaces are assumed related by the differential space map $d\mathbf{x}_{ts} = \beta d\mathbf{x}_{ps}$, where β is a continuous positive parameter. Space contraction is indicated by $0 < \beta < 1$, no scaling by $\beta = 1$, and expansion by $\beta > 1$. Additionally, time in the two spaces is related by a similar differential identity $dt_{ts} = g dt_{ps}$, where g is a positive continuous function of β . The aim of the theory is to construct transport equations in the physical space Ω_{ps} by projecting the governing equations in the trial space Ω_{ts} onto a facsimile of Ω_{ps} , which is denoted by Ω_β . For the sake of generality, the physics is described on moving control volumes denoted by Ω_{ts}^* , Ω_{ps}^* , and Ω_β^* (with boundaries Γ_{ts}^* , Γ_{ps}^* , and Γ_β^*), respectively. The movement of each control volume is dictated by velocity fields \mathbf{v}_{ts}^* , \mathbf{v}_{ps}^* , and \mathbf{v}_β^* , respectively. Coordinate points on the control volumes are transported by integration of differential identities $d\mathbf{x}_{ts}^* = \mathbf{v}_{ts}^* dt_{ts}$, $d\mathbf{x}_{ps}^* = \mathbf{v}_{ps}^* dt_{ps}$, and $d\mathbf{x}_\beta^* = \mathbf{v}_\beta^* dt_\beta$, respectively. Subscript β properties are obtained by operating on trial space properties and on setting $\mathbf{v}_\beta^* = g\beta^{-1}\mathbf{v}_{ts}^*$ and $dt_\beta = g^{-1}dt_{ts}$ (making $dt_\beta = dt_{ps}$) observe that $d\mathbf{x}_\beta^* = \mathbf{v}_\beta^* dt_\beta = \beta^{-1}\mathbf{v}_{ts}^* dt_{ts} = \beta^{-1}d\mathbf{x}_{ts}^*$ or equivalently $d\mathbf{x}_{ts}^* = \beta d\mathbf{x}_\beta^*$, which is similar to the space scaling map $d\mathbf{x}_{ts} = \beta d\mathbf{x}_{ps}$. Consequently, geometric measures on the control volumes Ω_β^* and Ω_{ts}^* can be related, i.e., $dV_\beta^* = \beta^{-3}dV_{ts}^*$ and $d\Gamma_\beta^* = \beta^{-2}d\Gamma_{ts}^*$. The whole apparatus along with reference spaces Ω_{ts}^{*ref} , Ω_{ps}^{*ref} and Ω_β^{*ref} , which are used to precisely define the motion of the moving control volumes, is depicted in Fig. 5.1. The dotted line between the moving control volumes in Ω_β and Ω_{ps} indicates uncertainty, which is resolved on defining the similitude rule applicable to the velocity field \mathbf{v}_β^* (limited to zeroth order in this work).

The transport equation (in its most generic form [159]) in the trial space is

$$\begin{aligned} \frac{D^*}{D^* t_{ts}} \int_{\Omega_{ts}^*} \rho_{ts} \Psi_{ts} dV_{ts}^* + \int_{\Gamma_{ts}^*} \rho_{ts} \Psi_{ts} (\mathbf{v}_{ts} - \mathbf{v}_{ts}^*) \cdot \mathbf{n}_{ts} d\Gamma_{ts}^* \\ = - \int_{\Gamma_{ts}^*} \mathbf{J}_{ts}^\Psi \cdot \mathbf{n}_{ts} d\Gamma_{ts}^* + \int_{\Omega_{ts}^*} \rho_{ts} \mathbf{b}_{ts}^\Psi dV_{ts}^* \end{aligned} \quad (5.1)$$

where ρ_{ts} , $\boldsymbol{\Psi}_{ts}$, \mathbf{v}_{ts} , \mathbf{J}_{ts}^Ψ , \mathbf{b}_{ts}^Ψ , \mathbf{n}_{ts} are density, physical field, velocity, boundary flux, a source term and the unit normal to boundary Γ_{ts}^* of the control volume Ω_{ts}^* .

This equation is projected onto the space Ω_β by means of substitution of $dV_\beta^* = \beta^{-3} dV_{ts}^*$, $d\Gamma_\beta^* = \beta^{-2} d\Gamma_{ts}^*$, and $dt_\beta = g^{-1} dt_{ts}$, along with multiplication by g and the scalar α_0^Ψ to yield

$$\begin{aligned} \alpha_0^\Psi T_0^\Psi(\beta) = & \frac{D^*}{D^* t_\beta} \int_{\Omega_\beta^*} \rho_\beta \boldsymbol{\Psi}_\beta dV_\beta^* + \int_{\Gamma_\beta^*} \rho_\beta \boldsymbol{\Psi}_\beta (\mathbf{v}_\beta - \mathbf{v}_\beta^*) \cdot \mathbf{n}_\beta d\Gamma_\beta^* + \int_{\Gamma_\beta^*} \mathbf{J}_\beta^\Psi \cdot \mathbf{n}_\beta d\Gamma_\beta^* \\ & - \int_{\Omega_\beta^*} \rho_\beta \mathbf{b}_\beta^\Psi dV_\beta^* = 0 \end{aligned} \quad (5.2)$$

where $\rho_\beta \boldsymbol{\Psi}_\beta = \alpha_0^\Psi \rho_{ts} \beta^3 \boldsymbol{\Psi}_{ts}$, $\mathbf{v}_\beta = \beta^{-1} g \mathbf{v}_{ts}$, $\mathbf{v}_\beta^* = \beta^{-1} g \mathbf{v}_{ts}^*$, $\mathbf{J}_\beta^\Psi = \alpha_0^\Psi \beta^2 g \mathbf{J}_{ts}^\Psi$ and $\rho_\beta \mathbf{b}_\beta^\Psi = \alpha_0^\Psi \rho_{ts} \beta^3 g \mathbf{b}_{ts}^\Psi$.

The form of this equation is typical of a transport equation expected for Ω_β and consequently Ω_β can be viewed as a physical space despite being a mere projection of Eq. (5.1). Eq. (5.2) is required to match the physical space transport equation at $\beta = \beta_0 = 1$, which is assured on setting $\rho_1 \boldsymbol{\Psi}_1 = \rho_{ps} \boldsymbol{\Psi}_{ps}$, $\mathbf{v}_1 = \mathbf{v}_{ps}$, $\mathbf{v}_1^* = \mathbf{v}_{ps}^*$, $\mathbf{J}_1^\Psi = \mathbf{J}_{ps}^\Psi$ and $\rho_1 \mathbf{b}_1^\Psi = \rho_{ps} \mathbf{b}_{ps}^\Psi$, and additionally $\alpha_0^\Psi(1) = 1$ and $g(1) = 1$. Observe the implicit dependence of all the fields of Eq. (5.2) on β as indicated by the notation employed, i.e., ρ_β , \mathbf{v}_β , $\boldsymbol{\Psi}_\beta$, \mathbf{J}_β^Ψ and \mathbf{b}_β^Ψ . Eq. (5.2) is not an approximation in the sense that it captures exactly trial-space physics yet projected onto Ω_β . The objective here though is to capture the behaviour of the physical space Ω_{ps} , which can be achieved with the application of similitude rules. The form the rules should take is as previously introduced in ref. [34] in the form of a recursive identity.

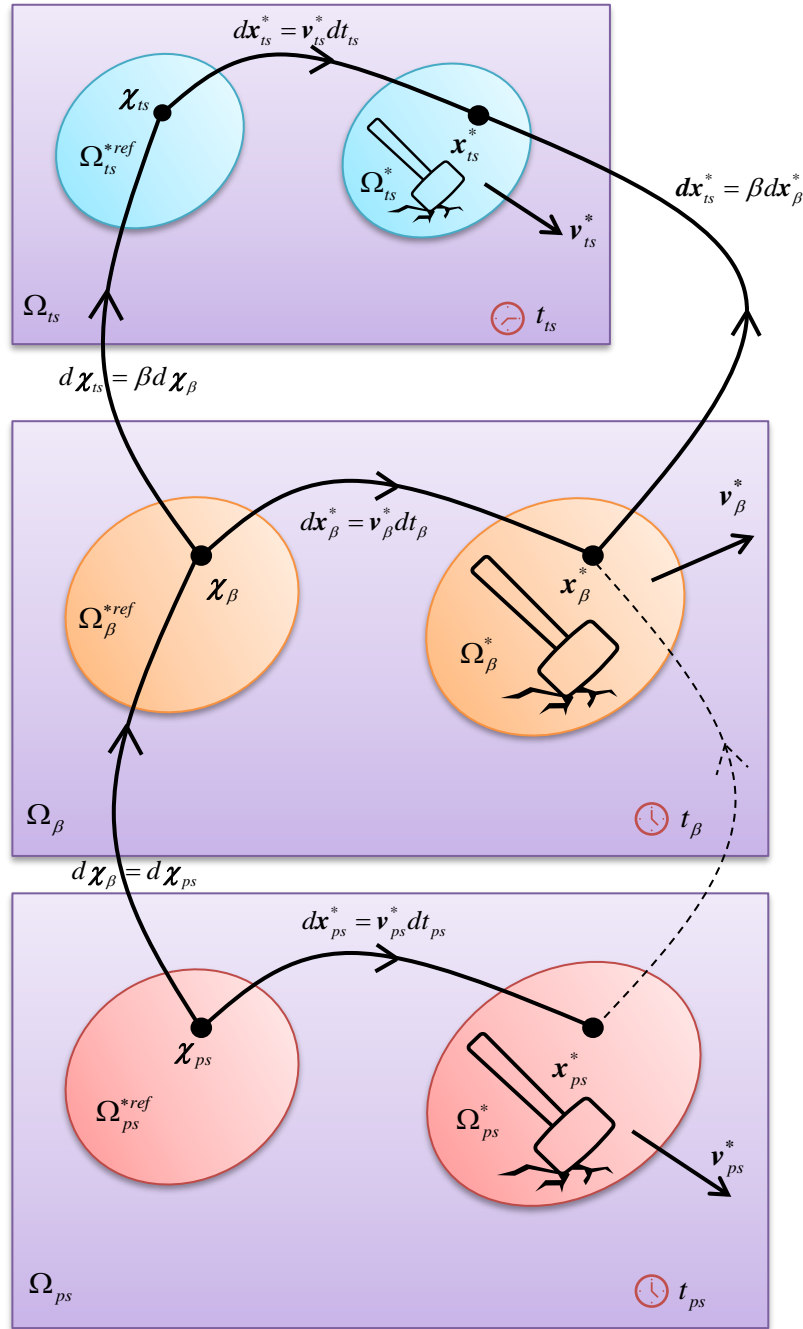


Figure 5.1: Velocity fields and associated reference and moving control volumes in the scaling spaces.

5.2.1 Definition (High-order finite similitude)

The concept of k^{th} -order finite similitude is identified by the lowest derivative that satisfies,

$$T_{k+1}^{\Psi} = \frac{d}{d\beta} (\alpha_k^{\Psi} T_k^{\Psi}) \equiv 0 \quad (5.3)$$

$\forall \beta > 0$, with $\alpha_0^\Psi T_0^\Psi$ defined by Eq. (5.2) and scalars α_k^Ψ are functions of β with $\alpha_k^\Psi(1) = 1$, where the symbol “ \equiv ” signifies that the derivative is identically zero.

The simplest invariance, which is equivalent to dimensional analysis, is returned on setting $k = 0$ and is simply $\frac{d}{d\beta}(\alpha_0^\Psi T_0^\Psi) \equiv 0$. This means that the transport equation Eq. (5.2) (i.e., $\alpha_0^\Psi T_0^\Psi = 0$) suffers no β – dependency. Integration of this rule (between the limits β_1 and $\beta_0 = 1$) gives $\alpha_0^\Psi T_0^\Psi(1) \equiv \alpha_0^\Psi T_0^\Psi(\beta_1)$ confirming that the behaviour on Ω_{β_1} captures exactly what is occurring on the physical space Ω_{ps} . This is the situation where the scaling problem suffers no scale effects as traditionally defined and it is the situation captured by dimensional analysis. Unfortunately, this rule is not applicable to fracture and fatigue since as established above a size effect is present. The rule that applies is the *first-order finite similitude* rule, which is obtained on setting $k = 1$ (i.e., $T_2^\Psi \equiv 0$) in the above definition to provide:

$$T_2^\Psi = \frac{d}{d\beta}(\alpha_1^\Psi T_1^\Psi) = \frac{d}{d\beta} \left(\alpha_1^\Psi \frac{d}{d\beta}(\alpha_0^\Psi T_0^\Psi) \right) \equiv 0 \quad (5.4)$$

which although is the focus of the work some reference is required to second order, which is obtained on setting $k = 2$ to provide:

$$\begin{aligned} T_3^\Psi &= \frac{d}{d\beta}(\alpha_2^\Psi T_2^\Psi) = \frac{d}{d\beta} \left(\alpha_2^\Psi \frac{d}{d\beta}(\alpha_1^\Psi T_1^\Psi) \right) \\ &= \frac{d}{d\beta} \left(\alpha_2^\Psi \frac{d}{d\beta} \left(\alpha_1^\Psi \frac{d}{d\beta}(\alpha_0^\Psi T_0^\Psi) \right) \right) \equiv 0 \end{aligned} \quad (5.5)$$

which involves three derivatives, so is a little more involved but needed here, nevertheless.

Like the zeroth order rule, Eqs. (5.4) and (5.5) can be readily integrated [189] to give:

$$\alpha_0^\Psi T_0^\Psi(1) = \alpha_0^\Psi T_0^\Psi(\beta_1) + R_1^\Psi (\alpha_0^\Psi T_0^\Psi(\beta_1) - \alpha_0^\Psi T_0^\Psi(\beta_2)) \quad (5.6)$$

and

$$\begin{aligned} \alpha_0^\Psi T_0^\Psi(1) &= \alpha_0^\Psi T_0^\Psi(\beta_1) + R_{1,1}^\Psi (\alpha_0^\Psi T_0^\Psi(\beta_1) - \alpha_0^\Psi T_0^\Psi(\beta_2)) \\ &\quad + R_2^\Psi R_{1,1}^\Psi (\alpha_0^\Psi T_0^\Psi(\beta_1) - \alpha_0^\Psi T_0^\Psi(\beta_2)) \\ &\quad + R_{1,2}^\Psi (\alpha_0^\Psi T_0^\Psi(\beta_2) - \alpha_0^\Psi T_0^\Psi(\beta_3)) \end{aligned} \quad (5.7)$$

where R_1^Ψ , $R_{1,1}^\Psi$, $R_{1,2}^\Psi$, and R_2^Ψ are parameters that to a certain extent are free to be set to the advantage of the scaling theory.

5.3 Finite Similitude Applied to Fatigue

Eq. (5.6) on application to the transport equations in Appendix B give rise to the identities in Table 5.1. Additional fields over and above those present in the transport equations are included in this table. All relevant fields salient to solid mechanics can be obtained, which is a feature of the finite similitude approach despite making no reference to constitutive laws.

Table 5.1. First-order finite similitude identities

Fields	Compact representation	Expanded representation
Displacement	$\mathbf{u}_1 = \mathbf{u}_{\beta_1} + R_1 (\mathbf{u}_{\beta_1} - \mathbf{u}_{\beta_2})$	$\mathbf{u}_1 = \beta_1^{-1} \mathbf{u}_{ts1} + R_1 (\beta_1^{-1} \mathbf{u}_{ts1} - \beta_2^{-1} \mathbf{u}_{ts2})$
Velocity	$\mathbf{v}_1 = \mathbf{v}_{\beta_1} + R_1 (\mathbf{v}_{\beta_1} - \mathbf{v}_{\beta_2})$	$\mathbf{v}_1 = g_1 \beta_1^{-1} \mathbf{v}_{ts1} + R_1 (g_1 \beta_1^{-1} \mathbf{v}_{ts1} - g_2 \beta_2^{-1} \mathbf{v}_{ts2})$
Body force	$\mathbf{b}_1 = \mathbf{b}_{\beta_1} + R_1 (\mathbf{b}_{\beta_1} - \mathbf{b}_{\beta_2})$	$\begin{aligned} \rho_1 \mathbf{b}_1^v &= \alpha_{01}^v \rho_{ts1} g_1 \beta_1^3 \mathbf{b}_{ts1}^v \\ &+ R_1 (\alpha_{01}^v \rho_{ts1} g_1 \beta_1^3 \mathbf{b}_{ts1}^v - \alpha_{02}^v \rho_{ts2} g_2 \beta_2^3 \mathbf{b}_{ts2}^v) \end{aligned}$
Stress	$\boldsymbol{\sigma}_1 = \boldsymbol{\sigma}_{\beta_1} + R_1 (\boldsymbol{\sigma}_{\beta_1} - \boldsymbol{\sigma}_{\beta_2})$	$\begin{aligned} \boldsymbol{\sigma}_1 &= \alpha_{01}^v g_1 \beta_1^2 \boldsymbol{\sigma}_{ts1} \\ &+ R_1 (\alpha_{01}^v g_1 \beta_1^2 \boldsymbol{\sigma}_{ts1} - \alpha_{02}^v g_2 \beta_2^2 \boldsymbol{\sigma}_{ts2}) \end{aligned}$
Strain	$\boldsymbol{\epsilon}_1 = \boldsymbol{\epsilon}_{\beta_1} + R_1 (\boldsymbol{\epsilon}_{\beta_1} - \boldsymbol{\epsilon}_{\beta_2})$	$\boldsymbol{\epsilon}_1 = \boldsymbol{\epsilon}_{ts1} + R_1 (\boldsymbol{\epsilon}_{ts1} - \boldsymbol{\epsilon}_{ts2})$
Strain rate	$\dot{\boldsymbol{\epsilon}}_1 = \dot{\boldsymbol{\epsilon}}_{\beta_1} + R_1 (\dot{\boldsymbol{\epsilon}}_{\beta_1} - \dot{\boldsymbol{\epsilon}}_{\beta_2})$	$\dot{\boldsymbol{\epsilon}}_1 = g_1 \dot{\boldsymbol{\epsilon}}_{ts1} + R_1 (g_1 \dot{\boldsymbol{\epsilon}}_{ts1} - g_2 \dot{\boldsymbol{\epsilon}}_{ts2})$

The zeroth-order condition $\mathbf{v}_{ps}^* = \mathbf{v}_1^* = \mathbf{v}_\beta^*$ with $\Omega_\beta^* = \Omega_{ps}^*$ permits differentiation with respect to β directly applied to the integrands in the transport equations. This means that, for first order finite similitude, identity Eq. (5.6) applies to fields and takes then form

$\frac{d}{d\beta} \left(\alpha_1 \frac{d\aleph_\beta}{d\beta} \right) \equiv 0$, where \aleph_β is any field under the compact-form header in Table 5.1.

Similarly, the second-order identity applies $\frac{d}{d\beta} \left(\alpha_2 \frac{d}{d\beta} \left(\alpha_1 \frac{d\aleph_\beta}{d\beta} \right) \right) \equiv 0$ for the same fields.

Note the following proposition and short proof along with an important hypothesis for fatigue.

Proposition: The product of two first order fields is second order in the sense that fields \aleph_β and Ξ_β defined on Ω_β satisfying $\frac{d}{d\beta} \left(\alpha_1 \frac{d\aleph_\beta}{d\beta} \right) = 0$ and $\frac{d}{d\beta} \left(\alpha_1 \frac{d\Xi_\beta}{d\beta} \right) = 0$, respectively, then the product $\aleph_\beta \Xi_\beta$ with $\alpha_2 = \alpha_1$ satisfies $\frac{d}{d\beta} \left(\alpha_2 \frac{d}{d\beta} \left(\alpha_1 \frac{d\aleph_\beta \Xi_\beta}{d\beta} \right) \right) = 0$.

Proof: Note that

$$\alpha_1 \frac{d}{d\beta} \left(\alpha_1 \frac{d\aleph_\beta \Xi_\beta}{d\beta} \right) = \alpha_1 \frac{d}{d\beta} \left(\alpha_1 \aleph_\beta \frac{d\Xi_\beta}{d\beta} + \alpha_1 \frac{d\aleph_\beta}{d\beta} \Xi_\beta \right) = 2 \left(\alpha_1 \frac{d\aleph_\beta}{d\beta} \right) \left(\alpha_1 \frac{d\Xi_\beta}{d\beta} \right) \quad (5.8)$$

which is identically zero on differentiation with respect to β , which confirms the result.

Hypothesis: The product $\Delta K_{ts} n_{ts}$ is second order with $\Delta K_{ts} n_{ts} = \Delta K_\beta n_\beta$, where ΔK_β and n_β are the stress intensity and number of cycles on Ω_β .

This hypothesis is hinting at the broad notion that empirical rules have a close association with finite-similitude rules, particularly in situations where scale effects (as previously defined) are eliminated. It is convenient to define scale effects more broadly with the arrival of finite similitude rules, with zeroth, first, and second-order scale effects referring to the respective similitude identities not being satisfied. The claim here is that the product $\Delta K_{ts} n_{ts}$ is a first-order scale effect (and zeroth order therefore), but not a second order one. The interest in the product $\Delta K_{ts} n_{ts}$ stems from the fact that as ΔK_{ts} increases the expectation is for n_{ts} to reduce. Note additionally stress intensity amplitude ΔK_{ts} is connected to the stress field through the identity $\Delta K_{ts} = F_{ts} \Delta \sigma_{ts} \sqrt{\pi a_{ts}}$, where F_{ts} is a shape factor, a_{ts} is crack length, and $\Delta \sigma_{ts}$ is the change in stress amplitude. But σ_β and σ_{ts} are related by $\sigma_\beta = \alpha_0^v \beta^2 g \sigma_{ts}$ with $a_\beta = \beta^{-1} a_{ts}$ and consequently $\Delta K_\beta = \alpha_0^v \beta^{3/2} g \sigma_{ts} \Delta K_{ts}$. Matching the stress field around the crack is a clear requirement, so $\sigma_\beta = \sigma_{ts}$ gives rise to $\alpha_0^v g = \beta^{-2}$ and ultimately $\Delta K_\beta = \beta^{-1/2} \Delta K_{ts}$. The hypothesis $\Delta K_{ts} n_{ts} = \Delta K_\beta n_\beta$ therefore provides $n_\beta = \beta^{1/2} n_{ts}$, and that ΔK_β and n_β are first order, satisfying differential equations

$\frac{d}{d\beta} \left(\alpha_1 \frac{d\Delta K_\beta}{d\beta} \right) = 0$ and $\frac{d}{d\beta} \left(\alpha_1 \frac{dn_\beta}{d\beta} \right) = 0$. These can be integrated to produce identities of the type found in Table 5.1, i.e.,

$$\Delta K_1 = \Delta K_{\beta_1} + R_1 (\Delta K_{\beta_1} - \Delta K_{\beta_2}) \quad (5.9a)$$

$$= \beta_1^{-1/2} \Delta K_{ts1} + R_1 (\beta_1^{-1/2} \Delta K_{ts1} - \beta_2^{-1/2} \Delta K_{ts2})$$

$$n_1 = n_{\beta_1} + R_1 (n_{\beta_1} - n_{\beta_2}) = \beta_1^{1/2} n_{ts1} + R_1 (\beta_1^{1/2} n_{ts1} - \beta_2^{1/2} n_{ts2}) \quad (5.9b)$$

which connect results obtained from two scaled experiments to the physical space.

Note that R_1 (along with α_1) is presently undefined, but imposition of the first-order identity $\frac{d}{d\beta} \left(\alpha_1 \frac{d\mathbf{u}_\beta}{d\beta} \right) \equiv 0$ on displacement with $\mathbf{u}_\beta = \beta^{-1} \mathbf{u}_{ts}$ and under the assumption that \mathbf{u}_{ts} is invariant of β provides $\frac{d}{d\beta} \left(\alpha_1 \frac{d\beta^{-1}}{d\beta} \right) = 0$ or equivalently $\alpha_1 = \beta^2$ satisfying $\alpha_1(1) = 1$. The same invariance applied to displacement in Table 5.1 gives

$$R_1 = \frac{1 - \beta_1^{-1}}{\beta_1^{-1} - \beta_2^{-1}} \quad (5.10)$$

which returns a definitive expression for R_1 .

It is worth noting that the identities $\frac{d}{d\beta} \left(\alpha_1 \frac{d\Delta K_\beta}{d\beta} \right) = 0$ and $\frac{d}{d\beta} \left(\alpha_1 \frac{dn_\beta}{d\beta} \right) = 0$ can be directly integrated (since $\alpha_1 = \beta^2$) to provide a form useful in empirical growth rules. Direct integration provides

$$n_\beta = \beta^{1/2} n_{ts} = -A\beta^{-1} + D \quad (5.11a)$$

$$\Delta K_\beta = \beta^{-1/2} \Delta K_{ts} = -H\beta^{-1} + E \quad (5.11b)$$

which are remarkably simple expressions relating stress-intensity amplitude and number of cycles to scale, where A , D , H and E are constants of integration.

Note additionally that $\Delta K_\beta = F_\beta \Delta \sigma_\beta \sqrt{\pi a_\beta}$, where $a_\beta = \beta^{-1} a_{ts}$, $\Delta \sigma_\beta = \Delta \sigma_{ts}$ and the shape factor $F_\beta = F_{ts}$ for the sake of simplicity is assumed to be zeroth order, i.e., independent of β , which is a large-plate assumption. The fact that $\Delta \sigma_\beta$ is zeroth order means that $\sqrt{a_\beta}$ is first order (since ΔK_β is assumed to be first order). This is equivalent to a_β being second order since it is the product of two first-order terms, i.e., $a_\beta = \sqrt{a_\beta} \sqrt{a_\beta}$. This result (under the large plate assumption) provides insight into constraints imposed on the form any empirical fatigue growth relationship might take. Consider a crack growth law of the form

$$\frac{da_\beta}{dn_\beta} = g_\beta(\Delta K_\beta, a_\beta, C_i) \quad (5.12)$$

which is assumed to exist on Ω_β , where g_β is a function of $\Delta K_\beta, a_\beta, C_i$, with C_i being material parameters assumed invariant with scale.

Eq. (5.12) can be written as $\frac{da_\beta}{d\beta} = g_\beta \frac{dn_\beta}{d\beta}$ and under the assumption that n_β is first order (as is ΔK_β) and a_β is second order it immediately follows that g_β must be first order. The proof for this follows exactly that for the proposition above, i.e., multiply throughout by α_1 differentiate with respect to β , multiply by α_1 again, and the expression disappears under the final differentiation if and only if g_β is first order. Consequently, g_β satisfies the relationships

$$g_1 = g_{\beta_1} + R_1 (g_{\beta_1} - g_{\beta_2}) = -B\beta^{-1} + G \quad (5.13)$$

where B and G are integration constants.

A question of immediate interest is does Paris law $(da_{ts}/dn_{ts}) = C_{ts}(\Delta K_{ts})^{m_{ts}}$ satisfy these requirements? Substitution of $n_{ts} = \beta^{-1/2}n_\beta$, $a_{ts} = \beta a_\beta$ and $\Delta K_{ts} = \beta^{1/2}\Delta K_\beta$ provides $(da_\beta/dn_\beta) = C_{ts}\beta^{-3/2}\beta^{m_{ts}/2}(\Delta K_\beta)^{m_{ts}} = C_\beta(\Delta K_\beta)^{m_\beta}$, which is of the form of Eq. (5.12), where $C_\beta = \beta^{-3/2}\beta^{m_{ts}/2}C_{ts}$ and $m_\beta = m_{ts}$. This leads to the following important proposition.

Proposition: Paris law $(da_\beta/dn_\beta) = C_\beta(\Delta K_\beta)^{m_\beta}$ is a first-order relationship.

Proof: The proof follows immediately since $g_\beta = C_\beta(\Delta K_\beta)^{m_\beta} = da_\beta/dn_\beta$ is first order as deduced above confirming that Paris law is first order.

An alternative more direct proof is to observe that a_β is second order with n_β being first order leads to the realisation that the derivative da_β/dn_β is first order and the result follows.

5.4 Practical Application of First Order Finite Similitude Rules.

The procedure for the application of first-order, finite-similitude rules for fatigue testing is presented in this section. It transpires that, despite its mathematical complexity, the application of the approach is reasonably straightforward. The application involves the following steps:

- (i) Confirm geometry, loading and boundary conditions, and material properties of the full-scale model.

- (ii) Decide on geometric scaling factors β_1 and β_2 for the scaled models.
- (iii) Set $\alpha_{01}^v g_1 = \beta_1^{-2}$ and $\alpha_{02}^v g_2 = \beta_2^{-2}$.
- (iv) Determine scaling factor R_1 using Eq. (5.10).
- (v) Determine boundary conditions and applied loads for the scaled models. Scaling factors $\alpha_{01}^v g_1$ and $\alpha_{02}^v g_2$ relate the applied loads in the scaled models to the full-scale model. For example, for an applied stress loading, $\sigma_{ts1} = \sigma_{ps} / \alpha_{01}^v g_1 \beta_1^2$. In the case of an applied force, $F_{ts1} = F_{ps} / \alpha_{01}^v g_1$.
- (vi) Perform experimental trials on the scaled models.
- (vii) Combine the results returned from the scaled model using the field equations presented in Table 5.1.
- (vii) Despite being second-order, crack length from the scaled models can be combined to good accuracy using the first-order approximation,

$$a_{ps} = \beta_1^{-1} a_{ts1} + R_1 (\beta_1^{-1} a_{ts1} - \beta_2^{-1} a_{ts2}) \quad (5.14a)$$

with the crack growth rate provided by

$$\left(\frac{da}{dn}\right)_{ps} = \beta_1^{-\frac{3}{2}} \left(\frac{da}{dn}\right)_{ts1} + R_1 \left(\beta_1^{-\frac{3}{2}} \left(\frac{da}{dn}\right)_{ts1} - \beta_2^{-\frac{3}{2}} \left(\frac{da}{dn}\right)_{ts2} \right) \quad (5.14b)$$

which is a first-order relationship for $(da/dn)_\beta$, obtained on substitution of $da_\beta = \beta^{-1} da_{ts}$ and $dn_\beta = \beta^{1/2} dn_{ts}$.

- (viii) Finally, stress intensity amplitude and the number of cycles to failure are obtained using Eq. (5.9a) and Eq. (5.9b), respectively.

The procedure presented here provides a framework for performing scaled-fatigue tests, which is applied to practical examples in the next section.

5.5 Numerical Experimentation

In this section three different case studies of fatigue loaded cracked components are studied encompassing both low and high cycle fatigue using the procedure outlined in section 5.4. The aim is to illustrate the ease of application of the theory and to demonstrate its effectiveness in dealing with challenging crack growth problems commonly encountered during the service life of structures (e.g., non-planar crack growth). The tests considered are the compact tension shear specimen (CTS), a wing fuselage-attachment lug, and a t-joint with an inclined semi-elliptical crack. ANSYS 2021 is the software of choice, and crack propagation is studied by means of the Ansys SMART solver [95]. For all the case studies,

full 3D models are established to closely reflect reality. For mixed mode crack growth problems, the following equations are employed in Ansys:

$$\Delta K_{equiv} = \frac{1}{2} \cos \left(\frac{\beta}{2} \right) [\Delta K_I (1 + \cos \beta) - 3 \Delta K_{II} \sin \beta] \quad (5.15a)$$

$$\beta' = \cos^{-1} \left[\frac{3(K_{II}^{max})^2 + (K_I^{max}) \sqrt{(K_I^{max})^2 + 8(K_{II}^{max})^2}}{(K_I^{max})^2 + 9(K_{II}^{max})^2} \right] \quad (5.15b)$$

$$\Delta K_I = K_I^{max} - K_I^{min} = (1 - R) K_I^{max} \quad (5.15c)$$

$$\Delta K_{II} = K_{II}^{max} - K_{II}^{min} = (1 - R) K_{II}^{max} \quad (5.15d)$$

where ΔK_{equiv} is the equivalent stress intensity factor, β is the direction of propagation, ΔK_I and ΔK_{II} are the variation in modes I and II stress intensity factors, respectively, and R is the load ratio, and superscripts min and max refer to minimum and maximum values, respectively.

The equivalent stress intensity factor ΔK_{equiv} is used in conjunction with Paris law to calculate the crack growth rate, which is the approach applied to all the case studies. Paris law is the recommended law for fatigue life predictions in industrial applications as per BS7910 standard [210] and the API 579 standard [211]. The Ansys SMART solver works by advancing the crack front by a small amount Δa and then updating the mesh around the new crack front. This process is repeated for a prescribed number of sub-steps until the desired final crack length a_f . For scaled models, the zeroth-order condition $\Delta a_{ts} = \beta \Delta a_{ps}$ for crack extension reasonably applies and consequently, matching the number of sub-steps for all models permits fracture-mechanics outputs to be combined at each sub-step according to the outlined procedure in Section 5.4. The newly introduced crack front is assumed to behave in accordance with a cohesive zone model. The automatic re-meshing capability of Ansys eliminates the major drawback of long pre-processing times associated with fatigue analysis within a conventional finite-element framework. The first-order similitude theory has been shown to replicate exactly the behaviour of cohesive zone models for both monotonic [189] and fatigue loading [190].

The work of Sajith et al. [212] on the CTS specimen is replicated first to provide confidence in the correctness of the simulation and to validate the fatigue crack growth results. Constant amplitude force or stress loadings are applied in all case studies. Mesh sensitivity studies have been performed for each case study to optimize solution accuracy and computational cost. An element size of 0.5 mm or smaller is employed local to the crack tip for all cases. Elements with a size of 1 mm are used in other regions of the specimen to reduce

computational costs. The number of elements is kept identical for all scaled models to eliminate the effects of mesh dependency, and second-order tetrahedral elements (SOLID187) [95] are employed throughout. This is achieved by multiplying the element sizes used in the full-scale model by the β value of the scaled model. Three different materials are considered to demonstrate that positive outcomes are not tied to a specific material. Al-6061 is used for case study 1 [212], structural steel [213] is used for case study 2, whereas AISI 316 stainless steel is the material of choice for the t-joint with material properties according to those in ref. [214]. All ΔK values in ref. [213] are in units $\text{MPa}\sqrt{\text{m}}$ ^{0.5} thus a conversion is applied to return a C value with the correct units in Table 5.2. Replica scaling is then focus here with identical material used for the full scale and all associated scaled-down models.

Table 5.2: Mechanical properties of materials used in numerical analysis [212-214]

Material	Young's Modulus (GPa)	Poisson's ratio, ν	Yield strength (MPa)	Ultimate tensile strength (MPa)	Paris law parameters	
					C (mm/cycle) $/(\text{MPa m}^{0.5})^m$	m
Al-6061 T6 alloy	68	0.33	270	307	4.34×10^{-7}	2.6183
AISI 316 stainless steel	192	0.27	295	582	4.05×10^{-8}	2.3483
Structural Steel	206	0.3	250	460	1.85×10^{-7}	2.26

5.5.1. Verification of numerical results

The focus of this section is performing a thorough validation of the Ansys SMART solver by comparison against previous published experimental and numerical data. This is to ensure that the fatigue life and crack path predictions returned are accurate before applying first-order finite similitude scaling rules. Sajith et al. [212] conducted fatigue tests on a compact tension shear (CTS) specimen for Al-6061 by means of the well-known Richard's apparatus [64]. Their findings were validated numerically by Fageehi and Alshoaibi [215]

using the same Ansys SMART solver in this study. Details of the geometry and boundary conditions are shown in Fig. 5.2. The specimen thickness is 15 mm. Two different loading angles (θ) corresponding to 30° and 60° are examined. The magnitude of the load P , remotely applied in the experiment is 16kN with a load ratio $R = 0.1$ for both cases. The finite element model however is loaded by the reaction forces generated at the six loading holes. The magnitude of the reaction forces for each loading hole is set by:

$$P_1 = P_4 = P \left(\frac{1}{2} \cos \theta + \frac{c}{b} \sin \theta \right) \quad (5.16a)$$

$$P_2 = P_5 = P \sin \theta \quad (5.16b)$$

$$P_3 = P_6 = P \left(\frac{1}{2} \cos \theta - \frac{c}{b} \sin \theta \right) \quad (5.16c)$$

where, P is the magnitude of the applied load, θ is the loading angle and P_i are the reaction forces at the loading hole, and additionally b and c are the lengths identified in Fig. 2.

Fig. 5.3 shows the evolution of crack length with time, where the numerical findings from the current study agrees with those of Fageehi and Alshoaibi [215] and the experimental data of Sajith et al. [212]. The deviation between the final value of the crack length for the 30° and 60° loading case obtained numerically in this work and experimental data [212] are 1% and 2%, respectively. A critical feature of a mixed-mode fatigue process is the initial direction of crack growth, which is defined by the crack-propagation angle (β), also referred to as the initiation angle in some works. The crack propagation angle is the angle formed between the propagated crack and the centreline of the specimen.

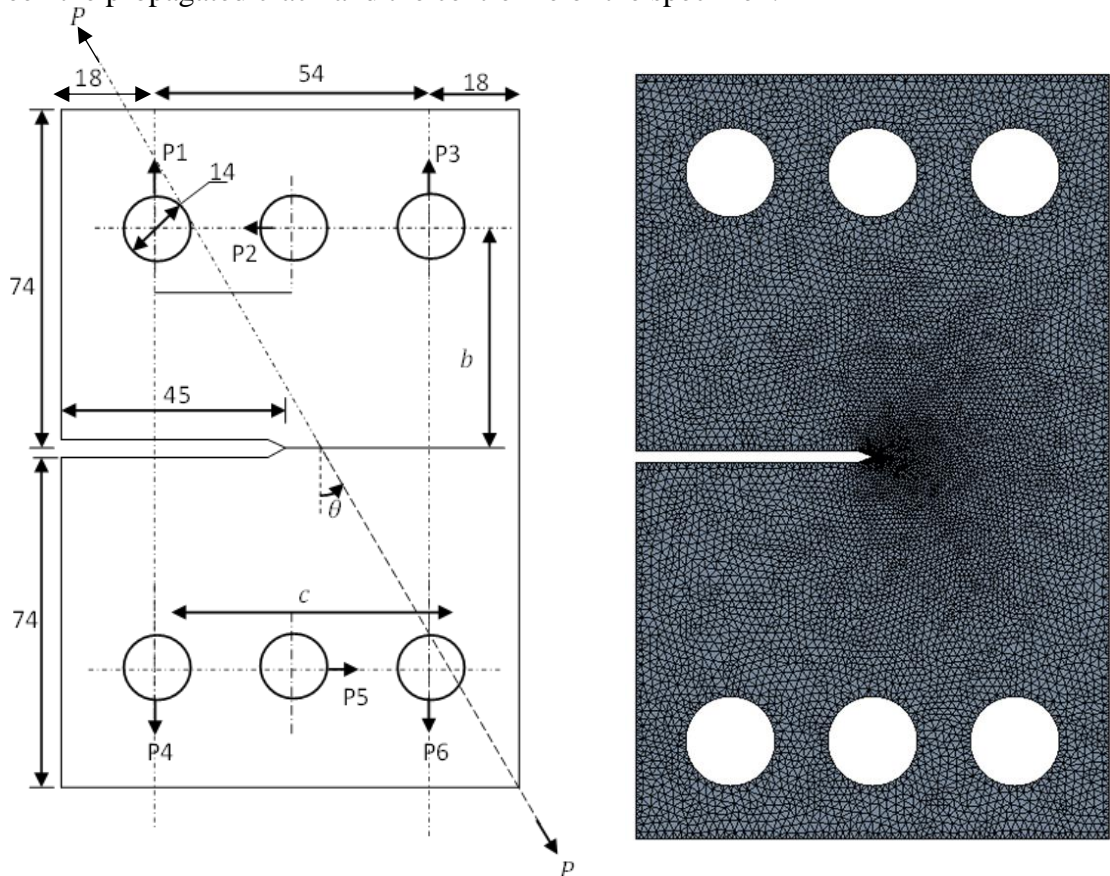


Figure 5.2: Compact tension shear (CTS) specimen dimensions and mesh.

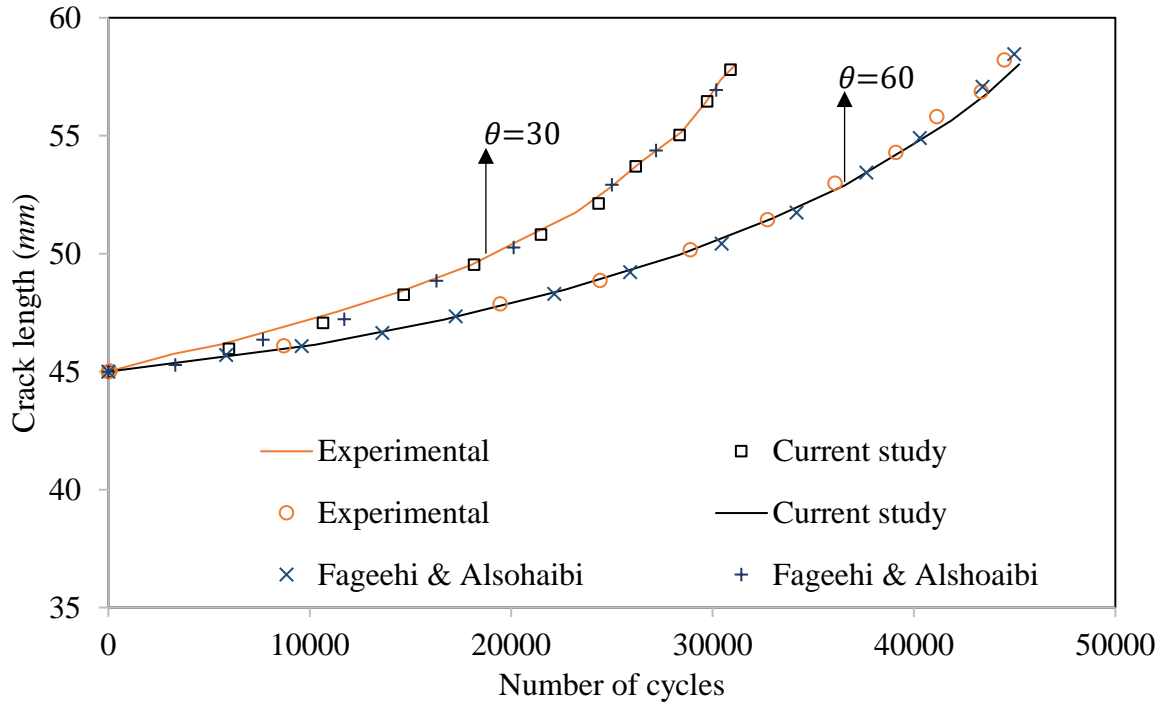


Figure 5.3: Comparison of fatigue life between the numerical results obtained from Ansys, experimental data [212] and numerical data [215] for 30° and 60° loading angles.

Tabulated in Table 5.3 is the crack-propagation angle for both loading angles for the current and previous studies. Under experimental loading the crack propagates upwards at an angle of 31.6° and 51.3° to the horizontal centre line of the specimen for the 30° and 60° loading angles, respectively. Numerical results in the present study obtained from Ansys return crack-propagation angles of 31° and 50°, respectively, which contrast favourable with the numerical results in ref. [212] with corresponding angles of 30.7° and 50.6°. Finally, the paths taken by the crack as it propagates is of interest and is examined in Fig. 5.4. A direct correlation can be observed between the increase in loading angle and the angle of crack propagation, where for 60° the crack propagates at a steeper propagation angle compared to a loading angle of 30°. The closeness of the results provides confidence in the application of the Ansys SMART solver to non-planar (mixed-mode fatigue) crack growth. The

validated numerical procedure is employed in the subsequent sections to investigate the efficacy of the proposed scaling method based on the first-order finite similitude theory.

Table 5.3. Comparison of crack propagation angle for 30° and 60° loading angles of numerical model, experimental data [212] and numerical data [212]

Model	Loading angle θ (°)	Propagation angle β' (°)	Error (%)	Loading angle θ (°)	Propagation angle β' (°)	Error (%)
Experiment [212]	30	31.6	-	60	52.1	-
Ansys numerical model	30	31.0	2	60	50	4
Numerical model [212]	30	30.7	3	60	50.6	3



Crack path for numerical model (30°)	Experimental crack path (30°) [212]
	
Crack path for numerical model (60°)	Experimental crack path (60°) [212]



Figure 5.4: Comparison of crack paths between the numerical results of the current study and experimental study of Sajith et al. [212]

5.5.2. Case study I: Compact tension shear specimen (CTS)

A compact tension shear specimen made from Al 6061 is analysed in this section. The geometry of the CTS specimen is exactly the same as highlighted in Fig. 5.2. The three upper loading pins are subjected to a cyclic applied force whereas the bottom three loading pins are fixed. For a loading angle of 30° the magnitude of the applied force is 18kN whereas for a loading angle of 60° its magnitude is 11kN. The load ratio R , for both cases is 0.1. A clear dependency on solution accuracy with mesh size exists thus a mesh sensitivity study was performed. For each loading angle and each case study in this work a separate mesh convergence study is undertaken to optimise the trade-off between solution accuracy and computational costs. Based on the findings, an element size of 0.5 and 0.2 mm was deemed sufficient around the crack tip for loading angles 30° and 60° , respectively. For both loading angles, the global element size was 0.8 mm resulting in 82,139 and 164,000 elements being generated. The same number of elements was used for all scaled models to eliminate mesh sensitivity effect influencing the scaled results. The findings are in line with Zhang et al. [178], who concluded that an element size of 0.5 mm or smaller is sufficient to capture the stress state around the crack tip for fatigue crack growth analysis.

The specimen dimensions and loading conditions for all specimens can be found in Table 5.4 and Table 5.5. Table 5.6 presents the dimensional scaling factors for all three specimens. Virtual models 1a, 2a and 3a denote the virtual models for loading angle 30° whereas virtual

models 1b, 2b and 3b are the virtual models for the loading angle of 60°. Virtual models are formed on combination of the results from two scaled models using the first-order finite similitude rule.

Table 5.4: Dimensions of CTS specimen at all scales

Model	β	Initial crack size a (mm)	Height (mm)	Ligament length (W-a) (mm)	Thickness (mm)	Width (mm)
Full scale	1.00	45.00	148	45.00	15.00	90.00
Scaled Model 1	0.80	36.00	118.4	36.00	12.00	72.00
Scaled Model 2	0.50	22.50	74	22.50	7.50	45.00
Scaled Model 3	0.25	11.25	37	11.25	3.75	22.50

Table 5.5: The loading conditions of CTS specimen at all scales

Model	β	Δa_1 (mm)	Δa_2 (mm)	Applied load 1 (kN)	Applied load 2 (kN)	Load ratio R
Full scale	1.00	0.50	0.20	250	11	0.1
Scaled Model 1	0.80	0.40	0.16	250	7.04	0.1
Scaled Model 2	0.50	0.25	0.10	250	2.75	0.1
Scaled Model 3	0.25	0.125	0.05	250	0.69	0.1

Table 5.6: Value of the scaling factors with different dimensional scaling factors

Virtual Model No.	β_1	β_2	$\alpha_{01}^v g_1$	$\alpha_{02}^v g_2$	R_1
1	0.80	0.50	1.56	4.00	0.33
2	0.80	0.25	1.56	16.00	0.09
3	0.50	0.25	4.00	16.00	0.50

After 5 mm of crack growth at a loading angle of 60°, the von-mises stresses at the crack tip are examined for the full scale, virtual and scaled models 1 and 2. The results are presented in Fig. 5.5, which indicate an exact representation of the stress state at the crack tip, captured by both the virtual and scaled-down models. A key parameter of interest in fatigue-crack growth experimentation is the crack tip driving force (i.e., the stress intensity factor) as this governs the crack propagation rate. For mixed mode fatigue cases, this is denoted by the equivalent stress intensity factor ΔK_{equiv} , which has contribution from modes I and II stress intensity factors (*i. e.*, ΔK_I and ΔK_{II}). The first-order finite similitude theory is applied here to determine how accurately the virtual models predict ΔK_{equiv} of the full-scale model using data from the scaled down models. The number of cycles it takes the crack in the full-scale model to grow 10 mm for the 30° loading angle and 5 mm for the 60° loading angle along with the ΔK_{equiv} at the final crack length is presented in Table 5.7 and Table 5.8, respectively.

To return the virtual model predictions, Eqs. (5.9a) and (5.9b) are used. The values of ΔK_{equiv} and n for the two scaled models obtained from the numerical experimentation at each sub-step are combined using Eq. (5.9a) and Eq. (5.9b) to obtain the corresponding virtual-model prediction for the equivalent stress intensity factor and number of cycles. Eq. (5.14a) is used to obtain the crack extension and exact predictions of the final crack length a_f (critical defect size) are obtained. Near exact predictions of the equivalent stress intensity factors are returned by the virtual models for both loading angles with a deviation of no more than 0.03%. The lifecycle predictions returned by all virtual models are within 6% error for both loading angles.

Crack length 10mm for the full-scale model	Crack length 10mm for the virtual model
---	--

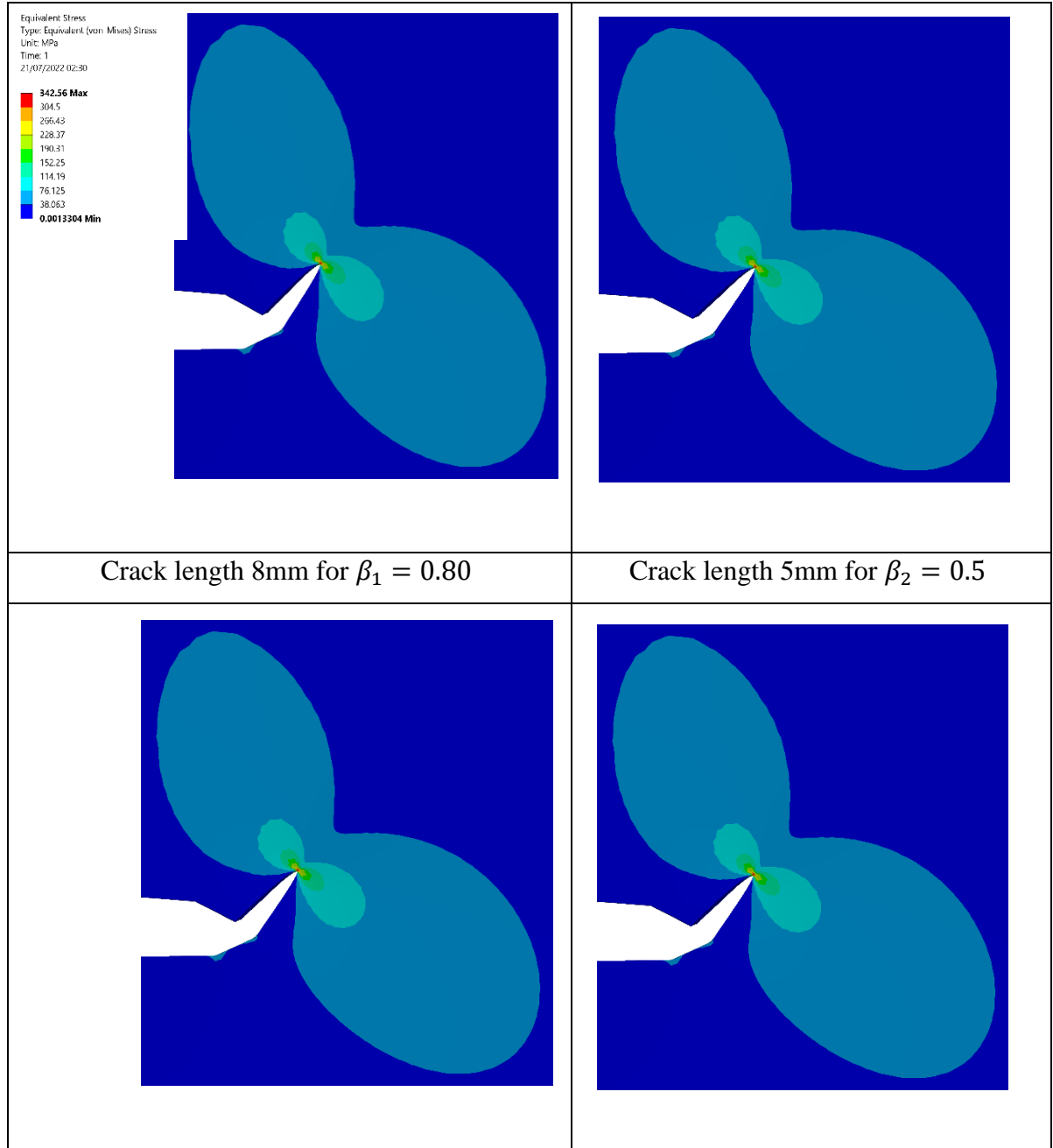


Figure 5.5: Von Mises stress distribution at the crack tip of CTS specimen after 25 sub steps for the full-scale model and the two scaled models for virtual model 1 at loading angle 60°.

Table 5.7. Stress intensity factor and number of cycles at final crack length of 55 mm for full scale and virtual models for 30° loading angle.

Model	a_f (mm)	Error (%)	$K_{equiv}(\text{MPam}^{0.5})$	Error (%)	n_{ps}	Error (%)
Full Scale	55	-	21.13	-	15578	-

Virtual Model 1	55	0	21.13	0.0	15454	0.01
Virtual Model 2	55	0	21.15	0.01	15291	2
Virtual Model 3	55	0	21.16	0.01	14573	6

Table 5.8. Stress intensity factor and number of cycles at final crack length of 50 mm for full scale and virtual models for 60° loading angle.

Model	a_f (mm)	Error (%)	K_{equiv} (MPam ^{0.5})	Error (%)	n_{ps}	Error (%)
Full Scale	50	-	8.71	-	62337	-
Virtual Model 1	50	0	8.71	0.00	61115	2
Virtual Model 2	50	0	8.70	0.02	60448	3
Virtual Model 3	50	0	8.69	0.03	57506	6

The most important consideration when evaluating the fatigue life of realistic and/or complex structures numerically is the accuracy of the predicted stress intensity factors. Fig. 5.6 presents the evolution of both mode I and II stress intensity factor values as the crack propagates. Clearly demonstrated in Fig. 5.6 is the near exact predictions returned by all virtual models for both K_I and K_{II} values. Note how K_I increases while K_{II} approaches zero during crack growth indicating that although initially the crack propagates under a mixed mode condition, mode-I becomes more dominant as propagation proceeds. This problem converges to a mode-I loading type as K_{II} tends to zero after the first 2mm of crack growth, with subsequent crack growth perpendicular to the loading axis. This is a well observed phenomenon in the literature, validated by the works of other researchers (see ref. [98]), and affirming the ability of the first-order similitude theory to reproduce exactly the correct mixed-mode fatigue behaviour.

The accurate predictions for K_I and K_{II} (see Fig. 5.6) result in an accurate prediction for the equivalent stress intensity factor, K_{equiv} thus the crack growth rate is predicted to a high degree of accuracy with the best models returning a lifecycle percentage error of 0.2, whereas a maximum error of 9% is returned by virtual model 3 for the 30° loading angle. For the 60° loading angle the same pattern is observed with virtual model 1 returning a maximum error of 2% and virtual model 3 returning a maximum error of 6%. Excellent agreement is achieved for the equivalent stress intensity factor at a crack length of 15 mm for the loading angle of 30° with a maximum error of 0.7 % predicted by virtual model 3. The plot of the crack length against number of cycles for both loading angles is shown in Fig. 5.7.

Table 5.9 presents the crack propagation angle after the first sub step of crack growth obtained by using Eq. 15b and substituting the predicted K_I and K_{II} values. This is a critical parameter that must be predicted with accuracy as it is a strong indicator of the path the crack takes as it propagates. Near exact predictions are returned by all virtual models for both loading angles clearly demonstrating the efficacy of the first-order theory as applied to fatigue.

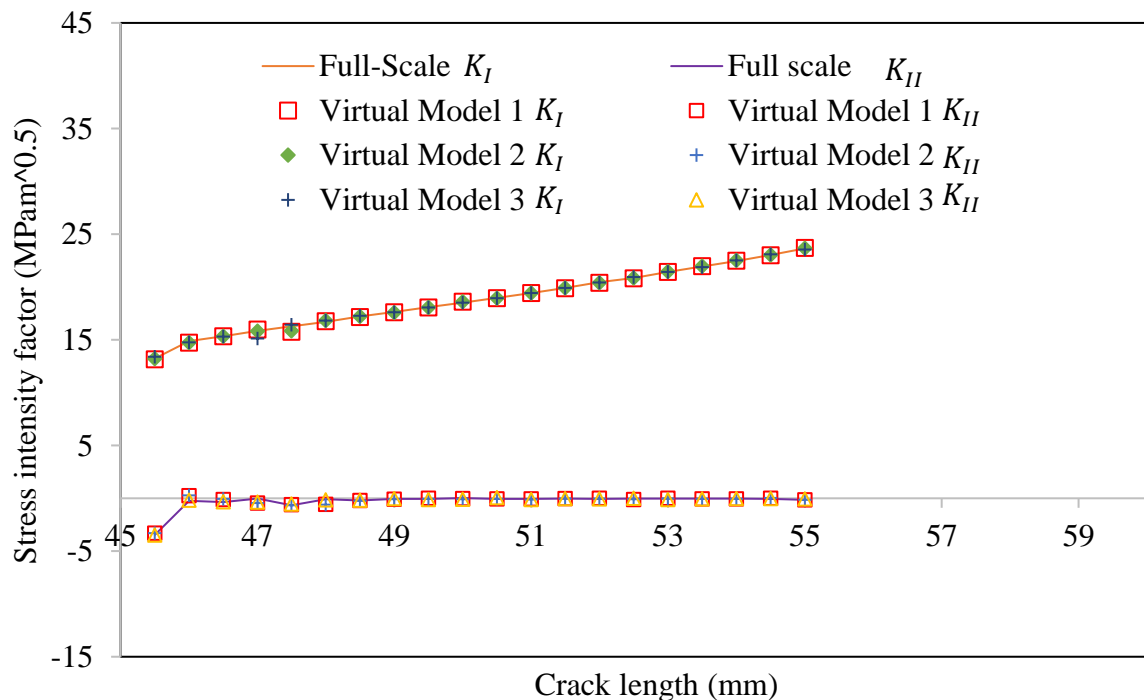


Figure 5.6: Evolution of mode 1 and 2 stress intensity factor with crack length for CTS specimen for full scale model and virtual models 1-3 at a loading angle of 30 degrees

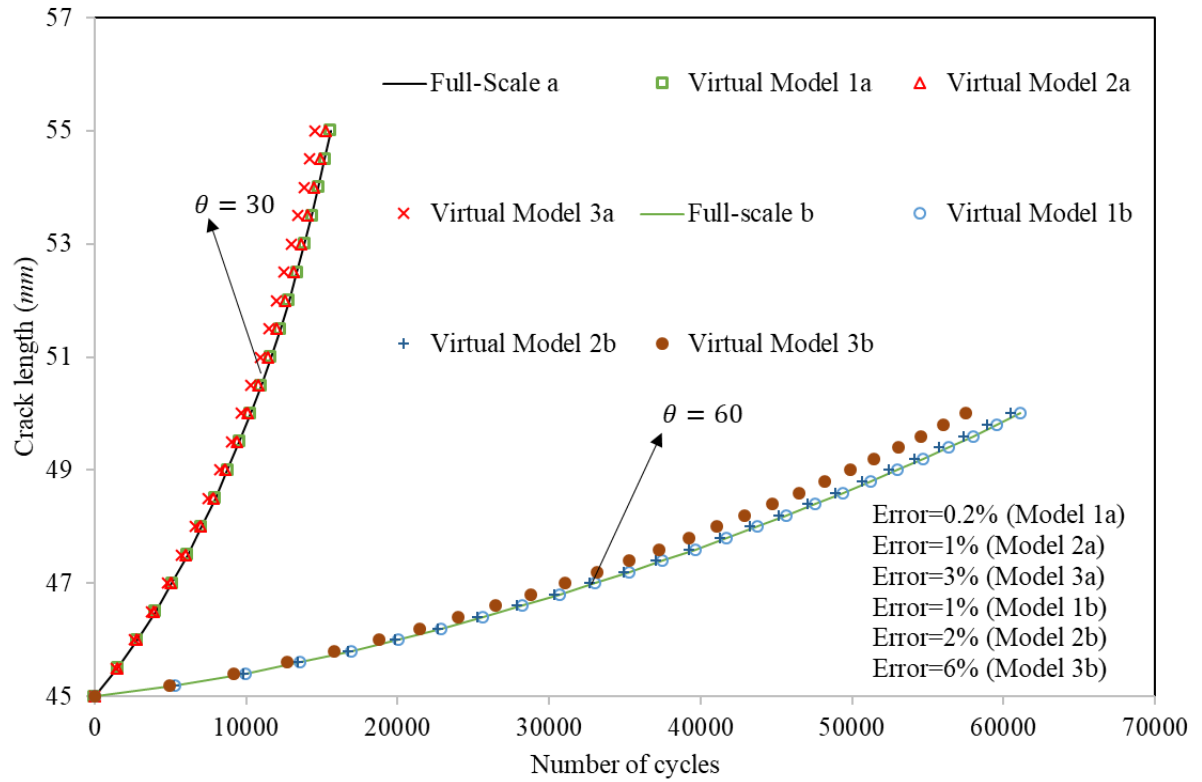


Figure 5.7: Crack length vs number of cycles for full scale and all virtual models for the CTS specimen

Table 5.9. Crack propagation angle for full scale and virtual models for 30° and 60° loading angle

Model	Loading angle θ (°)	Propagation angle β (°)	Error (%)	Loading angle θ (°)	Propagation angle β (°)	Error (%)
Full Scale	30	26.3	-	60	45.9	-
Virtual Model 1	30	26.1	0.8	60	45.7	0
Virtual Model 2	30	25.8	1.9	60	45.8	0
Virtual Model 3	30	26.1	0.8	60	46.4	1

Finally, the path which the crack takes as it propagates through the CTS specimen is investigated using Eq. (15b). The first-order theory is used to combine the associated displacements in the horizontal and vertical directions of the scaled models at each sub step of crack growth to form the virtual model. This is then contrasted with the co-ordinates of the crack at the full scale. The results are presented in Fig. 5.8. After the first step of crack growth, the influence of K_{II} on the crack path is negligible as its value is nearly zero thus crack growth and direction are controlled solely by K_I . The first order theory has been readily shown to capture both the K_I and K_{II} values as seen in Fig. 5.6 so it is no surprise that there is an exact agreement in the paths taken by the crack of the virtual models and full-scale models as degradation of the material occurs.

This is a truly remarkable finding as it proves scaled models can be used to predict the path taken by cracks during degradation of a structure. It is important to emphasize that the value of ΔK_{equiv} depends on some combination of individual K_I and K_{II} values, which the first order theory has been shown to predict to great accuracy. Hence, by extension despite the empirical criterion chosen the theory would always be able to predict the correct ΔK_{equiv} value and consequently both fatigue life and crack direction to a high degree of accuracy. This opens a whole host of possibilities for implementing this approach for structural integrity assessments in industry regardless of numerical software choice.

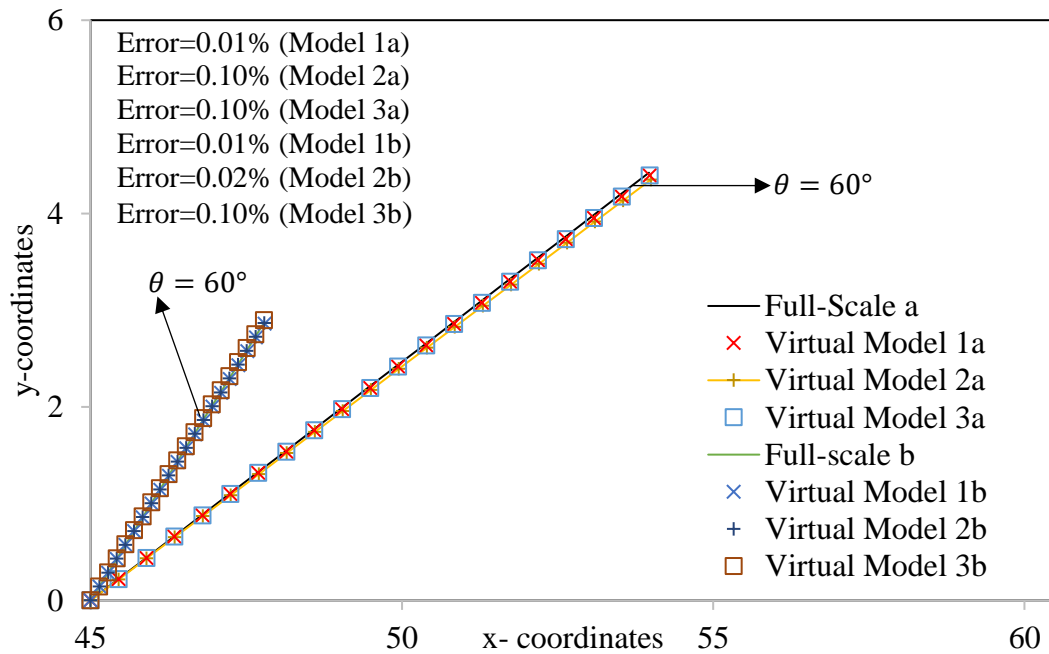


Figure 5.8: Crack path for full scale and all virtual models of the CTS specimen at 30° and 60° loading angles

5.5.3. Case study II: Fatigue of wing-fuselage attachment lug of a light aircraft

In this section the numerical analysis of a wing fuselage attachment lug of a light aerobatic aircraft Safat 03 is conducted and the first-order similitude rules applied to determine the fatigue life predictive capabilities of the theory for this realistic service structure. Attachment lugs are a critical component of any aircraft as they function as the primary means of connecting different components of the airframe. During flight, the transfer of loads from wings to fuselage is primarily by means of pin-loaded attachment lugs. Thus, the consequences of failure of the lug are enormous with wing loss a near certainty. The lug geometry is that of a light aircraft and is taken from the work of Solob et al. [213] and is depicted in Fig. 5.9. The meshed lug used in numerical analysis is shown in Fig. 5.10. The stress load applied to the pin hole is 250 MPa with a load ratio $R = -1$ due to both tensile and compressive loads exerted on the lug during flight. The lower portion of the lug is fixed in all directions. The dimensions and loading for the full scale and sub scale models are highlighted in Table 5.10 and Table 5.11. For the full-scale model, the element size at the crack tip is 0.25 mm and is set to 0.5 mm in the other regions resulting in 84 713 elements being generated. Δa_{ps} is 0.35mm and the crack is propagated for 10 sub steps. Dimensional scaling factors are presented in Table 5.6

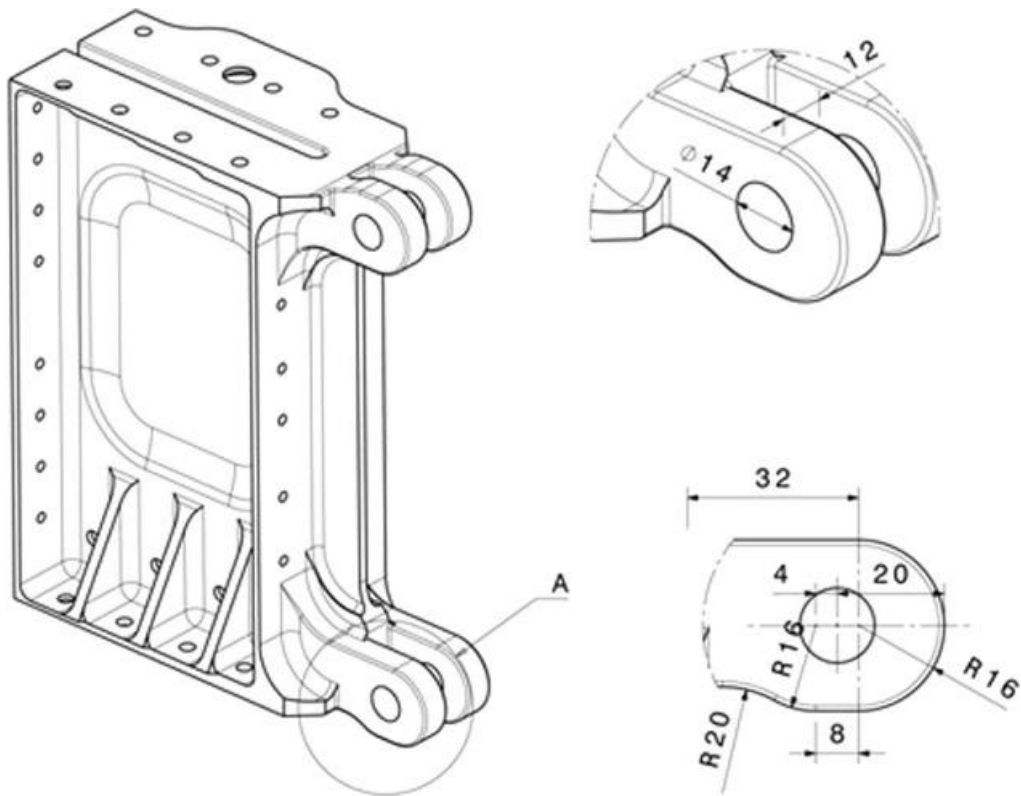


Figure 5.9: Safran O3- Wing fuselage attachment lug geometry and dimensions [213]

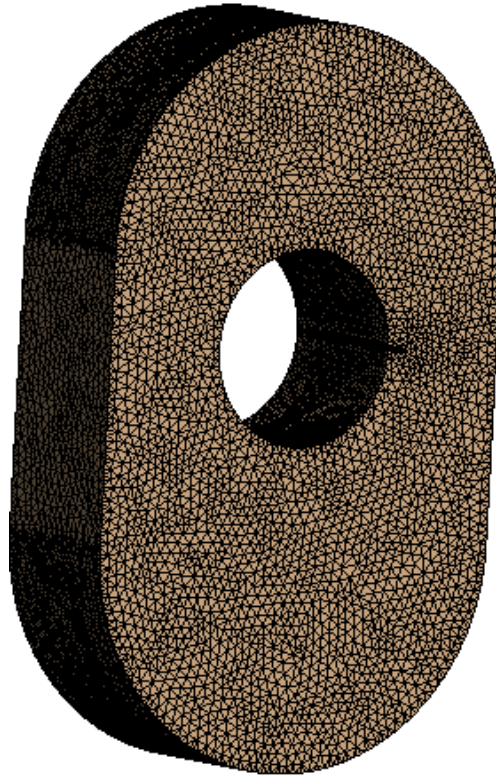


Figure 5.10: Meshed wing-fuselage attachment lug.

Table 5.10: Dimensions of wing-fuselage attachment lug at all scales

Model	β	Initial crack size a (mm)	Pin Diameter (mm)	Length (mm)	Thickness (mm)	Width (mm)	Applied load (MPa)
Full scale	1.00	1.00	14.00	53.00	12.00	32.00	200
Scaled Model 1	0.80	0.80	11.20	42.40	9.60	25.60	200
Scaled Model 2	0.50	0.50	7.00	26.50	6.00	16.00	200
Scaled Model 3	0.25	0.25	3.50	13.25	3.00	8.00	200

Table 5.11: The loading conditions of wing fuselage attachment lug at all scales

Model	β	Crack extension Δa (mm)	Applied pressure load (MPa)	Load ratio R
Full scale	1.00	0.350	200	-1
Scaled Model 1	0.80	0.280	200	-1
Scaled Model 2	0.50	0.175	200	-1
Scaled Model 3	0.25	0.875	200	-1

Solob et al [213] adopted a typical damage tolerant approach to fatigue analysis prevalent in industry. They determined the critical location of the lug by conducting a finite element analysis of the component in the absence of a crack. They found the location of maximum stresses to be at the midpoint of the loading hole, thus in this study a through thickness crack of length 1 mm is inserted at the right midpoint of the loading hole and propagated to a final crack length a_f of 4.5 mm. The number of cycles it takes to reach this final crack length and the corresponding equivalent stress intensity factor is tabulated in Table 5.12. The boundary conditions imposed on the lug induce a mixed mode stress state at the crack tip and the crack propagates upwards. The same path is taken by all scaled models. Predictions of the equivalent stress intensity factor are exact with very negligible error (maximum error of 0.08%). The full-scale lug fails at 1057 cycles indicating failure of the lug under low cycle fatigue. The lifecycle predictions by the virtual models are once again accurate with no more than 9% error in virtual model 3. The results are displayed in Fig. 5.11.

Table 5.12. Stress intensity factors and number of cycles at final crack length of 4.5 mm for full scale and virtual models

Model	a_f (mm)	Error (%)	K_{equiv} (MPam ^{0.5})	Error (%)	n_{ps}	Error (%)
Full Scale	4.5	-	89.11	-	1057	-

Virtual Model 1	4.5	0	88.32	0.90	979	7
Virtual Model 2	4.5	0	88.59	0.60	975	8
Virtual Model 3	4.5	0	89.81	0.80	960	9

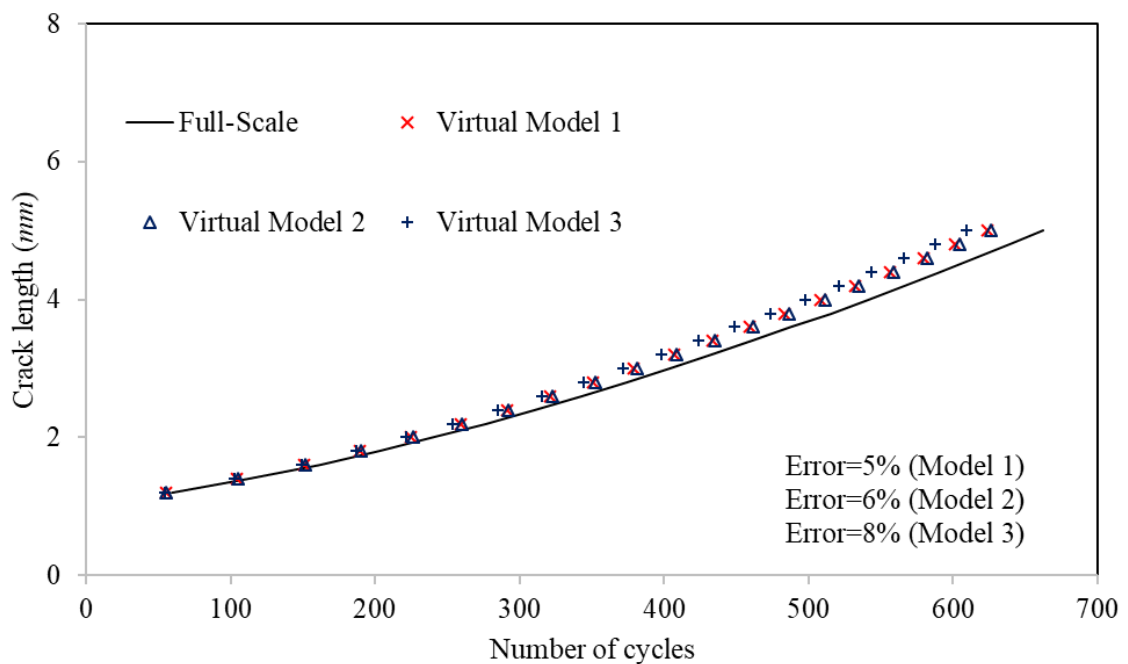


Fig 5.11: Crack length vs number of cycles for full scale and all virtual models of lug

5.5.4. Case study III: Friction stir welded t-joint with an inclined semi- elliptical crack

A t-joint is a typical joint type in welded structures. T-joints can be found in vehicles, bridges, offshore structures, ships and various other industrial fields. Due to the change of the section form, the stress concentration factor is high. Under cyclic loading, cracks initiate at regions of high stress concentration eventually resulting in fatigue fracture [216]. Friction stir welding (FSW) is a solid-state welding technology that offers advantages to traditional welding methods. This has led to its widespread adoption in the aerospace, automotive and marine industries [217]. The chief benefit is the increased fatigue resistance of joints manufactured by this process (up to 2.4x) as opposed to the single riveting method used in aerospace industry [217]. Most cracks observed in practice are predominantly surface cracks

and either semi elliptical in shape or can be closely approximated by a semi elliptical shape [219], so a surface elliptical crack surface crack is used in this study. To add further to the complexity of the analysis, the crack is inclined at an angle to the horizontal, hence the structure is undergoing mixed mode fatigue.

In this case study, a friction stir welded t-joint typically found in aerospace applications comprising an inclined semi elliptical surface crack at the centre is analysed with the geometry presented in Fig. 5.12. The top face is referred to as the skin and the bottom is the stringer. A common application is in the fuselage of the aircraft. The crack is 2 mm long and 1 mm deep (aspect ratio of 1) with its centre at the midpoint of the skin. A tensile load of 48kN is applied to the top face while the bottom face is fixed in all directions. AISI 316 stainless steel [214] is used for both the full scale and scaled-down models. Table 5.13 and Table 5.14 presents the geometrical dimensions and loading for all models. The R ratio is 0.1.

The main output of interest is the number of cycles it takes to propagate the crack 3.85 mm to a final crack length a_f of 5.85mm for the full-scale model. The crack extension Δa for the full-scale model is 0.35 mm (i.e., $\Delta a_{ps} = 0.35$ mm), and the crack is propagated for 11 sub-steps. An element size of 0.5 mm is used around the crack tip for the full-scale model and 1 mm in other regions. In addition, the crack front element size is set to 0.25 mm, generating a total of 149,295 elements. Dimensional scaling factors are the same values presented in Table 5.6.

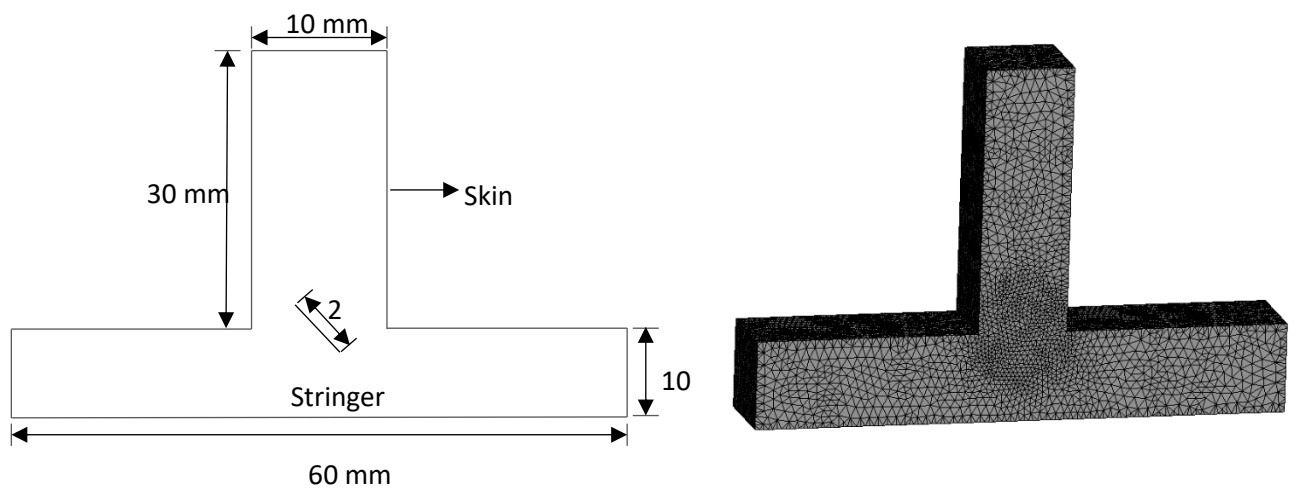


Figure 5.12: T-joint geometry and mesh

It is of interest in this study to confirm or otherwise if the Paris law parameters of AISI 316 stainless steel can be successfully predicted using two scaled models. Three different virtual models offer different predictions for the number of cycles by combining the data from the scaled models (see Table 5.6). It is shown that lifecycle and stress intensity predictions are accurate with a maximum of 9% deviation from the full-scale model for all virtual models. The stress intensity factors at the final crack length of 5.85 mm obtained at the left crack tip are tabulated in Table 5.15. The plot of crack length vs number of cycles is presented in Fig. 5.13.

Table 5.13: Geometrical dimensions of t-joint at all scales

Model	β	Initial crack size a_l (mm)	Initial crack size a_d (mm)	Δa (mm)	Length (mm)	Width (mm)	Thickness (mm)
Full scale	1.00	2.00	1.00	0.35	40.00	60.00	10.00
Scaled Model 1	0.80	1.60	0.80	0.28	32.00	48.00	8.00
Scaled Model 2	0.50	1.00	0.50	0.175	20.00	30.00	5.00
Scaled Model 3	0.25	0.50	0.25	0.875	15.00	15.00	2.50

Table 5.14: The loading conditions of t-joint at all scales

Model	β	Crack extension Δa (mm)	Applied load (MPa)	Load ratio R
Full scale	1.00	0.350	48.00	0.1
Scaled Model 1	0.80	0.280	30.72	0.1
Scaled Model 2	0.50	0.175	12.00	0.1

Scaled Model 3	0.25	0.875	3.00	0.1
-------------------	------	-------	------	-----

Table 5.15. Stress intensity factors and number of cycles at final crack length of 5.85 mm for full scale and virtual models

Model	a_f (mm)	Error (%)	$K_{equiv}(MPam^{0.5})$	Error (%)	n_{ps}	Error (%)
Full Scale	5.85	-	76.22	-	55627	-
Virtual Model 1	5.85	0	72.65	5	53576	4
Virtual Model 2	5.85	0	73.36	4	52989	5
Virtual Model 3	5.85	0	76.60	0.1	50435	9

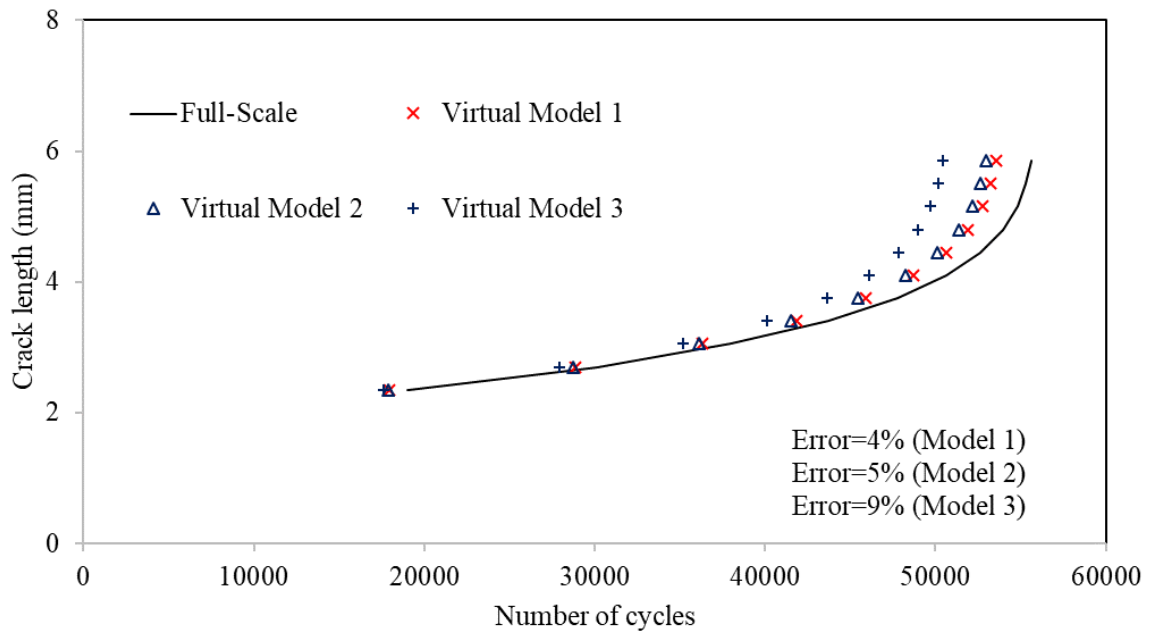


Figure 5.13: Crack length vs number of cycles for full scale and virtual models of t-joint

After 3.85 mm of crack propagation, the equivalent stress intensity factor in the full-scale model is 76.2 MPam^{0.5}. The first-order theory returns a value of approximately 72.7

MPam^{0.5} and 73.4 MPam^{0.5} for virtual models 1 and 2, and 76.6 MPam^{0.5} for virtual model 3 translating to a maximum error of 5%. The lifetime prediction is within a 9% deviation from full-scale fatigue strength for all virtual models.

The crack path after 3.85mm of crack growth is presented in Fig. 5.14. Despite the relatively complex crack path, all the scaled models follow the same exact path and deform in the same way. This is because of the scaled experiments being designed individually accordingly to the zeroth-order similitude rules and combined to satisfy first order. Hence, information about the crack path can be readily gleaned from the scaled models. The left crack tip of the inclined semi elliptical crack propagates upwards at an angle and cuts through the skin while the right crack tip propagates downwards at an angle cutting through the stringer. The crack growth rate is different at both crack tips, with the left crack tip propagating slightly faster. The right crack tip propagates slower as its path is through the stringer which is fixed in all directions whereas the left crack tip is propagating towards the face where the tensile load is applied. The crack path of the inclined crack obtained from the numerical simulation closely matches the experimentally observed crack paths of other researchers see ref. [200].

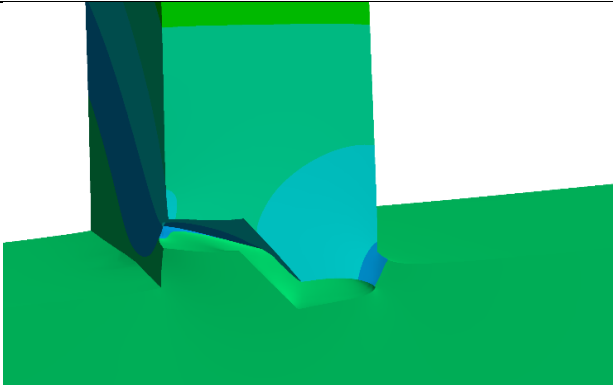
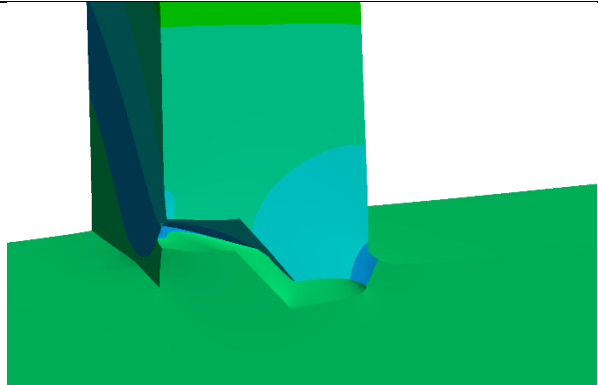
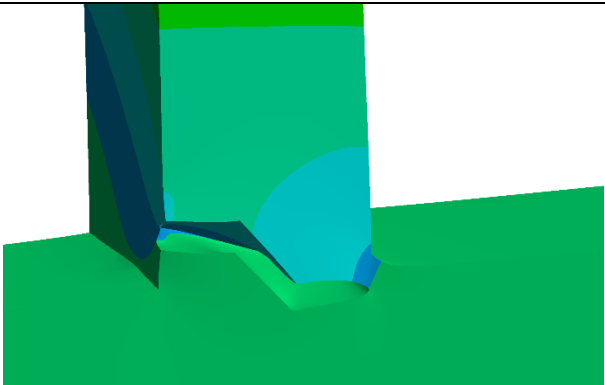
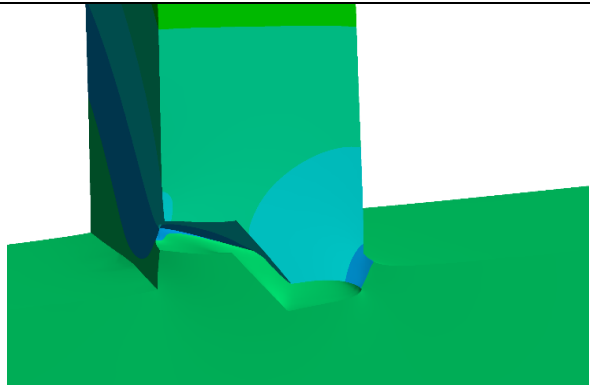
Crack length 5.85 mm for the full-scale model	Crack length 5.85 mm for the virtual model
	
Crack length 4.68 mm for $\beta_1 = 0.80$	Crack length 2.925 mm for $\beta_2 = 0.5$
	

Figure 5.14: Final crack path comparisons between the full-scale model, virtual model and scaled models 1 and 2.

The ‘gold’ standard for fatigue experimentation in both academia and industry is the ASTM E647 [174] handbook. It recommends the measured experimental outputs of crack growth rate and stress intensity factor be plotted on a log-log scale whereby the Paris law constants C and m can be extracted to describe the fatigue resistance of the material/component. A question of widespread interest therefore is whether scaled experiments can successfully predict the Paris law constants of the full-scale structure. The first order rules have been shown in this work to predict the crack length, number of cycles and stress intensity factor of the material of the full-scale models with high accuracy from the scaled tests (see Tables 5.7, 5.8, 5.12 and 5.15). These three parameters are the only parameters required to extract the Paris law constants thus the first order finite similitude approach offers a solution to this question.

Figure 5.15 presents the plot of crack growth rate vs the equivalent stress intensity factor for the full scale and virtual models of the t-joint according to ASTM E647 standard. The virtual models are formed by combining fatigue test data (a , K_{equiv}) of the scaled T-joint models. The Paris law parameters C and m of AISI 316 stainless steel obtained from the numerical full-scale model are 4.06×10^{-8} and 2.34 respectively. This is an exact match within numerical error when contrasted with the experimental data of Sajith et al. [214]. All virtual models formed provide an exact match with that of the full-scale model to within 1% error. It is confirmed that exact replication of the Paris-law parameters is achieved using two scaled experiments. The results of all three case studies in this section confirm that complete fatigue response of realistic structures with inherent defects under service loads can be predicted using two scaled experiments, designed strictly conforming to first order finite-similitude rules. Although the experimental campaign in this work is numerical, the value of the proposed framework lies in its applicability to physical laboratory experiments. Consequently, the focus of future work would be on fatigue outputs obtained directly from physical scaled experimentation, substituting for the numerical outputs performed in this work.

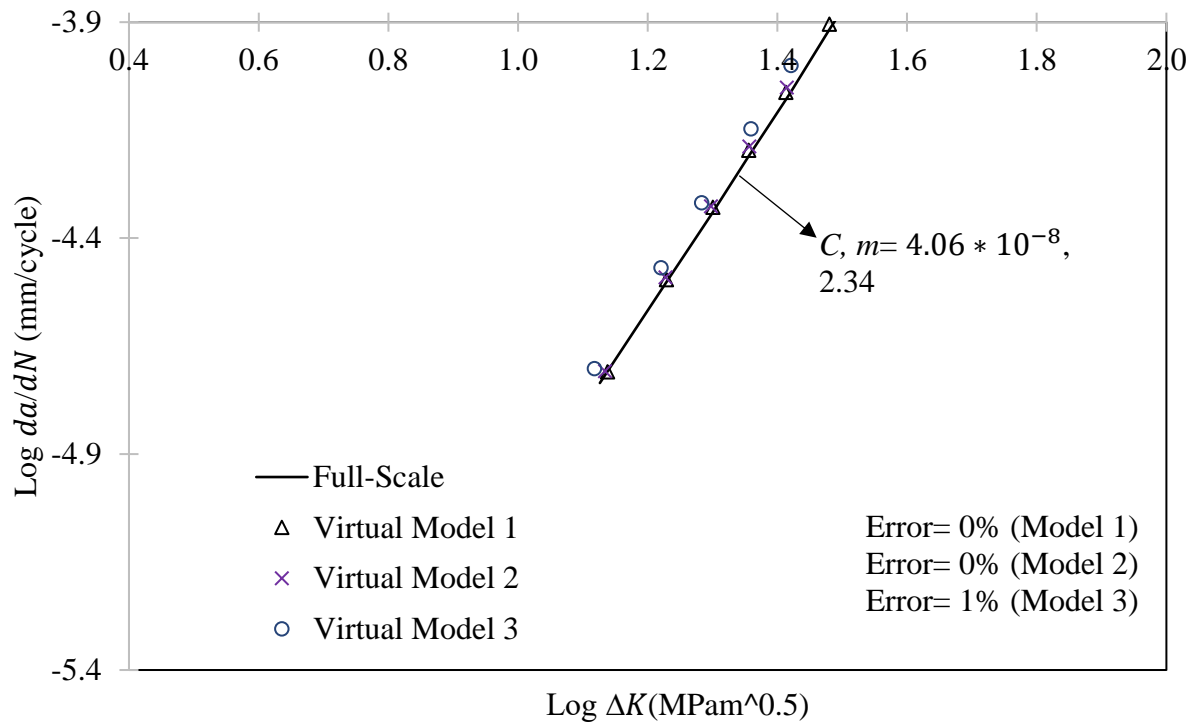


Figure 5.15: Crack growth rate vs equivalent stress intensity factor for the full-scale model and all virtual models of t-joint

5.6 Conclusions

This paper builds on previous work by the authors on scaling low cycle fatigue [46]. A novel approach for scaling empirical fatigue laws is introduced with particular focus on Paris law. A novel expression for number of cycles to fatigue life is proposed to predict the fatigue life of the prototype using two scaled experiments. Geometric size effects that arise in fatigue loaded structures with pre-existing cracks are examined to determine if they vanish upon conducting two scaled down tests. The first-order finite similitude theory is applied to combine information recorded at two scales to reconstruct full scale behaviour.

The following conclusions can be drawn from the analysis and results returned in the paper:

- Numerical experimentation was employed to investigate fatigue crack growth in a compact tension shear specimen, wing fuselage attachment lug and a welded t-joint. Simple radical functions of scale β were discovered for the number of cycles to failure and stress intensity amplitude. It is shown that the scale effects present in the fields pertinent to mixed mode fatigue analysis within the fracture mechanics framework such as the number of cycles to failure, stress intensity factor and crack growth rate are eliminated with two scaled experiments.

- By performing two scaled experiments, the fatigue life of the full-scale models was predicted very accurately in each case within a 1% error in the best models and no more than 9% deviation in the worst-case scenario. Critical fracture mechanics parameters such as the mode I and mode II stress intensity factor values, equivalent stress intensity factor values, crack propagation angle, crack path and crack tip stress distribution were accurately predicted by the theory. In addition, Paris law parameters C and m were predicted to up to 99% accuracy using two scaled experiments.
- The results from the case studies confirm that the first order finite similitude theory is a useful tool that can aid with structural integrity decisions in any field that employs a damage tolerant design approach by determining service inspection intervals. It can help reduce the amount of multiple full-scale fatigue tests needed (accounting for scatter by repeated small scale testing instead) with the obvious benefit being tremendous cost savings for laboratory fatigue testing of large structures such as aircrafts, bridges etc., and components built with expensive materials such as robots, biomedical devices, among many others.

6. Discussion

The aim of this thesis was to determine if the finite similitude theory can be applied to propagating fatigue cracks and successfully predict key fatigue damage parameters of a full-scale structure using two scaled down experiments. This was achieved by performing numerical fatigue experiments. The first order finite similitude framework was extended in this thesis with the development of a similitude relationship for the number of cycles to fatigue failure.

A major component of this work is the extensive numerical experimentation carried out alongside experimental validation with previous published fatigue experimental data using the fatigue capabilities of Ansys and Abaqus. The direct cyclic solver is used in Abaqus whereas the SMART solver is employed in Ansys. Realistic numerical models that are truly representative of fatigue crack growth in real components to replace physical testing were generated. The aim was to obtain fatigue crack growth outputs from the full scale and sub scale tests that typically would be obtained from laboratory tests. Both 2D and 3D fatigue crack growth finite element models for mode I and mixed mode fatigue were created in this thesis and validated against experimental tests (see Figs. 3.10, 4.4, 5.3 and 5.4). This promoted confidence in the use of a numerical experimentation campaign to validate the first order theory. The theory is then applied by conducting numerical tests according to the procedure outlined in section 5.4. This procedure enables creation of virtual models for fatigue outputs of interest that predict the full-scale fatigue output by combining the outputs from the scaled fatigue tests. This is the same procedure that should be followed in order to apply the first order theory to design and conduct physical fatigue tests in a laboratory/ industrial setting.

A key aspect of successful implementation of the theory with numerical fatigue tests is the setup of the geometry, mesh, boundary conditions and fatigue crack growth parameters for the full and scaled down models. Also, careful consideration needs to be given to how the output data is obtained. Mesh sizes affects the accuracy of finite element simulation results. Thus, a mesh sensitivity study was conducted for each case study in this thesis. The fatigue outputs such as the crack length, number of cycles to failure and stress intensity factor were checked for convergence in the smallest scale models. This is to eliminate any error in the outputs of the models due to mesh sensitivity and ensure that the fatigue outputs at each scale are representative of what would be obtained if each scaled test was conducted as a standalone physical fatigue test. The same material was used for the full scale and scaled

down models. Numerical fatigue crack growth simulations were performed with five different materials in this thesis (Aluminium 6061 alloy, S355 steel, 7% Nickel steel, Structural steel and AISI 316 stainless steel). The first order theory demonstrates accurate predictions of full-scale fatigue response regardless of material choice.

The number of elements in the full-scale model is kept the same for all scaled models to eliminate mesh sensitivity effects and to ensure any observed differences in fatigue outputs of interest are solely due to geometric changes in scale (geometric size effects). Advanced meshing techniques are used such as partitioning to refine the mesh in areas of interest such as the crack tip whereas a coarser mesh is employed elsewhere. This is done for two reasons, firstly to reduce the computational costs and secondly to enhance the accuracy of the results. Previous studies by researchers prescribed an element size of 0.5 mm or smaller around the crack tip, thus the element size in the case studies around the crack tip for the full-scale model are 0.5 mm or smaller to ensure accuracy of fatigue fracture mechanics parameters. Typically, an element size of either 1 mm or 0.8 mm is used in the other regions for the full-scale model. The requirement of keeping the same number of elements in all models implies that the element size used in the smaller models must be smaller. This is achieved by partitioning the sub scale models in the exact same manner as the full-scale model and multiplying all the element sizes in the partitions of the full-scale model by the β value of the scaled model being tested.

Another parameter that affects the accuracy of crack growth simulations is the crack front extension value Δa which determines the number of sub steps and consequently data points obtained for a given critical crack length a_f . Ideally, this should be set to a similar value to the element size at the crack tip. It can be smaller but if it is much larger than the element size at the crack tip, inaccuracies in the stress intensity factor values and number of cycles to failure arise. In this work, the outputs of the fatigue crack growth simulations need to be synchronized to apply the first order identities to each recorded data point (sub step) of the sub scale models. To achieve this, the crack front extension; Δa_{ps} of the full-scale model is set to a fixed value typically 0.2 mm in this work and the crack is propagated by the same value each sub step for a prescribed amount of sub steps till the crack reaches the desired crack length a_f . The number of sub steps must be kept the same for all scaled models, thus the crack front extension for the scaled models is set to ($\beta_i \times \Delta a_{ps}$). The stress intensity factor; ΔK is synchronised by taking the values at the same location of the crack front in all

models due to the non-uniform distribution of ΔK . In this work the stress intensity factor values are taken from midpoint of the crack front (deepest point for semi-elliptical cracks) in all models and Eq. (5.9a) is used to combine the scaled model ΔK values. The applied loads in this work are applied to the finite element models as either displacement, force or stress-controlled loading. Excellent agreements are achieved in all cases by the virtual models. Paris law is the fatigue crack growth law used in all case studies. Identical materials are used for scaled models so the Paris law input parameters in the scaled numerical models are set to the same value as the full-scale model.

In practical laboratory testing, the same procedure to synchronise the output data should be followed with the software set to record relevant fatigue data at prescribed fixed successive crack length increments Δa_{ps} with the scale model output data recorded at $\beta_i \times \Delta a_{ps}$ mm crack lengths. The first order identities should then be applied at the recorded data points of the scaled model to construct the virtual model.

Numerical experimentation in this thesis confirms that the procedure outlined in section 5.4 for the design and testing of scaled fatigue crack growth experiments enables replication of full-scale fatigue component response. Hence, the procedure can be applied to physical scaled down fatigue tests in a laboratory environment. Section 5.4 prescribes the identities needed to apply the correct forces, loads and boundary conditions in the design of scaled fatigue tests and additionally post process the required fatigue outputs after the physical tests have been performed. For example, the force that should be applied to a scaled model with a geometric scaling factor β is: $F_{ts1} = F_{ps} / \alpha_{01}^v g_1$. Where F_{ps} is the force experienced by the full-scale component/ structure in service and $\alpha_{01}^v g_1$ are scaling factors.

The first order identities in Table 5.1 describe how to combine the outputs of the scaled fatigue tests such as stress, stress intensity factor, crack length (displacement), number of cycles to failure etc. to create a virtual model that predicts the corresponding output of the full-scale structure. Numerical simulations for planar and non-planar crack growth show an increase in error for fatigue outputs when β value of the smallest model used in the virtual model is very small. However, fatigue output predictions are still within 10% of the full-scale component values. Thus, when conducting physical fatigue tests the smallest scale model employed should be circa 20% of full-scale size ($\beta = 0.2$). However, the numerical simulations demonstrate that the selection of β values for the scaled tests is not unique thus any β value in the range of $0.2 \leq \beta \leq 0.9$ can be employed.

In Chapter 3, the fatigue response of three different ASTM E647 specimens made from Aluminium Alloy 6061 under low cycle fatigue are simulated in Abaqus using the cohesive zone model, XFEM and the direct cyclic solver. 2D finite element models are created and the constitutive relationship for the cohesive zone model is a bi-linear traction separation law. The first order rules are applied to design and conduct the scaled fatigue tests. The stresses at the crack tip are captured exactly with virtual models constructed from the vertical stresses (σ_{yy}) obtained from Abaqus models. Both monotonic and cyclic loading were considered, and the force-displacement curve predicted by the virtual models are in exact agreement with the full-scale specimen. In addition, the stress intensity factor, crack length and number of cycles to failure are predicted to a high accuracy (see Figs. 3.20a, 3.20b). The expected trend of increase in stress intensity factor values with crack length is also observed. The focus here is on low cycle fatigue and the first order rules are shown to apply for the design and testing of both fracture and low cycle fatigue tests.

In chapter 4, additional complexity is introduced by considering high cycle fatigue. Ansys SMART solver is used to create 3D fatigue crack growth models for all case studies. A novel function relating the number of cycles to failure change with scale is proposed and validated by means of two experimental and three numerical case studies. Fatigue crack growth simulation of a single edge notched specimen was validated against published experimental data. The first order rules are applied for the design and testing of fatigue crack growth in a single edge notched specimen, pipeline with semi elliptical crack and a pressure vessel with a semi elliptical crack.

The lifecycle predictions for all three cases are highly accurate with a higher error occurring in virtual models with the smallest scale model ($\beta = 0.25$). Minimal errors are recorded for the stress intensity factor values. It is observed that the stress intensity factor distribution across the crack front in the full-scale model is non uniform. The first order rules are applied to create virtual models which predict the crack front distribution of the full-scale model accurately (Fig 4.14). Fig. 4.15 shows the plot of crack growth rate vs stress intensity factor for a pressure vessel. Observed clearly is the size effect in the scaled fatigue models which is consistent with observed experimental data [14, 127]. However, the size effect vanishes upon creating the virtual model and the Paris law parameters of the full-scale model are predicted with 99.9% accuracy.

In chapter 5, 3D mixed mode (mode I and mode II) fatigue crack growth simulations are performed in ANSYS. In practical cases, structures are under a combination of different loads acting on different planes thus the investigation here is to determine if the first order rules are still valid for the design and fatigue testing of real structures. The modified compact tension shear specimen is the most common specimen for extraction of Paris law parameters of structures under mixed mode loading conditions. Thus, a finite element model of the MCTS specimen was created in ANSYS and validated against previous experimental data. Both the crack growth rate (Fig 5.3) and path taken (Fig 5.4) agreed with previous experimental efforts.

The first order finite similitude rule is then used to design and test scaled fatigue crack growth experiments for the MCTS specimen, wing fuselage attachment lug and a welded t-joint following the procedure outlined in section 5.4. The virtual models constructed from the scaled fatigue tests predicted the critical crack length, residual life, mode I, mode II and the equivalent stress intensity factors to high accuracy (see Tables 5.7, 5.8, 5.12 and 5.15). The crack initiation angle is a key fracture mechanics parameter for structures under mixed mode loading as it controls the path taken by the crack as it propagates through the structure. The first order was able to predict both the crack initiation angle and the paths taken by the propagating cracks to a high degree of accuracy with a maximum error of 3% (Table 5.8). The crack path predictions by the theory (Fig 5.8) are exact. The fatigue crack growth curve of t-joint with an inclined crack made from AISI 316 steel is plotted in Fig 5.15 and contrasted with experimental data. The virtual models predict the Paris law parameters of AISI 316 stainless steel under mixed mode fatigue with up to 99% accuracy when contrasted with experimental data [214]. The impact of this work is that Paris law parameters C and m of realistic structures and components can now be predicted with 99% accuracy using two scaled experiments.

A major uncertainty in the characterisation of the fatigue strength of real components in industry is the transferability of fatigue test data obtained from specimens usually cylindrical smooth specimens to real service structures. The fitness for service flaw (FFS) assessment procedures for fatigue in industrial standards such as BS 7910 [210], API 579 [211], R6 [220], ASME Section VIII Division 2 [221] etc address this with typically large conservative safety factors however there is a greater push in recent times for less conservative structural integrity assessments. This is particularly important in life extension of structures such as pressure vessels where there is a need to keep the plant in operation past its initial design

life. In this scenario, a more accurate estimation of the actual crack growth rates of the structure is needed. The work presented here can be of benefit in the experimental campaign used for FFS assessments of structures and/or development of FFS industrial codes as full scale mock up tests are very costly. This is because accurate fracture mechanics fatigue outputs of full-scale components/ structures such as the mode I/ II stress intensity factors and number of cycles to fatigue failure are predicted from data obtained from the medium and small scale tests using the procedure presented in this work.

Although the focus in this work was on propagating cracks in a damage tolerant framework, during the research the novel hypothesis proposed in this work (the product $\Delta K_{ts} n_{ts}$ is second order) was discovered to have an analogous counterpart within the CFD framework ($S - N$ curves). The product $\Delta \sigma_{ts} n_{ts}$ is second order with $\Delta \sigma_{ts} n_{ts} = \Delta \sigma_{\beta} n_{\beta}$, where $\Delta \sigma_{\beta}$ and n_{β} are the stress amplitude and number of cycles on Ω_{β} . An initial exploratory study was performed using the procedure highlighted in section 5.4 to combine the number of cycles to failure n_f and the first order identity for stress; $\sigma_{ps} = \alpha_{01}^v g_1 \beta_1^2 \sigma_{ts1} + R_1 (\alpha_{01}^v g_1 \beta_1^2 \sigma_{ts1} - \alpha_{02}^v g_2 \beta_2^2 \sigma_{ts2})$ to validate this hypothesis.

Experimental data from fatigue rotary bending tests of cylindrical specimens (Diameters 8, 20, 30 and 40 mm) made from forged steel (SF50) conducted by Hatanaka et al. [222] was examined. Virtual models are created from the scaled fatigue tests to predict the fatigue strength σ_f corresponding to a number of cycles to failure n_f at 10^6 cycles. The fatigue strength of the full-scale specimen (D=40 mm) is 202.2 MPa. Virtual model 1 ($\beta_1 = 0.75, \beta_2 = 0.25$) and virtual model 2 ($\beta_1 = 0.5, \beta_2 = 0.2$) returned fatigue strength σ_f predictions of 207.7 MPa and 211.8 MPa respectively. This corresponds to 2.7 % and 4.8% error respectively. This is a significant discovery as it highlights the potential in conducting reliable scaled fatigue tests in the safe-life approach which is more commonly used in standards such as the ASME code [221]. It further confirms that fatigue crack growth is a first order process and complete similarity in crack growth rate is possible using two scaled experiments. More experimental data ($S - N$ and $\varepsilon - N$) curves would be examined to further validate the proposed hypotheses and would be the subject of future publications.

In conclusion, the numerical simulations demonstrate that the first order finite similitude theory provides a framework for connecting lab-based fatigue/fracture experiments to understand failure modes in real engineering components. It enables designers to design and conduct meaningful scaled fatigue tests that extract large scale (component-level)

mechanical data by following the procedure outlined in section 5.4. The scale effects present in the fields pertinent to the fatigue analysis within the fracture mechanics framework are eliminated with two scaled experiments.

Cost weight savings can be realised as less conservative safety factors can be applied now. The results from the case studies confirm that the first order finite similitude theory is a useful tool that can aid with structural integrity decisions in the field such as determining service inspection intervals by accurate prediction of critical defect size. It virtually eliminates the need for multiple full-scale fatigue tests with the obvious benefit being tremendous cost savings for fatigue testing of large structures such as aircrafts, bridges etc., and components built with expensive materials such as robots, bio medical devices, among many others. In situations where it is difficult to conduct full scale fatigue tests such as boiler pressure vessels in nuclear reactors, pipework in harsh operating conditions etc. the finite similitude theory offers a solution in providing accurate residual life predictions.

The first order theory is only valid for isotropic scaling where the geometric dimensions are scaled in all directions by the same β . The first order theory as presented deals only with the effect of changes in scale on the continuum kinematics as such the theory deals with geometric scale effects only. Material-based size effects can also play a significant role in fatigue crack growth thus the work presented is valid when the microstructure length scales influencing crack growth are much smaller than the component or sub-scale models. For example, at the component level the material may be mechanically isotropic; however, if the trial domain is small enough to resolve grains, the material behaviour will be anisotropic. The theory is applicable within the confines of a continuum-mechanics framework, indicating practical limitations on the size of the smallest scaled models, it is recommended that the size of the smallest scaled models should be no smaller than 20% of the full-scale structure. Experimental studies designed conforming strictly to first order similitude rules should be undertaken to further validate the results presented in this thesis. This work focused on LEFM long crack fatigue crack growth. Fatigue crack growth simulations accounting for plasticity is a subject of future work to validate the theory. Finally, the work presented is valid for replica scaling (the same material used for both the full scale and scaled down models).

7. Conclusions

The aim of this thesis was to determine if the finite similitude theory can be applied to propagating fatigue cracks and successfully predict key fatigue damage parameters of a full-scale structure using two scaled down experiments. Fatigue is the phenomenon whereby a structure fails due to the application of sub critical cyclic loads. With a very high percentage of all structural failures attributed to fatigue it is a key consideration in the design stage. With full scale fatigue testing not just costly but also time consuming, the use of smaller specimens sharing geometric characteristics with the larger structure is an alternative and, in some cases, the only option for physical testing purposes.

When performing scaled tests however, a similarity law is needed to select the appropriate parameters for the experimental test such as forces, boundary conditions etc in the first instance and relate the desired outputs behaviour to that of the full scale by applying scaling factors. In theory n should not change as it is dimensionless but observed experimental and numerical data show the number of cycles to failure has an inverse relationship with the structural size.

The first order similitude theory is a theory founded on space scaling that calls for the use of two scaled experiments. Scale effects are accommodated either explicitly or implicitly in its formulation. The zeroth order similitude theory now confirmed as akin to dimensional analysis uses a single scaled experiment and is used for the design of individual scaled fatigue experiments. The first order finite similitude theory then prescribes the scaling factors required to combine the outputs from the scaled model to form a virtual model that predicts full scale behaviour.

Within a damage tolerant design framework, fatigue and fracture has to be modelled using the fracture mechanics theory. The first order finite similitude rules have been shown to accurately describe the fracture behaviour of structures within both the linear elastic fracture mechanics framework and elastoplastic fracture mechanics framework. The theory is applied here to fatigue cases within the linear elastic fracture mechanics framework and its efficacy evaluated. Scaled fatigue tests of five different metals (steel, Al 6061 etc.) are designed and conducted following the first order finite similitude framework outlined in section 5.4.

This thesis presents contributions towards the use of smaller scaled down experiments for fatigue testing to predict full scale behaviour. The aim of the research was successfully achieved as it was revealed that the finite similitude theory can successfully predict

behaviour of propagating fatigue cracks within the linear elastic fracture mechanics (LEFM) framework. Both analytical and numerical studies show strong evidence that supports the use of first order finite similitude theory for fatigue testing. The fatigue crack growth rate of ASTM E647 standardised specimens can be accurately predicted using scaled models. Furthermore, for more practical cases as encountered in industry the first order theory is still able to make accurate predictions of full-scale fatigue response such as the critical/limiting defect size. The key conclusions from the thesis are summarised as follows:

- The complete fatigue crack growth response of metals (critical defect size, crack growth rate and path) can be simulated accurately using numerical software Abaqus (direct cyclic solver) for low cycle fatigue and Ansys (SMART solver) for both low and high cycle fatigue. The outputs correlate well with published experimental data.
- Geometric size effects are present in scaled fatigue testing for both mode I and mixed mode loading. One of the primary challenges in scaled experimentation in fatigue lies in the inability to scale the number of cycles to failure, n as it is a dimensionless number. This issue was resolved in this thesis by the proposal of a brand-new hypothesis viz: the product of the number of cycles to failure and change in stress intensity factor is second order (i.e., $\Delta K_{ts} n_{ts}$ is second order). This hypothesis led to the proposal of simple radical functions that relate the number of cycles to failure and stress intensity factor amplitude to change in geometric scale that were validated successfully both numerically and experimentally.
- Multiple subscale mixed mode fatigue testing is attempted for the first time in this thesis and near exact agreement of crack growth rate, path and crack propagation angle was achieved. Under mixed mode loadings, the crack path predicted using the SMART solver in Ansys was in good agreement with experimental data.
- The outcomes from the numerical experimentation confirmed that the fracture mechanics parameters that describe the fatigue behaviour of a full-scale component/structure for both low and high cycle fatigue can be predicted by a virtual model formed using two smaller replica models designed according to first order finite similitude rules with minimal error. Paris law was previously shown to exhibit incomplete similarity with scale according to dimensional analysis. It was proven for the first time in this work that complete similarity in Paris law is possible at two distinct scales. More generally, the fatigue crack growth rate da/dn behaves according to the first order rule.

- Fatigue crack growth rate is a first order rule consequently Paris law parameters C and m of a material can be predicted using scaled models with up to 99.9% accuracy.
- The fracture mechanics parameters predicted in this work are crack length, number of cycles to failure, stress intensity factor, crack path, mode I and II stress intensity factor and stress intensity factor distribution across the crack front. These parameters were predicted by the virtual models all within 10% error. These parameters would ordinarily be obtained using physical experiments, the numerical work in this thesis was performed as an alternative to obtain these parameters thus demonstrating the validity of the scaling theory to conducting real fatigue experiments in the laboratory or industrial settings using subscale models.
- Numerical simulations for planar and non-planar crack growth show an increase in error for fatigue outputs when geometric scaling factor (β) of the smallest model used in a virtual model is very small. However, fatigue outputs are still within 10% of the full-scale component values. Thus, when conducting physical fatigue tests the smallest scale model employed should be circa 20% of full-scale size ($\beta = 0.2$). Any β value in the range of $0.2 \leq \beta \leq 0.9$ can be employed in scaled fatigue tests.
- Numerical data showed an increase in fatigue life when the R ratio was increased (crack closure effect). Negative R ratios reduced the fatigue life. Stress intensity factor was observed to be non-uniform across the crack front. The highest stress intensity factor is recorded at roughly the midpoint of the crack front.
- Experimental data of three-point bending tests of concrete by previous researchers were examined, and first order rules applied to combine outputs from scaled models such as critical crack length, number of cycles to failure and Paris law parameters C and m . Good agreement was achieved despite the experiments not strictly designed and tested according to first order similitude rules in section 5.4.
- The ability to perform meaningful sub scale fatigue tests that are reflective of the full-scale component behaviour translates to cheaper cost, reduced time in the product lifecycle meaning new innovative products can be brought to market quicker and at a cheaper cost as multiple full scale fatigue tests are no longer a necessity.
- To accurately resolve the stress distribution at the crack tip and give accurate residual life predictions, the element size around the crack tip for full scale models should be set to 0.5mm or smaller for planar crack growth and for mixed mode fatigue cases 0.25mm or smaller to accurately resolve the stress distribution at the crack tip and

give accurate residual life predictions. The number of elements in the sub scale model should be the same as the full-scale model. This is achieved by multiplying the element sizes used in the full-scale model by the β value of the sub scale model.

- Excellent prediction of fatigue parameters enables engineers to make predictions of critical defect size as well as fatigue life and path of a component enabling remedial action to be undertaken in industrial settings. For example, by predicting the path accurately, measures can be taken to slow down crack growth to ensure the structural integrity of a component is intact such as drilling of stop holes, composite fibre patch repair, increasing redundant load paths, laser shot peening etc. Operating conditions (e.g., pressure in a pressure vessel) can be altered to achieve desired crack growth rates. It would enable engineers to determine service inspection intervals more accurately as the crack growth rates are more accurately predicted. This would result in cost savings by reducing unnecessary service inspections.
- Numerical experimentation confirms that the fatigue test output data must be synchronized to apply first order identities correctly in its point by point formulation. In the numerical work here, this is done by recording the variables of interest at the crack front advance points Δa . In a physical experiment, this can be achieved by recording data points such as stress intensity factor; ΔK and number of cycles at successive fixed crack length increments Δa_{ps} for the full-scale model, the data points for subscale model (β_i) should be recorded at $\beta_i \times \Delta a_{ps}$. Furthermore, ΔK values should be obtained at the same location in all samples. Typically, this would be at the midpoint of the crack front. The first order identities prescribed in section 5.4 can then be applied at these data points to predict full scale fatigue behaviour.
- Numerical simulations confirm that the first order theory predicts fatigue outputs accurately independent of the type of mechanical loading (stress, force, displacement, and pressure) and material (five different metals were tested).
- Limitations of the proposed framework are that the theory is only valid within the confines of continuum mechanics and thus there are practical limitations on the size of the smallest scaled experiment. In this work the smallest scaled experiment was circa 20% of the full-scale size. The size of the sub scale models has to be greater than the length scales where microstructure affects fatigue crack growth. The work here is limited to isotropic materials; only metals were tested. Furthermore, this work is applicable to geometrically similar structures only with an initial notch/defect.

8. Recommendations for future work

Fatigue is a very broad subject and it is impossible to investigate all the different factors that affect fatigue as scale changes within the limited time of a PhD study. The positive outcomes of the first order finite similitude theory as applied to fatigue presented in this thesis is a starting point for future research. The following recommendations are made for future efforts:

- The first recommendation is a physical scaled fatigue experimental investigation. Fatigue crack growth is demonstrated in this work to be a first order process. There is a distinct lack of experimental data describing the behaviour of propagating fatigue cracks at different scales. As a starting point, the ASTM E647 standardised specimens that were analysed numerically in this thesis should be tested. Isotropic scaling would be the focus with the same material used for the full-scale specimen and scaled down specimens. The experimental parameters such as the magnitude of the force applied to the scaled models would be calculated according to the procedure outlined in section 5.4. It is recommended that multiple fatigue tests at each scale are conducted with the mean values recorded to eliminate the statistical size effect ensuring that the observed differences at scale are caused solely by geometric sizing update. Relevant physical outputs from the experiment are the stress intensity factor, number of cycles to failure and crack length. The first order rules would then be used to combine the outputs to create a virtual model whose predictions can be contrasted with the outputs of the full-scale specimen. The Paris law constants C and m should be calculated according to ASTM E647 guidelines. This would be useful as it would add to the knowledge base presented in this thesis, further validating the efficacy of the theory.
- The numerical investigation performed in this thesis can be extended by considering a few different scenarios. Only Paris law was used for fatigue crack growth simulations in this work. The Ω_β introduced in this work, facilitates the study of changes in empirical fatigue laws with scale thus more empirical fatigue crack growth models (see section 2.4) should be tested. Industrial standards prescribe a correction factor to modify the Paris law exponent C and m (modified Paris law) for complex crack growth problems. However, complete similarity of the crack growth rate was demonstrated in this thesis, thus the expectation is that for more complex loading cases (e.g. residual stresses, crack closure effect etc.) the first order similitude

theory should still provide accurate predictions. Furthermore, constant amplitude loading was applied in all cases. Simulations of fatigue crack growth with components/ structures under variable loading should be conducted to determine if the virtual models constructed by the first order theory still give accurate predictions of the full-scale behaviour.

- Replica scaling was the focus of this thesis. However, there are situations where it is advantageous to use a different material in the testing phase than that of the prototype. A major reason for this is cost reduction. One can imagine a situation where a product is made from a very expensive material thus it would be very advantageous if a cheaper material can be used for the sub scale fatigue tests while still giving a good accurate prediction of the full-scale fatigue behaviour. It is anticipated that the material choices for the scaled models must be carefully considered with selected properties of the full-scale material chosen to match or be as close as possible. For example, the Young's modulus, yield strength, fracture toughness etc. Different materials would be used to determine the size effect on the fatigue response using a scaled experiment. The results from this study would inform the materials that should be used for the scaled models. A first attempt would involve using a different material to the prototype for both scaled models and examining the predictions of key fatigue parameters such as crack growth rate and stress intensity factor returned by the virtual models. If satisfactory results are achieved, then the complexity can be increased by using different materials for both scaled models that also differ from the full-scale model.
- This thesis is limited to structures with an initial defect i.e., crack or notch. It would be useful to determine if the first order theory can also capture the crack initiation life in addition to the crack propagation life for the safe life design approach. The cumulative fatigue damage (CFD) framework plots the stress amplitude against the number of cycles to failure. The empirical fatigue laws, Basquin law and Coffin Manson are then used to determine the fatigue strength by curve fitting the experimental data. A numerical investigation is possible as various commercial software can simulate fatigue damage using the CFD approach. Scaled models would be created using the same procedure in section 5.4 and the size effect in the $S - N$ and $\varepsilon - N$ curves examined. The use of an extra scaled model would be tested to determine if the size effects in the fatigue strength σ_f of the structure vanish.

Preliminary investigations on experimental fatigue data of forged steel [222] suggests that a slightly modified version of the hypothesis presented in this work is also valid for the CFD framework. The hypothesis is as follows; the product $\Delta\sigma_{ts}n_{ts}$ is second order with $\Delta\sigma_{ts}n_{ts} = \Delta\sigma_{\beta}n_{\beta}$, where $\Delta\sigma_{\beta}$ and n_{β} are the stress amplitude and number of cycles on Ω_{β} . The total life fatigue strength of the full-scale structure was predicted by the virtual models to within 5% error. Basquin law fatigue constants σ_f' and b were evaluated to great accuracy. This is significant as it suggests less conservative safety factors can be employed for fatigue assessments of structures in challenging operating conditions/environments such as offshore engineering structures, boiler pressure vessels, environmentally assisted fatigue, and in the characterisation of fatigue strength of new innovative materials such as different alloyed steels among others as more reliable fatigue strength predictions can be made using scaled models. It can be a useful tool to aid in the reduction of conservatism inherent in fitness for service assessment procedures in design codes. For example, the ASME code [221] applies a fatigue strength reduction factor of 20 to the value of the number of cycles to failure obtained from scaled tests to account for factors such as the size effect, surface finish etc when predicting the fatigue life of the full-scale component. More accurate $S - N$ curves can now be constructed from small/medium scale fatigue tests. Further validation of this hypothesis with more experimental data sets would be the focus in future publications.

Appendix: Publications

Published

1. Davey, K., Darvizeh, R., Akhigbe-Midu, O. and Sadeghi, H., 2022. Scaled cohesive zone models for fatigue crack propagation. *International Journal of Solids and Structures* 256, p.111956.
2. Davey, K., Akhigbe-Midu, O. Darvizeh, R., and Sadeghi, H., 2023. Scaled empirical fatigue laws. *Engineering Fracture Mechanics* 284 p.109258.
3. Davey, K., Akhigbe-Midu, O. Darvizeh, R., and Sadeghi, H., 2023. Scaled fatigue cracks under service loads. *Theoretical and Applied Fracture Mechanics* 127 p. 103991.

References

1. R. I. Stephens, A. Fatemi, R. R. Stephens, and H. O. Fuchs, *Metal Fatigue Engineering*, John Wiley & Sons, New York, NY, USA, 2001.
2. Schijve, J. ed., 2009. *Fatigue of Structures and Materials*. Dordrecht: Springer Netherlands.
3. Zhiping, Q., Zesheng, Z. and Lei, W., 2018. Numerical analysis methods of structural fatigue and fracture problems. *Contact Fracture Mechanics*, 12, p.235.
4. Anderson, T.L., 2017. *Fracture Mechanics: Fundamentals and Applications*. CRC press.
5. Marušić, Ž., Bartulović, D. and Maković, B., 2015. Methods to Detect and Prevent Fatigue in Ageing Aircraft Structures. *Tehnicki vjesnik/Technical Gazette*, 22(3).
6. Fajri, A., Prabowo, A.R., Muhayat, N., Smaradhana, D.F. and Bahatmaka, A., 2021. Fatigue analysis of engineering structures: State of development and achievement. *Procedia Structural Integrity*, 33, pp.19-26.
7. Toor, P.M., 1973. A review of some damage tolerance design approaches for aircraft structures. *Engineering Fracture Mechanics*, 5(4), pp.837-880.
8. Davidson, D.L. and Lankford, J., 1992. Fatigue crack growth in metals and alloys: mechanisms and micromechanics. *International Materials Reviews*, 37(1), pp.45-76.
9. Molent, L., Jones, R., Barter, S. and Pitt, S., 2006. Recent developments in fatigue crack growth assessment. *International Journal of Fatigue*, 28(12), pp.1759-1768.
10. Wöhler A. "Über die Festigkeitsversuche mit Eisen und Stahl", *Zeitschrift für Bauwesen* 20 (1870): 73-106.
11. Jones, R., 2014. Fatigue crack growth and damage tolerance. *Fatigue & Fracture of Engineering Materials & Structures*, 37(5), pp.463-483.
12. Ritchie, R.O., 1999. Mechanisms of fatigue-crack propagation in ductile and brittle solids. *International Journal of Fracture*, 100(1), pp.55-83.
13. Coutinho, C.P., Baptista, A.J. and Rodrigues, J.D., 2016. Reduced scale models based on similitude theory: A review up to 2015. *Engineering Structures*, 119, pp.81-94.
14. Bazant, Z.P. and Xu, K., 1991. Size effect in fatigue fracture of concrete. *ACI Materials Journal*, 88(4), pp.390-399.
15. Bažant, Z.P., 1984. Size effect in blunt fracture: concrete, rock, metal. *Journal of Engineering Mechanics*, 110(4), pp.518-535.
16. Paggi, M., 2009. A dimensional analysis approach to fatigue in quasi-brittle materials. *Frattura ed Integrità Strutturale*, 10, pp.43-53.

17. Carpinteri, A., Paggi, M., Daniewicz, S.R. and Dean, S.W. (2011). Dimensional Analysis and Fractal Modeling of Fatigue Crack Growth. *Journal of ASTM International*, 8(10),
18. Paggi, M., 2011. Modelling fatigue in quasi-brittle materials with incomplete self-similarity concepts. *Materials and Structures*, 44(3), pp.659-670.
19. Carpinteri, A., Spagnoli, A. and Vantadori, S., 2002. An approach to size effect in fatigue of metals using fractal theories. *Fatigue & Fracture of Engineering Materials & Structures*, 25(7), pp.619-627.
20. Spagnoli, A., 2005. Self-similarity and fractals in the Paris range of fatigue crack growth. *Mechanics of Materials*, 37(5), pp.519-529.
21. Paggi, M. and Carpinteri, A., 2009. Fractal and multifractal approaches for the analysis of crack-size dependent scaling laws in fatigue. *Chaos, Solitons & Fractals*, 40(3), pp.1136-1145.
22. Carpinteri, A. and Paggi, M., 2009. A unified interpretation of the power laws in fatigue and the analytical correlations between cyclic properties of engineering materials. *International Journal of Fatigue*, 31(10), pp.1524-1531.
23. Furuya, Y., 2010. Size effects in gigacycle fatigue of high-strength steel under ultrasonic fatigue testing. *Procedia Engineering*, 2(1), pp.485-490.
24. Brose, W.R. and Dowling, N.E., 1979. Size effects on the fatigue crack growth rate of type 304 stainless steel. In *Elastic-plastic Fracture*. ASTM International.
25. Garr, K.R. and Hresko III, G.C., 1998, January. A size effect on the fatigue crack growth rate threshold of alloy 718. In *Fatigue Crack Growth Thresholds, Endurance Limits and Design*.
26. Davey, K., Darvizeh, R. and Al-Tamimi, A., 2017. Scaled metal forming experiments: a transport equation approach. *International Journal of Solids and Structures*, 125, pp.184-205.
27. Irwin, G.R. (1958) *Fracture, Elasticity and Plasticity*. Springer, Berlin, 551-590.
28. Paris, P.C., 1961. A rational analytic theory of fatigue. *The Trend in Engineering*, 13, p.9.
29. D. Dugdale, "Yielding of steel sheets containing slits," *Journal of the Mechanics and Physics of Solids*, 8(2), pp. 100–104, 1960.
30. G. I. Barenblatt, "The mathematical theory of equilibrium cracks in brittle fracture," *Advanced Applied Mechanics*, 7(1), pp. 55–129, 1962.
31. Hillerborg, A., Mod  er, M. and Petersson, P.E., 1976. Analysis of crack formation and crack growth in concrete by means of fracture mechanics and finite elements. *Cement*

- and *Concrete Research*, 6(6), pp.773-781.
32. Melenk, J.M. and Babuška, I., 1996. The partition of unity finite element method: basic theory and applications. *Computer Methods in Applied Mechanics and Engineering*, 139(1-4), pp.289-314.
 33. Belytschko, T. and Black, T., 1999. Elastic crack growth in finite elements with minimal remeshing. *International Journal for Numerical Methods in Engineering*, 45(5), pp.601-620.
 34. Atar, M., Davey, K. and Darvizeh, R., 2021. Application of first-order finite similitude in structural mechanics and earthquake engineering. *Earthquake Engineering and Structural Dynamics*, 50(15), pp.4051-4075.
 35. Singal, L.C., Gill, R.S. and Mahajan, A., 2017. Fatigue Mechanical Life Design-A Review. *International Journal of Engineering Research and General Science*, 5(2), pp.247-51.
 36. Rayleigh, L., 1915, "The Principle of Similitude," *Nature*, 95, pp. 66–68
 37. Buckingham, E., 1914. On physically similar systems; illustrations of the use of dimensional equations. *Physical Review*, 4(4), p.345.
 38. Pavlou, D.G., 2018. The theory of the SN fatigue damage envelope: generalization of linear, double-linear, and non-linear fatigue damage models. *International Journal of Fatigue*, 110, pp.204-214.
 39. Hafezi, M.H., Abdullah, N.N., Correia, J.F. and De Jesus, A.M., 2012. An assessment of a strain-life approach for fatigue crack growth. *International Journal of Structural Integrity*, 3(4), pp.344-376.
 40. Frost, N.E., Pook, L.P. and Denton, K., 1971. A fracture mechanics analysis of fatigue crack growth data for various materials. *Engineering Fracture Mechanics*, 3(2), pp.109-126.
 41. Griffith, A.A., 1921. VI. The phenomena of rupture and flow in solids. *Philosophical transactions of the royal society of london. Series A, containing papers of a mathematical or physical character*, 221(582-593), pp.163-198.
 42. Bažant, Z.P., 2000. Size effect. *International Journal of Solids and Structures*, 37(1-2), pp.69-80.
 43. Harold M Westergaard. Bearing pressures and cracks. *Journal of Applied Mechanics*, 6(2):A49–A53, 1939.
 44. Irwin G.R. Analysis of stresses and strains near the end of a crack traversing a plate. *Journal of Applied Mechanics*, 24:361–364, 1957.

45. Perez N., 2004, *Fracture Mechanics*, Kluwer Academic Publishers, Boston.
46. Lewinsohn, C.A., 2000. *Mechanical Behavior of Materials*, Norman E. Dowling.
47. Paris, P.C., Tada, H. and Donald, J.K., 1999. Service load fatigue damage—a historical perspective. *International Journal of Fatigue*, 21, pp.S35-S46.
48. Hadley, I., 2018. BS 7910: 2013 in brief. *International Journal of Pressure Vessels and Piping*, 165, pp.263-269.
49. Anderson, T.L. and Osage, D.A., 2000. API 579: a comprehensive fitness-for-service guide. *International Journal of Pressure Vessels and Piping*, 77(14-15), pp.953-963.
50. Walker, K., 1970. The effect of stress ratio during crack propagation and fatigue for 2024-T3 and 7075-T6 aluminum.
51. Forman, R.G., Kearney, V.E. and Engle, R.M., 1967. Numerical analysis of crack propagation in cyclic-loaded structures.
52. Maierhofer, J., Pippan, R. and Gänser, H.P., 2014. Modified NASGRO equation for physically short cracks. *International Journal of Fatigue*, 59, pp.200-207.
53. Newman Jr, J.C. and Raju, I.S., 1984. Prediction of fatigue crack-growth patterns and lives in three-dimensional cracked bodies. In *Fracture 84* (pp. 1597-1608).
54. Klesnil, M. and Lukác, P., 1992. *Fatigue of Metallic Materials* (Vol. 71). Elsevier.
55. Wang, G.S., 1995. An EPFM analysis of crack initiation, stable growth and instability. *Engineering Fracture Mechanics*, 50(2), pp.261-282.
56. Farahmand, B., 2001. Elastic-plastic fracture mechanics (EPFM) and applications. In *Fracture Mechanics of Metals, Composites, Welds, and Bolted Joints* (pp. 180-236). Springer, Boston, MA.
57. Božić, Ž., Mlikota, M. and Schmauder, S., 2011. Application of the ΔK , ΔJ and $\Delta CTOD$ parameters in fatigue crack growth modelling. *Tehnički vjesnik*, 18(3), pp.459-466.
58. Qian, J. and Fatemi, A., 1996. Mixed mode fatigue crack growth: a literature survey. *Engineering Fracture Mechanics*, 55(6), pp.969-990.
59. Tanaka, K., 1974. Fatigue crack propagation from a crack inclined to the cyclic tensile axis. *Engineering Fracture Mechanics*, 6(3), pp.493-507.
60. Gdoutos, E.E., 2012. *Problems of mixed mode crack propagation* (Vol. 2). Springer Science & Business Media.
61. Peek, L. P., The fatigue crack direction and threshold behaviour of mild steel under mixed mode I and III loading. *International Journal of Fatigue*, 1985, 7, 21-30.
62. Hyde, T. H. and Chambers, A. C., A compact mixed mode (CMM) fracture specimen. *Journal of Strain Analysis for Engineering Design*, 23(2), pp.61-66.

63. Rozumek, D. and Macha, E., 2009. A survey of failure criteria and parameters in mixed-mode fatigue crack growth. *Materials science*, 45(2), pp.190-210.
64. Richard, H.A. and Benitz, K., 1983. A loading device for the creation of mixed mode in fracture mechanics. *International Journal of Fracture*, 22(2), pp.R55-R58.
65. Erdogan, F. and Sih, G.C., 1963. On the crack extension in plates under plane loading and transverse shear.
66. Sajith, S., Murthy, K.S.R.K. and Robi, P.S., 2018. Fatigue life prediction under mixed-mode loading using equivalent stress intensity factor models. In *MATEC Web of Conferences* (Vol. 172, p. 03005). EDP Sciences.
67. Ayhan, A.O. and Demir, O., 2021. Computational modeling of three-dimensional mixed mode-I/II/III fatigue crack growth problems and experiments. *Computers & Structures*, 243, p.106399.
68. Zienkiewicz, O.C. and Taylor, R.L., 2005. *The finite element method for solid and structural mechanics*. Elsevier.
69. Sauter, S.A. and Schwab, C., 2010. Boundary element methods. In *Boundary Element Methods* (pp. 183-287). Springer, Berlin, Heidelberg.
70. Zi, G. and Belytschko, T., 2003. New crack-tip elements for XFEM and applications to cohesive cracks. *International Journal for Numerical Methods in Engineering*, 57(15), pp.2221-2240.
71. M. Griebel and M. A. Schweitzer. *Meshfree Methods for Partial Differential Equations*. Springer, 2003.
72. Anaei, M.M., Khosravifard, A. and Bui, T.Q., 2021. Analysis of fracture mechanics and fatigue crack growth in moderately thick plates using an efficient meshfree approach. *Theoretical and Applied Fracture Mechanics*, 113, p.102943.
73. Schwalbe, K., Scheider, I. and Cornec, A., Guidelines for Applying Cohesive Models to the Damage Behaviour of Engineering Materials and Structures, 2013.
74. Roth, S., Hütter, G. and Kuna, M., 2014. Simulation of fatigue crack growth with a cyclic cohesive zone model. *International Journal of Fracture*, 188(1), pp.23-45.
75. Nojavan, S., Schesser, D. and Yang, Q.D., 2016. An in situ fatigue-CZM for unified crack initiation and propagation in composites under cyclic loading. *Composite Structures*, 146, pp.34-49.
76. Scheider, I. and Brocks, W., 2003. The effect of the traction separation law on the results of cohesive zone crack propagation analyses. In *Key Engineering Materials* (Vol. 251, pp. 313-318). Trans Tech Publications Ltd.

77. Zienkiewicz, O.C., Taylor, R.L., 2000. *The finite element method: solid mechanics* (Vol. 2). Butterworth-heinemann.
78. Reddy, J.N., 2014. *An Introduction to Nonlinear Finite Element Analysis Second Edition: with applications to heat transfer, fluid mechanics, and solid mechanics*. OUP Oxford.
79. Aygöl, M., Al-Emrani, M. and Urushadze, S., 2012. Modelling and fatigue life assessment of orthotropic bridge deck details using FEM. *International Journal of Fatigue*, 40, pp.129-142.
80. Reddy, J.N. and Gartling, D.K., 2010. *The finite element method in heat transfer and fluid dynamics*. CRC press.
81. Rege, K. and Lemu, H.G., 2017, December. A review of fatigue crack propagation modelling techniques using FEM and XFEM. *IOP Conference Series: Materials Science and Engineering*, (Vol. 276, No. 1, p. 012027). IOP Publishing.
82. Chan, S.K., Tuba, I.S. and Wilson, W.K., 1970. On the finite element method in linear fracture mechanics. *Engineering Fracture Mechanics*, 2(1), pp.1-17.
83. Parks, D.M., 1974. A stiffness derivative finite element technique for determination of crack tip stress intensity factors. *International Journal of Fracture*, 10(4), pp.487-502.
84. Brocks, W., Cornec, A. and Scheider, I., 2003. 3.03—Computational Aspects of Nonlinear Fracture Mechanics. *Comprehensive Structural Integrity Fracture of Materials from Nano to Macro; Milne, I., Ritchie, RO, Karihaloo, BBT, Eds*, pp.127-209.
85. Zhang, X., Li, L., Qi, X., Zheng, J., Zhang, X., Chen, B., Feng, J. and Duan, S., 2017. Experimental and numerical investigation of fatigue crack growth in the cracked gear tooth. *Fatigue & Fracture of Engineering Materials & Structures*, 40(7), pp.1037-1047.
86. Fulland, M., Sander, M., Kullmer, G. and Richard, H.A., 2008. Analysis of fatigue crack propagation in the frame of a hydraulic press. *Engineering Fracture Mechanics*, 75(3-4), pp.892-900.
87. Citarella, R., Lepore, M., Maligno, A. and Shlyannikov, V., 2015. FEM simulation of a crack propagation in a round bar under combined tension and torsion fatigue loading. *Frattura ed Integrità Strutturale*, 9(31), pp.138-147.
88. Poursaeidi, E., Kavandi, A., Vaezi, K., Kalbasi, M.R. and Arhani, M.M., 2014. Fatigue crack growth prediction in a gas turbine casing. *Engineering Failure Analysis*, 44, pp.371-381.
89. Rabold, F., Kuna, M. and Leibelt, T., 2013. Procrack: A software for simulating three-

- dimensional fatigue crack growth. In *Advanced finite element methods and applications* (pp. 355-374). Springer, Berlin, Heidelberg.
90. Rabold, F. and Kuna, M., 2014. Automated finite element simulation of fatigue crack growth in three-dimensional structures with the software system ProCrack. *Procedia Materials Science*, 3, pp.1099-1104.
 91. Richard, H.A., Fulland, M., Sander, M. and Kullmer, G., 2005. Fracture in a rubber-sprung railway wheel. *Engineering Failure Analysis*, 12(6), pp.986-999.
 92. Lin, X.B. and Smith, R.A., 1998. Fatigue growth simulation for cracks in notched and unnotched round bars. *International Journal of Mechanical Sciences*, 40(5), pp.405-419.
 93. Hou, J., Wescott, R. and Attia, M., 2014. Prediction of fatigue crack propagation lives of turbine discs with forging-induced initial cracks. *Engineering Fracture Mechanics*, 131, pp.406-418.
 94. Branco, R., Antunes, F.V. and Costa, J.D., 2015. A review on 3D-FE adaptive remeshing techniques for crack growth modelling. *Engineering Fracture Mechanics*, 141, pp.170-195.
 95. ANSYS. Academic Research Mechanical, Release 2021 R1, ANSYS, Inc.,
 96. Alshoaibi, A.M., 2022. Fatigue crack growth analysis under constant amplitude loading using finite element method. *Materials*, 15(8), p.2937.
 97. Doğan, O., Yuce, C. and Karpas, F., 2021. Effects of rim thickness and drive side pressure angle on gear tooth root stress and fatigue crack propagation life. *Engineering Failure Analysis*, 122, p.105260.
 98. Alshoaibi, A.M., 2021. Computational simulation of 3D fatigue crack growth under mixed-mode loading. *Applied Sciences*, 11(13), p.5953.
 99. Fageehi, Y.A. and Alshoaibi, A.M., 2020. Numerical simulation of mixed-mode fatigue crack growth for compact tension shear specimen. *Advances in Materials Science and Engineering*, 2020.
 100. Fageehi, Y.A., 2021. Fatigue Crack Growth Analysis with Extended Finite Element for 3D Linear Elastic Material. *Metals*, 11(3), p.397.
 101. Singh, I.V., Mishra, B.K. and Bhattacharya, S., 2011. XFEM simulation of cracks, holes and inclusions in functionally graded materials. *International Journal of Mechanics and Materials in Design*, 7(3), pp.199-218.
 102. Bhattacharya, S., Singh, I.V., Mishra, B.K. and Bui, T.Q., 2013. Fatigue crack growth simulations of interfacial cracks in bi-layered FGMs using XFEM. *Computational Mechanics*, 52(4), pp.799-814.

103. Pathak, H., Singh, A. and Singh, I.V., 2013. Fatigue crack growth simulations of 3-D problems using XFEM. *International Journal of Mechanical Sciences*, 76, pp.112-131.
104. Bergara, A., Dorado, J.I., Martin-Meizoso, A. and Martínez-Esnaola, J.M., 2017. Fatigue crack propagation in complex stress fields: Experiments and numerical simulations using the Extended Finite Element Method (XFEM). *International Journal of Fatigue*, 103, pp.112-121.
105. Pandey, V.B., Singh, I.V., Mishra, B.K., Ahmad, S., Rao, A.V. and Kumar, V., 2019. A new framework based on continuum damage mechanics and XFEM for high cycle fatigue crack growth simulations. *Engineering Fracture Mechanics*, 206, pp.172-200.
106. Chopp, D.L. and Sukumar, N., 2003. Fatigue crack propagation of multiple coplanar cracks with the coupled extended finite element/fast marching method. *International Journal of Engineering Science*, 41(8), pp.845-869.
107. Kumar, S., Singh, I.V. and Mishra, B.K., 2015. A homogenized XFEM approach to simulate fatigue crack growth problems. *Computers & Structures*, 150, pp.1-22.
108. Sghayer, A., Grbović, A., Sedmak, A., Dinulović, M., Doncheva, E. and Petrovski, B., 2017. Fatigue life analysis of the integral skin-stringer panel using XFEM. *Structural Integrity and Life*.
109. Ren, X. and Guan, X., 2017. Three dimensional crack propagation through mesh-based explicit representation for arbitrarily shaped cracks using the extended finite element method. *Engineering Fracture Mechanics*, 177, pp.218-238.
110. Yazid, A., Abdelkader, N. and Abdelmadjid, H., 2009. A state-of-the-art review of the X-FEM for computational fracture mechanics. *Applied Mathematical Modelling*, 33(12), pp.4269-4282.
111. Gibbings, J.C., 1980. On dimensional analysis. *Journal of Physics A: Mathematical and General*, 13(1), p.75.
112. O'Sullivan Jr, W.J., 1957. *Theory of aircraft structural models subject to aerodynamic heating and external loads* (No. NACA-TN-4115).
113. Goodier, J.N. and Thomson, W.T., 1944. *Applicability of similarity principles to structural models* (No. 933). National Advisory Committee for Aeronautics.
114. Casaburo, A., Petrone, G., Franco, F. and De Rosa, S., 2019. A review of similitude methods for structural engineering. *Applied Mechanics Reviews*, 71(3).
115. Soedel, W., 1971. Similitude approximations for vibrating thin shells. *The Journal of the Acoustical Society of America*, 49(5B), pp.1535-1541

116. Kline, S.J., 2012. *Similitude and approximation theory*. Springer Science & Business Media.
117. De Rosa, S. and Franco, F., 2008. A scaling procedure for the response of an isolated system with high modal overlap factor. *Mechanical Systems and Signal Processing*, 22(7), pp.1549-1565.
118. Westine, P.S., Dodge, F.T. and Baker, W.E., 2012. *Similarity methods in engineering dynamics: theory and practice of scale modeling*. Elsevier.
119. Zohuri, B., 2015. *Dimensional analysis and self-similarity methods for engineers and scientists*. Springer.
120. Gibbings, J.C., 2011. *Dimensional analysis*. Springer Science & Business Media.
121. Evans, J.H., 1972. Dimensional analysis and the Buckingham Pi theorem. *American Journal of Physics*, 40(12), pp.1815-1822.
122. Masuda, K., Ishihara, S. and Oguma, N., 2021. Effect of Specimen Thickness and Stress Intensity Factor Range on Plasticity-Induced Fatigue Crack Closure in A7075-T6 Alloy. *Materials*, 14(3), p.664.
123. Findley, W.N., 1972. An explanation of size effect in fatigue of metals. *Journal of Mechanical Engineering Science*. 14(6), pp.424-428.
124. Hu, X., Guan, J., Wang, Y., Keating, A. and Yang, S., 2017. Comparison of boundary and size effect models based on new developments. *Engineering Fracture Mechanics*, 175, pp.146-167.
125. Tridello, A., Niutta, C.B., Berto, F. and Paolino, D.S., 2021. Size-effect in very high cycle fatigue: a review. *International Journal of Fatigue*. 153, p.106462.
126. Kloos, K.H., Buch, A. and Zankov, D., 1981. Pure geometrical size effect in fatigue tests with constant stress amplitude and in programme tests. *Materialwissenschaft und Werkstofftechnik*, 12(2), pp.40-50.
127. Barenblatt, G.I. and Botvina, L.R., 1980. Incomplete self-similarity of fatigue in the linear range of crack growth. *Fatigue & Fracture of Engineering Materials & Structures*, 3(3), pp.193-202.
128. Le, J.L., Manning, J. and Labuz, J.F., 2014. Scaling of fatigue crack growth in rock. *International Journal of Rock Mechanics and Mining Sciences*, 72, pp.71-79.
129. Kirane, K. and Bažant, Z.P. (2016). Size effect in Paris law and fatigue lifetimes for quasibrittle materials: Modified theory, experiments and micro-modeling. *International Journal of Fatigue* 83, pp.209–220.
130. Ritchie, R.O. and Suresh, S., 1983. The fracture mechanics similitude concept:

- questions concerning its application to the behaviour of short fatigue cracks. *Material Science and Engineering* 57(2), pp.L27-L30.
131. Ritchie, R.O. and Knott, J.F., 1973. Mechanisms of fatigue crack growth in low alloy steel. *Acta Metallurgica*, 21(5), pp.639-648.
 132. Ritchie, R.O., 1999. Mechanisms of fatigue-crack propagation in ductile and brittle solids. *International Journal of Fracture*, 100(1), pp.55-83.
 133. Heiser, F.A. and Mortimer, W., 1972. Effect of thickness and orientation on fatigue crack growth rate in 4340 steel. *Metallurgical Transactions*, 3(8), pp.2119-2123.
 134. Ciavarella, M., Paggi, M. and Carpinteri, A., 2008. One, no one, and one hundred thousand crack propagation laws: a generalized Barenblatt and Botvina dimensional analysis approach to fatigue crack growth. *Journal of the Mechanics and Physics of Solids*, 56(12), pp.3416-3432.
 135. Turnbull, A. and De Los Rios, E.R., 1995. The effect of grain size on the fatigue of commercially pure aluminium. *Fatigue & Fracture of Engineering Materials & Structures*, 18(12), pp.1455-1467.
 136. Suresh, S. and Ritchie, R.O., 1984. Propagation of short fatigue cracks. *International Metals Reviews*, 29(1), pp.445-475.
 137. Mughrabi, H., 2013. Microstructural fatigue mechanisms: Cyclic slip irreversibility, crack initiation, non-linear elastic damage analysis. *International Journal of Fatigue*, 57, pp.2-8.
 138. Mughrabi, H., 1999. On the life-controlling microstructural fatigue mechanisms in ductile metals and alloys in the gigacycle regime. *Fatigue and Fracture of Engineering materials and Structures*, 22(7), p.633.
 139. McEvily, A.J., Eifler, D. and Macherauch, E., 1991. An analysis of the growth of short fatigue cracks. *Engineering Fracture Mechanics*, 40(3), pp.571-584.
 140. Suresh, S., Vasudevan, A.K. and Bretz, P.E., 1984. Mechanisms of slow fatigue crack growth in high strength aluminum alloys: role of microstructure and environment. *Metallurgical Transactions A*, 15, pp.369-379.
 141. Kramberger, J., Jezernik, N., Göncz, P. and Glodež, S., 2010. Extension of the Tanaka–Mura model for fatigue crack initiation in thermally cut martensitic steels. *Engineering Fracture Mechanics*, 77(11), pp.2040-2050.
 142. Taylor, D. and Knott, J.F., 1981. Fatigue crack propagation behaviour of short cracks; the effect of microstructure. *Fatigue & Fracture of Engineering Materials & Structures*, 4(2), pp.147-155.

143. Tanaka, K. and Mura, T., 1981. A dislocation model for fatigue crack initiation.
144. Zhu, X., Gong, C., Jia, Y.F., Wang, R., Zhang, C., Fu, Y., Tu, S.T. and Zhang, X.C., 2019. Influence of grain size on the small fatigue crack initiation and propagation behaviors of a nickel-based superalloy at 650° C. *Journal of Materials Science & Technology*, 35(8), pp.1607-1617.
145. D'Angela, D. and Ercolino, M., 2021. Fatigue crack growth in metallic components: Numerical modelling and analytical solution. *Structural Engineering and Mechanics* 79(5), pp. 541-556.
146. Nasri K and Zenasni M 2017 Fatigue crack growth simulation in coated materials using X-FEM *Comptes Rendus Mecanique*, 345(4), pp. 271-280.
147. Hu, X., Xu, J., Du, X., Zhang, Y. and Zhou, F., 2020. Research on Fatigue Crack Propagation of 304 Austenitic Stainless Steel Based on XFEM and CZM. *Metals*, 10(6), p. 727.
148. Kumar, S., Singh, I.V. and Mishra, B.K. (2015), "A homogenized XFEM approach to simulate fatigue crack growth problems", *Computers and Structures* 150, pp. 1-22.
149. Singh, I.V., Mishra, B.K., Bhattacharya, S., Patil, R.U., 2012. The numerical simulation of fatigue crack growth using extended finite element method. *International Journal of Fatigue*. 36 (1), pp. 109-119.
150. Farukh, F., Zhao, L., Jiang, R., Reed, P., Proppentner, D. and Shollock, B., 2015. Fatigue crack growth in a nickel-based superalloy at elevated temperature-experimental studies, viscoplasticity modelling and XFEM predictions. *Mechanics of Advanced Materials and Modern Processes*, 1(1), pp.1-13.
151. Galilei, G., and Weston, J., 1730, Mathematical Discourses Concerning Two New Sciences Relating to Mechanics and Local Motion: In Four Dialogues, John Hooke, London p. 104105.
152. Kline, S.J. and Radbill, J.R., 1966. Similitude and approximation theory. *Journal of Applied Mechanics*, 33(1), p. 238.
153. Bažant, Z.P. and Chen, E.-P., 1997. Scaling of Structural Failure. *Applied Mechanics Reviews*. 50(10), pp. 593–627.
154. Virkler, DA, Hillberry, BM, and Goel, PK., 1978. The Statistical Nature of Fatigue Crack Propagation, *Journal of Engineering Materials and Technology* 101(2): pp. 148-153.
155. Barenblatt G.I., 1996. Scaling, Self-similarity and Intermediate Asymptotics. Cambridge: Cambridge University Press.

156. Carpinteri, A., Spagnoli, A. and Vantadori, S., 2002. An approach to size effect in fatigue of metals using fractal theories. *Fatigue & Fracture of Engineering Materials & Structures*, 25(7), pp. 619-627.
157. Tomaszewski, T., Sempruch, J. and Piątkowski, T., 2014. Verification of selected models of the size effect based on high-cycle fatigue testing on mini specimens made of EN AW-6063. *Journal of Theoretical and Applied Mechanics*, 52(4), pp.883-894.
158. Ray, S. and Kishen, J.C., 2012. Fatigue crack growth due to overloads in plain concrete using scaling laws. *Sadhana*, 37(1), pp. 107-124.
159. Al-Tamimi, A., Darvizeh, R. and Davey, K., 2017. Scaling of metal forming processes. *Procedia Engineering*, 207, pp.1069-1074.
160. Sadeghi, H., Davey, K., Darvizeh, R. and Darvizeh, A., 2019a. Scaled models for failure under impact loading. *International Journal of Impact Engineering*, 129, pp. 36-56.
161. Sadeghi, H., Davey, K., Darvizeh, R. and Darvizeh, A., 2019b. A scaled framework for strain rate sensitive structures subjected to high rate impact loading. *International Journal of Impact Engineering*, 125, pp. 229-245.
162. Sadeghi, H., Davey, K., Darvizeh, R., Rajabiehfard, R. and Darvizeh, A., 2020. An investigation into finite similitude for high-rate loading processes: Advantages in comparison to dimensional analysis and its practical implementation. *International Journal of Impact Engineering*, 140, p. 103554.
163. Davey, K., Sadeghi, H., Darvizeh, R., Golbaf, A. and Darvizeh, A., 2021a. A finite similitude approach to scaled impact mechanics. *International Journal of Impact Engineering*, 148, p. 103744.
164. Davey, K., Darvizeh, R., Atar, M. and Golbaf, A., 2021c. A Study of Scale Effects in Discrete Scaled Dynamic Systems. *International Journal of Mechanical Sciences*, 199, p. 106399.
165. Davey, K., Atar, M., Sadeghi, H. and Darvizeh, R., 2021d. The scaling of nonlinear structural dynamic systems. *International Journal of Mechanical Sciences*, 206, p. 106631.
166. Ochoa-Cabrero, R., Alonso-Rasgado, T. and Davey, K., 2018. Scaling in biomechanical experimentation: a finite similitude approach. *Journal of The Royal Society Interface*, 15(143), p. 20180254.
167. Ochoa-Cabrero, R., Alonso-Rasgado, T. and Davey, K., 2020. Zeroth-order finite similitude and scaling of complex geometries in biomechanical

- experimentation. *Journal of The Royal Society Interface*, 17(167), p. 20190806.
168. Davey, K., Darvizeh, R. and Zhang, J., 2021b. Finite similitude in fracture mechanics. *Engineering Fracture Mechanics*, 245, p. 107573.
 169. Zhan Z, Hu W, Li B, Zhang Y, Meng Q and Quan Z., 2017 Continuum damage mechanics combined with the extended finite element method for the total life prediction of a metallic component *International Journal of Mechanical Sciences*, 124, pp. 48-58
 170. Davey, K. and Darvizeh, R., 2016. Neglected transport equations: extended Rankine–Hugoniot conditions and J-integrals for fracture. *Continuum Mechanics and Thermodynamics*, 28(5), pp. 1525-1552.
 171. Salih, S., Davey, K. and Zou, Z., 2016. Rate-dependent elastic and elasto-plastic cohesive zone models for dynamic crack propagation. *International Journal of Solids and Structures* 90, pp. 95-115.
 172. Turon, A., Davila, C.G., Camanho, P.P. and Costa, J., 2007. An engineering solution for mesh size effects in the simulation of delamination using cohesive zone models. *Engineering Fracture Mechanics*, 74(10), pp. 1665-1682.
 173. Hutchinson JW (1968) Singular behavior at the end of a tensile crack in a hardening material. *Journal of the Mechanics and Physics of Solids*, 16(1), pp. 13-31.
 174. ASTM E 647. Standard test method for measurement of fatigue crack growth rates; 2015.
 175. Farahani, B.V., Tavares, P.J., Belinha, J. and Moreira, P.M.G.P., 2017. A fracture mechanics study of a compact tension specimen: digital image correlation, finite element and meshless methods. *Procedia Structural Integrity*, 5, pp. 920-927.
 176. Abaqus 2019, Dassault Systemes (Providence, RI, USA).
 177. London, T., De Bono, D. and Sun, X., 2015. An evaluation of the low cycle fatigue analysis procedure in Abaqus for crack propagation: numerical benchmarks and experimental validation. In SIMULIA UK Regional Users Meeting.
 178. Zhang, Y.M., Fan, M., Xiao, Z.M. and Zhang, W.G., 2016. Fatigue analysis on offshore pipelines with embedded cracks. *Ocean Engineering*, 117, pp. 45-56.
 179. Davis, J.R. ed., 1992. *ASM materials engineering dictionary*. ASM international.
 180. Liu, P.F., Zhang, B.J. and Zheng, J.Y., 2012. Finite element analysis of plastic collapse and crack behavior of steel pressure vessels and piping using XFEM. *Journal of Failure Analysis and Prevention*, 12(6), pp. 707-718.
 181. D’Angela, D. and Ercolino, M., 2018. Finite element analysis of fatigue response of nickel steel compact tension samples using ABAQUS. *Procedia Structural Integrity*, 13,

- pp. 939-946.
182. Carpinteri, A. and Montagnoli, F., 2019. Scaling and fractality in fatigue crack growth: Implications to Paris' law and Wöhler's curve. *Procedia Structural Integrity*, 14, pp.957-963.
 183. Ilie, P. and Ince, A., 2022. Three-dimensional fatigue crack growth simulation and fatigue life assessment based on finite element analysis. *Fatigue & Fracture of Engineering Materials & Structures*, 45(11), pp.3251-3266.
 184. Carpinteri, A. and Montagnoli, F., 2020. Scaling and fractality in subcritical fatigue crack growth: Crack-size effects on Paris' law and fatigue threshold. *Fatigue & Fracture of Engineering Materials & Structures*, 43(4), pp.788-801.
 185. Kirane, K. and Bažant, Z.P., 2015. Size effect in Paris law for quasibrittle materials analyzed by the microplane constitutive model M7. *Mechanics Research Communications*, 68, pp.60-64.
 186. Bazant, Z.P. and Schell, W.F., 1993. Fatigue fracture of high-strength concrete and size effect. *ACI Materials Journal*, 90, pp.472-472.
 187. Spagnoli, A., 2005. Self-similarity and fractals in the Paris range of fatigue crack growth. *Mechanics of Materials*. 37(5), pp.519-529.
 188. Zhang, J., Davey, K., Darvizeh, R. and Sadeghi, H., 2022. A two-experiment approach to physical modelling: damage and failure under high-rate loading. *Thin-Walled Structures*, 179, p.109589.
 189. Davey, K., Zhang, J. and Darvizeh, R., 2022. Fracture mechanics: A two-experiment theory. *Engineering Fracture Mechanics* 271, p.108618.
 190. Davey, K., Darvizeh, R., Akhigbe-Midu, O. and Sadeghi, H., 2022. Scaled cohesive zone models for fatigue crack propagation. *International Journal of Solids and Structures* 256, p.111956.
 191. Zhou, R., Lu, Y., Wang, L.G. and Chen, H.M., 2021. Mesoscale modelling of size effect on the evolution of fracture process zone in concrete. *Engineering Fracture Mechanics*, 245, p.107559.
 192. Busari, Y.O., Manurung, Y.H., Leitner, M., Shuaib-Babata, Y.L., Mat, M.F., Ibrahim, H.K., Simunek, D. and Sulaiman, M.S., 2022. Numerical Evaluation of Fatigue Crack Growth of Structural Steels Using Energy Release Rate with VCCT. *Applied Sciences*, 12(5), p.2641.
 193. Kim, S.K., Lee, C.S., Kim, J.H., Kim, M.H., Noh, B.J., Matsumoto, T. and Lee, J.M., 2015. Estimation of fatigue crack growth rate for 7% nickel steel under room and

- cryogenic temperatures using damage-coupled finite element analysis. *Metals*, 5(2), pp.603-627.
194. Elber, W., 1971. The significance of fatigue crack closure.
 195. Aursand, M. and Skallerud, B.H., 2021. Mode I stress intensity factors for semi-elliptical fatigue cracks in curved round bars. *Theoretical and Applied Fracture Mechanics*, 112, p.102904.
 196. Ahmed, T., Yavuz, A. and Turkmen, H.S., 2021. Fatigue crack growth simulation of interacting multiple cracks in perforated plates with multiple holes using boundary cracklet method. *Fatigue & Fracture of Engineering Materials & Structures*, 44(2), pp.333-348.
 197. Wheeler, O.E., 1972. Spectrum loading and crack growth.
 198. Beden, S.M., Abdullah, S. and Ariffin, A.K., 2009. Review of fatigue crack propagation models for metallic components. *European Journal of Scientific Research*, 28(3), pp.364-397.
 199. Cui, W., 2002. A state-of-the-art review on fatigue life prediction methods for metal structures. *Journal of marine science and technology*, 7(1), pp.43-56.
 200. Blažić, M., Maksimović, S., Petrović, Z., Vasović, I. and Turnić, D., 2014. Determination of fatigue crack growth trajectory and residual life under mixed modes. *Strojniški vestnik-Journal of Mechanical Engineering*, 60(4), pp.250-254.
 201. DEMIR, O., Ayhan, A.O., Sedat, I.R.I.C. and Lekesiz, H., 2018. Evaluation of mixed mode-I/II criteria for fatigue crack propagation using experiments and modeling. *Chinese Journal of Aeronautics*, 31(7), pp.1525-1534.
 202. Richard, H.A., Schramm, B. and Schirmeisen, N.H., 2014. Cracks on mixed mode loading—theories, experiments, simulations. *International Journal of Fatigue*, 62, pp.93-103.
 203. Rozumek, D. and Macha, E., 2009. A survey of failure criteria and parameters in mixed-mode fatigue crack growth. *Materials Science*, 45(2), pp.190-210.
 204. Sih, G.C., 1974. Strain-energy-density factor applied to mixed mode crack problems. *International Journal of Fracture*, 10(3), pp.305-321.
 205. Hussain, M.A., Pu, L. and Underwood, J., 1974. Strain Energy Release Rate for. In *Proceedings of the 1973 National Symposium on Fracture Mechanics, University of Maryland, College Park, Md., 27-29 Aug. 1973* (Vol. 559, p. 2).
 206. Chang, K.J., 1981. On the maximum strain criterion—a new approach to the angled crack problem. *Engineering Fracture Mechanics*, 14(1), pp.107-124.

207. Carpinteri, A. and Spagnoli, A., 2004. A fractal analysis of size effect on fatigue crack growth. *International Journal of Fatigue*, 26(2), pp.125-133.
208. Paggi, M. and Carpinteri, A., 2009. Fractal and multifractal approaches for the analysis of crack-size dependent scaling laws in fatigue. *Chaos, Solitons & Fractals*, 40(3), pp.1136-1145.
209. Montagnoli, F., Invernizzi, S. and Carpinteri, A., 2019, September. Fractality and size effect in fatigue damage accumulation: Comparison between Paris and Wöhler perspectives. In *Conference of the Italian Association of Theoretical and Applied Mechanics* (pp. 188-196). Cham: Springer International Publishing.
210. BS 7910:201 'Guide to Methods for Assessing the Acceptability of Flaws in Metallic Structures'
211. API. Recommended practice for fitness-for-service. API 579. Washington, DC: American Petroleum Institute, 2000.
212. Sajith, S., Murthy, K.S.R.K. and Robi, P.S., 2020. Experimental and numerical investigation of mixed mode fatigue crack growth models in aluminium 6061-T6. *International Journal of Fatigue*, 130, p.105285.
213. Solob, A., Grbović, A., Božić, Ž. and Sedmak, S.A., 2020. XFEM based analysis of fatigue crack growth in damaged wing-fuselage attachment lug. *Engineering Failure Analysis*, 112, p.104516.
214. Sajith, S., Shukla, S.S., Murthy, K.S.R.K. and Robi, P.S., 2020. Mixed mode fatigue crack growth studies in AISI 316 stainless steel. *European Journal of Mechanics -A/ Solids*, 80, p.103898.
215. Fageehi, Y.A. and Alshoaibi, A.M., 2020. Numerical simulation of mixed-mode fatigue crack growth for compact tension shear specimen. *Advances in Materials Science and Engineering*, 2020.
216. Maksimović, K., Nikolić, V. and Maksimović, S., 2004. Efficient computation method in fatigue life estimation of damaged structural components. *Facta universitatis-series: Mechanics, Automatic Control and Robotics*, 4(16), pp.101-114.
217. Li, H., Gao, J. and Li, Q., 2018. Fatigue of friction stir welded aluminum alloy joints: a review. *Applied Sciences*, 8(12), p.2626.
218. El-Morsy, A.W., Ghanem, M. and Bahaitham, H., 2018. Effect of friction stir welding parameters on the microstructure and mechanical properties of AA2024-T4 aluminum alloy. *Engineering, Technology & Applied Science Research*, 8(1), pp.2493-2498.

219. Altamura, A. and Beretta, S., 2012. Reliability assessment of hydraulic cylinders considering service loads and flaw distribution. *International Journal of Pressure Vessels and Piping*, 98, pp.76-88.
220. Budden, P.J., Sharples, J.K. and Dowling, A.R., 2000. The R6 procedure: recent developments and comparison with alternative approaches. *International Journal of Pressure Vessels and Piping*, 77(14-15), pp.895-903.
221. Boiler, A.S.M.E. and Code, P.V., 2010. Section VIII, Division 2 and Annex 5A, "Linearization of Stress Results for Stress Classification," *The American Society of Mechanical Engineers*.
222. Hatanaka, K., Shimizu, S. and Nagae, A., 1983. Size effect on rotating bending fatigue in steels. *Bulletin of JSME*, 26(218), pp.1288-1295.